IntechOpen

Different Types of Field-Effect Transistors

Theory and Applications

Edited by Momcilo M. Pejovic
and Milic M. Pejovic

DIFFERENT TYPES OF FIELD-EFFECT TRANSISTORS - THEORY AND APPLICATIONS

Edited by **Momčilo M. Pejović**
and **Milić M. Pejović**

Different Types of Field-Effect Transistors - Theory and Applications
http://dx.doi.org/10.5772/65626
Edited by Momcilo M. Pejovic and Milic M. Pejovic

Contributors

Shovon Pal, Arne Ludwig, Andreas D. Wieck, Sascha R. Valentin, Vladimir Gennadievich Popov, Jonathan Sayago, Zhihui Yi, Miguel Dominguez, José Alberto Luna López, Francisco Flores, Pedro Rosales, Mario Moreno, Alfonso Torres, Toshihiro Yoshizumi, Yuji Miyahara, Ravindiran Munusami, Jingjing Chang, Zhenhua Lin, Chunfu Zhang, Yue Hao, Md. Kawsar Alam, Muhammad Navid Anjum Aadit, Sharadindu Gopal Kirtania, Farhana Afrin, Quazi Deen Mohd Khosru, Philippe Gaubert, Akinobu Teramoto

© The Editor(s) and the Author(s) 2017
The moral rights of the and the author(s) have been asserted.
All rights to the book as a whole are reserved by INTECH. The book as a whole (compilation) cannot be reproduced, distributed or used for commercial or non-commercial purposes without INTECH's written permission.
Enquiries concerning the use of the book should be directed to INTECH rights and permissions department (permissions@intechopen.com).
Violations are liable to prosecution under the governing Copyright Law.

Individual chapters of this publication are distributed under the terms of the Creative Commons Attribution 3.0 Unported License which permits commercial use, distribution and reproduction of the individual chapters, provided the original author(s) and source publication are appropriately acknowledged. If so indicated, certain images may not be included under the Creative Commons license. In such cases users will need to obtain permission from the license holder to reproduce the material. More details and guidelines concerning content reuse and adaptation can be foundat http://www.intechopen.com/copyright-policy.html.

Notice

Statements and opinions expressed in the chapters are these of the individual contributors and not necessarily those of the editors or publisher. No responsibility is accepted for the accuracy of information contained in the published chapters. The publisher assumes no responsibility for any damage or injury to persons or property arising out of the use of any materials, instructions, methods or ideas contained in the book.

First published in Croatia, 2017 by INTECH d.o.o.
eBook (PDF) Published by IN TECH d.o.o.
Place and year of publication of eBook (PDF): Rijeka, 2019.
IntechOpen is the global imprint of IN TECH d.o.o.
Printed in Croatia

Legal deposit, Croatia: National and University Library in Zagreb

Additional hard and PDF copies can be obtained from orders@intechopen.com

Different Types of Field-Effect Transistors - Theory and Applications
Edited by Momcilo M. Pejovic and Milic M. Pejovic
p. cm.
Print ISBN 978-953-51-3175-5
Online ISBN 978-953-51-3176-2
eBook (PDF) ISBN 978-953-51-4804-3

We are IntechOpen,
the first native scientific
publisher of Open Access books

3,250+
Open access books available

106,000+
International authors and editors

112M+
Downloads

151
Countries delivered to

Our authors are among the
Top 1%
most cited scientists

12.2%
Contributors from top 500 universities

CLARIVATE ANALYTICS
BOOK CITATION INDEX
INDEXED

WEB OF SCIENCE™

Selection of our books indexed in the Book Citation Index
in Web of Science™ Core Collection (BKCI)

Interested in publishing with us?
Contact book.department@intechopen.com

Numbers displayed above are based on latest data collected.
For more information visit www.intechopen.com

Meet the editor

Editor, Momcilo M. Pejovic received his BSc degree in Physics at the University of Belgrade, Serbia, and his MSc and PhD degrees in Electronics at the University of Nis, Serbia, in 1968, 1977, and 1980, respectively. In 1968, he worked at Electronic Industry Nis, Serbia. Between 1973 and 2011, he has worked at the Faculty of Electronic Engineering, University of Nis, as a professor of Physics and is now currently retired. He has authored and coauthored 15 books and more than 250 research papers, among which more than 115 papers have been published in international journals. His research interests include the reliability of field-effect transistors, application of MOSFET dosimeters, characterization of vacuum and gas-filled electrical devices and electrical discharge, and recombination processes in the afterglow periods in gases.

Editor, Milic M. Pejovic received his BSc and MSc degrees in Electronics at the University of Nis, Serbia, and PhD degree in Electronics at the University of Belgrade, Serbia, in 1999, 2003, and 2007, respectively. In 2002, he worked for Philips Semiconductor Company, Southampton, UK, in the DVD application sector. In 2007, he worked in Tyndall National Institute as visiting researcher. Currently, he is working as an assistant professor at the Faculty of Electronic Engineering, University of Nis. He has authored or coauthored more than 55 research papers, including 40 papers in international journals and coauthored 2 books. His research interests include process control and measurements as well as the reliability of field-effect transistors and MOSFET dosimeters and electrical characterization of vacuum and gas-filled components.

Contents

Preface

In 1959, Atalla and Kahng at Bell Labs produced the first successful field-effect transistor (FET), which had been long anticipated by other researchers, by overcoming the “surface states" that blocked electric fields from penetrating into the semiconductor material. Very quickly, they became the fundamental basis of digital electronic circuits. Up to this point, there are more than 20 different types of field-effect transistors, which are incorporated in various applications found in everyday’s life. Based on this fact, this book was designed to overview some of the concepts regarding FETs that are currently used as well as some concepts that are still being developed.

The first section “Field-Effect Transistor Theory" provides methodologies related to carrier mobility, one of the most important parameters of field-effect transistors. Carrier mobility, also known as carrier ability to move through the crystal, further defines electrical performances of the device. The knowledge regarding carrier mobility is very important in order to understand the physics of conduction mechanisms inside semiconductor devices, which further provides modeling of a single transistor and more complex circuits as well. Convenient methods for mobility measurements and conduction parameter extraction are also covered in this chapter. In addition, this section gives additional considerations of a new type of field-effect transistor with a gate and a channel on a basis of two-dimensional systems of carriers. The key point of the device is that the systems are different. In particular, they are formed in different quantum wells or valleys of the carrier spectrum.

In the section “High Electron Mobility Transistors," the focus is given to high electron mobility transistors, which undergo intensive attention in high-speed and high-power applications. HEMT devices are competent with traditional field-effect transistors and always replace traditional FETs due to their excellent performance at high frequencies. This chapter presents different structures of high electron mobility transistors as well as working principles. Furthermore, some of the latest researches on HEMTs and future trends are also covered in this section. Further, quantum mechanical phenomenon was reviewed, which induces various electrical and optical properties in low-dimensional semiconductor nanostructures such as high electron mobility transistors. This section is concluded with future trends in production of high electron mobility transistors, which is based on novel approach toward new materials and device structures in order to make the device more suitable for faster device operation with high frequency.

The section “Thin-Film Transistors" deals with the most common problems in production of thin-film transistors such as impact of metal-semiconductor interface, which can be further applied for other types of field-effect transistors. In this chapter, some alternatives to improve this interface are analyzed. Also, the influence of this interface on the electrical stability of these devices is presented.

The section “Organic Field-Effect Transistors" reviews the concepts of organic field-effect transistor physical mechanisms, materials, and fabrication process. In recent years, organic field-effect transistors have received much attention in various applications. The main effort is focused to achieve device performance with high charge carrier mobility and good stability. It is expected that proper combination of organic semiconductor materials and fabrication techniques could lead to production of high-speed devices, which can be used in various applications.

In the section “Applications," some examples regarding possible applications of different types of field-effect transistors in different fields of interest, such as gas-sensitive field-effect transistors as well as concepts of biosensors based on transistor structures with relevance in the field of easy-to-use, portable, and user-friendly devices for preventive personalized medical applications and point-of-care testing, are given.

The editors hope that the publication *Different Types of Field-Effect Transistors - Theory and Applications* could be a useful tool for researchers in related areas.

Prof. Dr. Momčilo M. Pejović and Dr. Milić M. Pejović
University of Niš
Faculty of Electronic Engineering
Niš, Serbia

Section 1

Field-Effect Transistor Theory

Carrier Mobility in Field-Effect Transistors

Philippe Gaubert and Akinobu Teramoto

Additional information is available at the end of the chapter

http://dx.doi.org/10.5772/67885

Abstract

Authors investigate the carrier mobility in field-effect transistors mainly when fabricated on Si(110) wafers. They showed that the methods developed to extract the conduction parameters cannot be implemented for Si(110) p-MOSFETs. Authors then developed a more accurate mobility model able to simulate not only the drivability but also the transconductance for these same devices. The study of the relation between the mobility, channel direction and wafer orientation revealed that the channel direction had a significant impact on the mobility for transistors fabricated on Si(110) wafers, the highest electron and hole mobilites being obtained for a channel along the <100> and <110> directions, respectively. No relations were found for Si(100) wafers. The study of the dependence of the scattering mechanism limiting the mobility in Si(110) n-MOSFETs showed that the Coulomb and surface roughness scattering mechanisms were responsible for the degradation of the mobility when compared to the one on Si(100) wafers. Finally, the measurement of the mobility in an accumulation-mode MOSFETs is not straightforward since a bulk contribution, owing to the SOI layer, is adding to channel current. A methodology has been successfully implemented that led to the experimental verification of the universal behaviour of the mobility in an accumulation layer.

Keywords: mobility, electron, hole, silicon, temperature, crystallographic orientation, channel direction, scattering mechanism, modeling, accumulation, extraction, (100), (110)

1. Introduction

The concept of employing an electric field to modulate the conductivity of a channel has been proposed first by Lilienfeld during the 1930s [1], long before its practical fabrication by Shockley et al. in 1947 [2]. Since, the field-effect transistor has taken several directions and is at the root of various devices such as the metal-oxide-semiconductor FET (MOSFET) [3], dual gate MOSFET [4], junction FET [5], high electron mobility transistor [6], four-gate transistor [7] and so on. Nevertheless, the most important parameter for all these devices is the mobility of

INTECH
open science | open minds

© 2017 The Author(s). Licensee InTech. This chapter is distributed under the terms of the Creative Commons Attribution License (http://creativecommons.org/licenses/by/3.0), which permits unrestricted use, distribution, and reproduction in any medium, provided the original work is properly cited.

the carrier flowing inside the channel. Their mobility, also known as their ability to move through the crystal, will define the electrical performances of the device. The mobility is consequently a paramount parameter, and its good knowledge is of prime importance to first understand the physics underlying the conduction mechanisms inside semiconductor devices and second to be able to model and simulate a single transistor and in turn more complex circuits. The mobility in field-effect transistors hinges on various physical and environmental parameters that we propose to investigate for MOSFETs fabricated on (100) and (110) silicon-oriented wafers.

In Section 2, the method to measure the mobility is briefly reviewed for different structures, while Section 3 investigates several methods to extract the conduction parameters such as the low field mobility in Si(100) and Si(110) p-MOSFETs. Thus, its modeling is presented in Section 4 for the same devices. Results regarding the impact of the channel direction and wafer orientation on the mobility are investigated in Section 5 while the impact of the temperature is reported in Section 6 for Si(110) n-MOSFETs. Recently, devices based on the majority carriers rather than the minority ones to generate the current showed promising results. A methodology to extract their mobility is presented in Section 7 and is applied to accumulation-mode Si (100) p-MOSFETs. Finally, Section 8 concludes the chapter.

2. Experimental measurement of the mobility

The knowledge of the experimental mobility of carriers that are flowing inside the channel of a FET is essential for the development of semiconductor devices and in turn electronic circuits. The direct measurement of the effective mobility μ_{eff} is not possible, but its calculation is enabled through the measurement of the drain current I_d—gate voltage V_g characteristic and of the gate-channel capacitance C as a function of the gate voltage. Both characteristics can be measured at V_d = 100 mV on a large gate transistor with at least a gate length L and gate width W above 50 μm in order to allow an accurate measurement of the capacitance. The substrate, source and drain electrodes are grounded, and the measurement of the capacitance is carried out on the gate electrode side at relatively low frequencies f between 1 and 100 kHz to neglect the serie resistances. Thus, the inversion charge Q_{inv} per unit area is calculated from the $C - V_g$ characteristic

$$Q_{inv}(V_g) = \int_{-\infty}^{V_g} C(Vg)dV_g. \tag{1}$$

The effective mobility μ_{eff} is finally calculated from

$$\mu_{eff}(V_g) = \frac{L}{W}\frac{I_d(V_g)}{V_d Q_{inv}(V_g)}. \tag{2}$$

At this stage, the effective mobility can be plotted as a function of the carrier sheet density by dividing the inversion charge Q_{inv} by the elementary charge q. It can also be plotted as a function of the transverse effective electric field E_{eff} that is calculated as follows:

$$E_{\mathrm{eff}}(V_g) = \frac{1}{\varepsilon_{\mathrm{Si}}\varepsilon_0}[Q_{\mathrm{dep}} + \eta Q_{\mathrm{inv}}(V_g)], \tag{3}$$

where Q_{dep} is the depletion charge per unit area, $\varepsilon_{\mathrm{Si}}$ is the dielectric constant of the silicon, ε_0 is the permittivity of the vacuum, and η is a term referring to the averaging of the transverse electric field over the carrier distribution inside the conduction channel. In Eq. (3), the depletion charge Q_{dep} is theoretically calculated from the doping concentration N_{sub} of the channel. It is expressed as follows:

$$Q_{\mathrm{dep}} = \sqrt{\frac{4\varepsilon_{\mathrm{Si}}\varepsilon_0\phi_B N_{\mathrm{sub}}}{q}}, \tag{4}$$

with

$$\phi_B = \frac{k_B T}{q}\ln\left(\frac{N_{\mathrm{sub}}}{n_i}\right), \tag{5}$$

being the bulk Fermi energy. In Eq. (5), k_B is the Boltzmann constant, T is the temperature in Kelvin, and n_i is the intrinsic carrier concentration. Takagi et al. [8] confirmed experimentally that in Eq. (3), η is equal to 1/3 for hole and to 1/2 for electron on Si(100) wafers [9]. Regarding Si (110) wafers, η is generally taken equal to 1/3 for both hole [3, 10] and electron [11].

Contrary to bulk transistors for which the methodology has been described previously, the substrate of transistors fabricated on silicon-on-insulator (SOI) wafers sometimes cannot be accessed and then cannot be grounded. The back-gate cannot be biased and can be floating as long as the applied gate voltage is large enough to neglect the impact of the back-gate [12]. The expression of the depletion charge Q_{dep} given by Eq. (4) must be rearranged in Eq. (3) since the buried oxide is preventing the expansion of the depletion. If the depletion is expending deeper than the buried oxide, Q_{dep} is given by $qN_{\mathrm{sub}}t_{\mathrm{SOI}}$ where t_{SOI} is the thickness of the SOI layer.

In the case of devices involving the majority carriers rather than the minority ones such as accumulation-mode transistors that will be studied in Section 7, the entire SOI layer is neutral when the accumulation layer is formed. The depletion charge Q_{dep} in Eq. (3) must be removed, and the calculation is involving the sole accumulation charge Q_{acc} [13, 14]. Eqs. (3) and (4) are rewritten as follows:

$$\mu_{\mathrm{eff}}(V_g) = \frac{L}{W}\frac{I_d(V_g)}{V_d Q_{\mathrm{acc}}(V_g)} \tag{6}$$

and

$$E_{\mathrm{eff}}(V_g) = \frac{\eta Q_{\mathrm{acc}}(V_g)}{\varepsilon_{\mathrm{Si}}\varepsilon_0}. \tag{7}$$

3. Mobility extraction methods

The knowledge of the conduction parameters is useful to model the drivability of a MOSFET and in turn simulate complex circuits. All extraction methods rely on the knowledge of the $I_d - V_g$ drain current-gate voltage characteristic measured for various gate lengths L and gate widths W.

The calculation procedures are based on the expression of the drain current in the linear region for a gate overdrive voltage $V_g - V_{th}$ (V_{th} being the threshold voltage) greater than the drain voltage V_d ($V_g - V_{th} \gg V_d$). In this range, the drain current I_d is expressed as follows:

$$I_d = \mu_{eff} C_{ox} \frac{W - \Delta W}{L - \Delta L} (V_g - V_{th})(V_d - I_d R_{acc}). \tag{8}$$

where R_{acc} is the parasitic access resistances located at the source and drain contacts and C_{ox} is the oxide capacitance. ΔW and ΔL are, respectively, the width and length gate channel reduction. In Eq. (8), the effective mobility μ_{eff} is generally replaced by the well known [15]:

$$\mu_{eff} = \frac{\mu_0}{1 + \theta(V_g - V_{th})}, \tag{9}$$

where μ_0 is the low field mobility and θ is the mobility attenuation factor.

Depending on the extraction method, it is possible to obtain the low field mobility μ_0, the mobility attenuation factor θ, the parasitic access resistance R_{acc} in series with the intrinsic resistance of the channel of the transistor, the channel width reduction ΔW and the channel length reduction ΔL.

3.1. Silicon wafers with a (100) crystallographic orientation

Four different extraction methods have been used to extract the conduction parameters in p-MOSFETs fabricated on (100) silicon-oriented wafers. These methods are the Schreutelkamp method [16, 17], the interpolation method explained in Tsividis book [18], the Ghibaudo method [19] and finally the Ciofi method [20].

The Schreutelkamp method is based on Eqs. (8) and (9) and requires the calculation of intermediate parameters around a given gate overdrive voltage $V_g - V_{th}$ that has been measured on several transistors featuring various gate length L for a given gate width W. A representation of this method is shown in **Figure 1** for $V_g - V_{th}$ = 1 V. I_d^{-1} is plotted as a function of the gate length L, and the intersection with the vertical and horizontal axis is collected as shown in the inset of **Figure 1**. The low field mobility μ_0 is extracted from the slope of the linear plot $(1/I_d)_{int}/L_{int}$ versus $(V_g - V_{th})^{-1}$, while the mobility attenuation factor θ is obtained from the intersection with the vertical axis. On the other hand, the intersection of the plot L_{int} versus $L_{int}/(1/I_d)_{int}$ with the vertical axis gives the channel length reduction ΔL, and the intersection with the horizontal axis gives the parasitic access resistance R_{acc}. The extracted data according to the Schreutelkamp method on Si(100) p-MOSFETs are reported in **Table 1**. Note that the Schreutelkamp method does not allow the obtaining of the gate width reduction ΔW. The

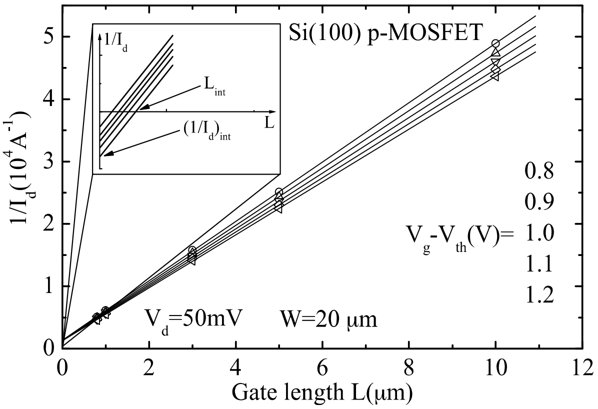

Figure 1. Example of the procedure to obtain L_{int} and $(1/I_d)_{int}$ for the centered V_g–V_{th} = 1 V in the frame of the Schreutlkamp method.

	Schreutelkamp	Interpolation	Ciofi	Ghibaudo
μ_0 (cm^2/Vs)	115	/	114	118
θ (V^{-1})	0.31	/	0.348	0.359
Racc (Ω)	98	106	68.9	67.41
ΔL (μm)	−0.1	−0.128	−0.121	−0.13
ΔW (μm)	/	−0.352	−0.322	−0.331

Table 1. Conduction parameters extracted using several methods for Si(100) p-MOSFETs at V_d = 50 mV [21].

impact of the centered gate overdrive voltage $V_g - V_{th}$ on the conduction parameters has been conducted. The results on the low field mobility μ_0 and channel length reduction ΔL are shown in **Figure 2**. Both values are strongly decreasing when the gate overdrive voltage is increased until $V_g - V_{th}$ = 0.8 V and are reaching a more stable behavior afterwards. For $V_g - V_{th}$ < 0.8 V, the transistor is not working in the linear regime, and Eq. (8) is inaccurate, thus the fast drop. Additionally, the mobility model does not fit accurately the effective mobility, making the calculation even more inaccurate. For $V_g - V_{th}$ > 0.8 V, the low field mobility μ_0 is slightly increasing, while the channel length reduction ΔL is slightly decreasing. The reason is that even if Eq. (8) can be applied, Eq. (9) does not perfectly model the effective mobility. For each centered $V_g - V_{th}$, the parameters that are modeling the mobility are slightly changing in order to accurately fit the effective mobility according to the centered $V_g - V_{th}$. In turns, the channel length reduction ΔL and the low field mobility μ_0 are not constant. An equivalent behavior has been also acknowledged when the mobility attenuation factor θ and the parasitic access resistance R_{acc} have been plotted as a function of the centered gate overdrive voltage $V_g - V_{th}$.

Like the previous method, the one developed by Ghibaudo is also based on the same equations; however, the calculation requires the derivative of the $I_d - V_g$ curves for different gate

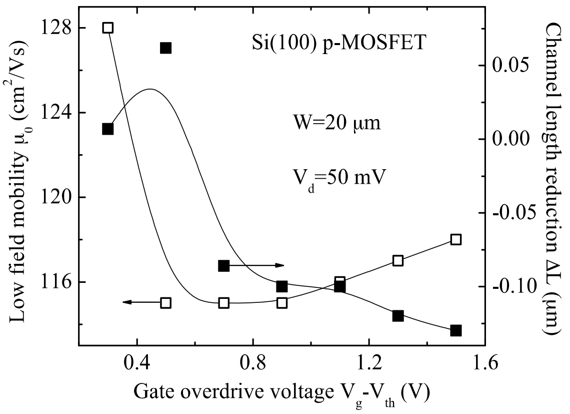

Figure 2. Evolution of the extracted low field mobility μ_0 and channel length reduction ΔL as a function of the centered gate overdrive voltage V_g–V_{th} in the frame of the Schreutlkamp method.

length L and gate width W, that is the transconductance g_m. Data measured around the threshold voltage are used. The plots $I_d/g_m^{0.5}$ and $g_m^{-0.5}$ as a function of $V_g - V_{th}$ allow the extraction of the intermediate parameters G_m and θ^*, respectively, since $I_d/g_m^{0.5} = (G_mV_d)^{0.5}(V_g - V_{th})$ and $g_m^{-0.5}=(G_mV_d)^{-0.5}[1 + \theta^*(V_g - V_{th})]$. Note that, the linear fittings are realized in the range $V_g>V_{th}$. The slope of the former fitting gives G_m, while the latter one allows the extraction of θ^*. Thus, the intersection of the plot G_m versus W with the horizontal axis gives the gate width reduction ΔW, and the intersection of the plot $G_m{}^{-1}$ versus L gives the gate length reduction ΔL. Finally, the mobility attenuation factor θ and the parasitic access resistances R_{acc} are obtained from the plot θ^* versus G_m since $\theta^*=\theta + G_mR_{acc}$. θ^* is the extrinsic mobility attenuation factor. The extracted parameters for Si(100) p-MOSFETs using the Ghibaudo method are reported in **Table 1**.

While the Ghibaudo method is making use of the derivative, the extraction method developed by Ciofi is based on the numerical analysis of the discretization of the $I_d - V_g$ characteristics and requires here as well the calculation of two intermediate parameters, K and H. They are extracted from the plot V_d/I_d versus $V_g - V_{th}$ for several gate lengths L and gate widths W since $V_d/I_d=K^{-1}((V_g - V_{th})^{-1} + H)$. H and K are related together by $H=\theta + KR_{acc}$, and the plot H versus K allows the obtaining of the mobility attenuation factor θ and the parasitic access resistances R_{acc}. Plotting K^{-1} versus L and K versus W, respectively, gives the gate length reduction ΔL and the gate width reduction ΔW at the intersection with the horizontal axis. Data measured at relatively high gate overdrive voltage for Si(100) p-MOSFETs have been used, and the results of the Ciofi method are reported in **Table 1**. θ^* versus G_m for the Ghibaudo method and H versus K for the Ciofi method have been plotted on the same **Figure 3**. The results in **Figure 3** are almost identical for both methods, so are the units. In fact, K and G_m are the transconductance parameter and equals to $\mu_0C_{ox}W/L$. Moreover, the similarity between both methods is obvious since $\theta + KR_{acc}=H=\theta^*=\theta + G_mR_{acc}$. Note that, for both the Ghibaudo and the Ciofi methods, the knowledge of the threshold voltage V_{th} prior their implementation is not mandatory since the threshold voltage V_{th} can be extracted during the procedures described above.

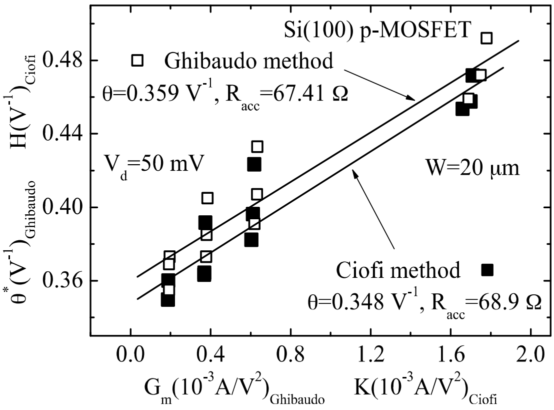

Figure 3. Fitting of $\theta^* = f_g(G_m)$ for the Ghibaudo method and $H = f_c(K)$ for the Ciofi method to obtain the access the parasitic access resistance R_{acc} and the mobility attenuation factor θ [21].

Even if the method is quite limited since the low field mobility μ_0 and the mobility attenuation factor θ cannot be evaluated, the interpolation method proposed in the book by Tsividis has been still implemented for Si(100) p-MOSFETs and the results are reported in **Table 1**.

The four methods have been successfully employed to extract the conduction parameters although a disagreement is visible in regards to the parasitic access resistances R_{acc}. The similarity between the Ciofi method and the Ghibaudo method leads to very similar data and in turn an undervaluation of the parasitic access resistances R_{acc} when compared with the values obtained using the two other methods.

3.2. Silicon wafers with a (110) crystallographic orientation

The extraction methods previously described have been implemented for p-MOSFETs fabricated on (110) silicon-oriented wafers in order to extract the conduction parameters. The results are reported in **Table 2**, and the extraction methods are consistent. Compared to Si (100) p-MOSFETs, the low field mobility μ_0 for Si(110) p-MOSFETs is almost three times higher, confirming the superiority of the hole mobility on (110) silicon surface [22].

At the same time, the mobility attenuation factor θ is 10 times weaker for Si(110) p-MOSFETs, indicating that the degradation of the effective mobility might be much more pronounced for Si

	Schreutelkamp	Interpolation	Ciofi	Ghibaudo
μ_0 (cm^2/Vs)	303	/	285	281
θ (V^{-1})	0.042	/	0.038	X
R_{acc} (Ω)	48	57.76	63	X
ΔL (μm)	−0.67	−0.44	−0.43	−0.38
ΔW (μm)	/	−0.39	−0.42	−0.39

Table 2. Conduction parameters extracted using several methods for Si(110) p-MOSFETs at V_d = 100 mV [21].

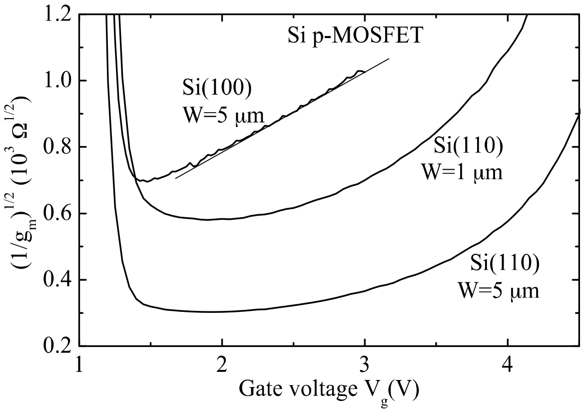

Figure 4. Plot of $g_m^{-0.5}$ as a function of the gate overdrive voltage V_g–V_{th} for transistors fabricated on Si(100) and Si(110) wafers. The linear fitting of the curve allows the extraction of the intermediate parameter G_m in the frame of the Ghibaudo method. L = 10 μm, V_d = 50 mV for Si(100) and V_d = 100 mV for Si(110) transistors.

(100) p-MOSFETs. However, the main result is the impossibility to extract the parasitic access resistances R_{acc} and the mobility attenuation factor θ with the Ghibaudo method, whereas the method has been successfully employed for Si(100) p-MOSFETs [23]. Indeed, as shown in **Figure 4**, whereas the extraction of G_m from $I_d/g_m^{0.5}$ has been possible, and in turn the extraction of the low field mobility μ_0, the gate length reduction ΔL and the gate width reduction ΔW, the linear fitting of $g_m^{-0.5}$ versus the gate voltage could not be done. Concerning the Schreutelkamp method, the same procedure as previously described has been carried out and a behavior similar to the one noticed for Si(100) p-MOSFETs has been acknowledged.

4. Modeling of the mobility

4.1. Silicon wafers with a (100) crystallographic orientation

The modeling of the hole mobility using Eq. (9) with the data reported in **Table 1** (μ_0 = 115 cm^2/Vs and θ = 0.35 V^{-1}) has been carried out and compared with the experimental data of the effective mobility for Si(100) p-MOSFETs. The result is reported with the dashed line in **Figure 5** and demonstrates the great accuracy of the extraction method and of the model provided by Eq. (9) when the effective electric field E_{eff} is above 0.3 MV/cm. Below this value, the model is inaccurate since the effective mobility is limited by the Coulomb scatterings, scatterings that are not taken into account in Eq. (9). The conduction parameters (μ_0 = 115 cm^2/Vs, θ = 0.35 V^{-1}, R_{acc} = 70 Ω, ΔL = −0.33 μm, ΔW = −0.13 μm, V_d = 50 mV and W = 20 μm) have been implemented in Eqs. (8) and (9) to model the drain current I_d in p-MOSFETs with different gate length L and the transconductance g_m has been calculated afterwards. The results are shown in **Figure 6** with the thick full lines. At the exception of $V_g<V_{th}$, the modeling is greatly fitting the experimental data for either I_d or g_m. The maximum of the transconductance g_m cannot be estimated because Eq. (9) does not model the Coulomb scatterings

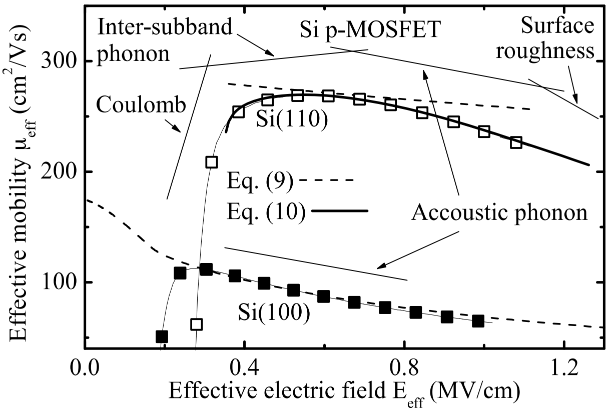

Figure 5. Effective mobility μ_{eff} as a function of the effective electric field E_{eff} for Si(100) and Si(110) p-MOSFETs. The dashed lines report the modeling carried out with Eq. (9), $\mu_0 = 115$ cm^2/Vs and $\theta = 0.35$ V^{-1} for the Si(100) wafers and $\mu_0 =$ 285 cm^2/Vs, $\theta = 0.038$ V^{-1} for the Si(110) ones. The full line reports the modeling with Eq. (10) and $\mu_0 = 280$ cm^2/Vs, $\theta_1 = 0$ V^{-1}, $\theta_2 = 0.05$ V^{-2}, and $\alpha = 0.04$ for Si(110) wafers.

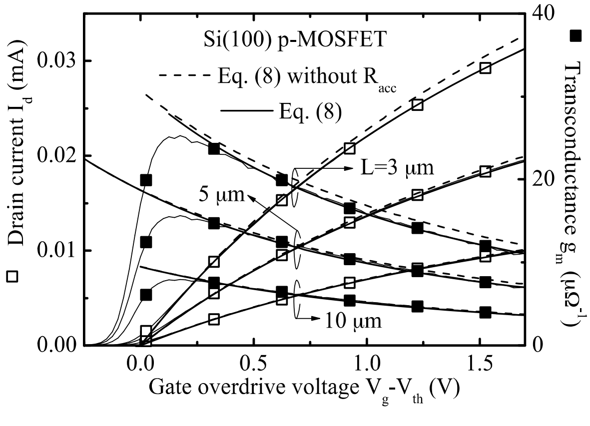

Figure 6. Drain current I_d (left) and transconductance g_m (right) as a function of the gate overdrive voltage V_g–V_{th} for Si (100) p-MOSFETs featuring different gate length. The lines are the modeling carried out with $\mu_0 = 115$ cm^2/Vs, $\theta = 0.35$ V^{-1}, Eqs. (9) and (8) with (full thick lines) and without (dashed lines) taking into account the parasitic access resistances $R_{acc} = 70\ \Omega$. $\Delta L = -0.33$ μm, $\Delta W = -0.13$ μm, $V_d = 50$ mV, W = 20 μm.

mechanisms. A second simulation has been calculated without taking into account the parasitic access resistances R_{acc} in Eq. (8), and the results are shown with the dashed line in **Figure 6**. The fact to neglect the parasitic access resistances R_{acc} leads to a discrepancy between the model and the experimental data that is enhanced when the size of the device is shrinked.

4.2. Silicon wafers with a (110) crystallographic orientation

The modeling of the mobility has been carried out for the Si(110) wafers with the parameters obtained in **Table 2**. $\mu_0 = 285$ cm^2/Vs and $\theta = 0.038$ V^{-1} have been implemented in Eq. (9), and the result is shown with the dashed line in **Figure 5** and does not provide a great accuracy like it was the case for Si(100) wafers. Nevertheless, the procedure has been moved forward, and the simulation of the drain current I_d and the transconductance g_m has been calculated with Eq. (8) and the following parameters: $\mu_0 = 285\ cm^2/Vs$ and $\theta = 0.038\ V^{-1}$, $\Delta L = -0.4\ \mu m$, $\Delta W = -0.4\ \mu m$ and $R_{acc} = 60\ \Omega$. The results for the drain current I_d are shown with the dashed lines in **Figure 7**, while the results for the transconductance g_m are shown in **Figure 8** with the dashed lines. The modeling is accurate at first but strongly divert from the experimental data when the gate overdrive voltage is increased. The use of Eq. (9) does not give at all satisfactory

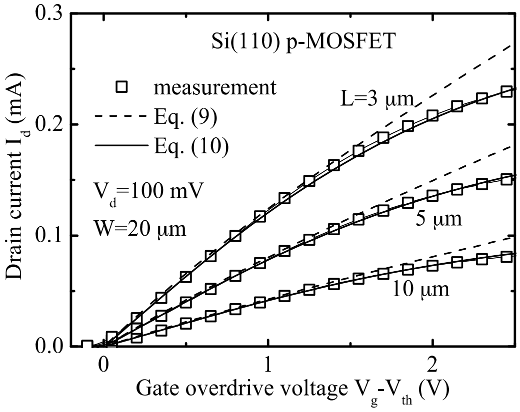

Figure 7. Drain current I_d as a function of the gate overdrive voltage $V_g–V_{th}$ for Si(110) p-MOSFETs featuring different gate length. The dashed lines are the modeling carried out with Eqs. (8), and (9), $\mu_0 = 285\ cm^2/Vs$ and $\theta = 0.038\ V^{-1}$. The full lines are the modeling carried out with Eqs. (1), and (10), $\mu_0 = 280\ cm^2/Vs$, $\theta_1 = 0\ V^{-1}$, $\theta_2 = 0.05\ V^{-2}$, and $\alpha = 0.04$. $\Delta L = -0.4\ \mu m$, $\Delta W = -0.4\ \mu m$ and $R_{acc} = 60\ \Omega$.

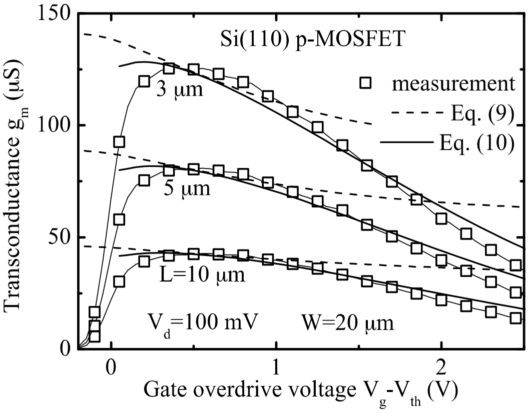

Figure 8. Transconductance g_m as a function of the gate overdrive voltage $V_g–V_{th}$ for Si(110) p-MOSFETs featuring different gate length. The dashed lines are the modeling carried out with Eqs. (8), and (9), $\mu_0 = 285\ cm^2/Vs$ and $\theta = 0.038\ V^{-1}$. The full lines are the modeling carried out with Eq. (8), and (10), $\mu_0 = 280\ cm^2/Vs$, $\theta_1 = 0\ V^{-1}$, $\theta_2 = 0.05\ V^{-2}$, and $\alpha = 0.04$. $\Delta L = -0.4\ \mu m$, $\Delta W = -0.4\ \mu m$ and $R_{acc} = 60\ \Omega$.

agreement with the experiment, especially concerning the transconductance g_m. The well-established model that is Eq. (9) cannot be used to simulate the mobility and thus the drivability of Si(110) p-MOSFETs. Other models [24, 25] have been implemented but did not give enough satisfactory results. Contrary to the (100) orientation for which the single phonon scattering mechanism is limiting the hole mobility over the working range, the hole mobility for the (110) orientation is limited by the Coulomb, phonon and surface roughness scatterings mechanism over the whole measurement range. Thus, a model able to take into account these three mechanisms is required. While Eq. (9), which models only the phonon scattering, is sufficient to simulate the Si(100) p-MOS transistors, a new model including all three scattering mechanisms is needed for the Si(110) wafers.

$\mu_{Coul} = A_{Coul}T^{-1}E_{eff}^{\beta_{Coul}}$ [26] with $\beta_{Coul} \geq 0$ and $\mu_{sr}=A_{sr}E_{eff}^{-2}$ [27] are simple ways to model the Coulomb scatterings and surface roughness scatterings, respectively. A_{Coul} and β_{Coul} are constants associated with the Coulomb scattering mechanism, while A_{sr} is a constant associated with the surface roughness scattering mechanism. T is the temperature. Assuming that the effective electric field E_{eff} is proportional to the gate overdrive voltage $V_g - V_{th}$, the dependence of the several scattering mechanisms can be introduced into Eq. (9), which is already modeling the Coulomb scatterings mechanisms to finally give [21]

$$\mu_{eff} = \mu_0 \frac{A_\alpha (V_g - V_{th})^\alpha}{1 + \theta_1 (V_g - V_{th}) + \theta_2 (V_g - V_{th})^2}. \tag{10}$$

μ_0 is the low field mobility. θ_1 corresponds to the conventional mobility attenuation factor seen in Eq. (9) and is related to the contribution coming from the phonon scatterings. θ_2 is a quadratic mobility attenuation factor related to the surface roughness scatterings. α is a parameter related to the Coulomb scatterings, while A_α equals to 1 and is introduced to maintain the uniformity of the unit system. As shown in **Figure 6** with the full line, Eq. (10) greatly matches the experimental data. The fitting parameters are as follows μ_0 = 280 cm^2/Vs, θ_1 = 0 V^{-1}, θ_2 = 0.05 V^{-2}, and α = 0.04. The simulation of the drain current I_d and the tranconductance g_m has been carried out for Si(110) p-MOSFETs featuring different gate length by implementing Eq. (10) into Eq. (8). μ_0 = 280 cm^2/Vs, θ_2 = 0.05 V^{-2}, α = 0.04, ΔL = −0.4 μm, ΔW = −0.4 μm, R_{acc} = 60 Ω, V_d = 100 mV and W = 20 μm. The results are reported with the full lines in **Figures 7** and **8**. The modeling of the drain current I_d is greatly accurate even for short gate length. The modeling of the transconductance g_m in **Figure 8** is also fairly accurate. Both, the results regarding the drain current I_d and the transconductance g_m testify of the good agreement of Eq. (10). In **Figure 8**, it seems that the maximum of the transconductance g_m, result of α the parameter related to the Coulomb scatterings, can be also calculated. This statement must be taken with care since the maximum of the transconductance is obtained for biases that do not correspond to the linear region, making Eq. (8) obsolete. Actually, the parameter α does not solely reflect the Coulomb scatterings. Indeed, the hole mobility in Si (110) wafers has a peculiar behavior in the form of the inter-subband phonon scatterings. Contrary to the acoustic phonon scatterings that are more and more limiting the mobility with an increase of the effective electric field, the inter-subband phonon scatterings have the specificity to decrease when the effective electric field is increased [21, 28] as sketched in **Figure 5**.

5. Relation between the mobility, the channel direction and the wafer orientation

Inversion-mode fully depleted p- and n-channel silicon-on insulator (SOI) MOSFETs have been fabricated on bonded SOI (100) and (110) crystallographic silicon-oriented wafers. For each wafer, transistors with different channel directions were manufactured. The process flow has been entirely conducted in the clean room of the Fluctuation Free Facility at Tohoku University. 33-mm-diameter wafers have been used after cutting them from 8 inches wafers. The doping concentration has been adjusted to 10^{16} cm^{-3} by ion implantation. The thickness of the SOI layer was 50 nm, and the thickness of the buried oxide was 100 nm. Prior the formation of the 7.5-nm-thick gate oxide by radical oxidation [29] an alkali-free process [22, 30] able to keep the silicon surface flat was used. The roughness of the Si/SiO_2 interface was further reduced by repeating several times the procedure radical oxidation–etching [31]. The procedure has been repeated two times for the Si(100) wafers and four times for the Si(110) ones and led to the same microroughness measured to 0.08 nm. The effective mobility has been measured according to the methodology presented in Section 2 at V_d = 50 mV. Measurements have been carried out on MOSFETs with a gate dimension of W = 100 μm and L = 100 μm.

5.1. Silicon wafers with a (100) crystallographic orientation

The low field mobility μ_0, the mobility attenuation factor θ, the gate length reduction ΔL, the gate width reduction ΔW and the parasitic access resistances R_{acc} have been extracted for Si (100) n- and p-MOSFETs and are available in a previous paper by Gaubert et al. [32]. The Ghibaudo and Ciofi methods have been used. **Figure 9** shows the effective mobility for hole and electron on Si(100) wafers. It is clear that n-MOSFETs own greater performances than p-MOSFETs since the mobility of the former ones is five times higher than the mobility of the latter ones. It is also clear that the channel direction has no impact on the mobility of the n-MOSFETs. However, a slight difference can be noticed for the hole, the highest mobility being measured for a channel along the <100> direction. The direction of choice for the

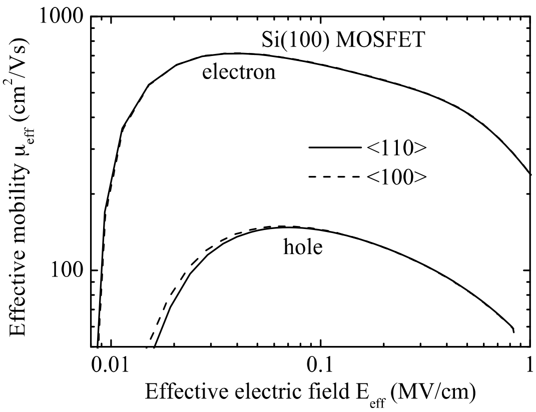

Figure 9. Electron and hole effective mobility μ_{eff} as a function of the effective electric field E_{eff} for Si(100) MOSFETs featuring a channel along the <110> (full lines) and <100> (dashed lines) directions.

http://dx.doi.org/10.5772/67885

electronic manufacturers is the <110> direction and an easy and costless way to slightly enhance performances of electronic devices would be to manufacture p-MOSFETs on Si(100) wafers with a channel following the <100> direction. The shift from the <110> direction for the <100> direction can give rise to a maximum enhancement of 10% of the drivability [12].

5.2. Silicon wafers with a (110) crystallographic orientation

It has been demonstrated in Section 3 that the extraction methods are difficult to set up for p-MOSFETs on Si(110) wafers. Nevertheless, the method proposed by Tsividis has been used for the Si(110) p-MOSFETs while the Ciofi and Ghibaudo method helped extract the conduction parameters for the Si(110) n-MOSFETs. The results are reported in a previous paper by Gaubert et al. [32]. The mobility in Si(110) p-MOSFETs is shown in **Figure 10**. The dependence with the channel is clearly visible. The highest mobility is obtained for a channel following the <110> direction, while the lowest one is obtained for a channel along the <100> direction. Furthermore, an increase in the mobility with the effective electric field can be noticed, especially for the <110> direction, where an increasing limitation by the phonon scatterings was expected. This behavior is caused by the inter-subband phonon scatterings as noticed in Section 4.2. The clear role played by the inter-subband phonon scatterings on limiting the mobility spans on a more visible way in **Figure 10** than in **Figure 5**. The reason is the lower doping concentration of the devices studied in this section that consequently shifts the Coulomb scattering limited mobility to lower effective electric fields. The inter-subband phonon scatterings are explained by the small energetic separation between the two lowest heavy-hole-like subbands, which is favoring the inter-subband transitions assisted by the absorption of optical phonon. This behavior reaches its maximum for a channel along the <110> direction since the holes in this direction have the lowest mass [12].

The $I_d - V_g$ curves for Si(110) n-MOSFETs have been measured, and the results are presented in **Figure 11** along with the corresponding tranconductances g_m. The larger drivability is ascribed to the <100> direction. From Ref. [32], the value of the attenuation factor θ for the Si(100)

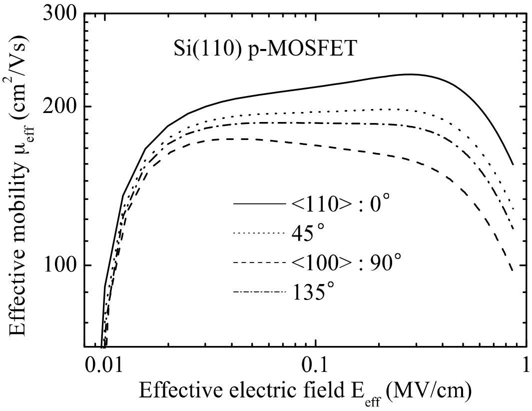

Figure 10. Effective mobility μ_{eff} as a function of the effective electric field E_{eff} for Si(110) p-MOSFETs featuring a channel along several directions.

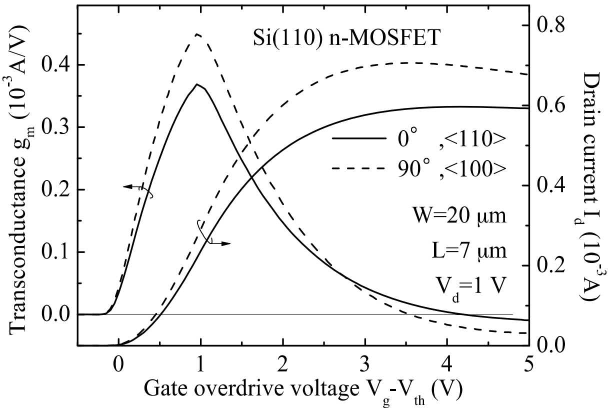

Figure 11. Drain current I_d (right) and transconductance g_m (left) as a function of the gate overdrive voltage V_g–V_{th} for Si (110) n-MOSFETs featuring a channel along the <110> (full lines) and <100> (dashed lines) directions.

n-MOSFETs is 0.175 V^{-1}, while the one obtained for the Si(110) n-MOSFETs is 0.6 V^{-1}. The larger value for Si(110) wafers reflects an unusual degradation of the mobility that makes the drain current I_d saturate and drop at high gate overdrive voltage V_g – V_{th}, as shown in **Figure 11**. The saturation and decrease in the drain current I_d are more pronounced for the <100> direction and find its origin in the balance of the linear product (current is proportional to nμ) between the increase in the number of carriers n and the decrease in the mobility μ. As shown in **Figure 11**, the unusual consequence is a negative transconductance g_m at high voltage. The mobility is shown in **Figure 12**. Like for the Si(110) p-MOSFETs and contrary to the Si(100) n-MOSFETs, there is a dependence between the mobility and the channel direction. The highest mobility is obtained for the <100> direction, and the lowest is obtained for the <110> direction, the opposite trend revealed for Si(110) p-MOSFETs. The surface roughness is limiting in more proportion the mobility of the transistors along the <100> direction and explains the more pronounced drop of the drain current I_d shown in **Figure 11**.

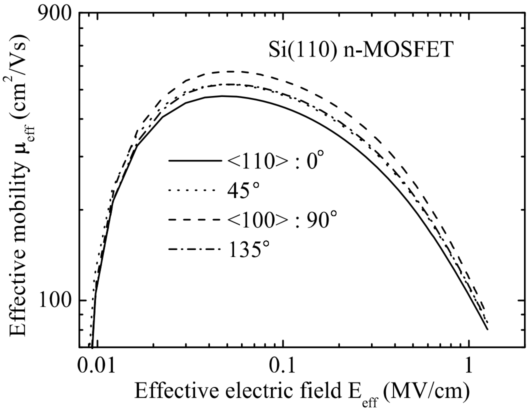

Figure 12. Effective mobility μ_{eff} as a function of the effective electric field E_{eff} for Si(110) n-MOSFETs featuring a channel along several directions.

6. Relation between the mobility and the temperature

It is well known that temperature has a major impact on the performances of MOSFETs. Every scattering mechanisms that are limiting the mobility have a specific response toward the change in temperature as Gaubert et al. demonstrated for Si(110) n-MOSFETs [33]. Contrary to p-MOSFETs fabricated on Si(110) wafers, the mobility of n-MOSFETs on this orientation is limited by the Coulomb scattering in the low range effective electric field, the phonon scattering in the middle range and finally the surface roughness scattering at high effective electric field. With the intention to understand the response of each scattering mechanisms taken individually to the temperature, a study has been conducted on Si(110) n-MOSFETs investigated in the precedent section. Transistors with a channel along the <100> direction have been studied for different temperatures from 213 to 473°K. **Figure 13** reports the drain current I_d and the associated transconductance g_m for three different temperatures. Increasing the temperature degrades the drivability and the transconductance even though a slight improvement in the latter quantity can be acknowledged at high gate voltage. In addition, the peculiar behavior acknowledged in the previous section for Si(110) n-MOSFETs, that is a saturation followed by a drop of the drivability with an increase of the gate voltage, is amplified with a decrease of the temperature and leads to even more negative transconductance in the high bias range. This suggests that the drop of temperature increases the degradation ratio generated by the surface roughness scattering mechanisms. The mobility for different temperatures is shown in **Figure 14**. As expected, the mobility is enhanced when the temperature is reduced. The scattering mechanisms have been studied separately by the means of the modeling. The mobilities shown in **Figure 14** have been modeled according the Matthiessen rule with the three main scattering mechanisms:

$$\frac{1}{\mu_{eff}} = \frac{1}{\mu_{Coul}} + \frac{1}{\mu_{Ph}} + \frac{1}{\mu_{SR}} = \frac{1}{A_{Coul}E_{eff}^{\beta}} + \frac{1}{A_{Ph}E_{eff}^{-0.3}} + \frac{1}{A_{SR}E_{eff}^{\gamma}}. \tag{11}$$

μ_{Coul} is the Coulomb-limited mobility, proportional to E_{eff}^{β} where β is a fitting parameter [34]. μ_{Ph} is the phonon-limited mobility, generally proportional to $E_{eff}^{-0.3}$ [11]. Finally, μ_{SR} is the surface

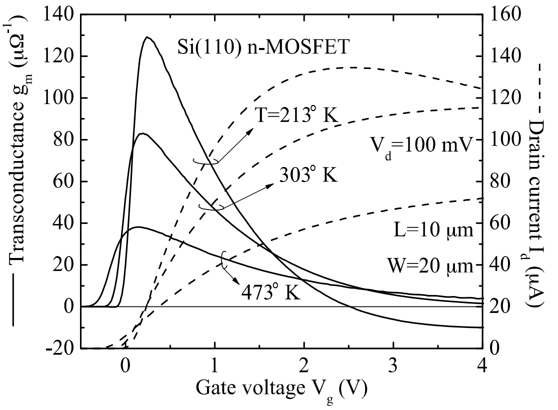

Figure 13. Drain current I_d (right) and transconductance g_m (left) as a function of the gate voltage V_g for Si(110) n-MOSFETs measured at three different temperatures.

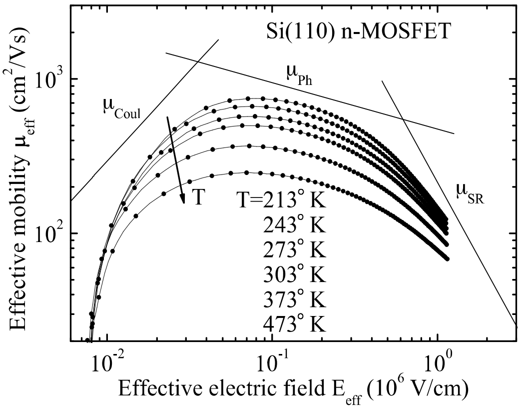

Figure 14. Effective mobility μ_{eff} as a function of the effective electric field E_{eff} for Si(110) n-MOSFETs measured at different temperatures. The several scattering mechanisms limiting the mobility have been also reported.

roughness-limited mobility. It is proportional to E_{eff}^{γ} [35] where γ is a fitting parameter generally found between −1 and −3. Quantities A_{Coul}, A_{Ph} and A_{SR} are fitting parameters associated, respectively, with the Coulomb, Phonon and Surface roughness scattering mechanisms.

The results for the Coulomb scattering mechanisms μ_{Coul} are shown in **Figure 15**. The Coulomb-limited mobility μ_{Coul} is temperature dependant, and β is varying between 0.8 and 1.2. A point independent of the temperature is visible for an effective electric field around 3×10^3 V/cm. It corresponds to the crossing point visible on the $I_d - V_g$ curves of **Figure 13** for V_g around 100 mV. Below that, point the temperature increases the energy of electron that are scattering less since the Coulomb interaction is weakening. Finally, results shown in **Figure 15** and those reported by Gaubert et al. [33] showing an attenuation of the variation of A_{Coul} with a decrease in the temperature suggests that the Coulomb-limited mobility μ_{Coul} might become independent of the temperature at low temperature. The results regarding the phonon-limited mobility μ_{Ph} are shown in **Figure 16**. The phonon-limited mobility μ_{Ph} is temperature

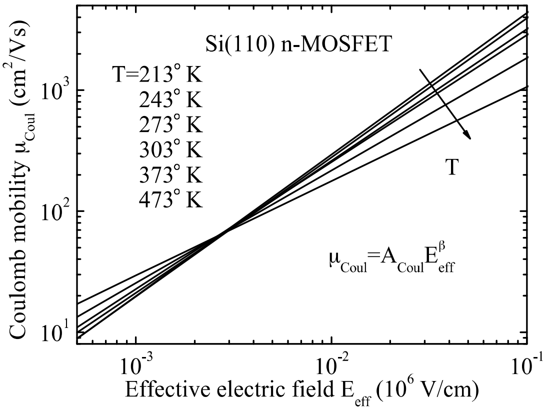

Figure 15. Extracted Coulomb mobility μ_{Coul} as a function of the effective electric field E_{eff} for Si(110) n-MOSFETs measured at different temperatures.

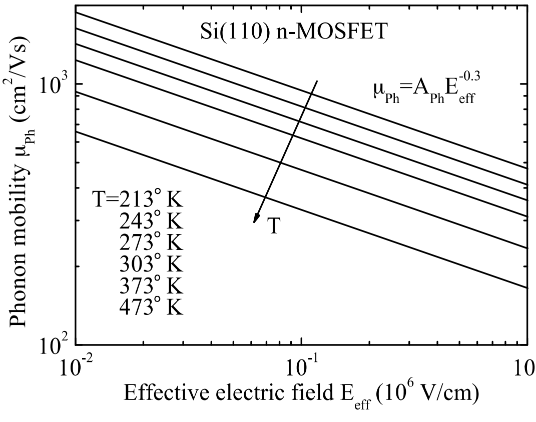

Figure 16. Extracted phonon mobility μ_{Ph} as a function of the effective electric field E_{eff} for Si(110) n-MOSFETs measured at different temperatures.

dependant according to a $T^{-1.3}$ law. Nevertheless, their ratio with the effective electric field remains unchanged with a change in temperature. The results regarding the surface-roughness-limited mobility μ_{SR} are shown in **Figure 17**. The surface-roughness-limited mobility μ_{SR} is temperature dependant. However, like for the Coulomb-limited mobility μ_{Coul}, the results at low temperature strongly suggest that the surface-roughness-limited mobility μ_{SR} becomes independent when the temperature is lowered down. Gaubert et al. [33] showed that A_{SR} is converging towards a constant value for temperature lower than 200°K, with γ reaching a value of -2. The surface-roughness-limited mobility μ_{SR} features a crossing point for effective electric field around 2 MV/cm, roughly corresponding to the breakdown of the gate oxide. Above this point, the increase in temperature is reducing the collision with the interface. The study of this peculiar behavior is made extremely difficult owing the impossibility to carry measurements on.

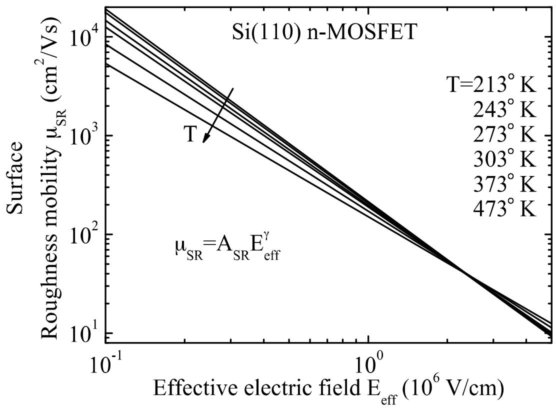

Figure 17. Extracted surface roughness mobility μ_{SR} as a function of the effective electric field E_{eff} for Si(110) n-MOSFETs measured at different temperatures.

To finish, the shift from the Si(100) wafers to the Si(110) wafers degrades the electron mobility as testified by results shown in **Figures 9** and **12**. The study of the mobility in Si(100) n-MOSFETs has been conducted in a similar way for 303° K exclusively, and the calculation of each scattering mechanisms showed that this degradation is actually the result of a strong limitation arising from the Coulomb and surface roughness scattering rather than the phonon mechanisms, results that has been demonstrated by Gaubert et al. [33].

7. Mobility in an accumulation layer

Even though making use of the majority carriers to generate the current [36, 37] is already known and has been investigated more than 40 years ago, this approach has recently gained interest, and recent studies have positioned the accumulation-mode MOSFETs as serious competitors [13, 14, 38–41] to take over the conventional transistors for future CMOS technologies. Scarce data have been published so far regarding the carrier mobility flowing inside an accumulation layer [14, 36], and a method to extract it from the conventional mobility measurement is proposed here since in accumulation-mode MOSFETs the conduction, and thus, the measured mobility involves the conduction inside the accumulation layer and the conduction occurring inside the SOI layer. Planar mode fully depleted silicon-on-insulator p-type MOSFETs on three different unibond p-type SOI (100) silicon oriented wafers have been fabricated in order to assess the mobility in an accumulation layer. The doping concentration of the SOI layer has been adjusted to 10^{15}, 10^{16} and 2×10^{17} cm^{-3}. A 7.5-nm-thick gate oxide has been formed by plasma oxidation after etching the SOI layer until reaching 50 nm. The mobility measurement method proposed in Section 2 has been followed with $Q_{dep} = 0$. The results are shown in **Figure 18**. The mobility for the conventional inversion-mode p-MOSFETs has been reported for comparison and accurately follows the universal curve by Takagi et al. [8] at high effective electric field E_{eff}. While the results suggest that the mobility for the accumulation-mode devices possessing a doping concentration of 10^{15} and 10^{16} cm^{-3} is following the universal curve, it is clear that the one with a doping concentration of 2×10^{17} cm^{-3}

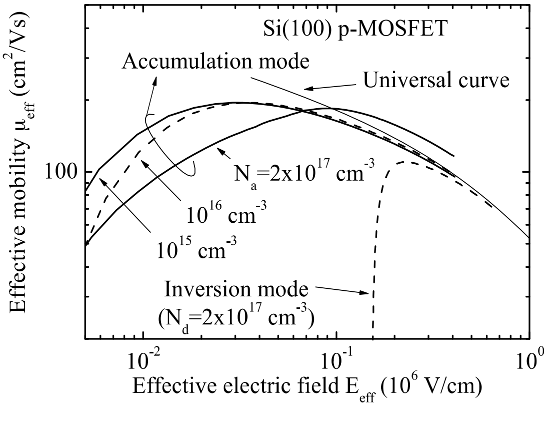

Figure 18. Experimental effective mobility μ_{eff} as a function of the effective electric field E_{eff} for accumulation- and inversion-mode Si(100) p-MOSFETs featuring different doping concentrations.

does not. As expressed previously, the SOI layer is contributing to the total measured current, and in turn, it is included in the calculation of the mobility as presented in Eq. (2). It is also clear from **Figure 19** that the calculation of Q_{acc} is false in the case of accumulation-mode MOSFETs. Indeed, the impact of the SOI layer is clearly visible and must be removed to obtain $C - V_g$ characteristics such as the one reported for an inversion-mode MOSFETs in **Figure 19**.

The appropriate evaluation of the mobility must be conducted from the relevant data, the accumulation charge and the current generated exclusively by the accumulation layer. At the flat-band voltage V_{fb}, the SOI current reaches its maximum value and its subtraction from the $I_d - V_g$ curves give the current generated by the accumulation layer. V_{bf} is evaluated from the knowledge of the flat-band capacitance C_{fb} obtained from

$$\frac{1}{C_{fb}} = \frac{1}{C_{ox}} + \frac{1}{C_{deb}}, \tag{12}$$

where C_{deb} is the Debye capacitance and can be easily calculated like C_{ox}. V_{fb} is obtained with the help of the $C - V_g$ curves shown in **Figure 19**. By turn, the maximum SOI current and SOI charge are evaluated, respectively, from the $I_d - V_g$ and $Q_{acc} - V_g$ curves and subtracted afterwards. The calculation of the effective mobility μ_{eff} and of the effective electric field E_{eff} has been conducted again for the three doping concentration, and the results are shown in **Figure 20**. All curves are now reaching the universal curve indicating that an accumulation layer has a universal behavior identical to the one seen for an inversion layer. The universal curve by Takagi et al. [8] is appropriate for both the inversion and accumulation layers. It is also confirming the rightfulness of $\eta = 1/3$ for the calculation of the effective electric field E_{eff} in Eq. (7) indicating again that the carriers in an accumulation layer are behaving in a similar way than the ones in an inversion layer with regard to the phonon and surface roughness scattering mechanisms as previously described by Chindalore et al. [42]. To finish contrary to the inversion layer, an early screening of the Coulomb scattering is occurring in the case of an accumulation layer, allowing the mobility in an accumulation layer to reach at first the bulk mobility

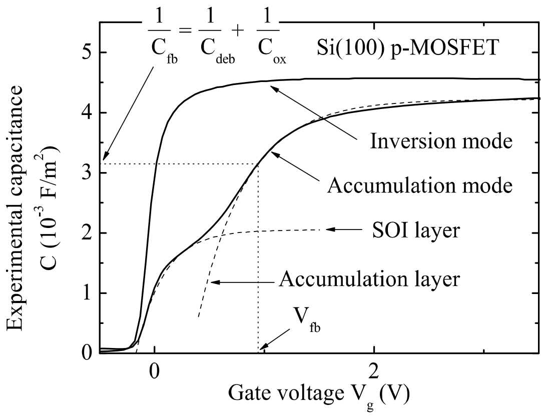

Figure 19. Experimental capacitance C as a function of the gate voltage V_g for accumulation- and inversion-mode Si(100) p-MOSFETs with a doping concentration $N_{d(a)} = 2 \times 10^{17}$ cm^{-3}. The capacitance has been measured at V_d = 100 mV and a frequency f = 100 kHz.

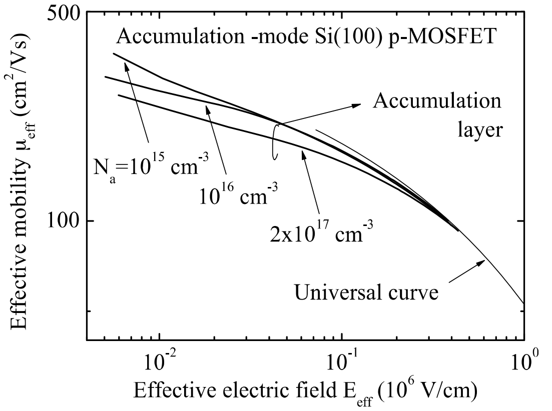

Figure 20. Calculated effective mobility μ_{eff} inside the accumulation layer of accumulation-mode Si(100) p-MOSFETs featuring different doping concentrations as a function of the effective electric field E_{eff}.

before the phonon scatterings dominate [14, 43], thus the monotonically decrease in the mobility seen at low effective electric field E_{eff} in **Figure 20**.

These last results indicate that even if the mobility shown in **Figure 18** for accumulation-mode MOSFETs with a doping concentration 10^{15} and 10^{16} cm^{-3} could have been interpreted as correct, are actually false owing to the contribution of the SOI layer.

8. Conclusion

In this chapter, we reviewed some of the main aspects of the mobility in field-effect transistors and especially for the (110) crystallographic silicon-oriented wafers. The mobility in p-MOSFETs on Si(110) wafers is limited by inter-subband scattering mechanism making its extraction by the means of the Ghibaudo method inappropriate and in turn its modeling inaccurate. A more adapted model relying on a physical approach has been developed. This new expression is incorporating the Coulomb, phonon and surface roughness scattering mechanism and is allowing a precise modeling of the drivability and transconductance in Si(110) p-MOSFETs. In addition, the study showed a clear dependency between the mobility and the channel direction for transistors fabricated on Si(110) wafers, while no impact has been noticed for conventional Si(100) wafers. The highest mobility has been revealed for a channel along the <100> direction for electron and along the <110> direction for hole. The study in temperature in Si(110) n-MOSFETs showed that the Coulomb and surface roughness scattering mechanisms are actually temperature dependent. More, the degradation of the electron mobility in Si(110) wafers has been explained by a substantial increase in the Coulomb and surface roughness scatterings than the phonon ones when compared with the Si(100) wafers. To finish, a methodology has been proposed and successfully employed to calculate the carrier mobility in the accumulation layer of newly developed accumulation-mode MOSFETs. The result showed afterwards that accumulation and inversion layers are behaving in a similar way in regard to the phonon and surface roughness scattering mechanism. Nevertheless, the mobility in an accumulation layer is monotonically decreasing from the bulk mobility when the electric field is increased, owing to an earlier screening of the carrier by the Coulomb scatterings.

Author details

Philippe Gaubert[1]* and Akinobu Teramoto[2]

*Address all correspondence to: gaubert@m.tohoku.ac.jp

1 Graduate School of Engineering, Tohoku University, Sendai, Japan

2 New Industry Creation Hatchery Center, Tohoku University, Sendai, Japan

References

[1] Lilienfeld, JE. Method and apparatus for controlling electric currents. U. S. Patent No. 1,745,175 (Filed October 8, 1926. Issued January 18, 1930).

[2] Brattain, Walter. Bell Labs Logbook (December 1947). pp. 7–8, 24. https://www.pbs.org/transistor/science/labpages/labpg5.html

[3] Teramoto A, Hamada T, Yamamoto M, Gaubert P, Akahori H, Nii K, et al. Very high carrier mobility for high-performance CMOS on a Si(110) surface. IEEE Trans Electron Dev. 2007;54(6):1438–1445.

[4] Barsan RM. Analysis and modeling of dual-gate MOSFET's. IEEE Trans Electron Dev. 1981;28:523–534.

[5] Chang D, Lee M, Chen D, Liva V. Power junction FETs (JFETs) for very low-voltage applications. Proc. IEEE APEC; Austin, USA, 2005, 1419–1423.

[6] Gill DM, Kane BC, Svensson SP, Tu DW, Uppal PN, Byer NE. High-performance, 0.1 μm InAlAs/InGaAs high electron mobility transistors on GaAs. IEEE Electron Dev Lett. 1996;17(7):328–330.

[7] Akarvardar K, Cristoloveanu S, Gentil P. Analytical modeling of the two-dimensional potential distribution and threshold voltage of the SOI four-gate transistor. IEEE Trans Electron Dev. 2006;53(10):2569–2577.

[8] Takagi S, Toriumi A, Iwase M, Tango H. On the universality of inversion layer mobility in Si MOSFET's: part I—effects of Substrate Impurity Concentration. IEEE Trans Electron Dev 1994;41(12):2357–2362.

[9] Sabnis AG, Clemens JT. Characterization of the electron mobility in the inverted <100> Si surface. Int Electron Dev Meet. 1979:18–21.

[10] Saitoh M, Kobayashi S, Uchida K. Physical understanding of fundamental properties of Si (110) pMOSFETs inversion-layer capacitance, mobility universality, and uniaxial stress effects. Int Electron Dev Meet. 2007:711–714.

[11] Takagi S, Toriumi A, Iwase M, Tango H. On the universality of inversion layer mobility in Si MOSFET's: part II—effects of surface orientation. IEEE Trans Electron Dev. 1994;41 (12):2363–2368.

[12] Gaubert P, Teramoto A, Cheng W, Ohmi T. Relation between the mobility, 1/f Noise, and channel direction in MOSFETs fabricated on (100) and (110) silicon-oriented wafers. IEEE Trans Electron Dev. 2010;57(7):1597–1607.

[13] Cheng W, Teramoto A, Hirayama M, Sugawa S, Ohmi T. Impact of improved high-performance Si(110)-oriented metal–oxide–semiconductor field-effect transistors using accumulation-mode fully depleted silicon-on-insulator devices. Jpn JAppl Phys. 2006;45 (4B):3110–3116.

[14] Gaubert P, Teramoto A, Sugawa S, Ohmi T. Hole Mobility in accumulation mode metal-oxide-semiconductor field-effect-transistors. Jpn J Appl Phys. 2012;51:04DC07-1~6.

[15] Merckel G, Borel J, Cupcea NZ. An accurate large-signal MOS transistor model for use in computer-aided design. IEEE Trans Electron Dev. 1972;19(5):681–690.

[16] Schreutelkamp RJ, Deferm L. Internal report IMEC, n° P30005-IM-FP-001. 1993.

[17] Schreutelkamp RJ, Deferm L. A new method for measuring the saturation velocity of submicron CMOS transistors. Solid-State Electron. 1995;38(4):791–793.

[18] Tsividis Y. Operation and Modeling of The MOS Transistor. s.l.: McGraw-Hill, 1999. p. 521.

[19] Ghibaudo G. New method for the extraction of MOSFET parameters. Electron Lett. 1988;24(9):543–545.

[20] Ciofi C, Macucci M, Pellegrini B. A new measurement method of MOS transistor parameters. Solid-State Electron. 1990;33(8):1065–1069.

[21] Gaubert P, Teramoto A, Ohmi T. Modelling of the hole mobility in p-channel MOS transistors fabricated on (110) oriented silicon wafers. Solid-State Electron. 2010;(54):420–426.

[22] Gaubert P, Teramoto A, Hamada T, Yamamoto M, Kotani K, Ohmi T. 1/f Noise Suppression of pMOSFETs Fabricated on Si(100) and Si(110) Using an Alkali-Free Cleaning Process. IEEE Trans Electron Devices. 2006;53(4):851–856.

[23] Gaubert P, Teramoto A, Suwa T, Ohmi T. Accurate extraction of conduction parameter in MOSFETs on Si(110) surface. Proc. 28th International Conference on the physics of semiconductors; Hawaii, USA 2006:1393–1394.

[24] Ong TC, Ko PK, Hu C. 50-Å Gate-oxide MOSFET's at 77 K. IEEE Trans Electron Devices. 1987;34(10):2129–2135.

[25] Ghibaudo G, Balestra F. A method for MOSFET parameter extraction at very low temperature. Solid State Electron. 1989;32(3):221–223.

[26] Stern F. Two-subband screening and transport in (001) Si inversion layers. Surf Sci 1976;73:197–206.

[27] Hartstein A, Ning TH, Fowler AB. Electron scattering in silicon inversion layers by oxide and surface roughness. Surf Sci 1976;58:178–181.

[28] Fischetti MV, Ren Z, Solomon PM, Yang M, Rim K. Six-band k.p calculation of the hole mobility in silicon inversion layers: dependence on surface orientation, strain, and silicon thickness. J ApplPhys 2003;94(2):1079–1095.

[29] Sekine K, Saito Y, Hirayama M, Ohmi T. Highly reliable ultrathin silicon oxide film formation at low temperature by oxygen radical generated in high-density krypton plasma. IEEE Trans Electron Devices. 2001;48(8):1550–1555.

[30] Ohmi T. Total room temperature wet cleaning for Si substrate surface. JElectrochem Soc. 1996; 143(9): 2957–2964.

[31] Morita Y and H. Tokumoto. Atomic scale flattening and hydrogen termination of the Si(001) surface by wet-chemical treatment. JVacSciTechnol A Vac Surf Films. 1996;14(3):854–858.

[32] Gaubert P, Teramoto A, Cheng W, Hamada T, Ohmi T. Different mechanism to explain the 1/f noise in n- and p-SOI-MOS transistors fabricated on (110) and (100) silicon-oriented wafers. JVacSci Technol. BMicroelectron ProcessPhenom. 2009;27(1):394–401.

[33] Gaubert P, Teramoto, Sugawa S, Ohmi T. The role of the temperature on the scattering mechanisms limiting the electron mobility in metal-oxide-semicoductor field-effect-transistors fabricated on (110) silicon-oriented wafers. Proc. 42th European Solid-State Device Research Conference; Bordeaux, France 2012:213–216.

[34] Stern F, Howard WH. Properties of semiconductor surface inversion layers in the electric quantum limit. Phys Rev. 1967;(163):816–835.

[35] Mazzoni G, Lacaita AL, Perron LM, Pirovano A. On surface roughness-limited mobility in highly doped n-MOSFETs. IEEE Trans Electron Dev. 1999;(46):1423–1428.

[36] Sun SC, Plummer JD. Electron mobility in inversion and accumulation layers on thermally oxidized silicon surfaces. IEEE Trans Electron Dev. 1980;27(8):1497–1508.

[37] Ando T, Fowler AB, Stern F. Electronic properties of two-dimensional systems. Rev Mod Phys. 1982;54:437–672.

[38] Colinge JP, Lederer D, Afzalian A, Yan R, Lee CW, Akhavan ND, Xiong W. Properties of accumulation-mode multi-gate field-effect transistors. Jpn J Appl Phys. 2009;48(3):034502-1∼7.

[39] Cheng W, Teramoto A, Ohmi T. Experimental demonstration and analysis of high performance and low 1/f noise Tri-gate MOSFETs by optimizing device structure. Microelectron Eng. 2009;86(7/9):1786–1788.

[40] Gaubert P, Teramoto A, Sugawa S. Impact of doping concentration on 1/f noise performances of accumulation-mode Si(100) n-MOSFETs. Jpn J Appl Phys. 2016;55:04ED08-1~6.

[41] Gaubert P, Teramoto A, Sugawa S. Performances of accumulation-mode n- and p-MOSFETs on Si(110) wafers. Jpn J Appl Phys. 2017;56:04CD15-1∼7.

[42] Chindalore GL, McKeon JB, Mudanai S, Hareland SA, Shih WK, Wang C, Tasch AF, Maziar CM. An improved technique and experimental results for the extraction of electron and hole mobilities in MOS accumulation layers. IEEE Trans Electron Dev. 1998;45:502–511.

[43] Mudanai S, Chindalore GL, Shih WK, Wang H, Ouyang Q, Tasch AF, Maziar CM, Banerjee SK. Models for electron and hole mobilities in MOS accumulation layers. IEEE Trans Electron Dev. 1999;46:1749–1759.

Chapter 2

Resonant Tunneling and Two-dimensional Gate Transistors

Vladimir Popov

Additional information is available at the end of the chapter

http://dx.doi.org/10.5772/intechopen.69069

Abstract

In this chapter, a new type of field-effect transistors is considered with a gate and a channel on a basis of two-dimensional systems of carriers. The key point of the device is that the systems are different. In particular, they are formed in different quantum wells or valleys of the carriers spectrum. Due to this difference, the coherent tunneling is reduced and inelastic tunneling requires additional excitations with significant momentum and energy. This decreases the tunneling rate significantly. For example, the intervalley tunneling rate is less than intravalley that in 9 orders of magnitude in GaAs/AlAs heterostructures. The two-dimensional character also can decrease the tunnel probability in a wide voltage range. Influence of further miniaturization will be discussed for the new types of the transistors.

Keywords: field-effect transistor (FET), two-dimensional system of carriers, resonant tunneling

1. Introduction

Size-shrinkage as a main trend of the electronics development has already brought not only cut-off frequency but also energy consumption increase. In addition, a current leakage of the field-effect transistor (FET) has also increased. The leakage current consists of a current from the drain to the source (I_{sd}) due to overlapping of the p-n transition regions in the contacts and a tunneling current from the gate to the channel (I_g). Moreover, in the FET size-shrinkage, the I_g part becomes more important; for example, at 130 nm technology, it takes less than 5% of whole leakage, at 90 nm, it takes 40%, and at 65 nm, it takes 90%, respectively [1]. To decrease the I_{sd}, SOI substrates and vertical orientations of the FET are used. This effectively decreases the width of the cross section for the I_{sd}. Note that this accompanies the two-dimensional character of the FET channel. To diminish the I_g, high-k dielectrics are used as the gate insulators. This increases the capacity between the gate and the channel and decreases the pinch-off voltage or energy of

INTECH
open science | open minds

© 2017 The Author(s). Licensee InTech. This chapter is distributed under the terms of the Creative Commons Attribution License (http://creativecommons.org/licenses/by/3.0), which permits unrestricted use, distribution, and reproduction in any medium, provided the original work is properly cited.

the tunneling carriers. Another way is to use quantum well for the FET channel, for example, InSb layer [2]. This also diminishes gate voltage because the band inversion is not required. As a result, the cut-off frequency can be increased up to 300 GHz. One can see that two-dimensional systems of carriers (2DSC) are inherent to the modern nanoFET.

In this chapter, an application of the 2DSC in a FET gate is considered for further leakage reducing.

2. Resonant tunneling of carriers

Tunneling has been revealed by Esaki [3] and studied mainly in semiconductor diodes since 1958. Several years before, Shriffer had proposed size-quantization of the carriers in semiconductor films [4] that was observed by Tsui in InAs tunneling diode [5]. Then Esaki [6] and Kazarinov and Suris [7] proposed carriers resonant tunneling (CRT) in semiconductor heterostructures. In 1974, this effect was observed [6]. On the base CRT, a resonant-tunneling diode (RTD) [8] and resonant-tunneling transistor (RTT) [9] are realized as highest-frequency solid-state devices up to date. Carriers tunneling is well-known to play a negative role in modern c CMOS transistors made on the base technology of 45 nm or less. However, the instances of the RTD and RTT give us a hope that a proper application of the CRT can improve the situation in the FET. To clarify this, let us consider the CRT in detail.

Usually, the CRT is observed in a double-barrier heterostructure, the conduction band profile of which is shown in **Figure 1**. In a thin layer of a narrow band gap semiconductors, the localized states are forming and called subband states or levels. The ground subband state has energy E_{z0}. As a result, the barriers transparency has sharp peaks up to 1 in its energy dependency when the incident-electron energy along z direction E_z approaches to E_{z0} and, what is more important to this chapter, it decreases down to $T_z = 10^{-4}$ at intermediate energy [6].

To calculate current-voltage characteristics, one can consider model of sequential tunneling [10]. In this model, tunneling of the electron can be described as sequential quantum transition perturbed by tunnel Hamiltonian T [11]. In first term of the perturbation theory, one can expect to find the probability of the transition as follows:

$$W_{if} = \frac{2\pi}{\hbar} |\Psi_i|T|\Psi_f|^2 \delta(E_f - E_i) \quad (1)$$

where $\hbar$ is Planck constant, $\Psi_{\mathrm{i,f}}$ are electron wave functions, $E_{\mathrm{i,f}}$ are energy of initial and final states. Since the potential is in the one z direction, the electron wave functions are as follows:

$$\Psi_{i,f} = \chi_{i,f}(z) \exp\left(\frac{i}{\hbar}[p_{xi,f}x + p_{yi,f}y]\right) \quad (2)$$

Then the matrix element of T is as follows:

$$\Psi_i|T|\Psi_f = T_{if}\delta(p_{xf} - p_{xi})\delta(p_{yf} - p_{yi}) \quad (3)$$

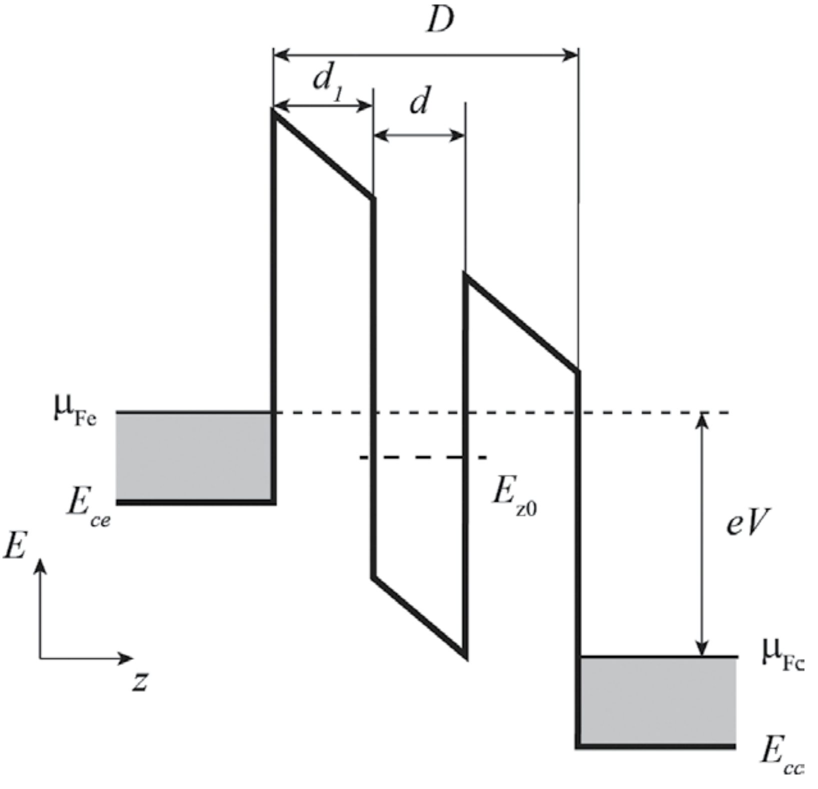

Figure 1. Energy profile of the conduction band bottom of the two barrier heterostructure.

where $T_{if} = \chi_i|T|\chi_f$. As one can see from Eqs. (1) and (3), the tunneling electrons save its energy and planar components of the momentum. Since the electron effective mass is equal on both sides of the barrier, the tunneling electron also saves E_z energy. To calculate current, one should sum transition probabilities timed on electron charge from given equation:

$$I = \sum_{i,f} eW_{if}(f_i - f_f) \tag{4}$$

where $f_{i,f,}$ Fermi-Dirac distribution functions of electrons in initial and final states. Let us suppose that T_{if} is a constant, then $T_{if} = \tau^{-1}$, where τ is a tunneling rate of the electrons. According to Eqs. (1) and (3), one can get the following:

$$I = \frac{e}{\tau} \sum_{i(E_{z0}),f(E_{z0})} (f_i - f_f) = \frac{e}{\tau}(N_i(E_{z0}) - N_f(E_{z0})) \tag{5}$$

where $i(E_{z0})$ and $f(E_{z0})$ are the initial and final states which have the same energy E_{z0} of motion in z direction; $N_i(E_{z0})$ and $N_f(E_{z0})$ are the number of electrons populating the initial and final states. Using low-temperature limit that is $kT << E_F$ and $kT << E_{z1}-E_{z0}$ and also supposing final states as empty that is $N_f(E_{z0}) = 0$ as usual, one can calculate $N_i(E_{z0})$ as a number of filled states on a Fermi-hemisphere intersection disk taking at a momentum p_{z0} in the phase space (see gray disc in **Figure 2**) where $E_{z0} = (p_{z0})^2/2m^*$ and m* is an electron effective mass. Thus, the tunnel current can be found as follows:

$$I = \frac{e(p_F^2 - p_{z0}^2)S}{(2\pi\tau\hbar^2)} = eg_{2D}S(E_{Fe} - E_{z0})/\tau \tag{6}$$

where e is an electron charge, p_F is a Fermi momentum of electrons, $g_{2\mathrm{D}}$ is a density of two-dimensional states of electrons, and S is a sample area.

Let us suppose the emitter grounded, i. e., $\mu_{\mathrm{fe}} = \mathrm{const}$, then the voltage dependence of $E_{z0}(V)$ determines the I-V curve. If the barriers width D is greater than the quantum well (QW) width d, then $E_{z0}(V)$ can be found from linear Stark effect:

$$E_{z0}(V) = E_{z0}(0) - eV/\alpha \tag{7}$$

where α is a leverage factor, i.e., $\alpha = D/(d_1 + d_2)$. Since usually $E_{z0}(0) > \mu_{\mathrm{fe}}$, there is a threshold voltage V_{th} higher than a resonant current I that has appeared when $E_{z0}(V_{\mathrm{th}}) = \mu_{\mathrm{fe}}$. Then combining Eqs. (6) and (7), one can get the following expression for the current I:

$$I = e^2 g_{2D}S(V - V_{th})/\alpha\tau \tag{8}$$

Eq. (8) is justified when $\mu_{\mathrm{fe}} > E_{z0}(V) > E_{\mathrm{ce}}$. At the current peak voltage $V_{\mathrm{p}},$ the subband energy E_{z0} approaches to E_{ce}, i.e., $E_{z0}(V_{\mathrm{p}}) = E_{\mathrm{ce}}$, and after that the resonant current drops down to zero.

As a result, the I-V curve of the RTD is shown in **Figure 3** as solid line. It is worth noting that Eq. (8) describes only resonant part of the current. Nonresonant current usually is monotonic

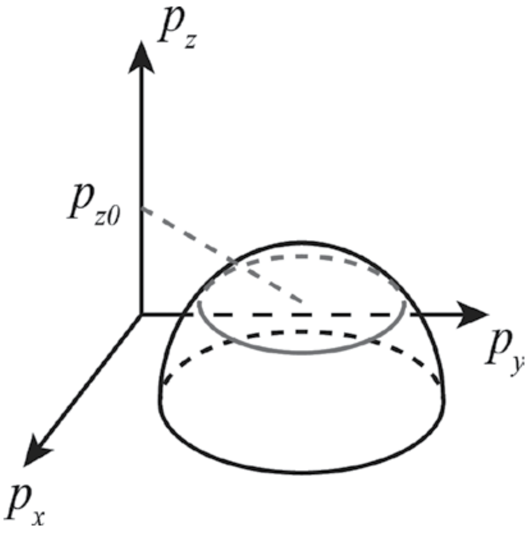

Figure 2. Momentum space of the emitter and states available for resonant tunneling.

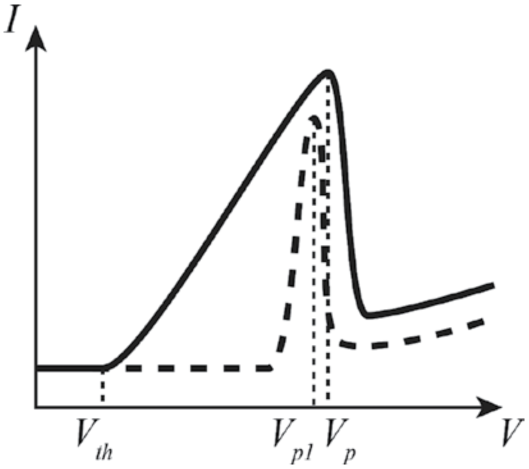

Figure 3. Current-voltage characteristics of RTD with a single quantum well between barriers (solid line) and a double quantum wells (dashed line).

function of the voltage and includes scattering tunneling and tunneling across all barriers. This provides nonzero current at any nonzero voltage. Thus, one can see that two-dimensional state in the QW produces the resonant tunneling in a finite resonant voltage range from V_{th} to V_{p} and depresses the resonant tunneling at other voltages. This resonant voltage range can be further shrunk if another QW will be used (see **Figure 4**). In this case, the resonant tunneling is possible only at resonant voltage V_{p1} when $E_{01}(V_{\mathrm{p1}}) = E_{02}(V_{\mathrm{p1}})$. This decreases significantly the width of the current peak in the I-V curve (see **Figure 3** dashed line).

Thus, the application of 2DSCs could significantly decrease the carriers tunneling in a wide range of the applied voltage. This means there is a new way to decrease carriers tunneling between a

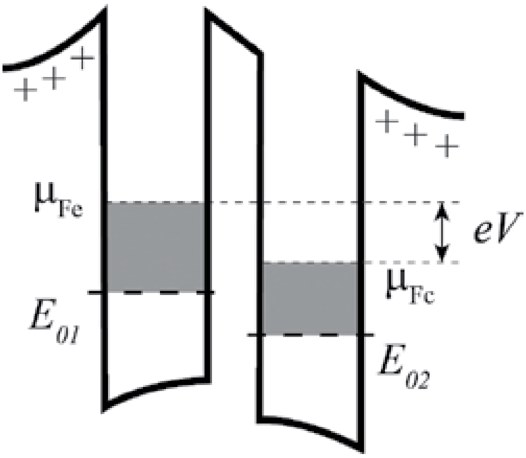

Figure 4. Energy profile of the conduction band bottom of the heterostructure with two quantum wells.

gate and a channel that is application 2DSCs in them. Semiconductor heterostructures with two 2DSCs separated by a tunnel barrier have been studied and demonstrated their properties [11].

3. Resonant tunnel transistors

As can be seen from **Figure 3**, tunneling current strongly depends on the energy of quantum level in the QW, so if you create a third electrical contact to control this energy, it is possible to obtain a transistor with a large transconductance value, and even with a negative transconductance. Several types of such transistors have been investigated and are shown in **Table 1**. They differ by base contact making as it is shown in **Figure 5**.

3.1. Bipolar resonant-tunneling transistor with QW

In this case, double-barrier heterostructure is located inside a vertical bipolar transistor in a thin layer being in connection with base contact [12]. One example implementation of such a heterostructure is shown in **Figure 6(a)** in the form of the band structure. QW layer is considerably doped with impurities of p-type, which allows change in the potential of QW almost independently of the potentials of the source and drain. Resonant tunneling through the QW starts at finite drain-source voltage (see **Figure 6(b)**). **Figure 7(a)** presents source-drain characteristics of the transistor at different values of voltage on the base. As one can see from **Figure 7(b)**,

	Unipolar transistors	Bipolar transistors
Base pin contacts to the QW	Unipolar RTT with contact to the QW	Bipolar RTT with QW contact
Base pin contacts layer close to the QW	Unipolar RTT on hot-electrons effect	Light-emitting RTT

Table 1. Resonant-tunneling transistors.

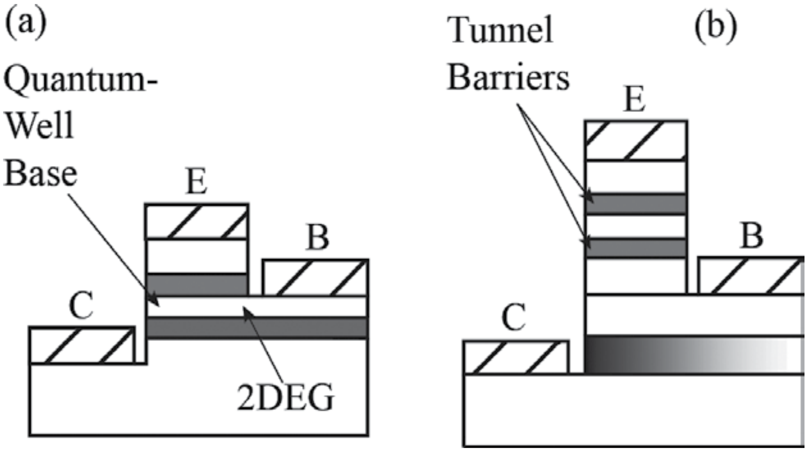

Figure 5. Topology of resonant-tunneling transistors. (a) RTT is shown where the base contact is connected directly to the QW and (b) RTT is shown where the base contact is connected to layer adjacent to the QW.

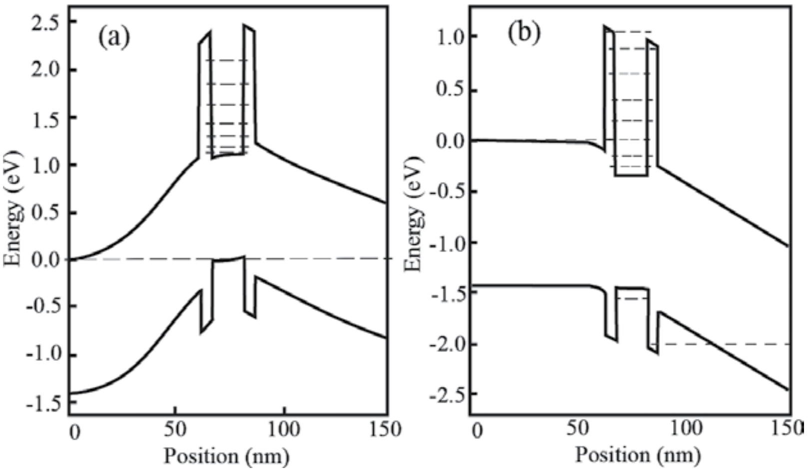

Figure 6. Band diagrams of the bipolar RTT with QW at zero drain-source voltage (a) and at finite applied voltage (b).

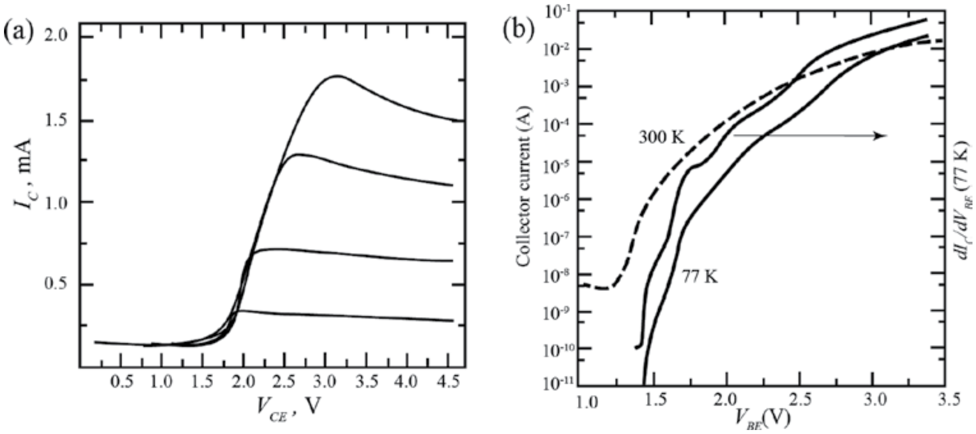

Figure 7. Characteristics of the bipolar RTT with QW taken from Ref. [12]. (a) Drain-source characteristics at different base voltages at 300 K and (b) source-base and transconductance characteristics at different temperatures.

the resonant tunneling provides just weak features in the transconductance of the transistor, which appears to be associated with a strong broadening of the levels of dimensional quantization in the QW, due to its disorder induced by doping impurities. The usage of modulated doping could significantly improve the situation, but further research in this direction is not followed. Perhaps because in the transistor the doped layer is placed outside the quantum well and the contact to the layer outside the quantum well.

3.2. Light-emitting resonant-tunneling transistor

In the case of a bipolar contact or p-n junction, the flow of electric current accompanied by the light emission resulted from the electron-hole recombination. Similar radiation was recorded

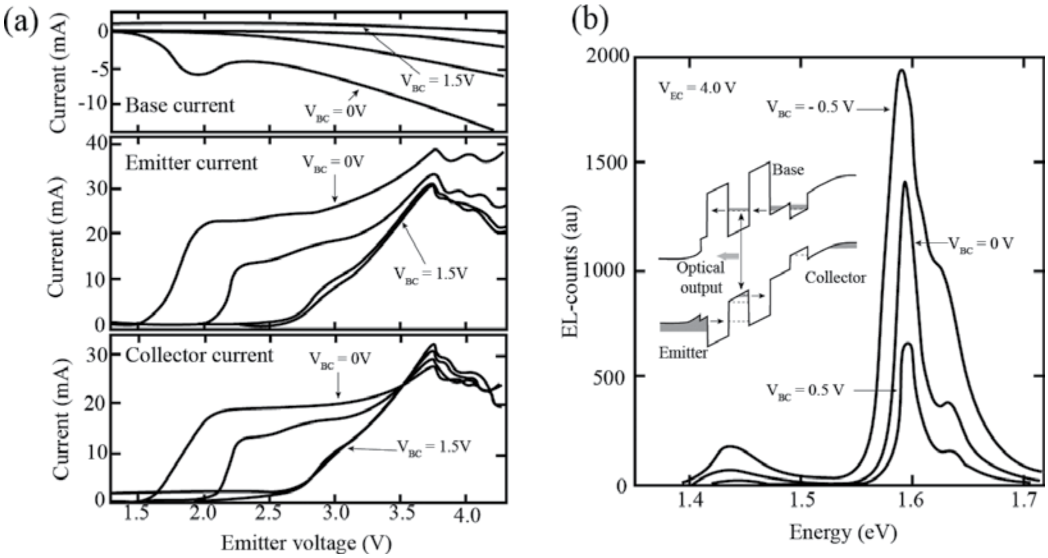

Figure 8. Electrical and optical characteristics of the bipolar RTT with base contact separated from active region taken from Ref. [14]. (a) Source or emitter, drain or collector and base currents are plotted versus applied source-drain voltage at different base voltages and (b) optical spectra at different base voltages.

in a bipolar RTD [13] and bipolar RTT [14]; in this sense, the third electrode can be considered as controlling not only current but also radiation. The presence of the region of negative differential conductance (NDC) allows to create not only an oscillator but also an optical pulsar with a clock frequency up to the THz range. One of the options for band structure of these transistors is shown in the insert in **Figure 8**. In this case, the base layer is doped by donors, but the contact is placed out from the side of the structure. This helped to maintain the quality of the QW between the tunneling barriers that has led to a significant effect of resonant tunneling. As a result, the region of the negative conductance and transconductance was present in all transistor characteristics (see **Figure 8(a)**).

3.3. Resonant-tunneling transistor with base contact to two-dimensional electron system

It is possible to make a deep QW between the tunneling barriers. The QW will be filled by carriers from adjacent layers, if a ground subband has energy E_0 below Fermi level [14]. Such QW can be connected via remote contact and has no disorder originated from doping (see **Figure 9**). In this case, the base contact is located remotely from active region on the side of the emitter and controls the potential of the QW (see **Figure 9**). Resonant tunneling of electrons through the level E_1 or through the first excited two-dimensional subbands. Source-drain current-voltage characteristics are shown in **Figure 10(a)**. It is seen in **Figure 10(b)** that, despite the observed NDC saturation current is not observed and there is a large nonresonant current. This behavior is expected because when tunneling takes place in the first excited subband, electrons tunnel with emission of a wide range of excitations, such as phonons, plasmons, and photons. These excitations transfer the electrons to the ground subband.

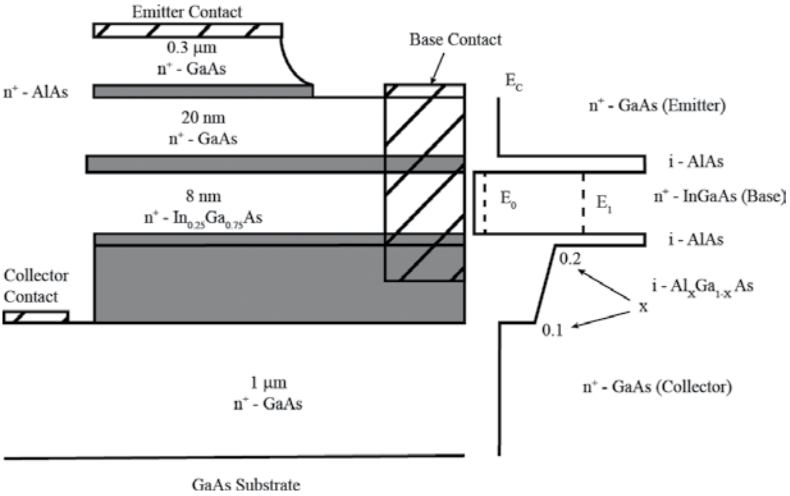

Figure 9. Resonant-tunneling transistor with deep QW. Topology of layers and contacts and conduction band bottom diagram of the active region of the RTT.

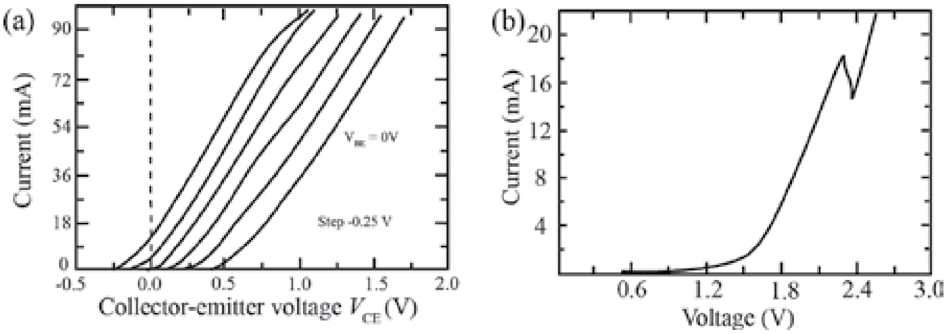

Figure 10. Electrical characteristics of the RTT with deep QW. (a) Source-drain current-voltage characteristics at different base voltage and (b) source-drain current-voltage characteristic at floating base potential.

3.4. Resonant-tunneling transistor on hot electrons

The removal of the base layer outside the quantum well improves the work of RTT, as demonstrated in Refs. [9, 15]. The topology of the transistor and its diagram of the conduction and composition of the layers is shown in **Figure 11**. In this case, the heavily-doped disordered base layer does not much influence the quality of the QW and bright NDC features are observed in all electrical characteristics. **Figure 12** shows transistor characteristics obtained. The thickness of the base layer is 50 nm (a) and 25 nm (b). From **Figure 12**, one can see that the wide-base layer degrades characteristics of NDC and increases the base current, decreasing the width of the layer characteristics improves characteristic and the gain current increases. It is worth noting that at low voltage, the current is very low because the ground subband has energy considerably higher the Fermi energy and only high energy electrons or hot electrons can tunnel.

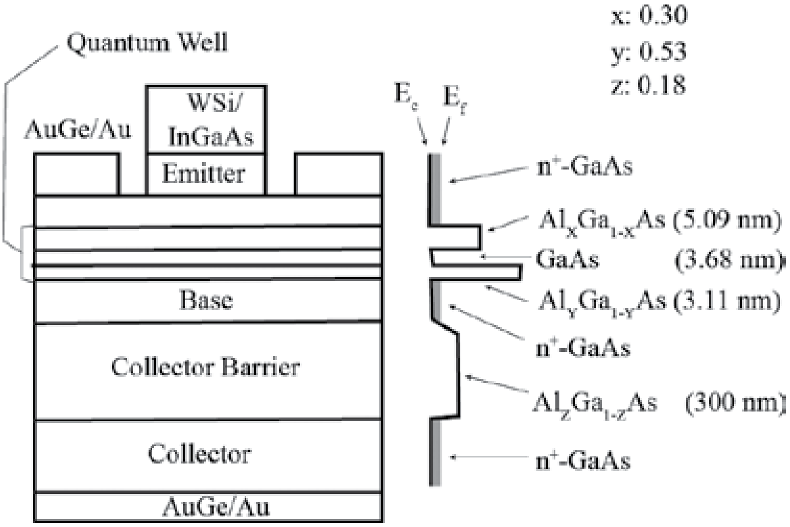

Figure 11. Resonant-tunneling transistor on hot electrons. Topology of layers and contacts and conduction band bottom diagram of the active region of the RTT.

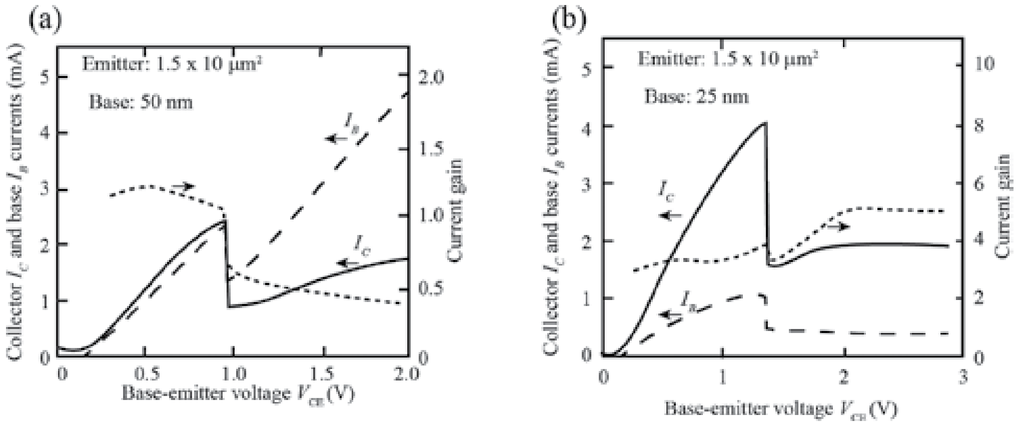

Figure 12. Electrical characteristics of the RTT on hot electrons. (a) Characteristics obtained on RTT with base layer of 50 nm thickness and (b) the same for 25 nm thickness.

4. Field-effect transistors with two-dimensional systems of carriers

Previously studied resonant-tunneling transistors have considerable disadvantages such as the tunnel current is very low and high frequency application is possible only in the region of NDC. However, the resonant tunneling can be used in conventional FET to shrink gate-voltage range where it takes place [16]. As already mentioned in Section 2, the situation can be significantly improved by using a structure with two quantum wells. In this case, the gate 2DCS has a carrier concentration different from the 2DCS concentration in the channel (see **Figure 13(a)**). To create such transistor, it requires an entire system of gates. The problem is

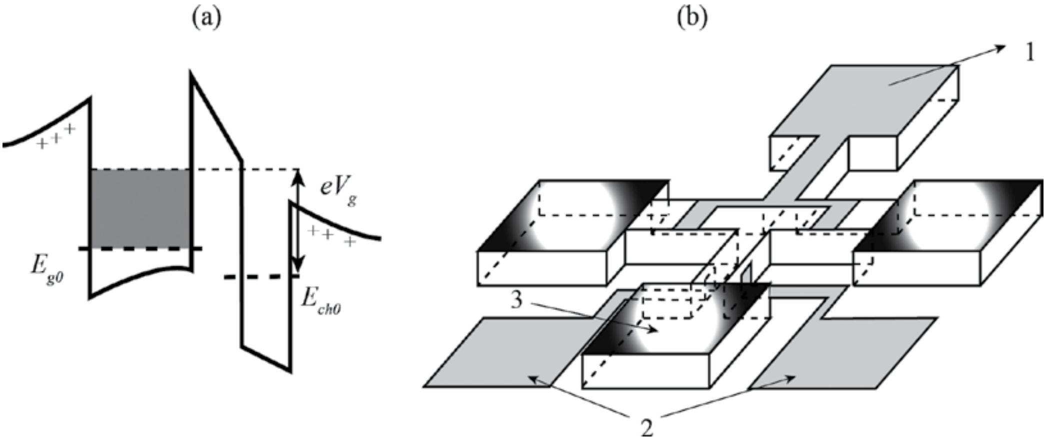

Figure 13. Field-effect transistor with QWs. (a) Conduction band bottom diagram of the active region of the FET and (b) topology of the contacts of the FET.

that two conductive layers are in close proximity to each other, which significantly complicates the creation of separate ohmic contacts to each layer. In this case, ohmic contacts to the both layers are made, and then, additional gates (1, 2 in **Figure 13(b)**) deplete one of the layers. So, gate 1 can be used by applying a negative voltage to the depletion of the upper layer and double gate 2 is used for the depletion of the lower layer. Due to the difference of the energies the resonant tunneling between the layers will be suppressed and the leakage current from the gate to channel will be low. It should be noted that when using this transistor to completely eliminate the resonant tunneling which is impossible as to deplete the channel, one must pass through the resonance voltage V_r, in which $E_{g0}(V_r) = E_{ch0}(V_r)$. However, even in this case, the current will not exceed the maximum current observed when the resonant tunneling takes place between a three-dimensional contact and QW (see **Figure 3**).

Another possibility of a FET is proposed in Ref. [17] with a gate and a channel on the basis of 2DSC in different valleys. The key point of the device is that the 2DSCs are different. In particular, they are formed in different valleys of the carrier spectrum (see **Figure 14(a)**). Due to this difference, the carrier tunneling requires additional excitations with significant momentum and energy. This decreases the tunneling rate significantly. For example, the intervalley tunneling rate is less than intravalley that in 9 orders of magnitude in GaAs/AlAs heterostructures [18]. Application of 2DSCs in the gate and channel in different valleys can significantly decrease the tunnel leakage and allow further cut-off frequency to increase. Moreover, in the case of low intervalley carriers scattering, the dielectric layer can be removed which increases the transconductance of the FET. Some realization of the conduction band bottom profile can be found in **Figure 14(b)**. The heterostructure is modulation-doped by Si donors. The AlAs is an indirect semiconductor where X-valley has lower energy than Γ-one. Hence, in the layer 2, a quantum well (XQW) is formed in the X-valley that is shown by long-dashed line in the profile. The XQW can be used as a FET gate. A GaAs quantum well is formed in Γ-valley (ΓQW) and can be used as a FET channel. A topology of the FET can be the same as in **Figure 13**. The source and drain are contacted to the ΓQW and the gate is contacted

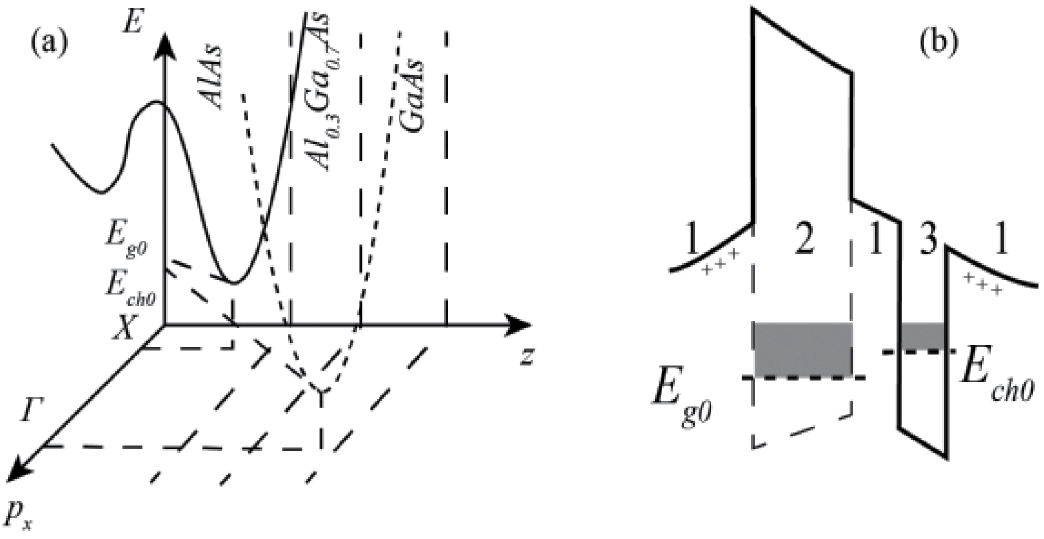

Figure 14. Electrons spectra in active region of the FET with QW in different valleys. (a) Electron dispersion curves in the XQW (solid curve) and ΓQW (dotted curve) and (b) conduction band bottom diagram of the proposed FET heterostructure.

to the XQW (see arrow 3 in **Figure 13**). The electric characteristics of the proposed FET are still under investigation. However, some discussion about their miniaturization is possible and follows in the next section.

5. Miniaturization of the field-effect transistors with two quantum wells

5.1. Cut-off frequency of the FET

As mentioned in Section 1, miniaturization of transistors is the main direction of development of microelectronics for more than 50 years and the reason is not only the attraction of investments or the usability of electronic devices. The main reason for miniaturization is to increase the cut-off frequency of semiconductor devices. Let us consider how the size reduction leads to an increase in the operating speed of a FET. In **Figure 15(a)**, one can see a typical topology of a FET with metal electrodes. The FET is plugged in the bias circuit through the contacts 1 (source) and 2 (drain). Offset E_c is necessary for the current saturation that one can see in the source-drain characteristics of the FET as shown in **Figure 15(b)**. The saturation velocity of the carriers in the channel (in gray in **Figure 15(a)**) does not change with applied voltage and it is possible to obtain the following expression for current:

$$I_{sd} = nevS_{ch} \tag{9}$$

Here, n is the carrier concentration in the channel, v is the velocity of the carriers, S_{ch} is a cross-sectional area in the channel. To change the concentration, the gate is used (see in **Figure 15(a)**). When voltage V_{in} is applied the carrier concentration n(V) is changed due to the finite capacitance between channel and gate Cp as follows:

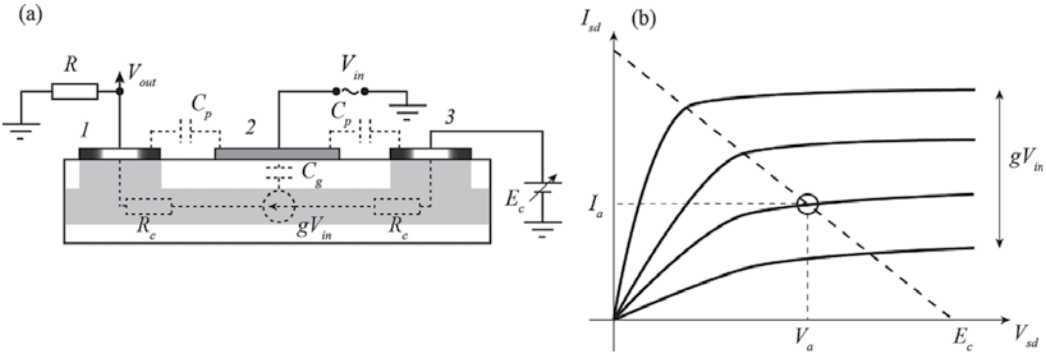

Figure 15. Topology and characteristics of the field effect transistor. (a) Topology of a field-effect transistor and the plug-in circuit. The dotted line shows the elements of the equivalent circuit of the transistor. (b) Source-drain characteristics of FET for different gate voltages V_{in}. The inclined straight line corresponds to the load straight line, its intersection with the source-drain characteristic corresponds to the operating point of the transistor, i.e., determines the current I_a and voltage V_a.

$$n(V) = n_0 + C_g V/(W_{ch} e) \tag{10}$$

where n_0 is the carrier concentration in the channel at zero gate voltage, $W_{ch} = S_{ch} L_{ch}$ is a volume of the channel, L_{ch} is a length of the gate or channel (see **Figure 15(a)**). Substituting the Eq. (10) in Eq. (8), one can get the following expression for the current:

$$I_{sd} = I_0 + \frac{v C_g V}{L_{ch}} = I_0 + gV \tag{11}$$

where g is a transconductance of the FET. In **Figure 15(a)**, dashed line presents the elements of the equivalent circuit of the transistor, i.e., elements for which the transistor can be modeled. In this case, the behavior of the semiconductor channel can be modeled by a current source dependent on the gate voltage V_{in}. Let us now consider the AC signal V_{in}, then there is a bias current δI_c through the parasitic capacitance of C_p and gate capacity C_g. The current through the capacitance is increased by increasing the frequency of the alternating voltage V_{in}, so there is a cut-off frequency at which the current through the capacitance is compared with the current in the semiconductor channel δI_a and then one can get the following equation:

$$\delta I_c = \omega (C_p + C_g) V = gV = \delta I_{sd} \tag{12}$$

Then taking into account Eq. (11), one can get the following expression for the cut-off frequency:

$$\omega = \frac{v}{L_{ch}(1 + C_p/C_g)} \tag{13}$$

This shows that by increasing the value of C_g and decreasing the value of C_p and L_{ch}, it is possible to increase the cut-off frequency of the transistor. To increase C_g, one can reduce the distance between the channel and the gate, i.e., d. By the way, the use of gate high-k dielectrics is another way of increasing C_g. The reduction in C_p may also be obtained by decreasing a width of the gate contact and increasing the distance between the contacts and gate contacts. However, the increase in the distance between electrodes is limited by increase of the serial resistance R_c. Actually, Eq. (13) describes the cut-off frequency of the active region of the transistor, i.e., the channel region under the gate, the output AC signal is measured when the current flows through the load resistance R. Resistance R_c is shunted by a capacitance of C_p, therefore, the cut-off frequency of AC signals cannot exceed $\omega_1 = 1/(R_c C_p)$. Since R_c increases with increasing interelectrode distance, the effect of increasing this distance is significantly reduced.

5.2. Size-quantization and its effect on resonant tunneling

Thus, reducing the size of the active area of the transistors leads to an increase in the cut-off frequency, which is the main physical reason for the miniaturization. However, as mentioned in Section 1, miniaturization of transistors has led to the increase in the leakage current, which significantly increases energy consumption and reduces the prospects for further development in this direction to zero. The use of resonant tunneling can significantly reduce leakage currents, but it is necessary to use a carrier system with reduced dimensions. These systems which appear in semiconductor nanoheterostructures, recently also actively studied the carbon nanomaterials. Here, there is a new problem with miniaturization. When reduction of L_{ch} size occurs up to 20 nm, lateral size-quantization takes place in the two-dimensional gate and channel. This significantly degrades the resonant nature of tunneling, and nullifies efforts to suppress it, as demonstrated in the study of RTD of nanometer sizes [8]. However, to date, it has been shown that a RTD with a transverse size of 5 μm, is capable of operating at frequencies above 4 THz, which is 2 orders of magnitude higher frequencies of modern high-frequency transistors. A major obstacle to the wide use of RTD is the high cost of producing semiconductor nanoheterostructures, which requires the involvement of molecular beam epitaxy. However, the development of relatively cheap methods of obtaining carbon nanomaterials creates serious prospects of using such materials for the creation of RTD. RTD have already been successfully created on the base of graphene films [19, 20], but their quality is inferior to semiconductor films.

6. Conclusion

In summarizing, we can state that application of resonant tunneling can significantly increase the operating speed of the FET and reduce leakage currents. However, the application of 2DCS systems imposes new restrictions on the miniaturization, reducing her prospects to almost zero. However, even relatively large RTD already working on the frequencies exceeding the frequencies of the transistors. It is shown that devices based on resonant tunneling are able to replace the conventional FET. The main problem of widespread use of such devices today is a significant high cost of the technology of molecular-beam epitaxy. Possible further development of technology toward a carbon nanomaterials. Carbon nanomaterials might allow high-quality RTD, which is significantly cheaper than semiconductor materials. In this case, we should expect serious changes in the architecture of classical computers and the emergence of new solutions in the field of quantum computing.

Author details

Vladimir Popov

Address all correspondence to: sokhatiy@gmail.com

Institute of Microelectronics Technology of Russian Academy of Science, Chernogolovka, Russia

References

[1] Shauly EN. CMOS Leakage and Power Reduction in Transistors and Circuits: Process and Layout Considerations. Journal of Low Power Electronics Applications. 2012;**2**:1–29

[2] Ashley T, Buckle L, Datta S, Emeny MT, Hayes DG, Hilton KP, Jefferies R, Martin T, Phillips TJ, Wallis DJ, Wilding PJ, Chau R. Heterogeneous InSb quantum well transistors on silicon for ultra-high speed, low power logic applications. Electronics Letters. 2007;**43**:14

[3] Esaki L. New Phenomenon in Narrow Germanium p–n Junctions. Physical Review. 1958;**109**:603

[4] ShrifferJ.R, Kingston RH, editor. Semiconductor Surface Physics. Philadelphia, USA: University of Pennsylvania Press; 1956. p. 68

[5] Tsui DC. Observation of Surface Bound State and Two-Dimensional Energy Band by Electron Tunneling. Physical Review Letters. 1970;**24**:303

[6] Chang LL, Esaki L, Tsu R. Resonant tunneling in semiconductor double barriers Applied Physics Letters. 1974;**24**:593

[7] Kazarinov R.F, Suris RA. Possibility of amplification of electromagnetic waves in a semiconductor with a superlattice. Semiconductors. 1971;**5**:707

[8] Mizuta H Tanoue T. The Physics and Applications of Resonant Tunneling Diodes. Cambridge, UK: Cambridge University Press; 1995

[9] Mori T, Ohnishi H, Imamura K, Muto S, Yokoyama N. Resonant tunneling hot-electron transistor with current gain of 5. Applied Physics Letters. 1986;**49**:1779

[10] Luryi S. Frequency limit of double-barrier resonant-tunneling oscillators. Applied Physics Letters. 1985;**47**:490

[11] Kane EO, Burstein L, Lundqvist S, editors. Tunneling Phenomena in Solids. New York, USA: Plenum Press; 1969. p. 4

[12] Seabaugh AC, Frensley WR, Randall JN, Reed MA, Farrington DL, Matyi RJ. Pseudomorphic bipolar quantum resonant-tunneling transistor. IEEE Transactions on Electron Devices. 1989;**36**:2328

[13] Eaves L. Low dimensional devices: High magnetic field and optical spectroscopy studies of resonant tunneling and quantum well phenomena. Microelectronic Engineering. 1991;**15**:661

[14] Genoe J, Van Hoof C, Fobelets K, Mertens R, Borghs G. pnp resonant tunneling light emitting transistor. Applied Physics Letters. 1992;**61**:1051

[15] Seabaugh AC, Kao Y-C, Randall J, Frensley W, Khatibzadeh. Room Temperature Hot Electron Transistors with InAs-Notched Resonant-Tunneling-Diode Injector. The Japanese Journal of Applied Physics. 1991;**30**:921

[16] Popov VG. Field effect transistor with two-dimensional gate and channel. Semiconductors. 2016;**50**:235.

[17] Popov VG. Field effect transistor with two-dimensional gate and channel with carriers in different valleys. In: Lukichev VF, Rudenko KV, editors. Proceedings of the International Conference Micro- and Nanoelectronics – 2016; October 3–7, 2016; Moscow – Zvenigorod. Moscow, Russia: Maks Press; 2016; p. 25

[18] Mendez EE, Calleja E, Goncalves da Silva CET, Chang LL, Wang WI. Observation by resonant tunneling of high-energy states in GaAs-$Ga_1{-}_XAl_XAs$ quantum wells. Physical Review B. 9 1986;**33**:7368

[19] Britnell L, Gorbachev RV, Jalil R, Belle BD, Schedin F, Mishchenko A, Georgiou T, Katsnelson MI, Eaves L, Morozov SV, Peres NMR, Leist J, Geim AK, Novoselov KS, Ponomorenko LA. Field-Effect Tunneling Transistor Based on Vertical Graphene Heterostructures. Science. 2012;**335**:947

[20] Britnell L, Gorbachev RV, Geim AK, Ponomorenko LA, Mishchenko A, Greenaway MT, Fromhold TM, Novoselov KS, Eaves L. Resonant tunnelling and negative differential conductance in graphene transistors. Nature Communications. 2013;**4**:1794

Section 2

High Electron Mobility Transistors

High Electron Mobility Transistors: Performance Analysis, Research Trend and Applications

Muhammad Navid Anjum Aadit,
Sharadindu Gopal Kirtania, Farhana Afrin,
Md. Kawsar Alam and Quazi Deen Mohd Khosru

Additional information is available at the end of the chapter

http://dx.doi.org/10.5772/67796

Abstract

In recent years, high electron mobility transistors (HEMTs) have received extensive attention for their superior electron transport ensuring high speed and high power applications. HEMT devices are competing with and replacing traditional field-effect transistors (FETs) with excellent performance at high frequency, improved power density and satisfactory efficiency. This chapter provides readers with an overview of the performance of some popular and mostly used HEMT devices. The chapter proceeds with different structures of HEMT followed by working principle with graphical illustrations. Device performance is discussed based on existing literature including both analytical and numerical models. Furthermore, some notable latest research works on HEMT devices have been brought into attention followed by prediction of future trends. Comprehensive knowledge of up-to-date results, future directions, and their analysis methodology would be helpful in designing novel HEMT devices.

Keywords: 2DEG, heterojunction, high electron mobility, polarization, power amplifier, quantum confinement

1. Introduction

The requirement of high switching speed such as needed in the field of microwave communications and RF technology urged transistors to evolve with high electron mobility and superior transport characteristics. The invention of HEMT devices is accredited to T. Mimura who was involved in research of high-frequency, high-speed III–V compound semiconductor devices at Fujitsu Laboratories Ltd, Kobe, Japan. Following that, HEMT was first commercially

INTECH
open science | open minds

© 2017 The Author(s). Licensee InTech. This chapter is distributed under the terms of the Creative Commons Attribution License (http://creativecommons.org/licenses/by/3.0), which permits unrestricted use, distribution, and reproduction in any medium, provided the original work is properly cited. CC BY

used as a cryogenic low-noise amplifier at Nobeyama Radio Observatory (NRO), Nagano, Japan in 1985 [1].

Working toward the need of high frequency, low noise, and high power density applications, traditional MOSFETs and MESFETs require to be built with very short channel lengths so that majority of the carriers face minimum impurity scattering and performance degradation is reduced. Such applications also imply design and performance limitations requiring high saturation current as well as large transconductance, which may be achieved by heavy doping. To overcome these limitations, HEMT devices incorporate heterojunctions formed between two different bandgap materials where electrons are confined in a quantum well to avoid impurity scattering. The direct bandgap material GaAs have been used in high frequency operation as well as in optoelectronic integrated circuits owing to its higher electron mobility and dielectric constant. AlGaAs are the most suitable candidate for barrier material of GaAs possessing nearly same lattice constant and higher bandgap than that of GaAs. That is why GaAs/AlGaAs heterostructure is considered to be the most popular choice to be incorporated in HEMTs. However, AlGaN/GaN HEMT is another excellent device that has been extensively researched in recent times. It can operate at very high frequencies with satisfactory performance as well as possess high breakdown strength and high electron velocity in saturation [2]. GaN shows very strong piezoelectric polarization which aids accumulation of enormous carriers at AlGaN/GaN interface. In these types of HEMTs, device performance depends on the types of material layer, layer thickness, and doping concentration of AlGaN layer providing flexibility in the design process. For its superiority over HEMT devices with other materials, AlGaN/GaN HEMT has been selected as an example for different topics in this chapter.

The chapter begins with brief explanation of different common structures and basic operating principle of HEMT devices. The main focus is to analyze HEMT device performance based on analytical and numerical analyses found in the literature. For example, *I-V* characteristics of HEMTs [3], two-dimensional electron gas (2DEG) estimation [4], short channel current collapse effect [5], capacitance calculation [6], and thermal effects [7] on HEMTs have been discussed in Section 4, which have been obtained using analytical study. Section 5 includes more rigorous methods such as drift-diffusion modeling [8], transport calculation [9], Monte Carlo simulation [10], Green's function formalism [11], and polarization-based shear stress analysis [12] that need significant numerical techniques to characterize HEMT device performance. Looking back into the very recent years, some up-to-date results have been presented in Section 6, namely "Latest Research" section. Section 7 presents some prediction on the future research trends based on these latest results. Finally, possible application fields of HEMT devices have been discussed in the last section.

2. Common HEMT structures

2.1. GaAs-based HEMTs

A typical GaAs-based HEMT structure is shown in **Figure 1**. With a view to separating the majority carriers from ionized impurities, an abrupt hetero-structure is created between the

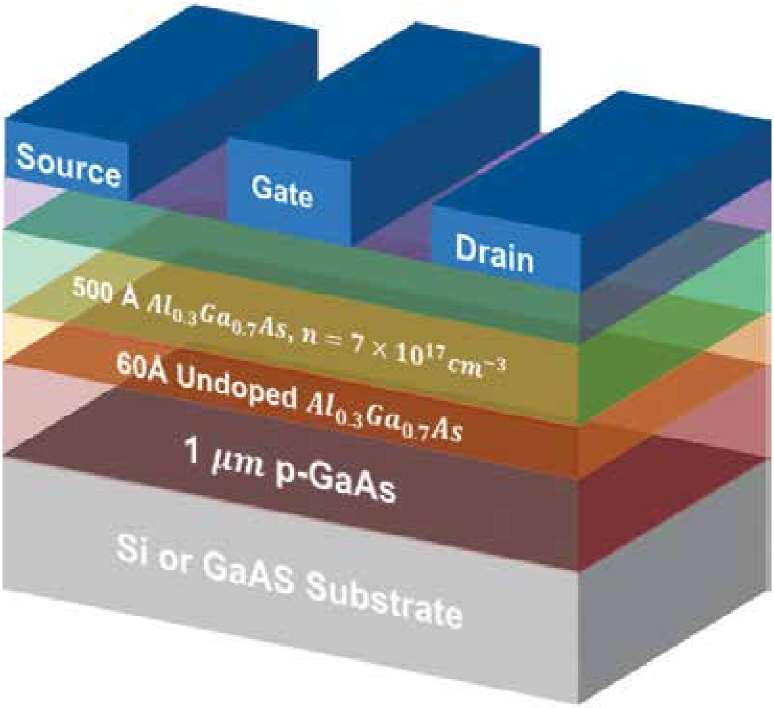

Figure 1. Structure of GaAs-based HEMTs.

wide bandgap material AlGaAs and lower bandgap material GaAs while the wide bandgap material is doped (e.g., doping density, $n = 7 \times 10^{17}$ cm^{-3}). Thus, a channel is formed at the interface of GaAs/AlGaAs heterojunction. To reduce coulombic scattering, a thin layer of undoped AlGaAs is used as spacer layer. At the bottom, the Si or GaAs layer serves as a substrate.

2.2. GaN-based HEMTs

GaN-based HEMTs have the similar layered structure to conventional GaAs-based HEMTs as shown in **Figure 2**. But no intentional doping is required in AlGaN/GaN HEMTs. Rather electrons come from surface states due to the spontaneous polarization found in wurtzite-structured GaN. This accumulation of free carrier forms high carrier concentration at the interface leads to a 2DEG channel. **Figure 2** also indicates donor-like surface traps (empty) on top and thereby the positively polarized charge at AlGaN/GaN interface. The 2DEG is an explicit function of the surface barrier, AlGaN thickness and the bound positive charge at the interface.

2.3. InP-based HEMTs

InP HEMTs result in lower electron effective mass in InGaAs channel layer compared to conventional GaAs-based HEMTs. These HEMTs contain comparatively large conduction band offset (approximately 0.5 eV) between the channel layer and adjacent barrier layer, InAlAs

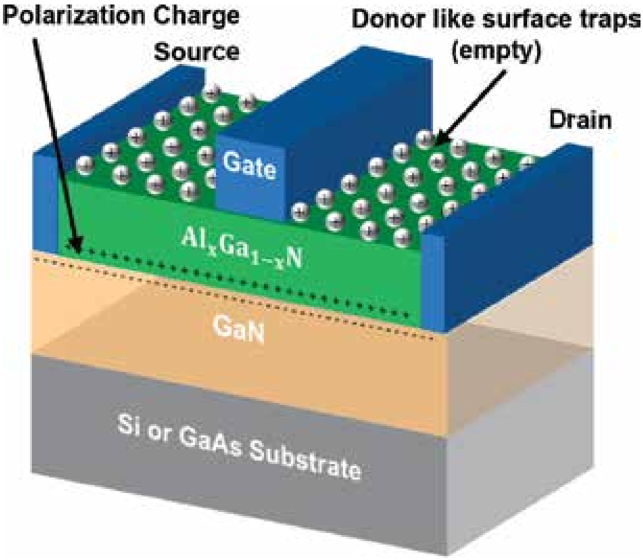

Figure 2. Structure of GaN-based HEMTs.

[13]. Hence, InP-based HEMTs show high electron mobility, high electron saturation velocity, and high electron concentration. The device usually consists of an InGaAs/InAlAs composite cap layer for enhanced ohmic contact, an undoped InAlAs as Schottky barrier and an InGaAs/InAs composite channel for superior electron transport properties as depicted in **Figure 3**.

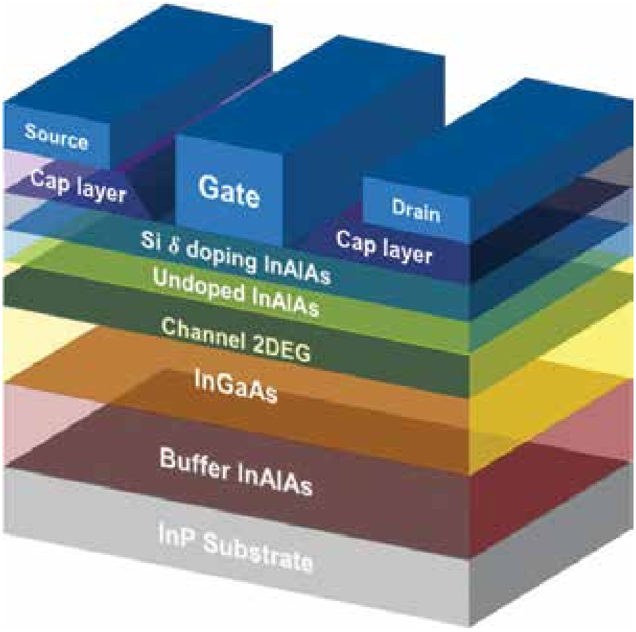

Figure 3. Structure of InP-based HEMTs.

3. Working principle of HEMTs

HEMTs are essentially heterojunctions formed by semiconductors having dissimilar bandgaps. When a heterojunction is formed, the conduction band and valence band throughout the material must bend to form a continuous level. The wide band element has excess electrons in the conduction band as it is doped with donor atoms (or due to polarization charge in GaN-based HEMTs). The narrow band material has conduction band states with lower energy. Therefore, electrons will diffuse from wide bandgap material to the adjacent lower bandgap material as it has states with lower energy. Thus, a change in potential will occur due to movement of electrons and an electric field will be induced between the materials. The induced electric field will drift electrons back to the conduction band of the wide bandgap element. The drift and diffusion processes continue until they balance each other, creating a junction at equilibrium like a p-n junction. Note that the undoped narrow bandgap material now has excess majority charge carriers, which yield high switching speed. An interesting fact is that the low bandgap undoped semiconductor has no donor atoms to cause scattering and thus ensures high mobility.

Another interesting aspect of HEMTs is that the band discontinuities across the conduction and valence bands can be engineered to control the type of carriers in and out of the device. This diffusion of carriers leads to the accumulation of electrons along the boundary of the two regions inside the narrow bandgap material. The accumulation of electrons can lead to a very high current in these devices. The accumulated electrons are also known as 2DEG. **Figure 4** shows the generalized band diagram formed at the heterojunction for typical HEMTs. Both

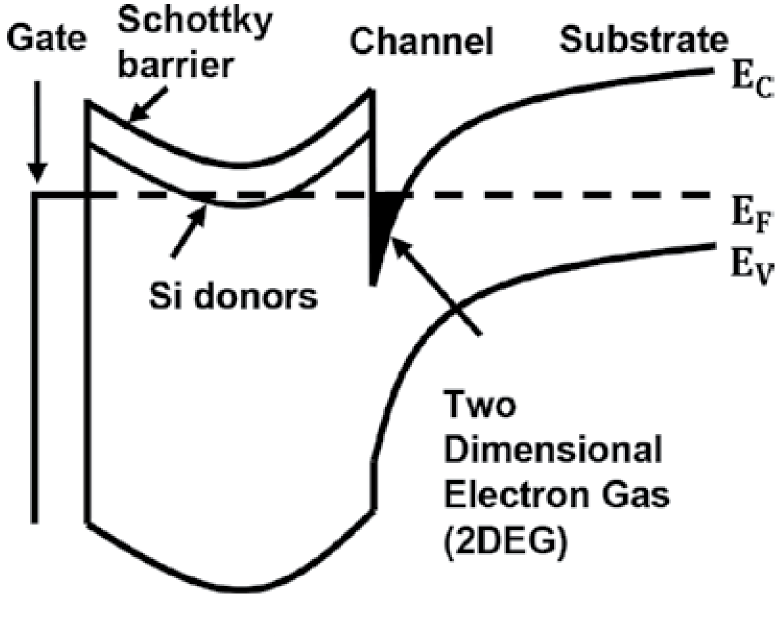

Figure 4. Generalized energy band diagram of HEMTs.

the conduction band (E_c) and valence band (E_v) bend with respect to the Fermi level (E_F) resulting in a quantum well filled with 2DEG and eventually, a conducting channel is formed.

4. Performance analysis: analytical approach

With rapidly growing popularity in high frequency and high power applications, HEMT devices have received extensive research attention in recent days. Many analytical models to study the characteristics of HEMTS as well as to improve device performance can be found in the literature. In this section, we present some of the eminent and effective analytical research works on AlGaN/GaN HEMTs.

4.1. Current-voltage characteristics using charge control model

An improved charge control model for *I-V* characteristics of AlGaN/ GaN HEMTs was presented in 2008 by Li et al. [3]. This model includes Robin boundary conditions in the solution of 1-D Schrödinger equation and customizable eigen values in the solution of 2-D Poisson's equation. Nonlinear polarization and parasitic resistance of source and drain have been incorporated in this model. The model estimates drain current assuming second-order continuity with analytical representation of transconductance. The device structure used in this model is almost similar to that of **Figure 2**. However, the only difference is that a doped AlGaN layer of 22 nm with doping concentration, $N_D = 2 \times 10^{18}$ cm^{-3} is present above the undoped AlGaN layer to enhance polarization. The *I-V* result plotted using this analytical model is shown here in **Figure 5** for different gate voltages.

4.2. Dependence of 2DEG charge density on gate bias

Khandelwal et al. proposed a physics-based analytical model for 2DEG density in AlGaN/GaN HEMTs [4]. Using this model, they show the interdependence between 2DEG and Fermi levels. The proposed model does not require any fitting parameters. It models 2DEG considering charge concentration in two different regions. One has higher first subband energy, while the other has lower first subband energy compared to the Fermi level. Moreover, a unified model is also presented combining these two regions. It presents variation of 2DEG with gate bias voltage as shown in **Figure 6**. The results show excellent agreement with numerical calculations.

4.3. Short channel *I-V*characteristics with current collapse

Current collapse is an undesirable but inevitable phenomenon in GaN-based HEMTs. It is a short channel nonideal effect where current depends on the previous memory of gate voltage. For *I-V* characteristics of AlGaN/GaN HEMTS in presence of current collapse, another compact model was proposed [5]. It incorporates trapping mechanism and gate edges and is based on experimental data. Capacitance-voltage (*C-V*) characteristics of AlGaN/ GaN HEMTs can also be calculated using this model. This model analyses device transconductance vs. gate bias when current collapse occurs. A comparative plot of transconductance with and without current collapse as determined by this compact short channel model is shown in **Figure 7**.

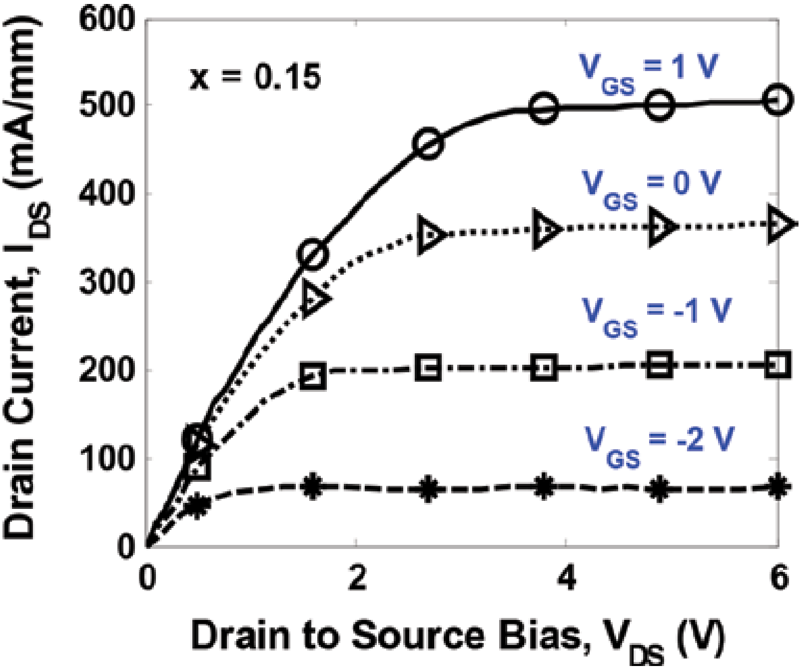

Figure 5. *I–V* characteristics for an $Al_{0.15}Ga_{0.85}N$/GaN HEMTs. The gate-to-source bias is swept from 1 to −2 V at a step of −1 V.

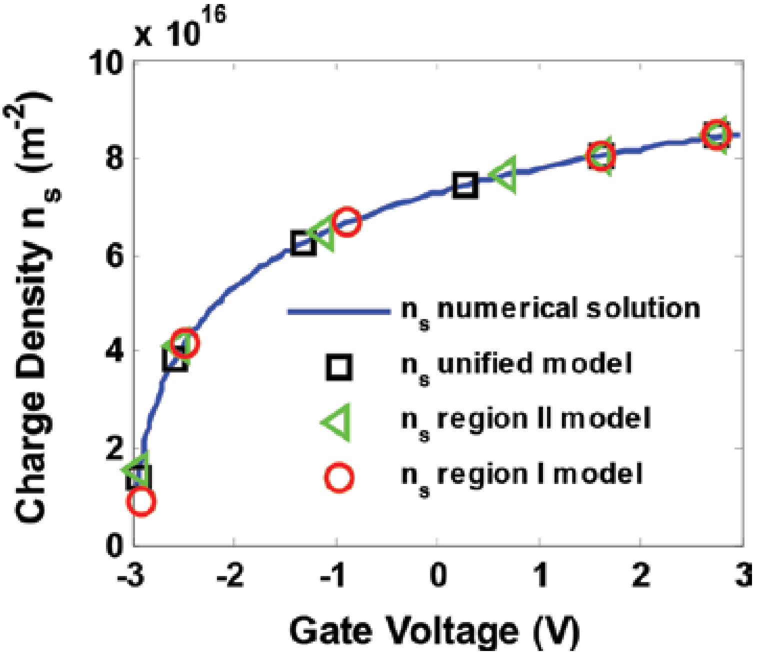

Figure 6. Comparison of 2DEG charge density, n_s with numerical calculations as a function of gate voltage.

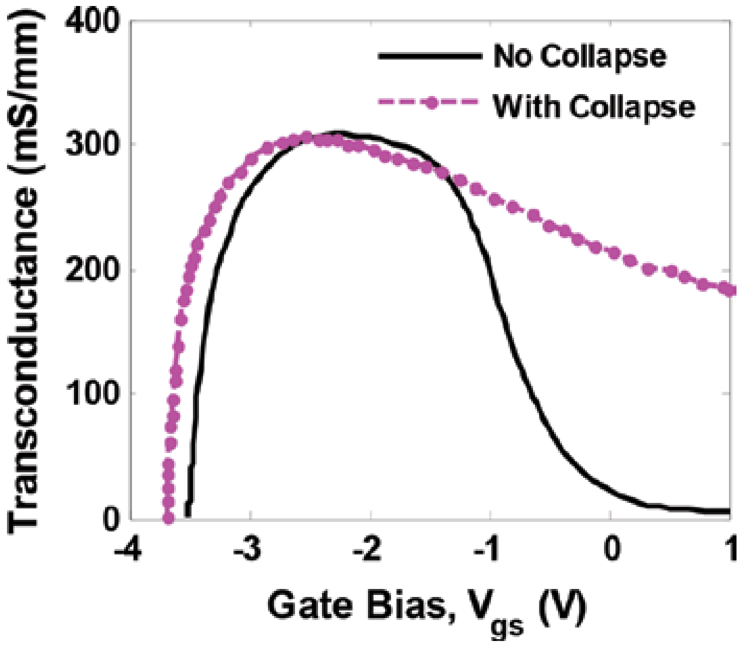

Figure 7. Comparison of transconductance with and without current collapse for AlGaN/GaN HEMTs.

4.4. Gate capacitance including parasitic components

Zhang et al. proposed a surface potential-based analytical model for calculating capacitance including parasitic components for AlGaN/GaN HEMTs [6]. The sheet charge density is modeled solving charge control equations and capacitance is calculated based on the concept of surface charge potential, which is consistent with the sheet charge density model. The parasitic components are further included in the model to provide a complete model. The developed model shows agreement with TCAD simulations and experimental data.

4.5. Thermal effects with complex structures

Although AlGaN/GaN HEMT is a promising device for high frequency and high power applications, its performance can be degraded at high temperatures. Therefore, a thermal modeling is required to predict device performance at different temperatures. Bagnall et al. developed such a thermal model that incorporates thermal effects with closed form analytical solutions for complex multilayer structured HEMTs [7]. This structure consists of N number of layers (j = 1, 2, 3, …, N) and a heat source placed within the layers as shown in **Figure 8(a)**. The analytical modeling is carried out using Fourier series solution and validated using Raman thermography spectra. Distribution of temperature along AlGaN/GaN x-axis interface including heat source as presented by the model is shown in **Figure 8(b)**.

Apart from these models, many other analytical models have been proposed for noise elimination, loss calculation, estimation of polarization, small signal analysis, etc.

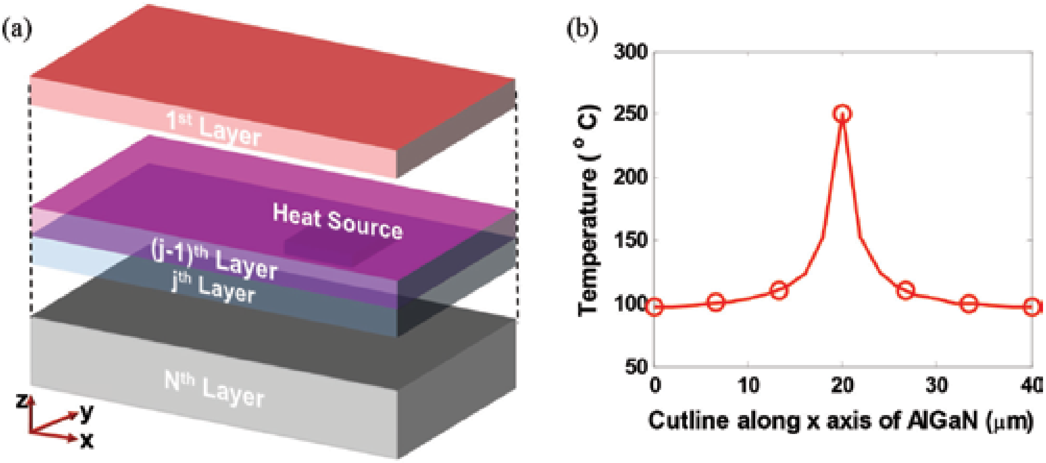

Figure 8. (a) Complex multi-layer HEMT structure with a heat source, and (b) Temperature distribution along *x* axis for AlGaN/GaN HEMTs including the heat source.

5. Performance analysis: numerical approach

Different numerical studies of HEMTs have been performed to analyze the influence of internal physical mechanisms. Some generalized numerical models reviewed from the literature are presented in this section.

5.1. Fully coupled drift-diffusion model

Yoshida et al. presented a two-dimensional numerical analysis of HEMTs to simulate device performance [8]. Anderson's model is used to generate the equations of band-edge lines and Boltzmann statistics is considered. Spatially continuous band-edge variation is not justified in this model as current across the hetero interface is neglected. The hole current and the generation-recombination current are also neglected. Finite difference approximation is used to discretize Poisson's equation and electron current continuity equation. After that, resultant equations are solved self consistently using Newton's method. This fully coupled model is traditionally known as drift-diffusion model [14].

5.2. Energy-transport model: transport calculation

Buot presented a two-dimensional numerical simulator based on the analysis of the first three moments of the Boltzmann equation, known as the energy-transport model [9]. It has been used to study various effects on the performance of AlGaAs/GaAs HEMTs [9]. The coupled transport equations (for details of energy transport equations, see Ref. [15]) were solved numerically using finite-difference technique on a uniform mesh, using iterative scheme. Using HISSDAY, a computer simulator program, the transport equations for the energy transport model are numerically solved using implicit scheme for the continuity equations; Scharfetter-Gummel method [16] for the current transport equation; and explicit forward differencing "marching" method for calculating the average energy. This model has an improvement over Widiger's energy transport model [17] where conduction is ignored in the AlGaAs layer [9].

5.3. Monte Carlo simulation

Ueno et al. presented Monte Carlo simulation of HEMTs to analyze 2DEG electron transport [10]. The analysis is based on electron–phonon interaction model proposed by Price [18]. In this framework, the 2DEG electrons are assumed to be scattered by bulk phonons. Thus, wave functions calculated by self-consistent analysis are used to evaluate the scattering rate. The channel region is not considered uniform and electrons near drain region are considered as three dimensional and near-source region are considered as two dimensional. In addition, electrons with high energy beyond the barrier height behave as three-dimensional electrons and are not confined in the quantum well. In these simulations, the initial condition is first evaluated. Then the sheet electron density at each position between the source and the drain are estimated using the current continuity relation along the channel. Next, Monte Carlo simulation is carried out by dividing the channel into different meshes and evaluating the scattering rates of the electronic states in each mesh. Then taking the potential distribution of the given device from two-dimensional Poisson equation, the steps are repeated until a steady state is obtained.

5.4. Noise current using Green's function formalism

Lee and Webb described a numerical approach to simulate the intrinsic noise sources within HEMTs [11]. A 2-D numerical device solver is used in this model. Spectral densities for the gate and drain noise current sources and their correlation are evaluated by capacitive coupling. After solving Poisson's and the continuity equations using 2-D numerical device solver, Green's functions are obtained. Here, Green's functions are used to determine local fluctuation (in terms of current or voltage at any point in the channel) at the gate and drain terminals. This approximate impedance field concept [19] helps determining the gate and drain noise sources and their correlation. For numerical simulation, the entire device is divided into some orthogonal areas and it is considered that 2-D simulation results will be consistent with the 3D simulation result. Spontaneous polarization and strain-induced piezoelectric polarization are also considered. It is assumed that the microscopic fluctuations in each segment are spatially uncorrelated which are originated from velocity fluctuation (diffusion) noise only.

5.5. High temperature shear stress analysis

Hirose et al. proposed a numerical model for AlGaN/GaN HEMT structures where shear stress due to the inverse piezoelectric effect is used to predict high-temperature DC stress test results [12]. In this model, lattice plane slip in the crystal is assumed to be the initial stage of crack formation. Shear stress causes the slip, and slip deforms the crystal when the shear stress exceeds the yield stress. In GaN-based HEMTs, the basal slip plane is (0001) and the slip direction is <1120>. The AlGaN layer is a wurtzite crystal grown in the <0001> direction [20]. Shear stress is assumed to be a result of the inverse piezoelectric effect. The mechanical stress and electric displacement occur due to the piezoelectric effect. Under the assumption of lattice mismatch in AlGaN layer, shear stress relates to the slip in the <1120> direction. However, to calculate shear stress, electric field is obtained from two-dimensional device simulation based on Poisson's equation and drift-diffusion current continuity equations. This model includes piezoelectric charges and the difference in spontaneous polarization charges in the AlGaN/GaN interface.

Among the numerical models, any one may have advantage over other models, but also have some limitations. For example, energy transport model can include hot electron effect [14]. Drift-diffusion model cannot predict performances of submicron level gate devices [9]. Monte Carlo approach is one of the advanced approaches [21]. All of these numerical models provide unique insights into the device physics and create opportunity of performance improvement with TCAD before device fabrication.

6. Latest research

With the upsurge of popularity, research works on HEMT devices are still going on. In this section, some very recent research works published in renowned scientific literature have been briefly highlighted.

6.1. GaN HEMT-based RF tuned cavity oscillator

Hörberg et al. presented a GaN-based oscillator for X band tuned by radio frequency microelectromechanical systems (RF-MEMS) [22]. The phase noise is reported to be reduced between the range of −140 and −129 dBc/Hz at 100 kHz offset, which is significantly low. This oscillator is suitable for reduced noise-based high frequency modulators.

6.2. A compact GaN HEMT power amplifier MMIC

A compact GaN HEMT-based X-band power amplifier MMIC has been reported with detailed performance analysis recently [23]. A good range of output power (47.5–48.7 dBm) can be obtained from this amplifier. Such amplifier can be used to build electronic systems that require airborne phased radar array or satellite transmitters. Improved output power of the amplifier also improves the stability, reliability, and performance of these electronic systems. **Figure 9** shows the output power performance in both pulse mode and continuous wave (CW) modes with frequency variation in this power amplifier.

6.3. Q-spoiling based on depletion mode HEMTs

Q-spoiling is a process where MRI coils are detuned for safety and protection. Traditionally, such decoupling or Q-spoiling is done using PIN diodes, which require high current and power drain. Lu et al. proposed an alternative technique of Q-spoiling, which replaces PIN diodes with depletion mode GaN HEMTs [24]. It is shown that the proposed technology detunes MRI coils effectively with low current and power drain compared to the traditional Q-spoiling technologies. It also provides suitable safety measures required for detuning the MRI coils.

6.4. GaN HEMT oscillators with low phase noise

Excellent figure of merit (FOM) has been achieved for low phase noise in designing GaN HEMT-based oscillators [25]. The design demonstrated that low phase noise can coincide

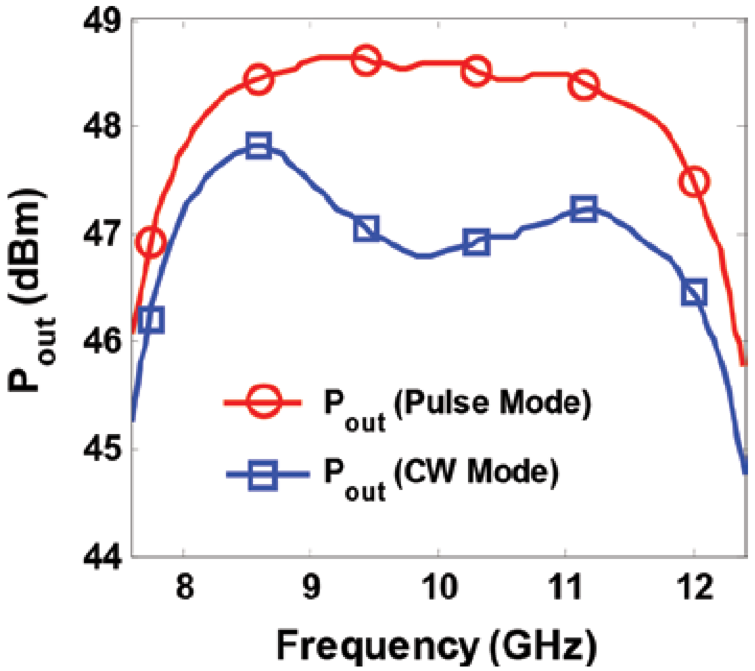

Figure 9. Output power performance of GaN HEMT power amplifier MMIC with frequency variation in pulse and CW modes.

with low bias power. The result is verified designing Colpitt and negative resistance oscillators and both of these present so far the best reported FOMs.

6.5. Kink effect in GaN HEMT technology

Crupi et al. investigated Kink effect (KE) in advanced GaN HEMT technology [26]. For better understanding, KE is studied comprehensively with change of temperature and bias conditions. It is shown that the dependence of KE on operating conditions is mainly due to device transconductance. Characterization of anomalous KE would be a useful tool for microwave engineers who need this knowledge of KE for designing and modeling devices with GaN HEMTs.

6.6. 600 V GaN HEMT switches for power converters

A total of 600 V GaN HEMT switches have been demonstrated experimentally to show performance comparison with silicon-based transistor switches such as IGBTs and MOSFETs [27]. HEMT switches, despite being beginners, show excellent performance compared to the matured counterparts, Si-based MOSFETs. It is shown that GaN switches offer higher boost converter efficiency than the MOSFET switches. Next, GaN switches are compared experimentally with IGBTs. Both Si body and SiC body-based IGBTs have been considered. It is found that at higher switching frequency, IGBT switches loss efficiency very rapidly, while HEMT switches loss efficiency monotonically as shown in **Figure 10**. Therefore, HEMTs offer superior performance to Si-based MOSFETs and IGBTs for high frequency power converter switching applications.

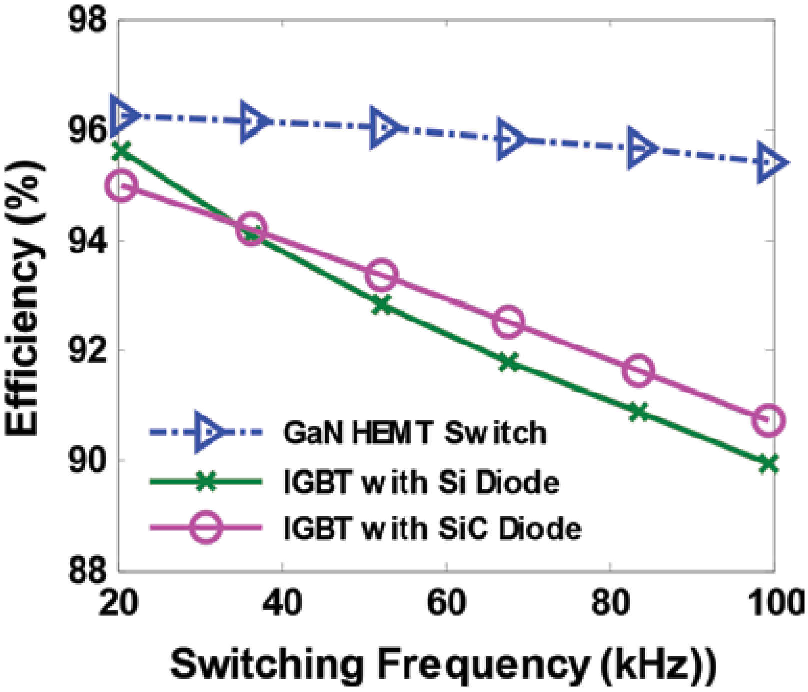

Figure 10. Comparison of efficiency for GaN HEMT switches with Si body IGBT and SiC body IGBT switches.

7. Future trends

The future HEMT devices based on two-dimensional carrier confinement seem very bright in electronics, communications, physics, and other disciplines. GaAs, InP, and GaN-based HEMTs will continue their journey toward higher integration, higher frequency, higher power, higher efficiency, lower noise, and lower cost. GaN, in particular, offers high-power, high-frequency territory of vacuum tubes and leads to lighter, more efficient, and more reliable communication systems.

HEMTs will continue to mold themselves into other kinds of FETs that will exploit the unique properties of 2DEG in various materials systems. In power electronics, GaN-based HEMTs can create a great impact on consumer, industrial, transportation, communication, and military systems. On the other hand, MOS-HEMT or MISFET structures are likely to be operated in enhancement mode with very low leakage current.

Si CMOS technology is rapidly advancing toward 10 nm gate regime. To achieve this, power dissipation management in future generation ultra-dense chips will be a significant challenge. Operating voltage reduction may be a solution to meet this challenge. However, currently, it is difficult to accomplish this with Si CMOS while maintaining quality performance. Quantum well-based devices such as InGaAs or InAs HEMTs offer very high potential. Therefore, HEMTs may extend the Moore's law for several more years which will be gigantic for the society [28].

From the past, it can be anticipated that, researching on new device models and structures of HEMTs will definitely result in new insights into the often bizarre physics of quantized electrons. ZnO, SiGe, and GaN have shown fractional quantum Hall effect (FQHE), the greatest exponent for impeccable purity and atomic order, which ensure the bright future of HEMT devices [29].

The concept of different kinds of physical and biosensors are still very new to these kind of devices. The ultra-high mobility that is possible in InAlSb/InAsSb-based system enables high-sensitivity micro-Hall sensors for many applications including scanning Hall probe microscopy and biorecognition [30]. Three-axis Hall magnetic sensors have been reported in micromachined AlGaAs/GaAs-based HEMTs [31]. These devices may be used in future electronic compasses and navigation. THz detection, mixing and frequency multiplication can also be used by 2DEG-based devices [32]. GaN and related materials have strong piezoelectric polarization, and they are also chemically stable semiconductors. Combining functionalized GaN-based 2DEG structures with free-standing resonators, there is a possibility of designing sophisticated sensors [33]. These can offer methods of measurements of several properties such as viscosity, pH, and temperature.

Without references, expansion of this technology in the machine to machine (M2M) field is expected to be used in cloud networking-based various sensing functions. Diverse applications such as environmental research, biotechnology, and structural analysis can be greatly benefited with the help of newly emerged sensing technology which has high speed, high mobility, and high sensitivity characteristics. HEMT technology is expected to make a great change in the intelligent social infrastructure from the device level. A smart city system, transport system, food industry, logistics, agriculture, health welfare, environmental science, and education systems are examples where this technology can make exceptions [34].

The rise of III-N-based solid-state lighting will lead to a continuous development of materials, substrates, and technologies pushed by a strong consumer market. In an analogy, III-N optoelectronics will challenge the light bulbs, while III-N electronics will challenge the electronic equivalent, the tubes [35].

8. Applications

Explosion of the internet multimedia communications has speedily spread over the world, which urgently demands the proliferation of transmission network capacity. HEMTs-based devices are the most attractive choices for breaking through the speed limit and high gain and noise free mechanism. Different companies worldwide develop and manufacture HEMT-based devices, and many possible applications have been suggested for these devices. Without considering all of those possibilities, some key applications are summarized in this section.

8.1. Broadband communication

Cellular communication has got the most important nonmilitary applications of HEMT devices by replacing Si transistors. For such broadband/multiband communication applications, we get a lot of advantages. The increase in relative bandwidth for a given power level is one of those. Some new circuit and system concepts provide bandwidth with increased efficiency. Linearity has been improved for the same output power. Reduction of memory effects is also found by using GaN HEMT devices [36].

8.2. Radar components and space applications

High gain and low noise amplifiers are the main characteristics for making radar components. GaN HEMTs are one of the first choices for such components. Active electronic sensor arrays are built from GaN-based HEMTs, which are used for airborne radars, ground-based air defense radars, and naval radars [37]. Ka-band missile applications at 35 GHz are also being discussed in literature [38]. Discrete HEMTs are almost always used as the preamplifier in a typical DBS receiver, followed by one or more GaAs MESFET monolithic microwave integrated circuits (MMICs) due to their excellent low-noise characteristics. The use of the low-noise HEMT preamplifier has resulted in substantial improvements in system performance at little additional cost. A low-noise down-converter consisting of a 0.25 pm HEMT and three GaAs MMIC chips has shown a system noise figure less than 1.3 dB with a gain of about 62 dB from 11.7 GHz to 12.2 GHz, which is phenomenal for a commercial, system [39]. Microwave equipment used for space applications are very expensive as they need extra protection from harsh environment in space to survive. Moreover, spacecraft shall be launched, and this implies that the equipment should also sustain without damage at high levels of vibrations and shocks. HEMTs can be fabricated to survive these conditions and have been extensively used in various fields. Generally, a microwave component for space applications is ten to hundred times more expensive than for commercial applications. Workers at the National Radio Astronomy Observatory (NRAO) have used the excellent cryogenic performance of HEMTs to receive signals during the Neptune flyby of the voyager spacecraft.

8.3. Sensor applications

In the recent decade, chemical sensors have gained importance for applications that include homeland security, medical and environmental monitoring, and food safety. The desirable goal is the ability to simultaneously analyze a wide variety of environmental and biological gases and liquids in the field and be able to selectively detect a target analyte with high specificity and sensitivity. The conducting 2DEG channel of HEMTs is very close to the surface and very sensitive to adsorption of analytes. Hence, HEMT sensors can be a good alternative for detecting gases, ions, and chemicals [40].

8.4. DNA detection

Au-gated AlGaN/GaN HEMTs functionalized in the gate region with label free 3'-thiol modified oligonucleotides serves as a binding layer to the AlGaN surface, which can detect the hybridization of matched target DNAs. XPS shows immobilization of thiol modified DNA covalently bonded with gold on the gated region. Drain-source current shows a clear decrease of 115 μA as this matched target DNA is introduced to the probe DNA on the surface, showing the promise of the DNA sequence detection for biological sensing [41].

8.5. Protein detection

Using amino-propyl silane in the gate region, ungated AlGaN/GaN HEMT structures can be activated, which can serve as a binding layer to the AlGaN surface for attachment of biotin. Biotin has a very high affinity to streptavidin proteins. When the chemicals are attached to AlGaN/GaN HEMTs, the charges on the attached chemicals affect the current of the device. The device shows a clear decrease of 4 μA as soon as this protein is collected at the surface, showing indication of protein sensing [41].

8.6. pH detection

The use of Sc_2O_3 gate dielectric produces superior results to either native oxide or UV ozone-induced oxide in the gate region. The ungated HEMTs with Sc_2O_3 in the gate region exhibit a linear change in current between pH 3–10 of 37μA/pH. The HEMT pH sensors show stable operation with a resolution of <0.1 pH over the entire pH range. The results indicate that HEMTs may have application in monitoring pH solution changes between 7 and 8, the range of interest for testing human blood [40].

9. Conclusion

In this chapter, device characteristics and performance analysis of HEMTs have been discussed based on the available literature. With a brief introduction of different structures and brief working principle, this chapter summarizes some prominent analytical and numerical research works on HEMTs. *I-V* characteristics, charge estimation, capacitance calculation, short channel effects, and thermal response of HEMTs have been discussed. Moreover, drift diffusion modeling, transport calculation, Monte Carlo simulation, Green's function formalism, and shear stress analysis have been discussed which rely on numerical approaches. HEMT-based oscillators, amplifiers, Q-spoilers, switches, and diodes are getting popularity in recent days. These have been overviewed based on latest reported researches. Based on these latest research studies, future research trends on HEMTs have been reviewed. Last but not the least, many important applications of HEMTs such as broadband and radar communications, space, and sensor constituents, DNA, protein, and pH detections have been listed to emphasize the immense prospects of HEMT devices. This chapter provides researchers of relevant fields a direction for future improvement of HEMT devices with prospective applications.

Author details

Muhammad Navid Anjum Aadit, Sharadindu Gopal Kirtania, Farhana Afrin, Md. Kawsar Alam* and Quazi Deen Mohd Khosru

*Address all correspondence to: kawsaralam@eee.buet.ac.bd

Department of Electrical and Electronic Engineering, Bangladesh University of Engineering and Technology, Dhaka, Bangladesh

References

[1] Mimura T. The early history of the high electron mobility transistor (HEMT). IEEE Transactions on Microwave Theory and Techniques. 2002 Mar;50(3):780–2.

[2] Gangwani P, Pandey S, Haldar S, Gupta M, Gupta RS. Polarization dependent analysis of AlGaN/GaN HEMT for high power applications. Solid-State Electronics. 2007 Jan 31;51(1):130–5.

[3] Li M, Wang Y. 2-D analytical model for current–voltage characteristics and transconductance of AlGaN/GaN MODFETs. IEEE Transactions on Electron Devices. 2008 Jan;55(1):261–7.

[4] Khandelwal S, Goyal N, Fjeldly TA. A physics-based analytical model for 2DEG charge density in AlGaN/GaN HEMT devices. IEEE Transactions on Electron Devices. 2011 Oct;58(10):3622–5.

[5] Koudymov A, Shur MS, Simin G, Chu K, Chao PC, Lee C, Jimenez J, Balistreri A. Analytical HFET *I-V* model in presence of current collapse. IEEE Transactions on Electron Devices. 2008 Mar;55(3):712–20.

[6] Zhang A, Zhang L, Tang Z, Cheng X, Wang Y, Chen KJ, Chan M. Analytical modeling of capacitances for GaN HEMTs, including parasitic components. IEEE Transactions on Electron Devices. 2014 Mar;61(3):755–61.

[7] Bagnall KR, Saadat OI, Palacios T, Wang EN. Analytical thermal model for HEMTs with complex epitaxial structures. In: 2014 IEEE Intersociety Conference on Thermal and Thermomechanical Phenomena in Electronic Systems (ITherm), 2014 May 27–30 (pp. 947–958), Orlando, FL, USA. IEEE.

[8] Yoshida J, Kurata M. Analysis of high electron mobility transistors based on a two-dimensional numerical model. IEEE Electron Device Letters. 1984 Dec;5(12):508–10.

[9] Buot FA. Two-dimensional numerical modelling of HEMT using an energy transport model. COMPEL-The International Journal for Computation and Mathematics in Electrical and Electronic Engineering. 1987 Jan 1;6(1):45–52.

[10] Ueno H, Yamakawa S, Hamaguchi C, Miyatsuji K. Monte Carlo simulation of HEMT. In: Proceedings, IEEE International Workshop on Physics and Computer Modeling of Devices Based on Low-Dimensional Structures. 1995 Nov 7 (pp. 85–89), Aizu-Wakamatsu, Japan. IEEE.

[11] Lee S, Webb KJ. Numerical noise model for the AlGaN/GaN HEMT. In: 2004 IEEE MTT-S International Microwave Symposium Digest, 2004 Jun 6 (Vol. 2, pp. 1057–1060), Fort Worth, TX, USA. IEEE.

[12] Hirose M, Matsushita K, Takagi K, Tsuda K. Numerical device model for reliable AlGaN/GaN HEMT structure design based on shear stress. In: 2013 IEEE Compound Semiconductor Integrated Circuit Symposium (CSICS), 2013 Oct 13 (pp. 1–4), Monterey, CA, USA. IEEE.

[13] Shinohara K, Matsui T. 3–7 Nano-gate transistor-world's fastest InP-HEMT. Journal of the National Institute of Information and Communications Technology. 2004;51:95–102.

[14] Loret D. Two-dimensional numerical model for the high electron mobility transistor. Solid-State Electronics. 1987 Nov 1;30(11):1197–203.

[15] Portengen T, Boots HM, Schuurmans MF. A priori incorporation of ballistic and heating effects in a four-moment approach to the Boltzmann equation. Journal of Applied Physics. 1990 Sep 15;68(6):2817–23.

[16] Glover GH. Study of electron energy relaxation times in GaAs and InP. Journal of Applied Physics. 1973 Mar;44(3):1295–301.

[17] Widiger D, Hess K, Coleman JJ. Two-dimensional numerical analysis of the high electron mobility transistor. IEEE Electron Device Letters. 1984 Jul;5(7):266–9.

[18] Price PJ. Two-dimensional electron transport in semiconductor layers. I. Phonon scattering. Annals of Physics. 1981 May 1;133(2):217–39.

[19] Shockley W, Copeland JA, James RP. The impedance field method of noise calculation in active semiconductor devices. Quantum Theory of Atoms, Molecules, and the Solid State, A Tribute to John C. Slater. Edited by Per-Olov Löwdin. New York: Academic Press, USA, 1966, p.537.

[20] Paufler P. RWK Honeycombe: The plastic deformation of metals. Edward Arnold (Publ.) ltd., Maidenhead, 1984, 483 p., paperback. ISBN 0713134682.

[21] Snowden CM. Compound Semiconductor Device Modelling. Miles RE, editor. Springer-Verlag; London, UK 1993 Mar.

[22] Hörberg M, Emanuelsson T, Ligander P, Lai S, Zirath H, Kuylenstierna D. RF-MEMS tuned GaN HEMT based cavity oscillator for X-band. IEEE Microwave and Wireless Components Letters. 2017 Jan; 27(1); 46–48.

[23] Tao HQ, Hong W, Zhang B, Yu XM. A compact 60W X-band GaN HEMT power amplifier MMIC. IEEE Microwave and Wireless Components Letters. 2017 Jan; 27(1); 73–75.

[24] Lu JY, Grafendorfer T, Zhang T, Vasanawala S, Robb F, Pauly JM, Scott GC. Depletion-mode GaN HEMT Q-spoil switches for MRI coils. IEEE Transactions on Medical Imaging. 2016 Dec;35(12):2558–67.

[25] Lai S, Kuylenstierna D, O¨zen M, Horberg M, Rorsman N, Angelov I, Zirath H. Low phase noise GaN HEMT oscillators with excellent figures of merit. IEEE Microwave and Wireless Components Letters. 2014 Jun;24(6):412–4.

[26] Crupi G, Raffo A, Marinkovic Z, Avolio G, Caddemi A, Markovic V, Vannini G, Schreurs DM. An extensive experimental analysis of the kink effects in S_{22} and h_{21} for a GaN HEMT. IEEE Transactions on Microwave Theory and Techniques. 2014 Mar;62(3):513–20.

[27] Mitova R, Ghosh R, Mhaskar U, Klikic D, Wang MX, Dentella A. Investigations of 600-V GaN HEMT and GaN diode for power converter applications. IEEE Transactions on Power Electronics. 2014 May;29(5):2441–52.

[28] Del Alamo, Jesus A. The High-Electron Mobility Transistor at 30: Impressive Accomplishments and Exciting Prospects. In: 2011 International Conference on Compound Semiconductor Manufacturing Technology, 2011 May (pp. 16-19), Indian Wells, California, USA. IEEE.

[29] Chen YZ, Trier F, Wijnands T, Green RJ, Gauquelin N, Egoavil R, Christensen DV, Koster G, Huijben M, Bovet N, Macke S. Extreme mobility enhancement of two-dimensional electron gases at oxide interfaces by charge-transfer-induced modulation doping. Nature Materials. 2015 Aug 1;14(8):801–6.

[30] Bando M, Ohashi T, Dede M, Akram R, Oral A, Park SY, Shibasaki I, Handa H, Sandhu A. High sensitivity and multifunctional micro-Hall sensors fabricated using InAlSb/InAsSb/InAlSb heterostructures. Journal of Applied Physics. 2009 Apr 1;105(7):07E909.

[31] Vorob'ev A, Chesnitskiy A, Toropov A, Prinz V. Three-axis Hall transducer based on semiconductor microtubes. Applied Physics Letters. 2013 Oct 21;103(17):173513.

[32] Dyakonov M, Shur M. Detection, mixing, and frequency multiplication of terahertz radiation by two-dimensional electronic fluid. IEEE Transactions on Electron Devices. 1996 Mar;43(3):380–7.

[33] Brueckner K, Niebelschuetz F, Tonisch K, Michael S, Dadgar A, Krost A, Cimalla V, Ambacher O, Stephan R, Hein MA. Two-dimensional electron gas based actuation of piezoelectric AlGaN/GaN microelectromechanical resonators. Applied Physics Letters. 2008 Oct 27;93(17):173504.

[34] Joshin K, Kikkawa T, Masuda S, Watanabe K. Outlook for GaN HEMT technology. Fujitsu Scientific and Technical Journal. 2014 Jan 1;50(1):138–43.

[35] Quay R. Gallium Nitride Electronics. Springer Science & Business Media; Berlin, Germany 2008 Apr 5.

[36] Wen CP, Wang J, Hao Y. Current collapse, memory effect free GaN HEMT. In: 2010 IEEE MTT-S International Microwave Symposium Digest (MTT), 2010 May 23 (pp. 149–152), Anaheim, CA, USA. IEEE.

[37] Mancuso Y, Gremillet P, Lacomme P. T/R-modules technological and technical trends for phased array antennas. In: 2005 European Microwave Conference, 2005 Oct 4-6 (pp. 614–617), Paris, France. IEEE.

[38] Hommel H, Feldle H. Current status of airborne active phased array (AESA) radar systems and future trends. In: 34th European Microwave Conference, 2004 Oct 12-14 (pp. 121–124, Amsterdam, Netherlands. IEEE.

[39] Kiehl RSollner T. High Speed Heterostructure Devices. 1st ed. Boston: Academic Press; 1994.

[40] Chu BH, Kang BS, Wang HT, Chang CY, Tseng Y, Goh A, Sciullo A, Wu WS, Lin JN, Gila BP, Pearton SJ. AlGaN/GaN HEMT and ZnO nanorod-based sensors for chemical and bio-applications. In: SPIE OPTO: Integrated Optoelectronic Devices 2009 Feb 12 (pp. 72162A–72162A). San Jose, CA, USA. International Society for Optics and Photonics.

[41] Kang BS. Fabrication and Characterization of Compound Semiconductor Sensors for Pressure, Gas, Chemical, And Biomaterial Sensing (Doctoral dissertation, University of Florida).

Quantum Confinement in High Electron Mobility Transistors

Shovon Pal, Sascha R. Valentin, Arne Ludwig and
Andreas D. Wieck

Additional information is available at the end of the chapter

http://dx.doi.org/10.5772/intechopen.68374

Abstract

Modulation-doped semiconductor nanostructures exhibit extraordinary electrical and optical properties that are quantum mechanical in nature. The heart of such structures lies in the heterojunction of two epitaxially grown semiconductors with different band gaps. Quantum confinement in this heterojunction is a phenomenon that leads to the quantization of the conduction and the valence band into discrete subbands. The spacing between these quantized bands is a very important parameter that has been perfected over the years into device applications. Most of these devices form low-dimensional charge carriers that potentially allow optical transitions between the subbands in such nanostructures. The transition energy differences between the quantized bands/levels typically lie in the infrared or the terahertz region of the electromagnetic spectrum and can be designed according to the application in demand. Thus, a proper understanding and a suitable external control of such intersubband transitions (ISTs) are not only important aspects of fundamental research but also a necessity for optoelectronic device applications specifically towards closing the terahertz gap.

Keywords: heterojunction, HEMT, terahertz, infrared, intersubband transition

1. Introduction

Low-dimensional semiconductor heterostructures, otherwise known as semiconductor nanostructures, have tremendously revolutionized both the technical and the fundamental aspects of semiconductor industry in terms of device applications. With the ability to grow clean and high-quality samples, device implementations have become a huge success [1–3]. When the dimensions of a region with free carriers (electrons) are reduced as compared to the bulk and approach the deBroglie wavelength, the electronic motion is quantized, thus resulting in carrier confinement that is quantum mechanical in origin. The phenomenon has

INTECH
open science | open minds

© 2017 The Author(s). Licensee InTech. This chapter is distributed under the terms of the Creative Commons Attribution License (http://creativecommons.org/licenses/by/3.0), which permits unrestricted use, distribution, and reproduction in any medium, provided the original work is properly cited.

been widely used for carrier confinement in one, two and three dimensions that consequently gives rise to nanostructures such as quantum wells, quantum wires and quantum dots, respectively. Due to the quantum confinement, the energy bands (i.e. the conduction and valence bands) are quantized into discrete energy levels/bands and are no longer continuous as in the bulk systems. These quantized energy states are known as subbands for 2D or 1D systems and sublevels for 0D systems. The energetic spacings between these quantized subbands and the sublevels are very important parameters that define the device applications both from an optical and from an electrical point of view.

The intersubband spacings in GaAs-based 2D systems are typically in the order of 10–30 meV [4, 5], as seen in the case of two-dimensional electron gas (2DEGs) with a triangular confinement potential formed across a GaAs/Al$_x$Ga$_{1-x}$As heterojunction (x being typically 0.3) of a high electron mobility transistor (HEMT) structure. The intersubband transitions (ISTs) typically cover the terahertz (THz) or far-infrared region of the electromagnetic spectrum. However, in the case of a square potential well or in a different material system such as GaN/AlGaN heterojunction, these spacings can be designed to be even in the mid-infrared or near-infrared region. Stacking of quantum wells can further enhance the response of intersubband resonance (ISR), and such designs are the key for various applications like photodetectors or intersubband lasers [6]. One of the very common and sophisticated examples in this regard is the quantum cascade laser [7–9], which is based on the cascade phenomena and intersubband transitions across many layers of quantum wells. Such compact and powerful lasers are used for practical applications in THz spectroscopy [10–13], sensing technology [14, 15], biomedical applications [16, 17] and also in security applications [11, 18]. Structures based on quantum wells have also made significant advancement in the detector technology, for example, quantum well infrared photodetectors [19, 20]. In this chapter, we present a broad overview of the ISTs in a 2DEG formed at the GaAs-Al$_x$Ga$_{1-x}$As interface of a HEMT structure. We also discuss possible methods to probe the spacing between the subbands and also to tune them significantly by applying an external bias across the sample. Furthermore, we present a fundamental study on the coupling of the ISRs with the 2DEG cyclotron resonance in the presence of tilted magnetic fields. The knowledge of ISTs and the ability of wide electrical tuning of these resonances are then exploited to study the light-matter interaction at THz frequencies in these HEMT structures. The integrated device with 2DEG in a HEMT structure and metamaterials (frequency-selective artificially designed structures) is electrically driven from an uncoupled to a coupled regime of light-matter interaction and then again back to the uncoupled regime. A strong coupling is thus observed when the frequencies of both systems are brought in resonance with each other, manifested as an avoided crossing at that point.

2. High electron mobility transistor design

The low-dimensional charge carriers, trapped in the heterojunction of the HEMT design, form the core of such field-effect transistors. This transistor design also goes by the name of modulation-doped field-effect transistors (MODFET). These designs are used in various high-power [21] and high-speed [22] electronics, high-resolution imaging [23] and various gas, chemical and biomedical applications [24]. We begin with the design concept of this semiconductor heterostructure along with an overview of its band structure (see **Figure 1(a)**) that is obtained by solving the *Schrödinger-Poisson's* equations self-consistently [25, 26] and adding the band discontinuity at the heterojunctions. A schematic of the layer sequence of the transistor structure is shown in **Figure 1(b)**. On a semi-insulating GaAs substrate/wafer, we start the molecular beam epitaxy (MBE) growth by typically a 50-nm-thin GaAs layer. Then, approximately 10 periods of a GaAs/AlAs short period superlattice (SPS) are grown (not shown in the band diagram). The SPS layers help to smoothen the surface of the bare substrate for the later epitaxial growth and trap eventually surface-segregating unintentional impurities, which have always a tendency to stick at the stoichiometric interfaces of GaAs/AlAs. Moreover, this SPS keeps unwanted charge carriers away, forbidding them to tunnel into the 2DEG layer grown on top. Since the substrate is typically undoped (or semi-insulating), the conduction (or valence) band has no curvature at this point corresponding with Poisson's equation, which states that the charge density is proportional to the second derivative of the potential with respect to the space coordinate. After the growth of the SPS layer, the first charged layer is the 2DEG that is formed at the heterojunction of the

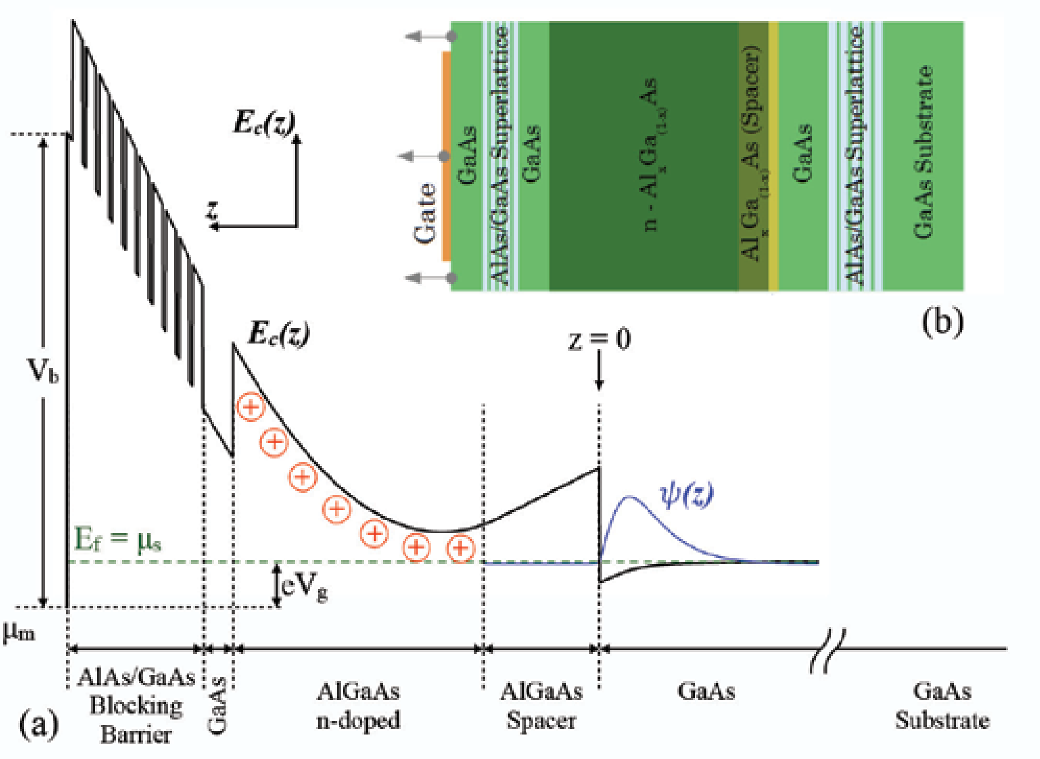

Figure 1. (a) The conduction band diagram of a HEMT structure along the growth direction z. The growth starts from the substrate, that is from right to left in the above figure, after the growth of a 50-nm GaAs layer. μ_m and μ_s are the quasi-Fermi levels in the metal and semiconductor, respectively $(\mu_s - \mu_m = eV_g)$. V_b is the built-in voltage. The *Fang-Howard* wavefunction of the ground state is also plotted across the heterojunction (which is assumed to be zero in the growth axis). (b) A schematic of the layer sequence.

undoped GaAs and an undoped $Al_{0.33}Ga_{0.67}As$ spacer layer. Since the 2DEG is essentially electrons and negatively charged, the conduction band curves downwards and reaches the maximum slope at the heterojunction between the GaAs and the $Al_{0.33}Ga_{0.67}As$ layer, at which point the conduction band ($E_c(z)$) jumps by ΔE_c due to the band discontinuity. This is followed by the $Al_{0.33}Ga_{0.67}As$ spacer layer where charge carriers are absent and the slope of the conduction band almost remains constant. In the doped $Al_{0.33}Ga_{0.67}As$ layer, the positive charges of the donor ions cause the band to bend upwards, thus reversing the slope. Further moving to the GaAs layer, $E_c(z)$ jumps downwards due to the band discontinuity and continues with a constant slope. On top of the GaAs layer, AlAs/GaAs SPS (also known as blocking barrier) is grown to prevent leakage of charge carriers in and out of the 2DEG channel and also to prevent leakage of surface charges into the channel. Finally, the band hits the gate grown on top of the sample with a barrier height equivalent to the Schottky barrier height. Ideally, metals (e.g. Cr or Au) are evaporated on the sample to serve as gates after the completion of the growth. The samples are typically grown by MBE. While a lot of work has been done previously using metallic Schottky gates, nonetheless, these gates suffer from huge drawbacks. These gates limit the forward bias voltage to the turn-on voltage of the Schottky diode. Furthermore, they fail to grow lattice matched on the semiconductor, are poly-crystalline and thus induce potentially a lot of strain on the semiconductor layer below. Moreover, they oxidize over time and thus may become highly ohmic. Due to high reflectivity and certain Drude absorption of their free charge carriers, such gates are also opaque to the incident light, thus limiting their application in optoelectronic devices. Recently, we have introduced epitaxial, complementary-doped, electrostatic and transparent gates that are grown on top of the sample [27–29]. These gates are grown within the UHV conditions of the MBE and thus incorporate a minimum of the unwanted impurities, leading to unpreceded gate perfection, reliability and reproducibility.

These gates circumvent all the abovementioned disadvantages of Schottky gates and are typically composed of a 25-nm-thick bulk carbon-doped GaAs layer (with an acceptor density of $N_A = 3 \times 10^{18}$ cm^{-3}) followed by approximately 40 periods of carbon-delta-doped and 0.5-nm carbon-doped GaAs layers with an average acceptor density $N_A = 1 \times 10^{19}$ cm^{-3}. In order to solve Poisson's equation for the evaluation of the band structure, the knowledge of the charge density is necessary. However, it is not possible to calculate the density of charge carriers until the energy bands are known, thus requiring a self-consistent mechanism that is otherwise adopted in the 1D Poisson solver [26].

3. Characteristics of HEMTs

After being introduced in 1980s, these transistors based on high-mobility modulation-doped heterostructures have revolutionized the semiconductor industry in terms of being the most high-performance compound semiconductor FETs.

Due to spatial separation of the electrons from the ionized impurities, the scattering between them is highly reduced as compared to the bulk semiconductors, enhancing the electron mobility especially at low temperatures where the abovementioned scattering mechanism is dominant. The spacer layer further increases the electron-to-donor separation. While the larger separation reduces the scattering mechanism, as a negative contribution, the carrier concentration is also reduced which reduces the performance. Hence, the spacer thickness should be optimized. Typical values range from 1 to 30 nm. In order to explain how the high mobility of the electrons in HEMT makes them fast transistors, we use the *Shockley's gradual channel approximation model* for an FET operation, which states that the rate of change of saturation drain current, $I_{D,sat}$, with respect to the change in the gate-source voltage, V_{GS} (also known as the transconductance, $g_{m,sat}$), scales proportionally to the mobility (μ) and inverse proportionally to the distance between the gate electrode and the electron channel (d), both of which are satisfied by the HEMTs:

$$g_{m,sat} = \frac{\partial I_{D,sat}}{\partial V_{GS}} = \frac{\epsilon \mu Z}{d L_G}(V_{GS} - V_{th}), \tag{1}$$

where Z is the total impedance, L_G is the dimension of the gate and V_{th} is the threshold voltage. The HEMTs have a clear advantage of lower access resistance particularly in terms of channel resistance due to the high mobility electrons in the channel in comparison to standard FETs. To summarize, the HEMT design principles allow:

- High carrier concentration of 2DEG in the channel
- High mobility by optimization of the spacer-layer thickness
- Low access resistance by using buried/recessed gates
- Better confinement of carriers in the channel due to high barriers
- Reduced interface and alloy scattering mechanisms, thus enhancing mobility

Typical transistor characteristic curves of GaAs/AlGaAs HEMT structures under dark and after 1 s of illumination with a near-infrared light emitting diode (NIR LED) are shown in **Figure 2 (a)** and **(b)**, respectively. Let us now briefly discuss the transistor operation. Even under zero bias or for a small positive voltage applied to the gate, an inversion layer is formed at the semiconductor surface, the *two-dimensional electron gas*. Now, if a small source-drain voltage is applied, a current will flow from the source to the drain through the conducting 2DEG channel. The channel here is highly conducting, that is, offers very small resistance, and the source-drain current (I_{SD}) is proportional to the source-drain voltage (V_{SD}). This is the linear region. As V_{SD} increases, I_{SD} deviates from the linear relationship since the channel potential reduces the charge near the drain end. This eventually reaches a point at which the inversion charge at the drain end is reduced to nearly zero. This is called the pinch-off point. Beyond this source-drain bias, the drain current remains essentially the same, the pinch-off point starts to move towards the source, but the voltage at this pinch-off point remains the same. Thus, the number of carriers arriving at the pinch-off point from the source and hence the current remains essentially the same. In terms of the conduction band diagram, when a large enough negative bias is applied to the gate, the conduction band is lifted up across the chemical potential (or *quasi-Fermi level*), thus depleting the channel completely. This results in a zero source-drain current even when the source-drain voltage is increased. As a positive bias is applied, the channel is filled with mobile electrons, and with the increase of the source-drain

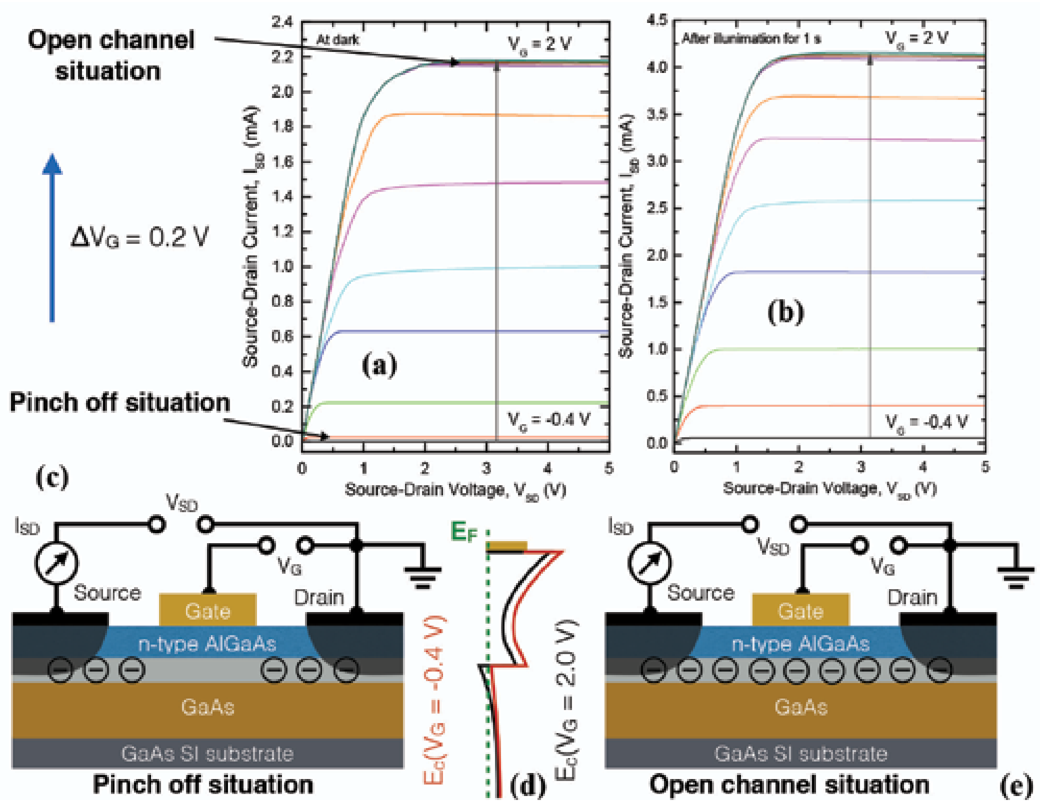

Figure 2. Transistor I_{SD}-V_{SD} curves measured at 4.2 K for a range of gate voltage applied from −0.4 to 2 V in steps of 0.2 V (a) at dark and (b) after illuminating the sample with a near-infrared light emitting diode for 1 s. (c) The schematic of the pinch-off situation. (d) A simplified schematic of the conduction band diagram under two different gate bias: −0.4 V (in red for the complete depletion of the channel) and 2 V (in black when the channel is filled with charge carriers). (e) The schematic of the open channel situation. SI indicates semi-insulating. The complete layer sequence is not shown in the schematic for simplicity.

voltage, the source-drain current first increases linearly, then non-linearly and finally reaches a saturation value, as described earlier. A schematic of these situations is depicted in **Figure 2(c)** and **(e)**, while the simplified schematic of the conduction band diagram is shown in **Figure 2(d)**. When the structure is illuminated, it becomes rather difficult to deplete the channel completely out of electrons with the previously applied negative bias, and, moreover, the saturation current also increases with the same gate bias applied before.

3.1. Quantum confinement and intersubband transitions in HEMTs

One of the most popular terms in nanoscience is the *quantum confinement* that results from changes in the atomic structure as a consequence of direct influence of ultra-small length scale on the energy band structure [30]. The length scale corresponding to the regime of quantum confinement ranges from 1 to 25 nm for typical IV, III–V or II–VI semiconductors [31]. This leads to the fact that the spatial extent of the electronic wavefunction is comparable to the particle size, making the electrons *feel* the presence of the particle boundaries and respond to changes in particle size by adjusting their energy. This phenomenon is known as the quantum-size effect. Quantization effects become most important when the particle dimension of a semiconductor is near to and below the bulk semiconductor Bohr exciton radius (in bipolar systems) or the deBroglie wavelength (in unipolar systems), making the properties of the material size-dependent.

In low-dimensional semiconductor nanostructures, the restriction of the electronic motion in one, two and three dimensions leads to the modification of the density of states (DOS) as compared to the bulk states. The electronic DOS is defined as the number of electronic states per unit volume per unit energy, the finiteness of which is a result of the *Pauli's exclusion principle*, which states that only two electrons with opposite spins can occupy one volume element in the phase space [32]. The confinement of electronic motion results in the quantization of the conduction and the valence band. With the knowledge of these quantized states, their filling can be explained. The number of occupied subbands depends on the electron density and also on the temperature [33]. In a 2D system, the density of electrons per unit area, $n_{2\mathrm{D}}$, is given by the integration of the product of 2D DOS, $n(E)$ and the Fermi-Dirac occupation function [34]:

$$n_{2\mathrm{D}} = \int_{-\infty}^{\infty} n(E) f(E, E_F) dE, \tag{2}$$

where E_F is the quasi-Fermi energy. The subbands can thus be split as:

$$n_{2\mathrm{D}} = \sum_i n_i, \tag{3}$$

where n_i is the number of electrons in the subband with energy ε_i. The above classical Boltzmann distribution, f, is given by [33]:

$$f(E, E_F, T) \sim \exp\left(-\frac{E - E_F}{k_B T}\right), \tag{4}$$

where k_B is the Boltzmann constant and T is the temperature in Kelvin. Using the above equation, we obtain:

$$n_i = \frac{m}{\pi\hbar^2} \int_{\varepsilon_i}^{\infty} f(E, E_F) dE = \frac{m k_B T}{\pi\hbar^2} \ln\left[1 + \exp\left(\frac{E_F - \varepsilon_i}{k_B T}\right)\right]. \tag{5}$$

In the limit of low temperature, where electrons are degenerate, the 2D electron density is given by [33]:

$$n_{2D} = \sum_i n_i = \frac{m}{\pi\hbar^2} \sum_i (E_F - \varepsilon_i) \Theta(E_F - \varepsilon_i). \tag{6}$$

Figure 3(a) and **(b)** show a triangular potential well and a schematic of the filling of the subbands, respectively. Based on the position of the Fermi level, the corresponding subbands are occupied. Under triangular confinement potential (as in the HEMT design), the energy spacing decreases for higher subband energies and finally forms the continuum. When the Fermi energy E_{F1} is higher than ε_1 but less than ε_2, only the ground subband is filled. Similarly, when the Fermi level E_{F2} is above ε_2, but less than ε_3, the lower two subbands are filled with electrons and so on. The position of the quasi-Fermi level can be tuned by changing the band structure externally, that is, by applying either an electric or a magnetic field. With the external field, the conduction band can be raised or lowered with respect to the quasi-Fermi level around the Fermi-pinning point, hence depleting or filling the subbands with electrons. **Figure 3(c)** shows a schematic of the intersubband transition from the filled ground subband to an empty excited subband. In quantum mechanics, Fermi's golden rule is used to calculate the transition rate (i.e. the probability of a transition to occur per unit time), from one state with a given eigenenergy to another state of higher eigenenergy or to the continuum of energy eigenstates, subjected to some kind of perturbation. According to Fermi's golden rule, this rate of transition, $W_{i\rightarrow f}(\omega)$ from an initial state $|i\rangle$ to a final state $|f\rangle$ under the *electric-dipole approximation*[1] ($\vec{e}\ .\hat{p}$), is given by:

$$W_{i\rightarrow}(\omega) = \frac{2\pi}{\hbar}\left(\frac{eE_0}{m^*\omega}\right)^2 |\langle f|\ \vec{e}\ .\hat{p}|i\rangle|^2 \delta(E_f - E_i - \hbar\omega), \tag{7}$$

where E_0 is the amplitude of the electric field and e and m^* are the charge and the effective mass of electrons. E_i and E_f are the energies of the initial and the final state. Now, the absorption coefficient, α_{2D}, is defined as the ratio of the absorbed electromagnetic energy per unit time and area (considering a 2D system) and the intensity of the incident radiation, summed over all the filled initial and empty final states. In order to ensure that the initial state is filled and the final state is empty, a condition necessary for the transition to occur, we introduce the Fermi factors: $\zeta(E_i)$ for the initial state and $\left[1 - \zeta(E_f)\right]$ for the final state. The absorption coefficient is thus given by:

$$\alpha_{2D} = \frac{2e^2\pi}{\int_0 cn\omega m^{*2}} \cdot \sum_{i,f} |\langle f|\ \vec{e}.\hat{p}|i\rangle|^2 \left[\zeta(E_i) - \zeta(E_f)\right]\delta(E_f - E_i - \hbar\omega), \tag{8}$$

where ϵ_0 is the absolute permittivity, c is the velocity of light and n is the refractive index of the material. The intersubband absorption takes place within the quantized levels of the conduction or the valence band, schematically shown in **Figure 3(c)**. The total wavefunction can be written as the product of the lattice-periodic Bloch wave (for electrons in a crystal), $'u'$ [35], and

---

[1] In optical experiments with wavelengths λ in the order of micrometers, the width of the quantum well, which practically sets the scale of the electronic wavefunctions, is much shorter than λ. To a good approximation, the momentum of the photon can be neglected and the electric field can be assumed as constant across the electronic states (with or at $\vec{k} = 0$). This approximation is also known as the *electric-dipole approximation*.

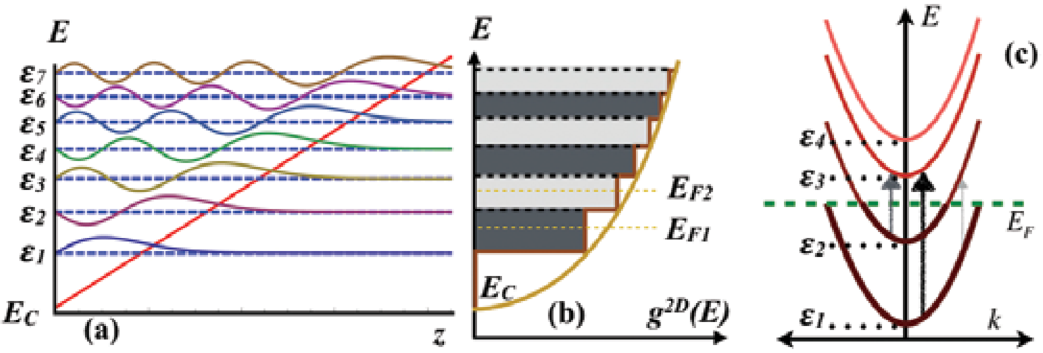

Figure 3. (a) A triangular potential well showing the subband energies and the associated *Fang-Howard Airy* wavefunctions. (b) A schematic depiction of the 2D density of states that appears step-like for each quantized state. (c) A schematic representation of the subbands in the energy-momentum space for a triangular quantum well. The thick parts of the parabola indicate filled states and the arrows indicate the allowed dipole transitions.

a slowly varying envelope function $'\vartheta'$. According to the *Bloch ansatz*, the envelope function reduces to the plane wavefunction; hence, the total wavefunction is given by:

$$\psi(\vec{r}) = \frac{1}{\sqrt{A}} e^{i\vec{k}_\perp \cdot \vec{r}} \cdot \varphi_s(z) \cdot u_v(\vec{r}), \tag{9}$$

where A is the normalization constant, v indicates the index for the bands and s represents the subband indices. The complete matrix element in $\langle f| \vec{e} \cdot \hat{p}|i\rangle$ can be split as follows:

$$\langle f| \vec{e} \cdot \hat{p}|i\rangle = \vec{e} \cdot \langle u_{v^f}|\hat{p}|u_{v^i}\rangle\langle \vartheta_{s^f}|\vartheta_{s^i}\rangle + \vec{e} \cdot \langle u_{v^f}|u_{v^i}\rangle\langle \vartheta_{s^f}|\hat{p}|\vartheta_{s^i}\rangle, \tag{10}$$

where the first term indicates the interband transition and the second term is the intersubband transition. The first term has the dipole matrix element of the Bloch functions that explains the selection rule for the interband transition and an overlap integral of the envelope functions. In case of transitions within the subbands of the conduction or the valence band, the first term vanishes and the second term becomes more relevant in the *one-band model* that consists of an overlap integral of the Bloch function and a dipole matrix element of the envelope function. Further simplification of the matrix elements of the envelope function gives:

$$\langle \vartheta_{s^f \vec{k}_\perp^f} | \vec{e} \cdot \hat{p} | \vartheta_{s^i \vec{k}_\perp^i} \rangle = \frac{1}{A} \int d^3r \left[e^{-i\vec{k}_\perp^f \cdot \vec{r}} \varphi^*_{s^f}(z) \{e_x p_x + e_y p_y + e_z p_z\} e^{-i\vec{k}_\perp^i \cdot \vec{r}} \varphi_{s^i}(z) \right]. \tag{11}$$

It can be observed that only the third term, $e_z p_z$, in the curly bracket survives, giving a contribution at a finite frequency. Except for $s^i = s^f$ and $\vec{k}_\perp^i = \vec{k}_\perp^f$ (i.e. the initial and the final states are equal), all the other terms vanish, implying the free-carrier absorption at zero frequency when no scattering processes are involved [36]. Hence, only the following matrix element determines the intersubband absorption in the one-band model:

$$\langle s^f|p_z|s^i\rangle = \int dz\varphi^*_{s^f}(z)p_z\varphi_{s^i}(z). \tag{12}$$

The above equation states that the electric field of the incident radiation must have a component perpendicular to the semiconductor layers or parallel to the growth direction (which is a necessary condition) in order to couple to the ISTs. This is known as the *polarization selection rule* for the ISTs. In simple words, it states that the electric field vector of the exciting electromagnetic wave or at least a finite component of it must be perpendicular to the 2DEG. Another important quantity in this regard is the oscillator strength [34] defined as:

$$f_{s^is^f} = \frac{2}{m^*\hbar\omega_{s^fs^i}}|\langle s^f|p_z|s^i\rangle|^2 = \frac{2m^*\omega_{s^fs^i}}{\hbar}|\langle s^f|z|s^i\rangle|^2. \tag{13}$$

The above quantity is used to understand and compare the strength of the transitions between initial and final states in different physical systems and obeys the *Thomas-Reiche-Kuhn sum rule* [37]. It is important to note that for a symmetric quantum well, only parity changing transitions (odd-even or even-odd) are allowed due to the inversion symmetry of the potential well. However, for asymmetric quantum wells, like that of the triangular potential well, the inversion symmetry with respect to the quantum well centre is broken by some means (i.e. internal electric fields or band structure engineering, etc.). This leads to the relaxation of the selection rule, thus allowing transitions between all the subbands.

4. Intersubband-Landau coupling under tilted magnetic fields

When a magnetic field is applied in a plane perpendicular to the semiconductor surface, the free electrons that carry the electric charge perform an orbital motion in the plane perpendicular to the magnetic field direction. This motion is quantized, and equally spaced levels (called the Landau levels) separated in energy are formed. The Hamiltonian of the quantum mechanical system thus gets decoupled into a magnetic and an electric component, and the energy spectrum consists of a series of Landau ladders for each subband. In the presence of a magnetic field, the Drude conductivity, normalized to $\epsilon_0 c$, is given by [38–42]:

$$\sigma(\omega) = \frac{n_{2\mathrm{D}}e^2\tau}{2m^*\epsilon_0 c}\left[\frac{1}{1+i(\omega+\omega_c)\tau} + \frac{1}{1+i(\omega-\omega_c)\tau}\right], \tag{14}$$

where $n_{2\mathrm{D}}$ is the electron density, τ is the relaxation time constant and c is the velocity of light in free space. Using Maxwell's theory, the transmittance, t, can be written as:

$$t = \frac{2}{1+\sqrt{\epsilon}+\sigma} \tag{15}$$

The transmission, T, is thus given by [41, 42]:

$$T = |t|^2 = \frac{4}{\left(1+\sqrt{\epsilon}+\sigma_r\right)^2+\sigma_i^2}, \tag{16}$$

where σ_r is the real part of the conductivity and σ_i is the imaginary part. Using the above equation, the normalized transmission can be written as [41, 42]:

$$\frac{T(B)}{T(0)} = 1-\frac{\left(1+\omega_p\tau\right)^2-1}{2}\left[\frac{1}{\left(1+\omega_p\tau\right)^2+(\omega+\omega_c)^2\tau^2}+\frac{1}{\left(1+\omega_p\tau\right)^2+(\omega-\omega_c)^2\tau^2}\right], \tag{17}$$

where $\omega_p = \frac{n_{2\mathrm{D}}e^2}{m^* c\epsilon_0(1+\sqrt{\epsilon})}$ is the plasma frequency. From the quantum mechanical description of such a system, when electrons in 2DEG are subjected to a space-charge potential, $V(z)$ and a magnetic field B tilted at an angle of θ with respect to the horizontal direction, the total Hamiltonian of the system is given by [4, 43]:

$$H = -\frac{\hbar^2}{2m^*}\frac{\partial^2}{\partial x^2}+\frac{e^2B_\perp^2}{2m^*}x^2-\frac{\hbar^2}{2m^*}\frac{\partial^2}{\partial z^2}+V(z)+\frac{e^2B_{||}^2}{2m^*}z^2-\frac{e^2B_{||}B_\perp}{2m^*}xz. \tag{18}$$

where $B_{||} = B\sin\theta$ and $B_\perp = B\cos\theta$. The first two terms in the above equation describe the magnetic field quantization into Landau levels (similar to the harmonic potential). The third and the fourth terms illustrate the quantization due to the space-charge potential within the triangular well approximation. The z^2 term results in the positive diamagnetic shift due to the parallel magnetic field component, $B_{||}$. The last term, proportional to the product xz, couples the Landau and subband quantization at all angles $0^\circ < \theta < 90^\circ$.

Using the perturbation theory, one can solve the above Hamiltonian treating θ as the perturbation parameter. In order to solve the above problem, the product of Airy wavefunctions ($|i\rangle$) and Hermite functions ($|n\rangle$) is taken as the basis set. From the first order perturbation theory, there is no correction to the zeroth-order energies, expect for the degenerate situation $E_{i'i} = E_{i'} - E_i = \hbar\omega_{c\perp}$. This is commonly addressed as the full-field coupling regime. In the non-resonant regime, second-order effects are present, and hence using perturbation theory of the second order for non-degenerate levels, the total energy eigenvalues are obtained as [4]:

$$E_{i,n} = E_i+\hbar\omega_{c\perp}\left(n+\frac{1}{2}\right)+\frac{e^2B_{||}\left((z^2)_{ii}-(z_{ii})^2\right)}{2m^*}-\frac{e^2B_{||}^2}{2m*}\sum_{i\neq i'}\frac{(z_{i'i})^2\left(1-\frac{E_{i'i}(2n+1)}{\hbar\omega_{c\perp}}\right)}{1+\left(\frac{E_{i'i}}{\hbar\omega_{c\perp}}\right)^2}, \tag{19}$$

where $z_{i'i}$ are the matrix elements for the ISTs from ith subband to i'th subband. The first two terms represent the linear zeroth-order terms, corresponding to the subband energies and the Landau energies respectively. The third term represents the diamagnetic shift, and the fourth term results from the coupling Hamiltonian. This non-resonant regime is known as the half-field coupling, where the splitting is proportional to θ^2. Thus, larger tilt angles are required for the observation of the splitting in the half-field coupling regime. Transmission measurements are performed on a HEMT sample using the magnetic field chopping scheme. A fixed number of spectra are taken at a certain magnetic field (*T*(*B*)), and then the magnetic field is turned off, during which the same number of transmission scans (*T*(0)) are taken. At first, the transmission experiments are performed under no tilt of the magnetic field. A contour plot of the normalized transmission spectra for different fields in the range 3.6–4.2 T is plotted in **Figure 4(a)**. Clearly, the only visible resonance observed is the cyclotron resonance under perpendicular magnetic fields that scales linearly with the field. On introduction of the tilt (approximately 30°), a clear anti-crossing is observed at around 3.9 T (see **Figure 4(b)**). The apparent observation of the satellite peaks (shown by black arrows in **Figure 4(c)**) in the presence of the

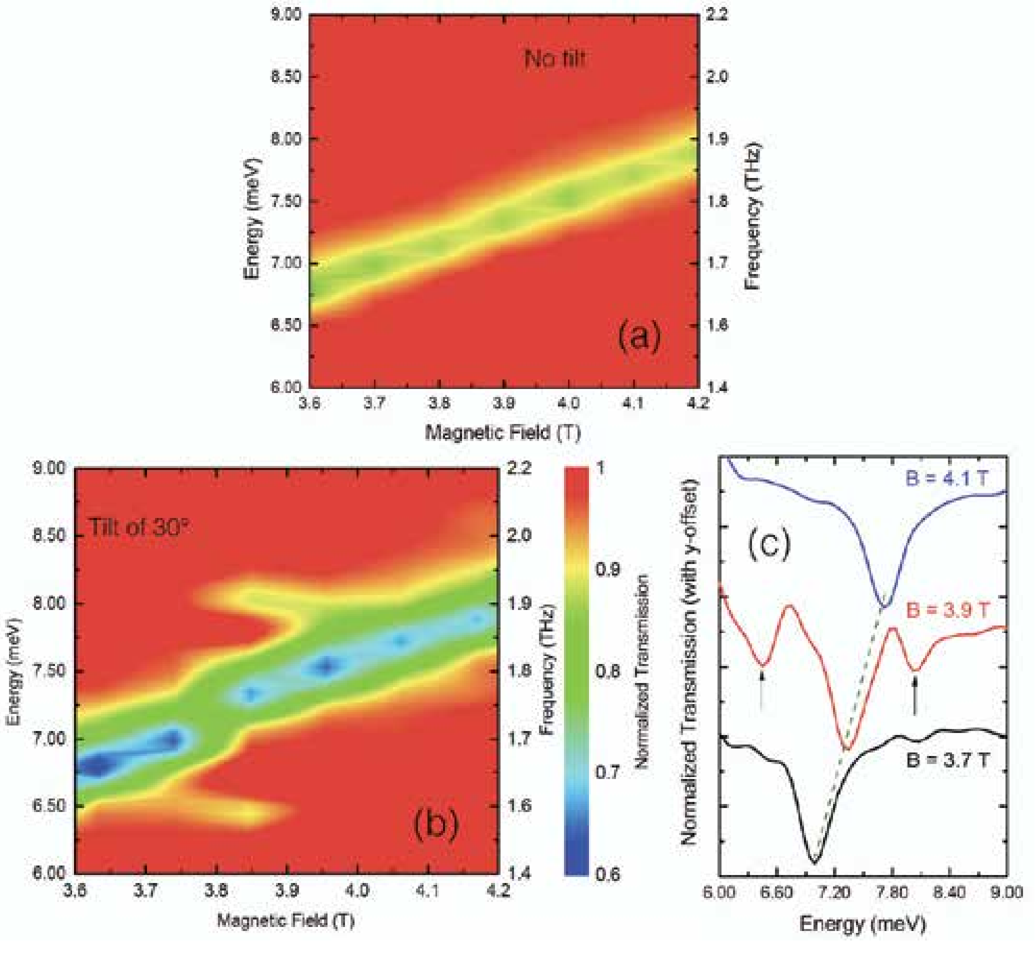

Figure 4. (a) A contour plot of the normalized transmission spectra under perpendicular magnetic fields without any tilt. (b) A contour plot showing the anti-crossing between the cyclotron resonance and the intersubband resonance in the normalized transmission spectra under tilted magnetic fields. This feature appears as the satellite peaks across the cyclotron resonance. (c) Normalized transmission plots for three magnetic fields where satellite peaks (highlighted by black arrows) are seen at 3.9 T.

magnetic field at the anti-crossing point is a manifestation of the subband-Landau coupling and hence the resonance splitting (the splitting between the two satellite peaks across the dominant cyclotron resonance). The spacings of the subbands are twice the value of the splitting at the anti-crossing frequency (according to the half-field coupling regime). This corresponds to $E_{01} = 2hcv_{c\perp} = 11.1$ meV where $v_{c\perp}$ is the wavenumber corresponding to the cyclotron frequency at the anti-crossing point. All magnetic chopping measurements are performed under zero bias. This phenomenon of avoided crossing is an indirect experimental method to evaluate the intersubband spacing via the so-called magnetic field chopping scheme [44, 45]. A more direct method is by application of the electric fields across the structure and this is discussed in the next section.

5. Tuning and probing of intersubband transitions electrically

Intersubband transitions are the most fundamental optical transitions that can be excited in low-dimensional semiconductor nanostructures. The observation of ISRs is a result of the fact that the component of the incident infrared electric field perpendicular to the semiconductor layers or parallel to the growth direction selectively couples, thus exciting the electrons from the lower occupied subband to the higher empty subband. By applying a voltage across the structure, it is possible to deplete and selectively populate the subbands. Thus, a more direct scheme of transmission measurement is proposed to study the intersubband spacing in such semiconductor nanostructures (viz. HEMT) even in the absence of an external magnetic field.

The change in the transmission, $T(V_{g,n})/T(V_{r,0})$, due to the 2D space-charge layer for a normally incident light polarized in the perpendicular direction (say z) is given by [38]:

$$\frac{T(V_{g,n})}{T(V_{r,0})} = 1 - \frac{2\mathrm{Re}(\sigma_{zz})}{\sqrt{\epsilon_0/\mu_0}\left(1 + \sqrt{\epsilon_{SE}/\epsilon_0}\right) + \sigma_g}, \tag{20}$$

where ϵ_{SE} is the dynamic dielectric function of the substrate, σ_g is the conductivity of the gate and σ_{zz} is the conductivity tensor element of the 2D layer. ϵ_0 and μ_0 are the absolute permittivity and permeability of the free space, respectively. The Drude model very well describes the dynamic conductivity response of the quasi-free charge carriers in the 2D space-charge layer [41, 42]:

$$\sigma_{Drude}(\omega) = \frac{e^2 n_{2\mathrm{D}} \tau}{m^*} \frac{1}{1 + i\omega\tau}, \tag{21}$$

where τ is the scattering time, $n_{2\mathrm{D}}$ is the carrier density and m^* is the effective mass. However, for the ISTs, observed under normally incident light, with the sample tilted at an angle, the conductivity can be described by replacing σ_{zz} by σ_{ISR} [41, 42]:

$$\sigma_{ISR} \propto \frac{|\langle z_{ii'} \rangle_z|^2}{\omega^2 - \omega_{ISR}^2 + i\omega/\tau}, \tag{22}$$

where $|\langle z_{ii'} \rangle_z|^2$ is the matrix element for the IST from the *i*th state to the *i'*th state. The ISR frequency can however differ from the observed one due to resonance screening (depolarization shift) arising from the many body effects [46]. In the density-chopping scheme, a certain number of scans are taken at the reference voltage (a voltage much below the threshold voltage), when the 2DEG is completely depleted of charge carriers. Then, the gate voltage is slowly increased to a value when the subbands start populating (this can be well seen from the capacitance-voltage spectrum in **Figure 5(a)** where the change in capacitance is measured during the broadband absorption onset upon changing the gate voltage and modulating it with the LockIn technique). The same number of scans is taken at this higher gate voltage. The voltages are then changed alternatively, and the respective scans are co-added and averaged over long measurement times. The long measurement time ensures that any drift arising from the complicated experimental setup can be averaged out to zero and a good signal-to-noise ratio is obtained. **Figure 5(b)** shows the density-chopped transmission spectra of a HEMT

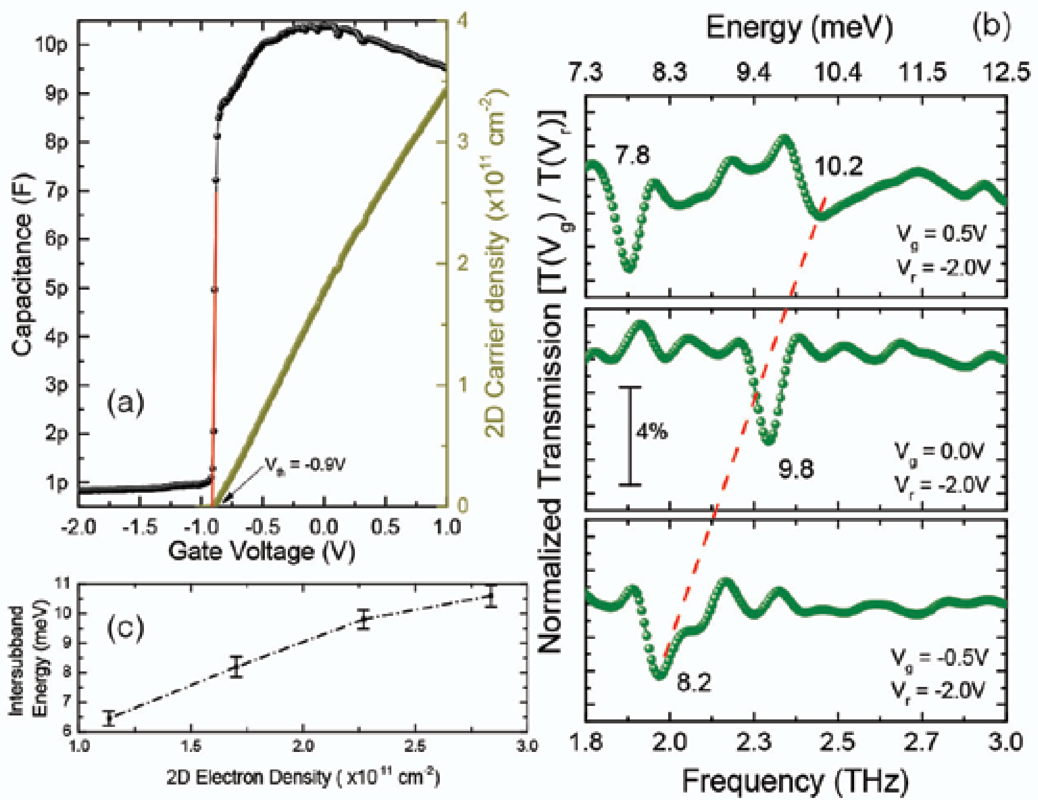

Figure 5. (a). Capacitance-voltage spectrum of the HEMT structure showing a sharp increase of the capacitance as the voltage is increased above −0.9 V (threshold voltage). This indicates the filling of the ground subband with charge carriers. The corresponding 2D carrier density is also plotted as a function of the gate voltage that agrees well with the Hall measurements performed on the same sample (not shown). (b) The normalized transmission spectra at different gate voltages chopped (or normalized) with respect to the reference voltage (−2 V). A clear shift of the intersubband resonance is observed towards higher values as the gate voltage is increased. (c) The wide electrical tunability of the intersubband resonance as a function of the 2D carrier density (or the applied electrical bias).

sample. With the increase of the gate voltage, the conduction band is pulled below the quasi-Fermi level. This results in the steepening of the triangular potential well, resulting in an increase of the intersubband spacing. Thus, by applying a bias on the gate, the intersubband resonance can be significantly tuned over a wide frequency (1–3 THz) or energy (4–12 meV) range, as can be seen in **Figure 5(c)**.

6. An access to the interior of HEMT via artificial structures

Artificial structures such as metamaterials are engineered in the sub-wavelength sizes for certain desired properties. They are designed in assemblies of multiple individual elements called unit cells. These structures possess unique properties such as negative [47] or zero [48] refractive indices, magnetism at optical frequencies [49], etc. The special properties are not inherent to the materials but the design of the structures and the way electromagnetic field interacts with them. They can also be treated as planar cavities with certain resonance frequencies. When electromagnetic radiation with a certain polarization is incident on these structures, the electric or the magnetic field couples to the cavity and exhibits a resonance that is known as the cavity resonance or resonance frequency of the metamaterials. In transmission measurements, this appears as a dip at that particular resonance frequency. An array of interconnected double split-ring resonators (see **Figure 6(a–d)**) is adopted for the metamaterial design, whose dimensions and the characteristic frequency response are first simulated by the standard finite difference time domain solver (like CST microwave studio). For simplicity and small computation time, only one unit cell, as shown in **Figure 6(e)**, is used for the simulation with a periodic boundary condition in the planar directions. Moreover, these meta-atoms are placed far apart from each other to avoid any influence of inter-meta-atom interactions. For the right coupling of the electromagnetic radiation, the electric fields are confined in the two narrow capacitor arms of the double split-ring resonator (see **Figure 6(e)**). Moreover, the fringing field effect ensures that there is a strong electric field component along the growth direction that extends over a few 100 nm [29]. This component of the electric field couples with the HEMT to excite the ISRs in accordance with the polarization selection rule as discussed before.

Two transmission minima (or dips) are observed—one at 1.2 THz and the other at 2.4 THz (see **Figure 6(f)**). The experimental characterization of the metamaterial array is performed by a standard THz time-domain spectroscopy at room temperature, where the thermal energy, $k_B T$ (= 25 meV), is higher than the subband spacings. This thermal occupation of higher subbands consequently prevents us from observing the ISR (ground-to-first excited state) in the 2DEG layer. Hence, the response from the sample is purely due to metamaterials. A Ti:Sa laser with an 80 fs pulse duration (a centre wavelength of 800 nm) and a repetition rate of 80 MHz is used to generate the THz radiation by exciting an inter-digitated photoconductive antenna [9] processed on a GaAs substrate. A fixed DC bias is applied on the antenna. The THz generation is obtained under the transmission geometry of the antenna. Four 90° off-axis parabolic mirrors are used for the collection and collimation of the THz beam. The detection is based on free space electro-optic sampling [8, 29] of the THz electric field by using a birefringent, 2-mm-thick ZnTe crystal. As compared to the simulation, the transmission is normalized with respect

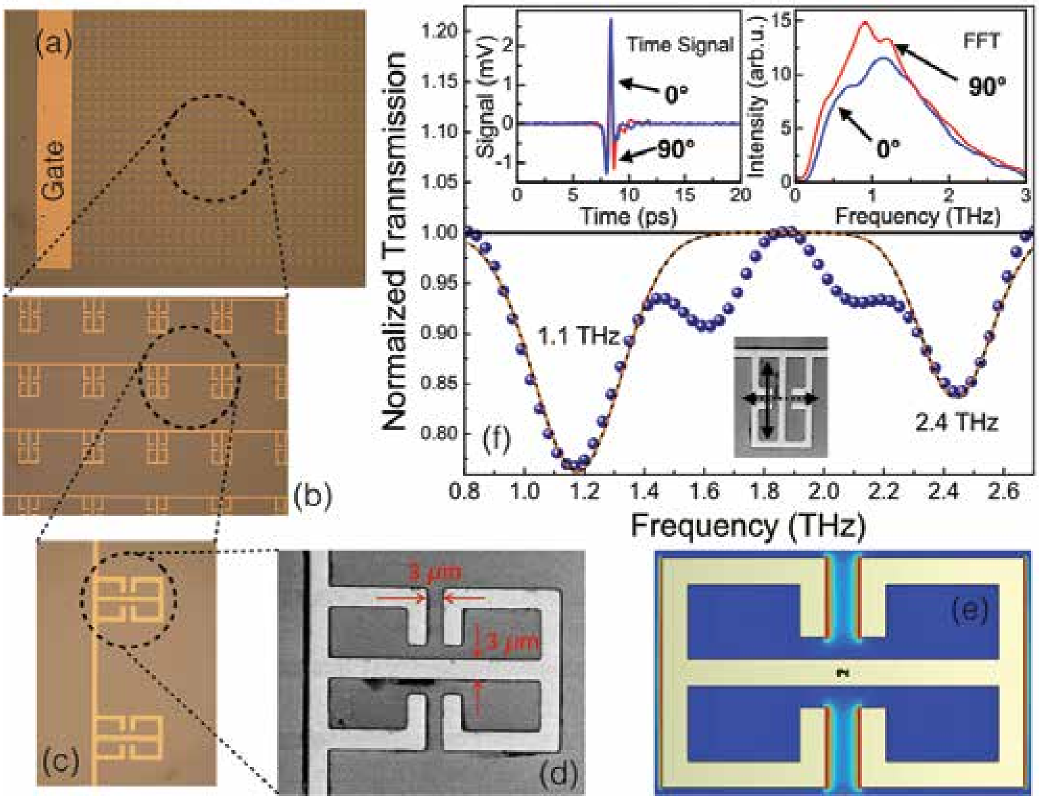

Figure 6. (a–c). Gradual zoomed-in optical images of the metamaterial design, showing the gate and the interconnected double split-ring resonator arrays. (d) An SEM micrograph of the metamaterial unit cell. The length and the gap size are both 3 μm, the total structure being 26 by 40 μm. (e) In-plane electric field distribution of the surface of the structure showing a strong confinement of the field in the capacitive arm of the structure. (f) Normalized transmission spectrum of the metamaterial taken at room temperature, showing two strong resonances. The dots are experimental data while the black curves are the deconvoluted resonance dips and the dashed line is the complete spectrum obtained from the deconvoluted peaks. Inset: Time domain signals (left) and the corresponding Fourier transform signals (right). The black-dashed arrow indicates the orientation of the structure when the electromagnetic fields do not couple while the solid-black arrow when the field couples.

to the orientation of the metamaterial. The electric field component of the THz source is in the plane parallel to the optical table. Hence, when the metamaterials are oriented at 0° (solid-black arrow in **Figure 6(f)**), the incident infrared radiation couples into the structures. When the metamaterials are oriented at 90° (black-dashed arrow in **Figure 6(f)**), the field does not couple. By normalizing the transmitted spectrum of the metamaterial at 0° with respect to the one at 90°, two transmission dips are obtained—one at 1.2 THz and the other at 2.4 THz as shown in **Figure 6(f)**.

Once the sample is cooled down to liquid helium temperatures, at first, the characterization of the voltage range is performed over which the density-chopping measurements are to be taken. The change in capacitance with the gate voltage is measured by capacitance-voltage spectroscopy, mentioned before, as shown in **Figure 7(a)**. A typical charging spectrum of

2DEG has a capacitance close to zero in the beginning and then as the gate voltage is increased, the conduction band is pulled below the quasi-Fermi level and subsequently the 2DEG subbands are filled with electrons. The filling is observed as a steep increase in the capacitance. The region of interest is the steep slope, where increasing the gate voltage increases the 2DEG ISRs. This is due to the fact that with more positive gate voltage, the slope of the triangular potential confinement steepens and hence increases the subband spacings, thus shifting the ISRs to higher energies. This phenomenon is well known as the *quantum-confined Stark effect*. It is also necessary to completely ionize the donor-exchange centres (*DX centres*[2]). As more DX centres are ionized, less forward bias is required to charge the 2DEG subbands with electrons. With longer illumination, all the DX centres are successively ionized, leading to the shift of the charging slope in the capacitance-voltage spectra towards more negative biases. The spectrum shown in **Figure 7(a)** is obtained after 3 h of continuous illumination. The shaded region in the charging spectra, shown in **Figure 7(a)**, indicates the region where the density-chopped infrared transmission measurements are performed. The density-chopping scheme is similar to that explained before, where the change in transmission, $T(V_{g,n})/T(V_{r,0})$, is recorded. According to the charging spectrum, the reference voltage V_r is chosen much below the threshold voltage (-0.2 V), that is at -2 V, and the gate voltage V_g is varied from -0.25 to 0 V in steps of 20 mV. The spectra are recorded alternatively between the gate voltage and the reference voltage and successively co-added and averaged over long measurement times. A contour plot of all the normalized transmission spectra is shown in **Figure 7(b)**. It is observed that at low temperatures, the cavity resonance slightly shifted to a higher frequency as a result of the lower losses in the cavity in comparison to the room temperature measurements. At $V_g = -0.14$ V, a clear splitting of the ISR can be observed when the ISR (ground-to-first excited state, E_{01}) of the 2DEG crosses the resonance of the metamaterials at 2.4 THz. The width of the splitting is found to be 0.47 THz. By applying bias on the gated and networked-metamaterial layer, a significant modulation of the intensity of cavity resonance is observed [50, 51]. Thus, in our chopping scheme, the metamaterial resonance at 2.4 THz disappears for biases between -0.16 V and -0.04 V, where new states appear, known as the upper and the lower polaritons. Polaritons are defined as the quasi particles that result from intense light-matter interactions. The separation between them determines how strong the interaction is and is given by the light-matter coupling constant. For a fermionic intersubband system, the value of this coupling constant, Ω, is given by [42]:

$$\Omega = \frac{\hbar e f_{01}}{2m^*}\sqrt{\frac{n_{2D}}{2\epsilon\epsilon_0\hbar\omega_{01}V_{\text{mode}}}}, \tag{23}$$

where f_{01} is the oscillator strength of the ground-to-first excited state ISR with an energy of $\hbar\omega_{01}$. V_{mode} is the mode volume of the microcavity, given by (to a very good approximation) [39]:

---

[2] They are isolated donor atoms, which can be occupied by the electrons in connection with a large lattice relaxation also known as a deep-donor complex (DX center) in $Al_xGa_{1-x}As$.

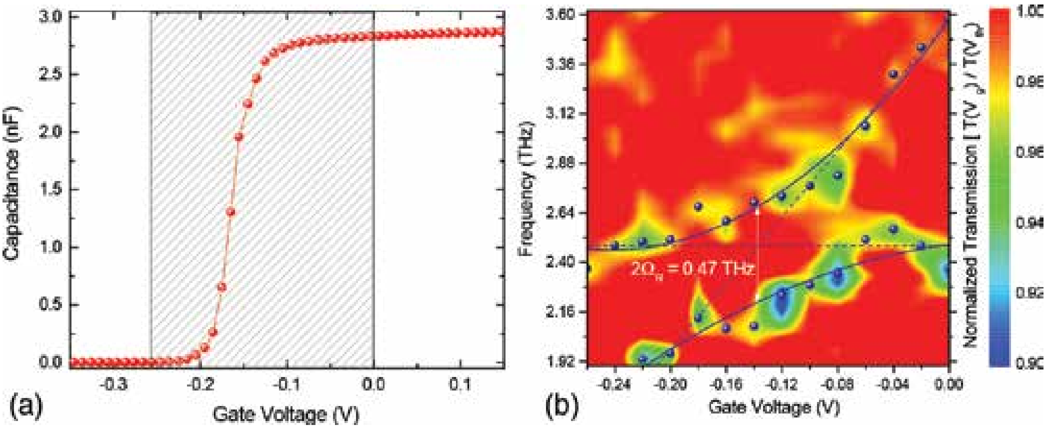

Figure 7. (a). Capacitance-voltage spectrum taken after illumination with the far-infrared source for 3 h, where the visible part of the beam saturates the DX centres. The shaded region in the spectrum denotes the voltage range over which the coupling experiments are performed. (b) A contour plot of the normalized transmission showing the formation of polaritonic states at the avoided crossing point. A strongly coupled system is formed with a resonance splitting of 0.47 THz.

$$V_{\text{mode}} = \frac{\iiint \epsilon(\vec{r})|\ \vec{E}\ (\vec{r})|^2 d^3\ \vec{r}}{max\left\{\epsilon|\ \vec{E}(\vec{r})|^2\right\}}, \tag{24}$$

where $\vec{E}$ is the electric field. The coupling strength depends on three important parameters. First, it is proportional to $1/\sqrt{V_{\text{mode}}}$, implying that the cavity mode volume should be small for higher coupling strength. Second, the higher the transition energy, the smaller the coupling strength ($1/\sqrt{\hbar\omega_{ij}}$). And finally, the coupling strength scales as $\sqrt{n_{2\text{D}}}$, which is a characteristic feature of the fermionic systems. The higher the carrier density, the greater is the coupling. The voltage tuning of our device is based on the quantum-confined Stark effect. The dependence of the coupling strength, $\Omega/2$, on the number of quantum wells as shown Gabbay et al. [52] can be written as:

$$\frac{\Omega}{2} = \frac{\aleph}{2}\sqrt{\frac{1 - e^{-2\alpha_{avg}\Delta Z N_{QW}}}{1 - e^{-2\alpha_{avg}\Delta Z}}}, \tag{25}$$

where α_{avg} is the average absorption coefficient, $\aleph$ is a constant, which is proportional to the average light-matter interaction and ΔZ is the distance between the QWs. For a single QW, as in the present investigation, the coupling strength is proportional to the value of $\aleph/2$. In the theoretical studies, Gabbay et al. found the value of $\aleph$ to be 1, which implies that for a single QW, the coupling strength is 0.5. The splitting in our experiments is found to be 0.47 THz, which agrees well with the theoretical value. It is well known that if the splitting is significantly above the sum of the full width at half maximum of both the ISR and the metamaterial resonance, then the coupling can be assigned to be in the strong coupling regime. Thus, an ultra-strong light-matter interaction regime is achieved by employing a single triangular quantum well in a HEMT heterostructure with a normalized coupling ratio of 0.19.

7. Conclusion

In conclusion, we have reviewed the quantum mechanical phenomenon that governs various electrical and optical properties in the low-dimensional semiconductor nanostructures such as a HEMT. We have demonstrated how one could electrically, or in combination with magnetic fields, probe and tune the intersubband transitions in the heterojunction of a HEMT structure. Such structures primarily have a triangular confinement potential. In the presence of a magnetic field, each subband is further split into a series of Landau levels or cyclotron orbits. Upon optical excitation with an infrared source, the intersubband resonances couple to the cyclotron resonance under tilted magnetic fields. This leads to the appearance of satellite peaks at the anti-crossing point. From the values of splitting at the anti-crossing points, the spacing between the corresponding subbands can be evaluated. Experiments performed in the absence of magnetic fields demonstrated that it is also possible to directly measure and tune these spacings via density-chopped infrared transmission spectroscopy. The subband spacings are measured directly and found to be in the far-infrared region (wide electrically tunable from 6 to 12 meV) of the electromagnetic spectrum. New epitaxial, complementary-doped, semi-transparent electrostatic gates that have better optical transmission are introduced [29]. The integrated device with a 2DEG in a high electron mobility transistor structure and artificial metamaterials forms a strongly coupled system that can be electrically driven from an uncoupled to a coupled and again back to the uncoupled regime. In the strongly coupled regime, a periodic exchange of energy between the two systems is observed as a splitting of 0.47 THz at the point of avoided crossing. This is a very high-energy separation, considering the fact that only one quantum well is employed and thus the achievement of a strong coupling regime can be safely claimed. The tuning mechanism is attributed to the quantum-confined Stark effect. This device architecture is particularly interesting in designing devices like modulators and detectors specifically in the THz regime. The integrated device has the high-speed dynamic characteristics of the HEMT design and the appropriate frequency-controlling ability of the metamaterials. From the design perspective of the metamaterials, they can be made particularly for the THz regime with appropriate dimensions (like the one used in this chapter). Upon excitation with a broadband source, this layer selects the desired frequency for which it is designed, and under the application of an external electrical field across the structure, the transmission of this frequency can be controlled and also modulated. This control dynamics can be very fast, simply owing to the fast dynamics of the HEMT design [52, 53]. Furthermore, this design can also be used to detect THz frequencies. Various other 2D materials (like graphene [54–56] or black phosphorous [57, 58]) are also used these days in the transistor configuration for developing THz detectors, simply utilizing the fast dynamics of the transistor design. These novel devices have thus helped to reduce the long-debated THz gap in the electromagnetic spectrum, where there is a severe lack of fast electronic devices.

Author details

Shovon Pal[1–3]*, Sascha R. Valentin[1], Arne Ludwig[1] and Andreas D. Wieck[1]

*Address all correspondence to: shovon.pal@ruhr-uni-bochum.de

1 Applied Solid State Physics, Ruhr University Bochum, Bochum, Germany

2 Terahertz Spectroscopy and Terahertz Technology, Ruhr University Bochum, Bochum, Germany

3 Department of Materials, ETH Zurich, Vladimir-Prelog-Weg, Zurich, Switzerland

References

[1] Pfeiffer L, West KW, Stormer HL, Baldwin KW. Electron mobilities exceeding 10^7 cm^2/Vs in modulation-doped GaAs. Applied Physics Letters. 1989;**55**:1888

[2] Dingle R, Stormer HL, Gossard AC, Wiegmann W. Electron mobilities in modulation-doped semiconductor heterojunction superlattices. Applied Physics Letters. 1978;**33**:665

[3] Saku T, Horikoshi Y, Tokura Y. Limit of Electron Mobility in AlGaAs/GaAs Modulation-doped Heterostructures. Japanese Journal of Applied Physics. 1996;**35**:34

[4] Wieck AD, Thiele F, Merkt U, Ploog K, Weimann G, Schlapp W. Subband–Landau-level coupling in GaAs/$Ga_{1-x}Al_xAs$ heterojunctions. Physics Review B. 1989;**39**:3785

[5] Haboeck U, Goñi AR, Danckwerts M, Thomsen C, Eberl K. Coupling of intersubband charge-density excitations to longitudinal-optical phonons in modulation-doped GaAs quantum wells. Solid State Communications. 2000;**115**:85

[6] Einspruch NG, Frensley WR. Heterostructures and Quantum Devices. In: VLSI Electronics Microstructure Science. Elsevier Science; Amsterdam, Netherlands; 2014.

[7] Faist J, Capasso F, Sivco DL, Sirtori C, Hutchinson AL, Cho AY. Quantum cascade laser. Science. 1994;**264**:553

[8] Oustinov D, Jukam N, Rungsawang R, Madéo J, Barbieri S, Filloux P, Sirtori C, Marcadet X, Tignon J, Dhillon S. Phase seeding of a terahertz quantum cascade laser. Nature Communications. 2010;**1**:69

[9] Nong H, Pal S, Markmann S, Hekmat N, Mohandas RA, Dean P, Li L, Linfield EH, Davies AG, Wieck AD, Jukam N. Narrow-band injection seeding of a terahertz frequency quantum cascade laser: Selection and suppression of longitudinal modes. Applied Physics Letters. 2014;**105**:111113

[10] Curl RF, Capasso F, Gmachl C, Kosterev AA, McManus B, Lewicki R, Pusharsky M, Wysocki G, Tittel FK. Quantum cascade lasers in chemical physics. Chemistry Physics Letters. 2010;**487**:1

[11] Tonouchi M. Cutting-edge terahertz technology. Nature Photonics. 2007;**1**:97

[12] Williams BS. Terahertz quantum cascade lasers. Nature Photonics. 2007;**1**:517

[13] Kumar S. Recent progress in terahertz quantum cascade lasers. IEEE Journal of Selected Topics in Quantum Electronics. 2011;**17**:38

[14] Corrigan P, Martini R, Whittaker EA, Bethea C. Quantum cascade lasers and the Kruse model in free space optical communication. Optics Express. 2009;**17**:4355

[15] Liu X, Cheng S, Liu H, Hu S, Zhang D, Ning H. A survey on gas sensing technology. Sensors. 2012;**12**:9635

[16] Kim SM, Hatami F, Harris JS, Kurian AW, Ford J, King D, Scalari G, Giovannini M, Hoyler N, Faist J, Harris G. Biomedical terahertz imaging with a quantum cascade laser. Applied Physics Letters. 2006;**88**:153903

[17] Pickwell E, Wallace VP. Biomedical applications of terahertz technology. Journal of Physics D. 2006;**39**: R301

[18] Pushkarsky MB, Dunayevskiy IG, Prasanna M, Tsekoun A, Go R, Patel CKN. High-sensitivity detection of TNT. Applied Physics Letters. 2006;**103**:19630

[19] Levine BF. Quantum-well infrared photodetectors. Journal of Applied Physics. 1993;**74**:1

[20] Schneider H, Liu HC. Quantum Well Infrared Photodetectors: Physics and Applications. Springer Series in Optical Sciences. Vol. **126**, Springer; Berlin; Heidelberg, Germany; New York; 2007.

[21] Saito W, Takada Y, Kuraguchi M, Tsuda K, Omura I. Recessed-gate structure approach toward normally off high-Voltage AlGaN/GaN HEMT for power electronics applications. IEEE Transactions on Electronic Devices. 2006;**53**:356

[22] del Alamo JA. Nanometre-scale electronics with III–V compound semiconductors. Nature. 2011;**479**:317

[23] Tessman A. 220-GHz metamorphic HEMT amplifier MMICs for high-resolution imaging applications. IEEE Journal of Solid-State Circuits. 2005;**40**:2070

[24] Ren F, Pearton SJ. Semiconductor Device-Based Sensors for Gas, Chemical, and Bio Applications. CRC Press; Cleveland, OH; Boca Raton, FL; 2011.

[25] Tan IH, Snider GL, Chang LD, Hu EL. A self-consistent solution of Schrödinger-Poisson equations using a nonuniform mesh. Journal of Applied Physics. 1990;**68**:4071

[26] Snider GL, Tan IH, Hu EL. Electron states in mesa-etched one-dimensional quantum well wires. Journal of Applied Physics. 1990;**68**:2849

[27] Pal S, Valentin SR, Kukharchyk N, Nong H, Parsa AB, Eggeler G, Ludwig A, Jukam N, Wieck AD. Infrared transmission spectroscopy of charge carriers in self-assembled InAs quantum dots under surface electric fields. Journal of Physics: Condensed Matter. 2014;**26**:505801

[28] Pal S, Nong H, Valentin SR, Kukharchyk N, Ludwig A, Jukam N, Wieck AD, Density-chopped Far-infrared Transmission Spectroscopy to Probe Subband-Landau Splittings and Tune Intersubband Transitions, in CLEO: 2015, OSA Technical Digest (online) (Optical Society of America, 2015), paper JW2A.43

[29] Pal S, Nong H, Marksman S, Kukharchyk N, Valentin SR, Scholz S, Ludwig A, Bock C, Kunze U, Wieck AD, Jukam N. Ultrawide electrical tuning of light matter interaction in a high electron mobility transistor structure. Scientific Reports. 2015;**5**:16812

[30] Takagahara T, Takeda K. Theory of the quantum confinement effect on excitons in quantum dots of indirectgap materials. Physics Review B. 1992;**46**:15578

[31] Sattler KD. Handbook of Nanophysics: Principles and Methods. CRC Press; Cleveland, OH; Boca Raton, FL; 2010

[32] Schubert E, Physical Foundations of Solid-State Devices E. Fred Schubert; Rensselaer Polytechnic Institute, Troy, NY; 2015

[33] Davies JH, The Physics of Low-dimensional Semiconductors: An Introduction. Cambridge University Press; London; Cambridge, UK; New York; 1998.

[34] Harrison P. Quantum Wells, Wires and Dots: Theoretical and Computational Physics of Semiconductor Nanostructures. Wiley; New York; 2011.

[35] Bloch F. Über die Quantenmechanik der Elektronen in Kristallgittern. Zeitschrift für Physik. 1929;**52**:555

[36] Helm M. In Liu H, Capasso F, editors. Intersubband Transitions in Quantum Wells: Physics and Device Applications I, Semiconductors and Semimetals. Vol. **62.** Elsevier; Amsterdam, Netherlands; 1999. pp. 1–99.

[37] Peeters FM, Matulis A, Helm M, Fromherz T, Hilber W. Oscillator strength and sum rule for intersubband transitions in a superlattice. Physics Review B. 1993;**48**:12008

[38] Batke E, Heitmann D. Rapid-scan Fourier transform spectroscopy of 2-D space charge layers in semiconductors. Infrared Physics. 1984;**24**:189

[39] Wieck AD, Maan JC, Merkt U, Kotthaus JP, Ploog K, Weimann G. Intersubband energies in GaAs-$Ga_{1-x}Al_xAs$ heterojunctions. Physics Review B. 1987;**35**:4145

[40] Wieck AD, Bollweg K, Merkt U, Weimann G, Schlapp W. Combined intersubband-cyclotron resonances in a $GaAs-Ga_{1-x}Al_xAs$ heterojunction. Physics Review B. 1998;**38**:10158

[41] Wieck AD. Wechselwirkung der Intersubbandresonanz zweidimensionaler Systeme mit Elementaranregungen in Halbleitern. Universität Hamburg; 1987

[42] Pal S. Terahertz transmission spectroscopy of charge carriers under surface electric fields. Ruhr-Universität Bochum; 2015.

[43] Ando T. Theory of intersubband cyclotron combined resonances in the silicon space-charge layer. Physics Review B. 1979;**19**:2106

[44] Batke E, Weimann G, Schlapp W. Quenching of collective phenomena in combined intersubband-cyclotron resonances in GaAs. Physics Review B. 1991;**43**:6812

[45] Becker C, Vasanelli A, Sirtori C, Bastard G. Electron–longitudinal optical phonon interaction between Landau levels in semiconductor heterostructures. Physics Review B. 2004;**69**:115328

[46] Allen SJ, Tsui DC, Vinter B. On the absorption of infrared radiation by electrons in semiconductor inversion layers. Solid State Communications. 1976;**20**:425–428

[47] Zhang S, Fan W, Malloy KJ, Brueck SRJ, Panoiu NC, Osgood RM. Demonstration of metal–dielectric negative-index metamaterials with improved performance at optical frequencies. The Journal of the Optical Society of America B. 2006;**23**:434

[48] Huang X, Lai Y, Hang ZH, Zheng H, Chan CT. Dirac cones induced by accidental degeneracy in photonic crystals and zerorefractive-index materials. Nature Materials. 2011;**10**:582

[49] Yen TJ, Padilla WJ, Fang N, Vier DC, Smith DR, Pendry JB, Basov DN, Zhang X. Terahertz magnetic response from artificial materials. Science. 2004;**303**:1494

[50] Shrekenhamer D, Rout S, Strikwerda AC, Bingham C, Averitt RD, Sonkusale S, Padilla WJ. High-speed terahertz modulation from metamaterials with embedded high electron mobility transistors. Optics Express. 2011;**19**:9968

[51] Chen H-T, Padilla WJ, Zide JMO, Gossard AC, Taylor AJ, Averitt RD. Active terahertz metamaterial devices. Nature. 2006;**444**:597

[52] Gabbay A, Brener I. Theory and modeling of electrically tunable metamaterial devices. Optics Express. 2012;**20**:6584

[53] Nouman MT, Kim H-W, Woo JM, Hwang JH, Kim D, Jang J-H. Terahertz modulator based on metamaterials integrated with metal-semiconductormetal varactors. Scientific Reports. 2016;**6**:26452

[54] Vicarelli L, Vitiello MS, Coquillat D, Lombardo A, Ferrari AC, Knapp W, Polini M, Pellegrini V, Tredicucci A. Graphene field effect transistors as room-temperature terahertz detectors. Nature Materials. 2012;**11**:865

[55] Mittendorff M, Winnerl S, Kamann J, Eroms J, Weiss D, Schneider H, Helm H. Ultrafast graphene-based broadband THz detector. Applied Physics Letters. 2013;**103**:021113

[56] Tong J, Muthee M, Chen S-Y, Yngvesson SK, Yan J. Antenna enhanced graphene THz emitter and detector. Nano Letters. 2015;**15**:5295

[57] Horiuchi N. Black phosphorus detector. Nature Photonics. 2015;**9**:631

[58] Viti L, Hu J, Coquillat D, Politano A, Knapp W, Vitiello MS. Efficient Terahertz Detection in Black-Phosphorus Nano-Transistors With Selective and Controllable Plasma-Wave, Bolometric and Thermoelectric Response. Scientific Reports. 2016;**6**:20474

Group III–V Semiconductor High Electron Mobility Transistor on Si Substrate

Ravindiran Munusami and Shankar Prabhakar

Additional information is available at the end of the chapter

http://dx.doi.org/10.5772/intechopen.68181

Abstract

High electron mobility transistor (HEMT) is the futuristic development of the transistor in migration of the nm technology for integration of many devices in a single chip. Moving beyond the silicon-based devices to reach out the bottlenecks in the scaling and sizing of transistors has become an interesting topic of research. This research area includes the novel approach towards new materials and device structures. Materials focus is on composites made of binary, ternary and quaternary elements. Nanostructures made of two-dimensional electron gas (2DEG), quantum well and tunnel barrier make the electron transport in devices interesting. A similar approach is adopted in the present work to make the device more suitable for faster device operation with high frequency.

Keywords: high electron mobility transistor, two-dimensional electron gas, heterojunction, ternary composite

1. Introduction

High electron mobility transistors (HEMTs) have become the vital device in high-speed operation for microwave applications. Group III–V devices are generally used as HEMT due to the high electron mobility and electron density. Higher charge density in the device makes a changeover in the conductance oscillation of the device with the variation in the electrons behaviour [1]. These properties make the device operate at higher switching speed and low power. Higher switching speed with low power requirement of the devices makes it more suitable for integration of many devices on a single chip. Scaling and sizing of the device without compromising the performance will make the device more suitable for the advanced application in electronics [2]. Heterojunction is formed when different materials are placed on over the other. Generally, these heterojunctions are formed with the superlattice structures,

INTECH
open science | open minds

© 2017 The Author(s). Licensee InTech. This chapter is distributed under the terms of the Creative Commons Attribution License (http://creativecommons.org/licenses/by/3.0), which permits unrestricted use, distribution, and reproduction in any medium, provided the original work is properly cited.

which normally are made of different materials. Group III–V elements such as AlGaAs/GaAs, AlGaN/GaN and InGaAs/GaAs were used in the fabrication of HEMT devices [3–5]. Traditional HEMTs have achieved higher operating speed of 60 GHz and the data rates higher than 10 Gbit/s [6]. Moving beyond the rated speed of operation and data rates, the material and device structure should be worked on further. Group III–V elements have higher electron densities that help in faster movement of electrons. Among III–V elements, InSb has very good electronic property with less effective mass and higher electron concentration, and better lattice constant and narrow energy gap as shown in **Figure 1**.

InSb has very good magnetic property with spin-dependent phenomenon to explore the spin orientated applications such as modulators, memories, sensors, etc. based on the ferromagnetic heterostructures [8]. InSb has narrow band gap of 0.17 eV with a low effective mass of 0.014 ME, which makes the room temperature electron mobility almost 7000 cm^2/V s, and makes the device more suitable for high-speed operation. InSb have high carrier mobility with good surface morphology [9]. The narrow band gap InSb semiconductor when doped with other elements has interesting properties, which can be used for various electronic applications. Doping of Mn into InSb results in the dilute magnetic semiconductor (DMS) property of the material with different doping ratios. Mn doping results in the increased carrier-mediated magnetic coupling in the ferromagnetic semiconductor [10]. Several works have been reported on Mn doping into InSb for analysis of the dilute magnetic semiconductor application with ferromagnetic nature in the hysteresis curve. The magnetic property analysis for the InMnSb compound was made for both powder samples and thin films with varying compositions of doping. Mn doping into InSb results in some interesting properties such as photo-induced spin effect, optical response, cyclotron resonance and magneto transport [11–17].

InSb and doped InSb composites are used for various applications due to its better electronic property. InSb-based devices involve field effect transistors (FET), quantum well transistors, micro hall device, nanowire FET, quantum dot device and heterostructure device. A single crystalline InSb nanowire synthesized by pulsed laser chemical vapour deposition demonstrates a good n-type semiconductor behaviour, which makes it suitable for FET device property [18].

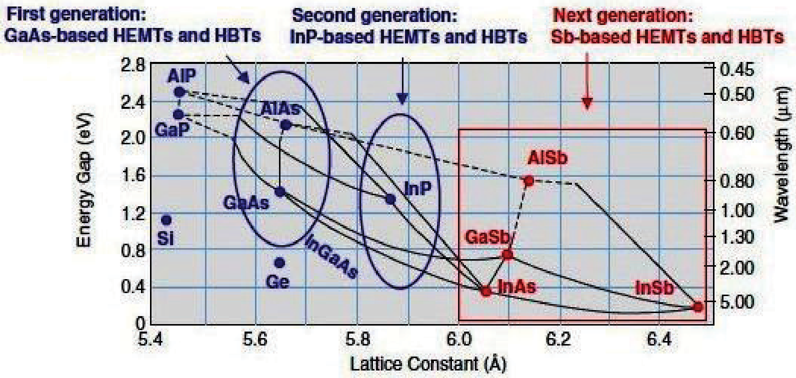

Figure 1. Lattice constant and band gap of Group III–V compound semiconductors, Source: Bennett et al. [7].

InSb-based device was made of metal organic vapour phase epitaxy for fabricating heterostructures of InSb and InAs. Measurement of the fabricated quantum dot device has coulomb blockade effect of 4.2 kA [19]. Fabricated InAs/InSb nanowire heterostructure FET shows unipolar and bipolar operation with the temperature-dependent electrical measurements by applying bias on the InAs side and InSb side. Conductivity is increased very strongly due to the electron transport across the heterostructure junction. InSb nanowire FETs are used for high-speed ultra-low power applications with the analysis based on the performance for varying nanowire diameters. This low power and high-speed operation makes the device more suitable for low power digital logic application when fabricated as enhancement and depletion of InSb-based quantum well transistor.

To make the device perform better the gate length of the InSb quantum well transistors was reduced to 0.2 μm, which resulted in the device exhibiting high electron mobility of 30,000 cm^2/V s with a sheet carrier density of 1 ×1012 cm^{-2} [19, 20]. Modified approaches have been adopted to improve the performance of the device such as strained P channel quantum well InSb transistor. The performance metrics compared with the standard P channel MOSFET show that InSb-based device exhibits low power dissipation and high transconductance [20, 21]. Device fabrication involves some tedious process involved like deposition, etching and lithography. Hence before getting into the process of fabrication, an alternative approach was used to analyse the device by device modelling. Similar approach was adopted based on atomistic modelling for the thickness dependence (3–16 nm) for electron transport in the quantum well FET [22].

Quantum well devices made of InSb have vital magnetic sensing application, which can be used as micro hall magnetic field sensor for detecting pT. Similar to the magnetic sensing application, InAs/InSb nanowire FET devices have application in detecting THz frequencies [23, 24]. Similar to the nanowire FET, Tunnel FET made of InSb has a very good mobility due to the narrow band gap when fabricated. This higher mobility of the device makes a faster switching speed, which is a good property to be considered to look into the device scaling with InSb-based device structures. It is observed that InSb is a vital composite to be used in transistor applications. Proposed method deals with the InMnSb compound and Si made of P, N-type to form a HEMT device. The composite was made as a thin tunnel layer to be formed between the source and the drain regions to make the charge carriers flow through the channel with an electron spin.

InMnSb compound exhibits an exceedingly good DMS property with the doping concentration and works as dilute magnetic semiconductor (DMS). The HEMTs made of magnetic tunnel junction has an improved electron transport when compared to the existing device structures. Magnetic tunnel junctions were made by inserting the magnetic materials between the source, channel and the drain of the high electron mobility transistor (HEMT) to enhance the performance. Conductivity of the proposed device structure reveals that the device has a very good electron transport due to the magnetic materials and will amplify low-frequency signals. The proposed device structure with the InMnSb tunnelling layer is shown in **Figure 2**. Functionality of the device was tested with different architectures to identify the better device operation for high-speed application. Density functional theory (DFT) calculations were performed to identify the device performance. Charge density was considered as vital factor to analyse the device performance.

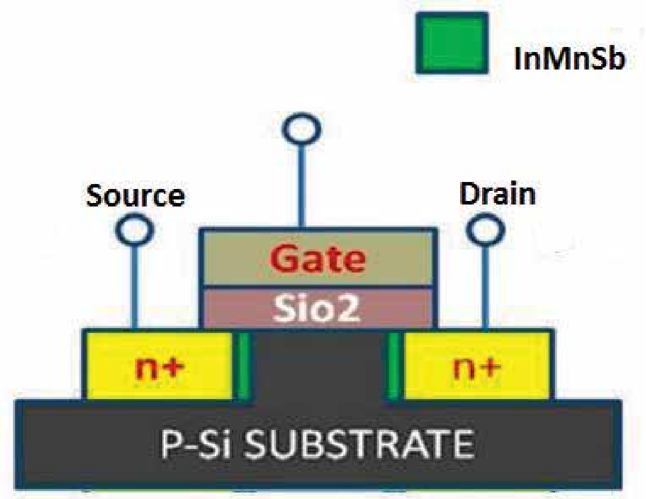

Figure 2. Proposed HEMT device structure.

2. HEMT with InMnSb tunnel layer

Propose HEMT device structure has a P type Si substrate and over that **N-**type Si deposition with the intermediate InMnSb layers in between the source/channel and channel/drain regions of the transistor. The P type Si substrate is made of trivalent boron doping in the intrinsic silicon and N-type Si was made with the pentavalent phosphorus doping. Due to the spin alignment of electrons in an InMnSb layer the conductivity of the device is increased by 10-folds when compared to the NPN device structure. **Figure 3** shows the conductivity of the NFPFN device that is 64.5 mS, which is 10-folds more than the conductivity of the NPN device of 6.5 mS.

Electron transport in the proposed device structure is understood that the electron travels through the two tunnel layers and two DMS layers, which is represented by Eq. (1).

$$\Delta F1 * \mu es + \Delta F2 * \mu es \tag{1}$$

$\Delta F1$ and $\Delta F2$ describe the tunnelling at junctions 1 and 2, respectively. μes represents the magnetic moment of the DMS layer at the source and the drain regions. The carriers travel through both the junctions and the DMS layer to travel from the source to drain region. The rate at which the particle tunnels through the region is represented by the tunnel rate and is represented by Eq. (2). The magnetic moment when the electron travels in the DMS layer is described by Eq. (3). Tunnelling at the junction $\Delta F1$ and $\Delta F2$ is expressed in Eqs. (4) and (5).

$$\tau(\Delta F) = \frac{\Delta F}{e^2 R\tau\left(\exp\left(\frac{\Delta F}{KT}\right) - 1\right)} \tag{2}$$

$$\mu es = \gamma(e2m)\,S \tag{3}$$

$$\Delta F1 = eC\Sigma\left\{e2 + \left(vb2\,[\,2C2 + Cg] - VgCg + ne\right)\right\} * \mu es \tag{4}$$

$$\Delta F2 = eC\Sigma\left\{e2 + \left(vb2\,[\,2C1 + Cg] + VgCg - ne\right)\right\} * \mu es \tag{5}$$

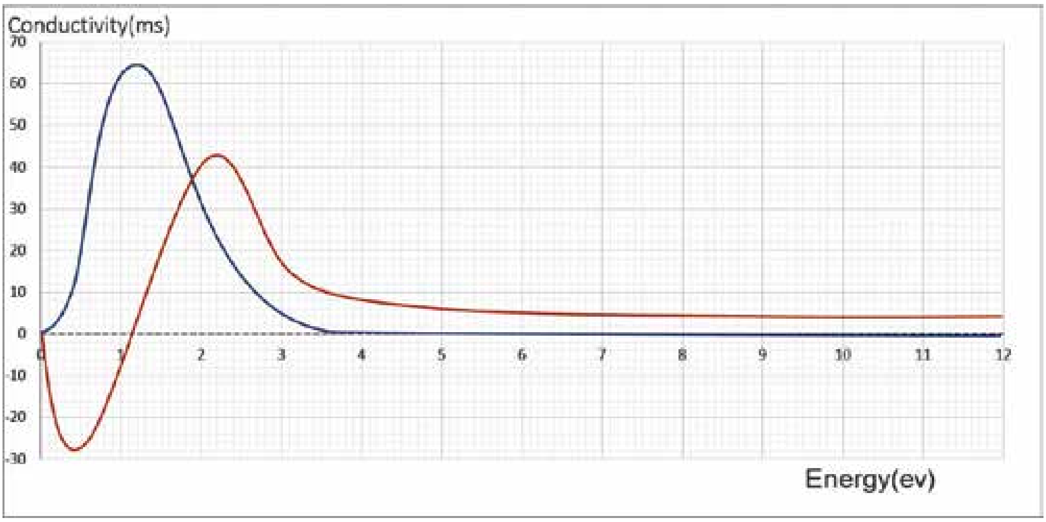

Figure 3. Conductivity graph of HEMT using DFT calculation.

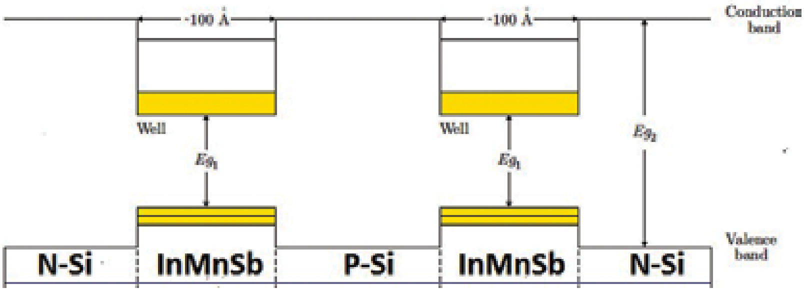

Figure 4. Band structure of the proposed device.

Tunnelling equation on both the junctions consider the gate capacitance, junction capacitances 1 and 2, gate voltage and the number of electrons. Considering all these factors and the magnetic moments, the electrons travel through the DMS layers and the channel from source to the drain of the HEMT. Band structure of the proposed device structure with the energy gap and the band alignment at stable condition with no applied voltage is shown in **Figure 4**.

The band structure reveals energy band gap between the conduction and valance band of each layer of the device. There is a narrow band gap in the InMnSb region when compared to the Si layer. This narrow band gap in the InMnSb layer allows the charge carriers travel faster from valance band to the conduction band. Since the InMnSb has dilute magnetic semiconductor (DMS) nature, it allows the electron to travel much faster with a spin magnetic moment. The layers are repeated structures rather than single, which makes the electron confined at the interface of the heterostructures called as heterointerference. Formation of the quantum well is always a possibility in the repeated structure. The depth of the well and the barrier thickness of the

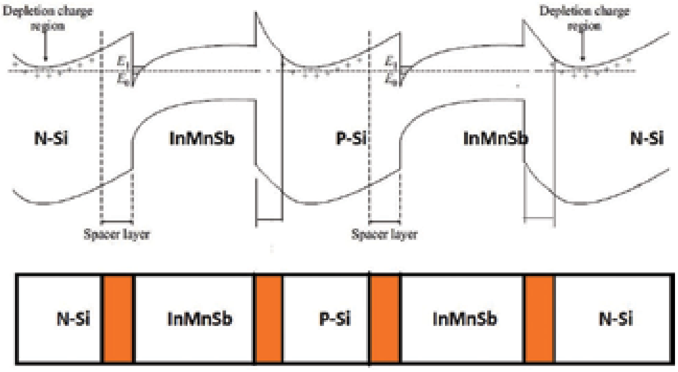

Figure 5. Band alignment and 2DEG.

device vary with the doping concentration. Confinement of the electron makes it at higher energies resulting in formation of discrete sub-bands. The confined structures make a two-dimensional electron gas (2DEG) resulting in less scattering and improved mobility. Considering the electron confinement and the 2DEG structure, the electron transport and band alignment is shown in **Figure 5**.

The number of electrons confined in 2DEG depends on the thickness of the layers and the doping concentration [25].

3. HEMT electron mobility

3.1. Mobility with low electric field

Electron mobility in the band of the different layers with low electric field depends on the doping density in regards to the ionized impurity scattering effects at rated temperature. Reduced ionized impurity scattering with modulated doping makes a smaller number of carriers with high mobility. Higher doping concentration of the doping in the HEMT devices makes the career screening resulting in higher mobility of the carriers. So the carrier concentration, mobility of the electrons, ionized scattering effect and the temperature have the correlation between each other factor resulting in the HEMT device conductivity.

3.2. Mobility with high electric field

The 2DEG electrons attain greater energy and become hot with the moderate or higher electric field. There will be an energy separation between the sub-bands, and the high mobility electrons in the lower sub-band get the needed energy from the applied electric field to move into the lower energy adjacent sub-band. Higher initial mobility in the lower sub-band results in the faster decay in mobility with the applied voltage [25]. Hence with the applied electric field, the electrons at different sub-bands get the needed energy to move from their initial state and to move into the next state. This process makes the generation and recombination rate much faster resulting in better conduction of the device.

4. Drain characteristics

Drain current and the drain source voltage characteristics of the proposed HEMT device is shown in **Figure 6**. The curve reached a stable drain current at 2.5 mA and continues to be stable. Further increase in the drain current will be achieved with the increasing gate source voltage of the device. The stable saturation region in the drain characteristics will make the device operate at stable Q point resulting in proper amplification of the device when used in amplifier applications. Increasing drain current with the lower gate voltage makes the device more suitable for faster switching operation. Faster switching speed makes the devices more suitable for the high frequency applications. This improved drain characteristics of the device proves the ability of the device to be used for the microwave application. Similar to the drain characteristics, proposed device transfer characteristics is also very high when compared to the other HEMT devices.

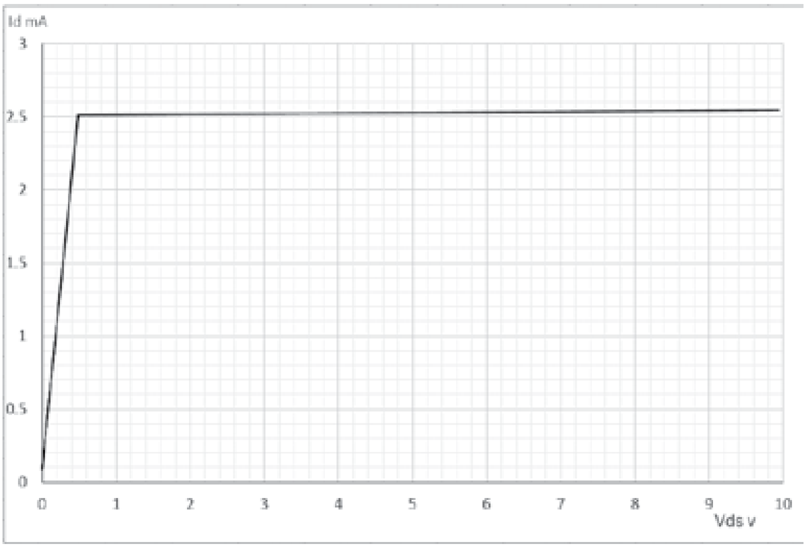

Figure 6. Drain characteristics of proposed HEMT.

5. Transfer characteristics

Transfer characteristics with the drain current versus gate source voltage graph are shown in **Figure 7**. The results reveal that the proposed HEMT device has very high drain current of 22 A. The transfer characteristics of the HEMT device made of different materials and architectures are shown in **Figure 8**.

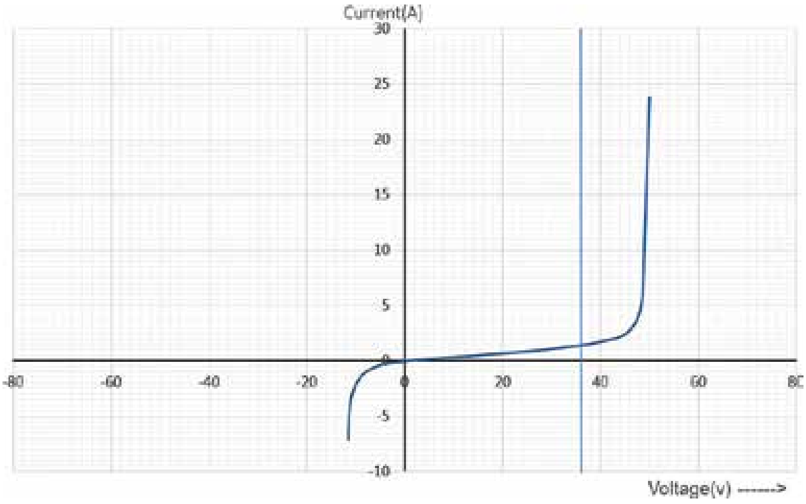

Figure 7. Transfer characteristics of the proposed device.

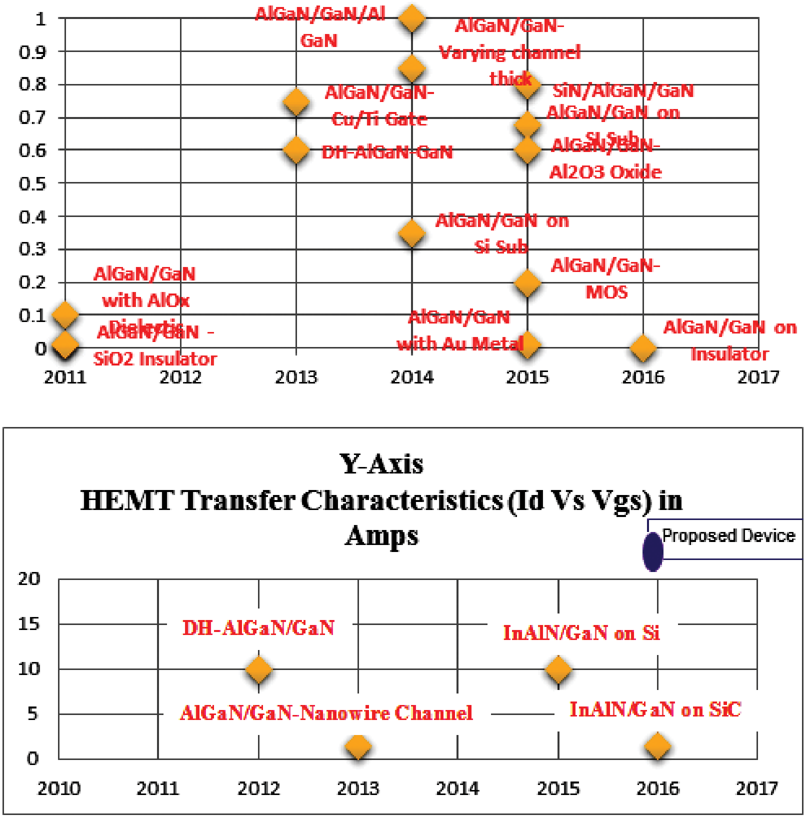

Figure 8. Transfer characteristics of other HEMT device in comparison with proposed HEMT device.

6. Conclusion

Superlattice structure for HEMT applications has shown good progress over the last few decades, to match the suitability of the device for high-speed applications. This chapter has dealt with the improved performance of the HEMT device due to the DMS layer made with the InMnSb layer resulting in improved conductivity and VI characteristics. The resulted band structure with the proposed device structure has made the low-dimensional structure with the 2DEG allowing the electron to travel without any collusion. The collision-free transport of the particle in the device structure is predicted to make a better conductivity resulting in better device performance. Comparison of the proposed HEMT device with the other existing devices has substantiated the improved device characteristics in par with the other HEMT devices. Hence it is evident that the proposed device will have a very good prospect in high-speed applications.

Author details

Ravindiran Munusami [1]* and Shankar Prabhakar[2]

*Address all correspondence to: ravmun@gmail.com

1 Electronics & Communication Engineering, Saveetha School of Engineering, Saveetha University, India

2 School of Engineering, Amrita University, Chennai, India

References

[1] Kastner MA. The review of high electron mobility transistor. Review of Modern Physics.1992;**64**(3):849.

[2] Yu S, Hwang SW, Ahn D. Macromodeling of single-electron transistor for efficient circuit simulation. IEEE Transactions on Nanotechnology. 1999;**46**(8): 1667-1671.

[3] Zhu J. Review of III–V based high electron mobility transistors. IOSR Journal of Engineering. 2015;**5**(4):2278-8719

[4] Vimala P. Modelling. Simulation of unilateral power gain. International Journal of Advanced Engineering and Global Technology. 2016;**4**(4):2105-2109

[5] Mahon SJ. Determination of device structure from GaAs/AlGaAs HEMT DC I–V characteristic curves. IEEE Transactions on Electron Devices. 1992;**39**(5):1041-1049

[6] Takser PJ. High electron monility transitor. In: Morgan DV, Williams RH, editors. Physics and Technology of Heterojunction Devices. 1st ed. United Kingdom: Peter Peregrinus Ltd; 1991

[7] Hwang E, Mookerjea S, Hudait MK, Datta SA. Investigation of scalability of In0.7Ga 0.3As quantum well field effect transistor (QWFET) architecture for logic applications. 2011;62;01:82-89.

[8] Matsukura F, Ohno H, Dietl T. III–V ferromganteic semiconductors. In: Buschow KHJ, editor. Hand Book of Magnetic Materials. 1st ed. Amsterdam: Elsevier; 2002, Volume 15; ISBN 0-444-51459-7.

[9] Udayashankar NK, Bhat HL. Growth and characterization of indium. Bull Mater Science. 2001;**21**:445-453

[10] Csontos M, Mihlay G. Furdyna JK. Pressure induced ferromagnetism in (InMn) Sb dilute magnetic semiconductor. Nature Materials. 2005;**4**:447-449

[11] Nontapot K, Kini RN, Khodaparast GA. Relaxation of photo induced spins and carriers in ferromagnetic InMnSb films. Applied Physics Letters. 2007;**90:143109**.

[12] Ivanov VA, Pashkova ON, Galera RM. Cluster ferromagnetism in Mn doped In. Organic Materials. **2008;44**:1041-1046

[13] Frazier M, Kini RN, Furdyna JK. Time resolved magneto optical studies of ferromagnetic InMnSb films. Applied Physics Letters. 2008; **92:061911**

[14] Lari L, Lea S, Lazarov VK. Characterization of InMnSb epitaxial films for spintronics. Journal Physics: Conference Series. 2012; **371:012032**

[15] Sergey A, Obukhov S. A new type of low temperature conductivity in InSb doped with Mn. AIP Advances. 2012; **2:022116**

[16] Khodaparast GA, Matsuda YH, Furdyna J. Cyclotron resonance in ferromagnetic InMnAs and InMnSb. Physical Review B. 2013;**88**: 012056

[17] Kochura AV, Aronzon BA, Lahderanta E. Magnetoresistance and anomalous hall effect of InSb doped with Mn. Journal of Nano and Electronics Physics. 2013;**5**(04015)

[18] Khayer MA. The quantum capacitance limit of high-speed, low-power InSb nanowire field effect transistors. Electron Devices Meeting. 2008; DOI: 978-1-4244-2378-1; **ISBN**: 978-1-4244-2377-4

[19] Datta S, Ashley T, Chau R. 85 nm gate length enhancement and depletion mode InSb quantum well transistor for ultrahigh speed and very low power digital logic applications. Electron Devices Meeting. 2005:763-766

[20] Radosavljevic M, Ashley T, Andreev A, Chau R. High-performance 40nm gate length InSb p-channel compressively strained quantum well field effect transistors for low-power (VCC = 0.5 V) logic applications. IEEE International Electron Devices Meeting. 2008. DOI: 978-1-4244-2378-1; **ISBN**: 978-1-4244-2377-4

[21] Kunets VP, Easwaran S, Salamo GJ. InSb quantum well based micro hall devices: Potential for pT detectivity. IEEE Transactions Electron Devices. 2009;**56**:683-687

[22] Nilsson HA, Caroff P, Wernersson LE. Unipolar and bipolar operation of InAs/ InSb nanowire heterostructure field effect transistor. Journal of Applied Physics. 2011;**110**: 064510

[23] Hwang E, Mookerjea S, Hudait MK, Datta SA. Investigation of scalability of $In_{0.7}Ga_{0.3}As$ quantum well field effect transistor (QWFET) architecture for logic applications. 2011;62;01: 82-89.

[24] Pitanti A, Coquillat D, Vitiello MS. Terahetz detection by heterostructed InAs/InSb nanowire based field effect transistors. Applied Physies Letters. 2012;**101**:141103

[25] Chang CY, Kai F, editors. GAAS High Speed Devices – Physics, Technology and Circuit Applications. 1st ed. New York, Singapore, Toronto, Brisbane: John Wiley & Sons; 1994. p. 395

Section 3

Thin-Film Transistors

Metal-Semiconductor Interfaces in Thin-Film Transistors

Miguel Dominguez, Pedro Rosales, Alfonso Torres,
Jose A. Luna-Lopez, Francisco Flores and
Mario Moreno

Additional information is available at the end of the chapter

http://dx.doi.org/10.5772/intechopen.68327

Abstract

The metal-semiconductor interface in thin-film transistors (TFTs) is one of the bottlenecks on the development of these devices. Although this interface does not play an active role in the transistor operation, a low-quality interface can be responsible for a low performance operation. In a-Si TFTs, a doped film can be used to improve this interface, however, in other TFT technologies, there is no doped film to be used. In this chapter, some alternatives to improve this interface are analysed. Also, the influence of this interface on the electrical stability of these devices is presented.

Keywords: thin-film transistors, metal-semiconductor, contact resistance, short channel effects

1. Introduction

In all electronic devices, an electrical connection to the real world is necessary. In the case of thin-film transistors (TFTs), the quality of this electrical connection may be the difference in having high or low performance devices. The connection is made by source/drain electrodes in contact with the active layer. These metal-semiconductor interfaces have not played an active role in the transistor operation. However, a low-quality interface can be responsible for a low performance operation. Indeed, this research topic is one of the bottlenecks on the development of thin-film transistor technologies.

© 2017 The Author(s). Licensee InTech. This chapter is distributed under the terms of the Creative Commons Attribution License (http://creativecommons.org/licenses/by/3.0), which permits unrestricted use, distribution, and reproduction in any medium, provided the original work is properly cited.

It is desirable to have the closest to an ideal metal-semiconductor interface or an ohmic contact with very low contact resistance; in other words, source/drain contacts with no barriers for the carrier flow in either positive or negative voltage polarization. Ideally, this occurs when metal and semiconductor work functions are of similar value and there are no interface states. However, having metal-semiconductor contacts without interface states is difficult and matching the semiconductor and metal work functions is nearly impossible. For these reasons, it is important to find alternatives to improve the metal-semiconductor interface in TFTs.

In metal-semiconductor interfaces, one may have several cases: ohmic contacts with low or high contact resistance and non-ohmic contacts with low or high contact resistance. Being this last, the most commonly obtained. The contact resistance can be extracted experimentally by the extrapolation of the width-normalized resistance (RW), obtained from the linear regime of the output characteristics I_{ds} vs. V_{ds}, for different channel lengths and gate voltages V_{gs}, as indicate in **Figure 1** [1, 2].

The problem associated with a high contact resistance is that it induces a potential drop at the drain/source contacts, affecting the electrical performance of the device [1–4]. On short channel TFTs, as the channel length is reduced, the source/drain contact resistance may be higher

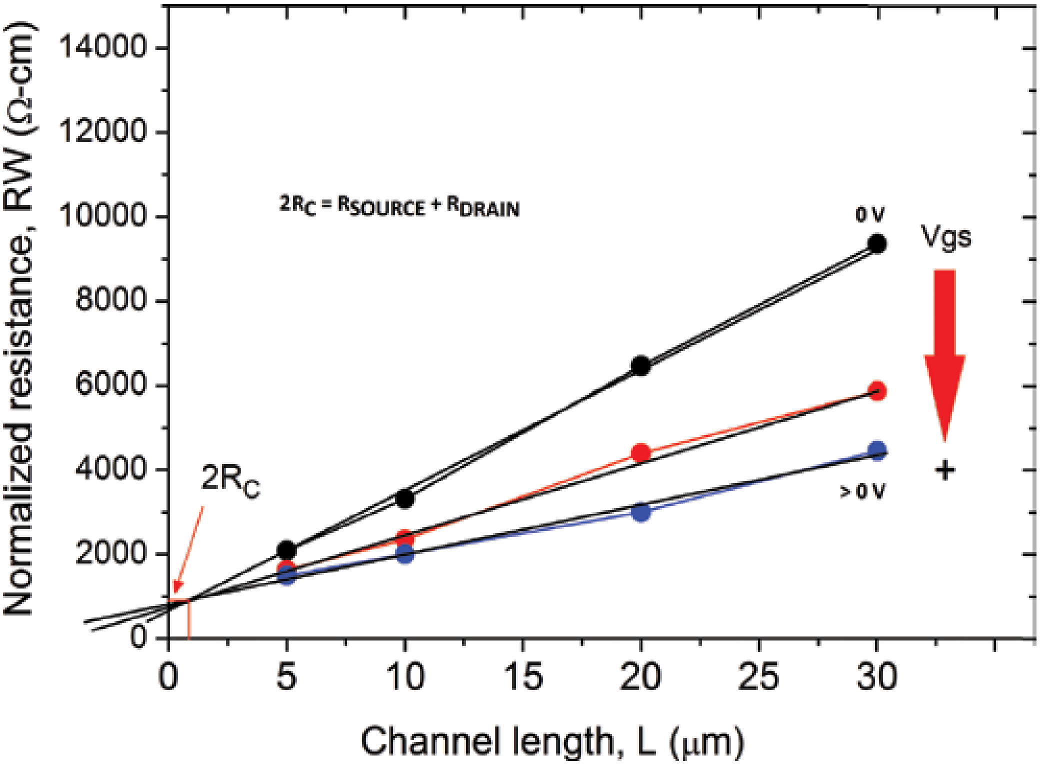

Figure 1. Width-normalized resistance (RW) (obtained from the linear regime of the output characteristics) for different channel lengths and gate voltages V_{gs}.

than the channel resistance, as result the electrical behaviour may be governed by the contact resistance. This may induce several mechanisms: some of them reported the degradation of the transconductance, drop of carrier mobility, impact ionization, among others. Indeed, there is not a value of channel length to determine if short channel effects will be exhibited on the electrical characteristics of the TFT. Reported TFTs exhibited short channel effects at channel lengths *L* lower than 20 μm, meanwhile other TFTs (some with high contact resistance) did not exhibited short channel effects at *L* of 10 μm [1, 3–10]. Moreover, a TFT may exhibit high contact resistance effects at considered long channel values. These effects can be presented as superlinear behaviour or current crowding in output characteristics [1, 11, 12]. It is always desirable to have a low contact resistance; however, the channel resistance must be dominant.

2. Experimental section

The high quality SiO_2 film was obtained by spin-coating of SOG (SOG700B Filmtronics) diluted with deionized water and cured at 200°C. The a-SiGe:H active layer was deposited using low frequency (110 kHz) plasma-enhanced chemical vapor deposition (PECVD) at 200°C, pressure of 0.6 Torr and an RF power of 300 W. The a-SiGe:H films were deposited from SiH_4 and GeH_4 feed gases with H_2 dilution. The flow rate of SiH_4 (10% H_2) and H_2 was 45 sccm and 1000 sccm, respectively, and the GeH_4 (90% H_2) flow rate was 105 sccm. The n+ a-Ge:H film was deposited using low frequency PECVD at 200°C with a pressure of 0.6 Torr and RF power of 300 W, with a GeH_4 (90% H_2) flow of 250 sccm, H_2 flow of 3500 sccm and PH_3 (99% H_2) flow of 20 sccm. The aluminium was e-gun evaporated.

3. Alternatives for metal-semiconductor interface improvement

The requirements for getting a high-quality metal-semiconductor interface are complex. Typically, in field-effect transistors, a heavily doped interlayer or contact region film is used between the semiconductor and source/drain electrodes in order to improve the metal-semiconductor interface. However, in amorphous semiconductors, the doping efficiency drops at high doping levels. Moreover, in some TFT technologies, there are no doped interlayer films to improve the metal-semiconductor interface. These make even more complex to obtain a high-quality interface.

3.1. Doped regions for source/drain contacts

In the case of hydrogenated amorphous silicon (a-Si:H), Le Comber and Spear [13] reported that amorphous silicon prepared by plasma-enhanced chemical vapor deposition (PECVD) can effectively be doped by adding small amounts of phosphine (PH_3) or diborane (B_2H_6) to the silane (SiH_4) in the discharge gas. As expected, the conductivity increases at low doping levels. However, at higher doping levels, the conductivity decreases presumably due to the generation of defect states.

Figure 2 shows the contact resistance of a-Ge:H films at 200°C as function of the PH_3 flow. At low flow of PH_3 the contact resistance decreases, but at higher flow it increases. This behaviour agrees with the reported by Le Comber and Spear. Similarly, **Figure 3** shows the contact resistance of the p-type a-Ge:H film as a function of the B_2H_6 flow. At low flow of B_2H_6, the contact resistance increases but at higher flow it decreases and finally increases again. This behaviour also agrees with the reported by Le Comber and Spear. These interlayer films enhance the tunnelling of carriers through the metal-semiconductor interface, reducing the contact resistance and improving the interface. The n-type a-Ge:H film was successfully used as a contact region film in ambipolar a-SiGe:H TFTs [14].

3.2. Plasma processes to improve the contact resistance

In this section, the improvement of carrier mobility, on/off-current ratio and threshold voltage using hydrogen plasma at the active layer prior to define the source/drain contacts is presented. Firstly, an over-etching in the active layer before forming the source/drain contacts is performed. This over-etching closes the source/drain contacts to the induced channel layer, as indicate in **Figure 4**.

Figure 4a shows the structure of the TFT after the deposition of the gate electrode, gate insulator, active layer and passivation layer. Typically, after this step, the passivation layer is etched to form the source/drain contacts (**Figure 4b**). In this case, added to the etching of the passivation layer, an over-etching in the active layer is performed, as indicate in **Figure 4c**. Moreover,

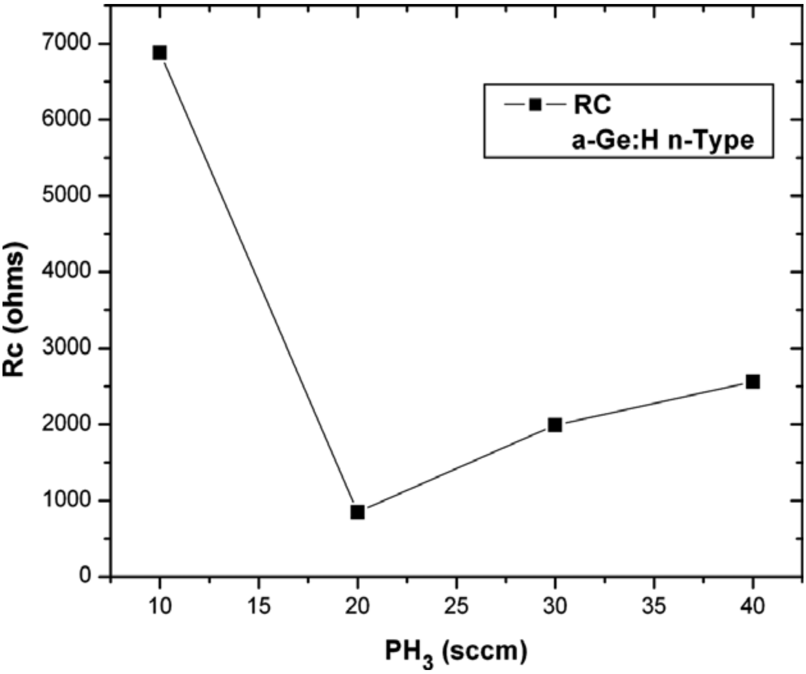

Figure 2. Contact resistance of the n-type a-Ge:H films as a function of the PH_3 flow.

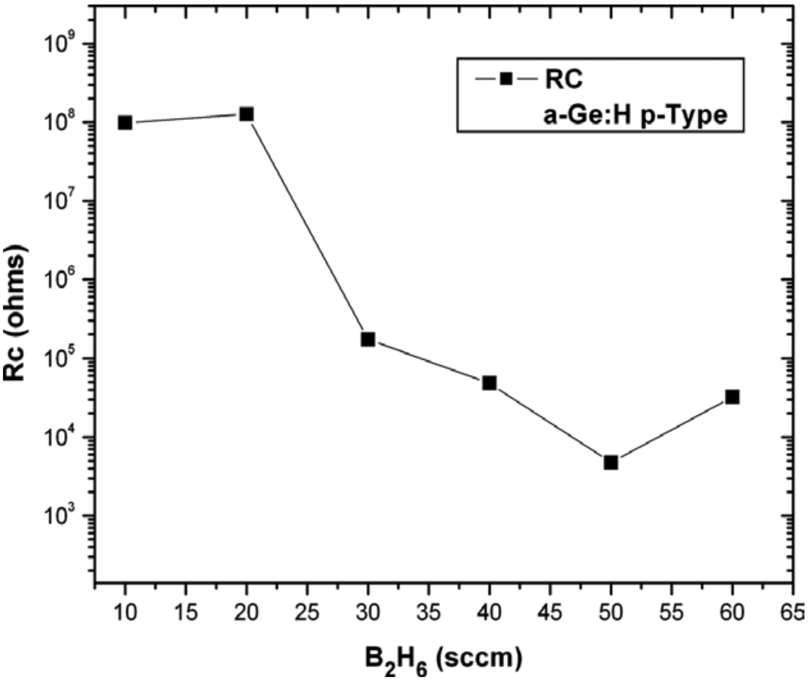

Figure 3. Contact resistance of the p-type a-Ge:H films as a function of the B_2H_6 flow.

a hydrogen plasma is applied [15]. For comparison, a set of devices without hydrogen plasma was fabricated. Finally, the source/drain contacts are formed (**Figure 4d**).

Figure 5 shows the transfer characteristics of the TFTs with and without hydrogen plasma. The TFTs with applied hydrogen plasma exhibit an on/off-current ratio approximately of 10^6 and an off-current approximately of 300 fA at 0 V_{gs}. While the TFTs without hydrogen plasma exhibit an on/off-current ratio of 10^3 and off-current of 20 pA. The subthreshold slopes values for both TFTs with and without hydrogen plasma were 0.56 and 0.61 V/DEC, respectively. The slopes are very similar. Typically, in TFTs, the subthreshold slope is largely decided by the quality of gate insulator-active layer interface. The subthreshold slope is dependent on the trap density in the active layer (N_T) and at the interface (D_{it}). The subthreshold slope can be approximated as the following equation [15]:

$$S = qK_B T(N_T ts + D_{it})/C_{ox} \log(e) \tag{1}$$

where q is the electron charge, K_B is the Boltzmann constant, T is the absolute temperature, ts is the active layer thickness and C_{ox} is the gate insulator capacitance per unit area. If N_T or D_{it} is separately set to zero, the respective maximum values of N_T and D_{it} are obtained. The N_T and D_{it} values were of 2.65 × 10^{17} cm^{-3}/eV and 2.65 × 10^{12} cm^{-2}/eV, respectively, for TFTs with applied hydrogen plasma. For TFTs without hydrogen plasma, the values were of 2.88 × 10^{17} cm^{-3}/eV and 2.88 × 10^{12} cm^{-2}/eV, respectively. Since both TFTs have identical insulator-semiconductor interface and the over-etching process only affects the source/drain regions, we do not expect any difference in the quality of the insulator-semiconductor interface of the devices.

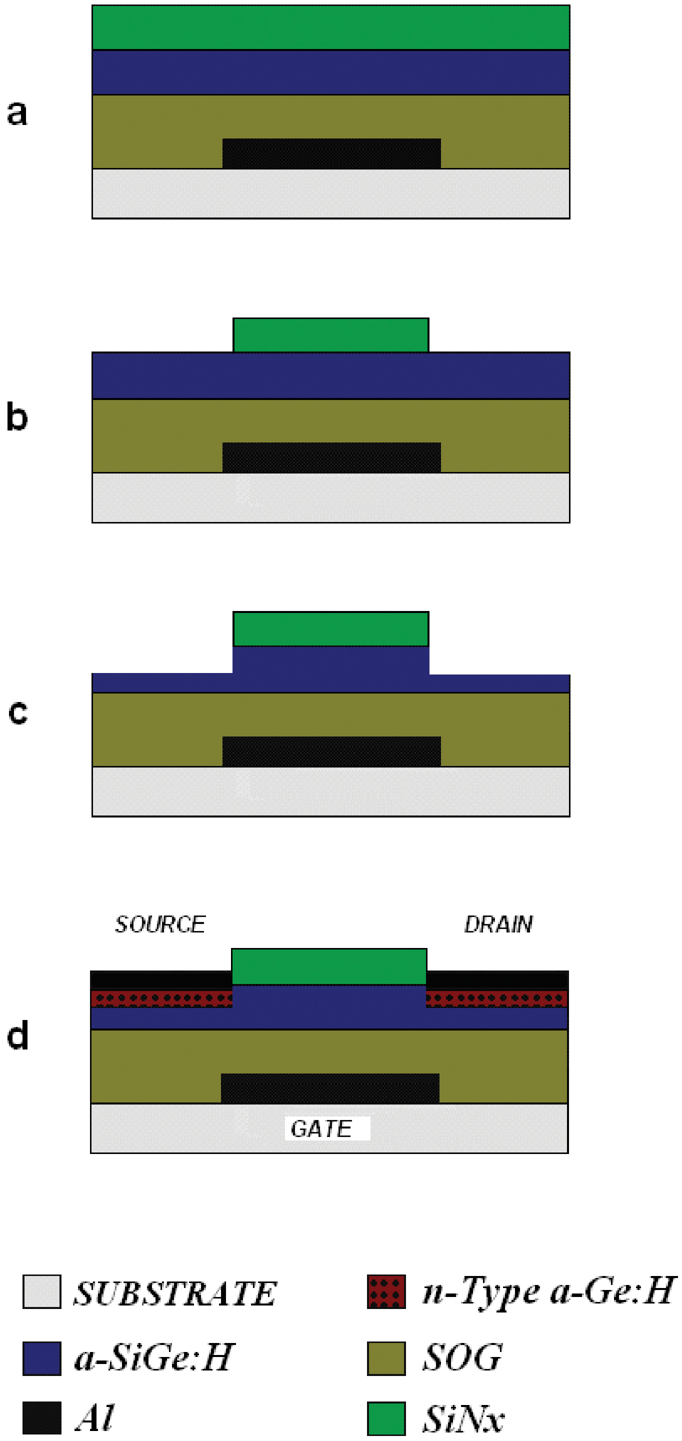

Figure 4. Process flow and cross-section of the TFT with over-etching at source/drain regions. (See text for description).

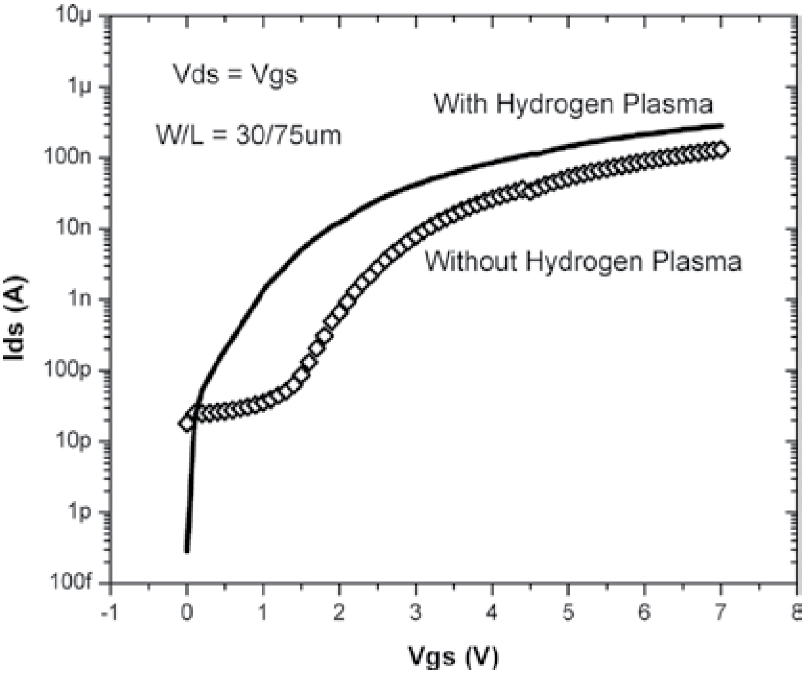

Figure 5. Transfer characteristics of the TFTs with and without hydrogen plasma.

On the other hand, **Figure 6** shows the square root of I_{ds} vs. V_{gs} of the TFT at a saturation regime. The threshold voltage and field-effect mobility can be extracted from the intercept with V_{gs} axis and slope, using Eq. (2).

$$I_{ds} = \mu_{FE} C_{ox}(W/2L)(V_{gs} - V_T)^2 \tag{2}$$

where μ_{FE} is the field-effect mobility, C_{ox} is the capacitance per unit area of the gate insulator, W and L are the channel width and the length, respectively, and V_T is the threshold voltage. The extracted threshold voltage and field-effect mobility were of 0.8 and 0.85 cm^2/Vs, respectively, for TFTs with hydrogen plasma. While 1.86 and 0.52 cm^2/Vs were extracted for TFTs without hydrogen plasma.

It is well known that hydrogen saturates dangling bonds in amorphous films [16]. Thus, the hydrogen plasma reduces the plasma-induced damage in the source/drain regions of the active layer, and as result the contact resistance of the TFT is improved. This can be corroborated with the higher values of carrier mobility and on-current.

Figures 7 and **8** show the output characteristics of the TFTs with and without hydrogen plasma. The output characteristics of TFTs without hydrogen plasma exhibit a high contact resistance that appears in the form of current crowding, in the bias range of 0–1V of V_{ds}. Also, the driving current capability is higher for TFTs with hydrogen plasma, as indicated by their values of I_{ds}. These results confirm the hydrogen plasma reduces the plasma-induced damage and improve the metal-semiconductor interface. These processes in the source/drain regions lead to form good ohmic contacts.

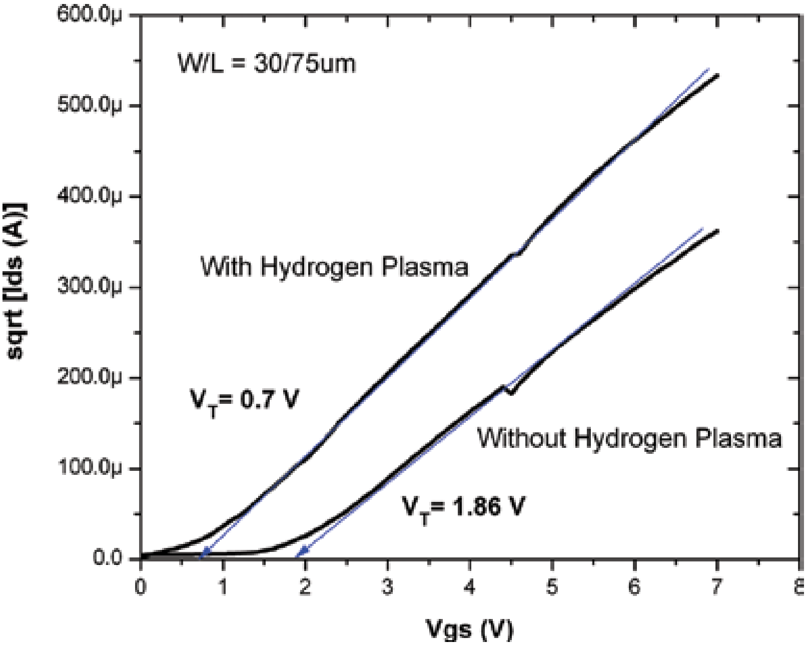

Figure 6. Square root of I_{ds} vs. V_{gs} of the TFT at saturation regime.

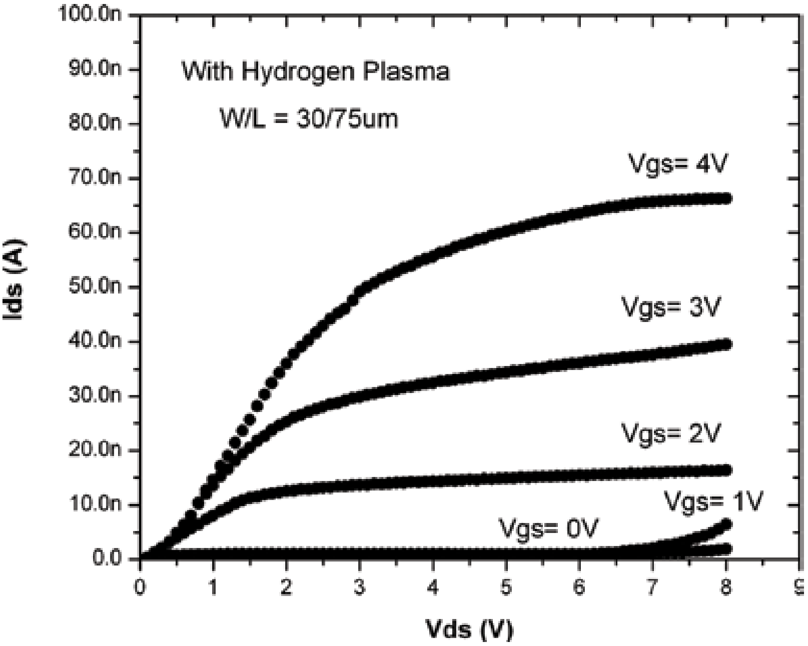

Figure 7. Output characteristics of TFTs with over-etching and hydrogen plasma.

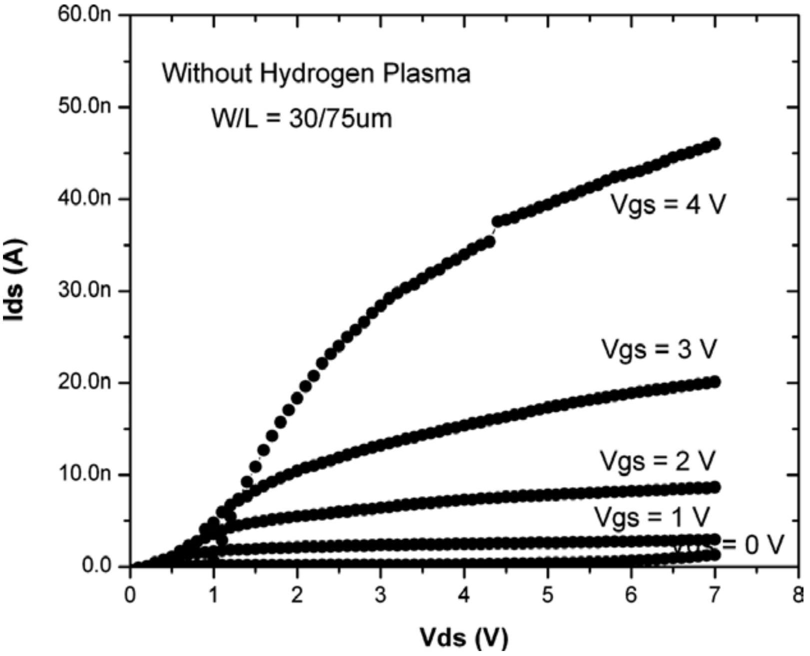

Figure 8. Output characteristics of TFTs with over-etching but without hydrogen plasma.

3.3. Planarization of the gate electrode in bottom-gate TFTs

Thin-film transistors are successfully employed in active-matrix displays [17]. In this application, the inverted staggered structure is the most used [17]. In an inverted structure, the gate electrode is placed at the bottom of the structure (bottom-gate structure). The advantage of using this inverted structure is that the gate electrode protects the active layer from backplane light. The problem is when the active-matrix displays become larger, the number of address lines must increase and the gate lines must be narrower and longer. To avoid an increase in the resistance of the gate line, which results in delay on the display performance, the gate line must be thicker. Then, the problem with this thicker gate is that the gate insulator tends to be thinner around the corners of the gate, increasing the leakage current and electric stress due to the high electric field at the corner [18]. In order to reduce these effects, the planarization of the gate electrode was proposed by other groups [19, 20].

As far as we know, the only work related to the study of the planarization of the gate electrode is conducted by Chen et al. [18]. They reported a reduction in the contact resistance attributed to the planarization process. However, this improvement in the contact resistance is difficult to understand, since the planarization of the gate electrode improves the insulator-semiconductor interface but not the metal-semiconductor interface. Firstly, the experimental characteristics of planarized and unplanarized TFTs are presented. After that using a physically based simulator (SILVACO), the main interfaces are analysed to understand the origin of this improvement.

The experimental transfer characteristics of unplanarized and planarized TFTs are shown in **Figure 9**. The planarized TFT shows a subthreshold slope ~0.45 V/DEC and ~0.49 V/DEC, for n-type and p-type regions, respectively, while on/off-current ratios around 10^5 were obtained for n-type and p-type regions. On the other hand, the unplanarized TFT shows a subthreshold slope ~1 V/DEC for an n-type region and 1.3 V/DEC for a p-type region, on/off-current ratios ~10^4 and 10^3 for n-type and p-type regions, respectively.

The threshold voltage and field-effect mobility were extracted from the transfer characteristics operating in the saturation regime ($V_{ds} = V_{gs}$), using Eq. (2). For planarized TFTs, the threshold voltage was 1.11 and −2.18 V for n-type and p-type regions, respectively. The extracted field-effect mobilities were 0.68 and 0.15 cm^2/Vs for n-type and p-type regions, respectively. For unplanarized TFTs, the threshold voltage was 2.4 and −3.35 V for n-type and p-type regions, respectively. The extracted field-effect mobilities were 0.11 cm^2/Vs for an n-type region and 0.02 cm^2/Vs for a p-type region.

Figure 10 shows the output characteristics for planarized and unplanarized TFTs. It is important to mention that the output characteristics show an ambipolar behaviour. A detailed discussion and modelling can be found in Ref. [14]. In the output characteristics of unplanarized TFTs, current crowding appears in the bias range from 0 to 1 V of V_{ds}. This high contact resistance effect slightly appears in planarized TFTs. To corroborate this effect, the contact resistance was extracted from the n-type region of both planarized and unplanarized TFTs. The contact resistance was extracted by the extrapolation of the width-normalized contact resistance as indicated in **Figure 1**. The contact resistance was approximately 1413 Ωcm for

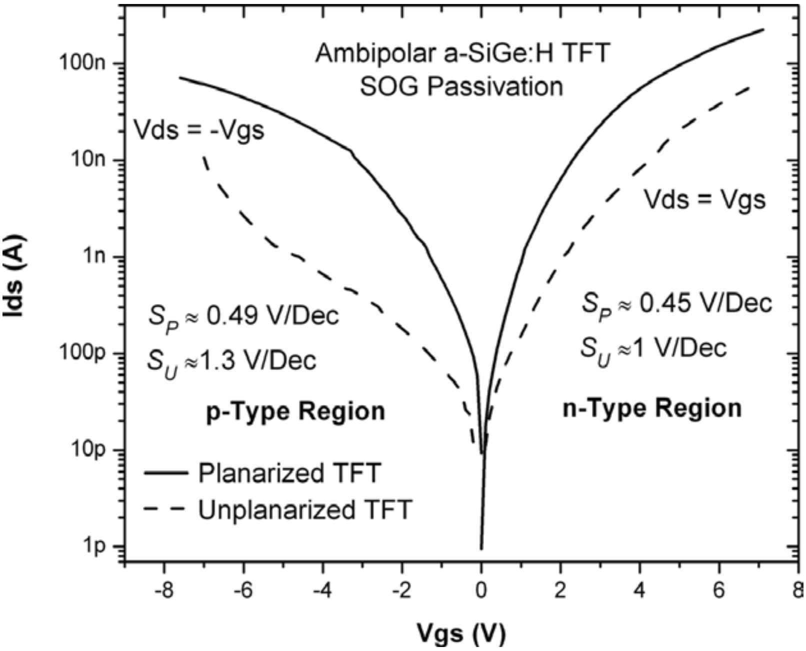

Figure 9. Transfer characteristics of unplanarized and planarized TFTs.

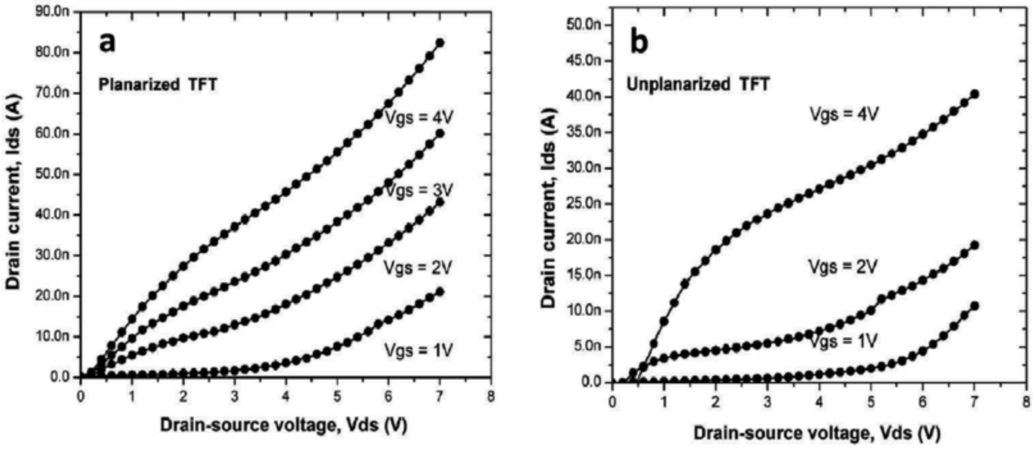

Figure 10. Output characteristics for planarized and unplanarized TFTs. a) Planarized and b) Unplanarized.

unplanarized TFTs and 589 Ωcm for planarized TFTs. This agrees with the higher values of drain current in planarized TFTs. It is important to note that subthreshold slope is improved in planarized TFTs. Some authors suggest a better injection of carriers from the source electrode into the active layer [21]. Also, other authors have reported a better subthreshold slope after improving the contact resistance [22, 23].

The experimental results agree with the reported previously by Chen et al. However, the improvement in contact resistance by the planarization process is unexplained. Using ATHENA, both planarized and unplanarized structures were simulated. Then, using ATLAS, electrical measurements were simulated. The cutline tool within the ATLAS simulator generates one-dimensional profiles from the insulator-semiconductor and metal-semiconductor interfaces. Ideal contacts were considered for source/drain contacts in both unplanarized and planarized simulated TFTs (ohmic contacts without contact resistance).

Figure 11 shows a comparison of the cross-section of planarized and unplanarized TFTs simulated by ATHENA. Applying a positive gate bias of 5 V, the electric field of the planarized and unplanarized gate electrodes was extracted by ATLAS (**Figure 12**). As expected, for the planarized TFT, the electric field is uniform through the insulator-semiconductor interface. However, for the unplanarized TFT, the electric field is not uniform through the insulator-semiconductor interface. There is an increase of the electric field due to the thinner gate insulator. This increase in the electric field causes an accumulation of electrons in the channel close to the corners of the gate, as shows **Figure 13**.

The difference of the electron concentration in the channel works as a scattering mechanism, limiting the mobility of the carriers. This can explain the lower extracted field-effect mobility in the unplanarized TFTs. Also, the variations of the electron concentration reflect an increase in the conduction band energy of the active layer close to the source/drain contacts, as show in **Figure 14**. This increase in energy acts as a barrier for the electrons, where only electrons with higher energy can pass the barrier. As result, the device contact resistance apparently

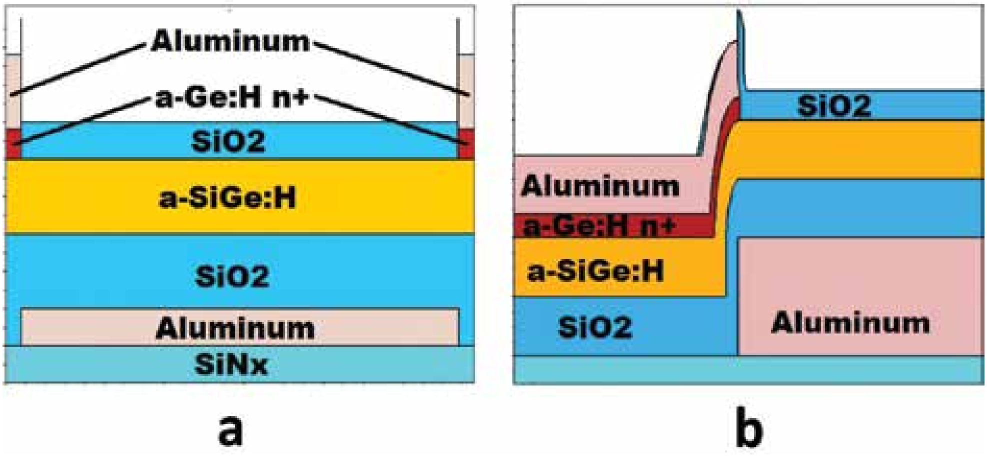

Figure 11. Cross-section of planarized and unplanarized TFTs simulated by ATHENA. a) Planarized and b) Unplanarized.

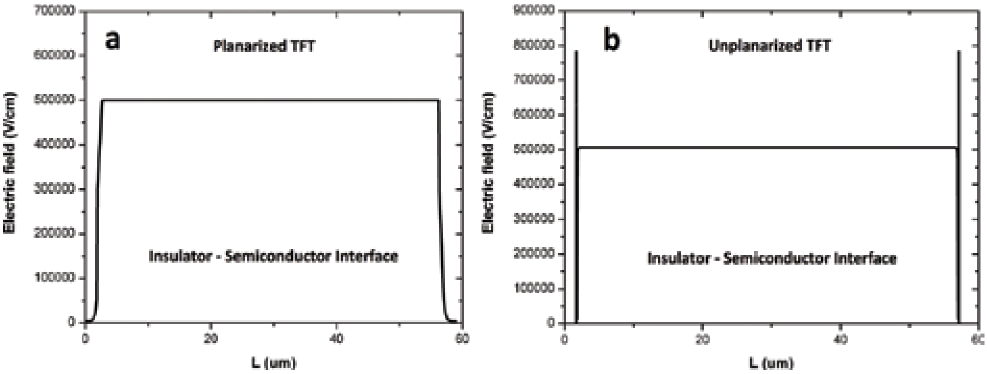

Figure 12. Electric field of the planarized and unplanarized TFTs simulated by ATLAS. a) Planarized and b) Unplanarized.

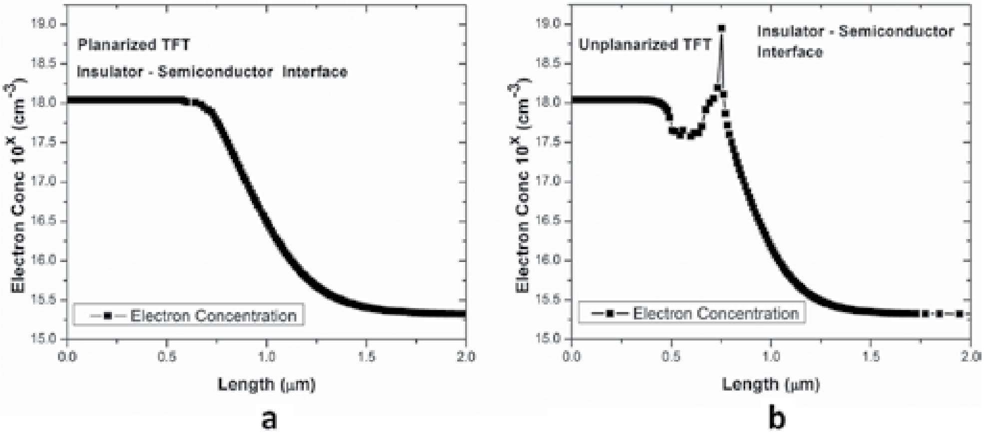

Figure 13. Accumulation of electrons in the channel close to the corners of the gate simulated by ATLAS. a) Planarized and b) Unplanarized.

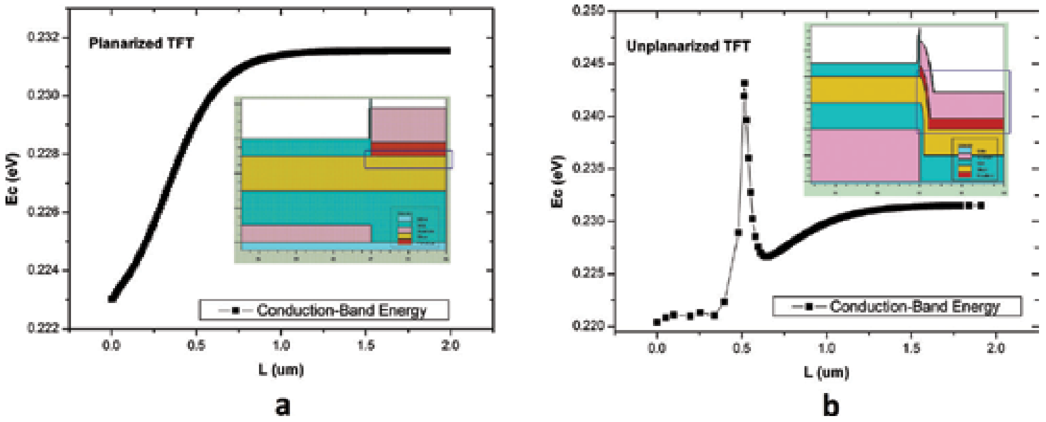

Figure 14. Conduction band energy of the active layer close to the source/drain contacts. a) Planarized and b) Unplanarized.

increases. To corroborate these assumptions, **Figure 15** shows the simulated output characteristics of both planarized and unplanarized TFTs. The simulation agrees with the behaviour exhibited in the experimental and simulated results.

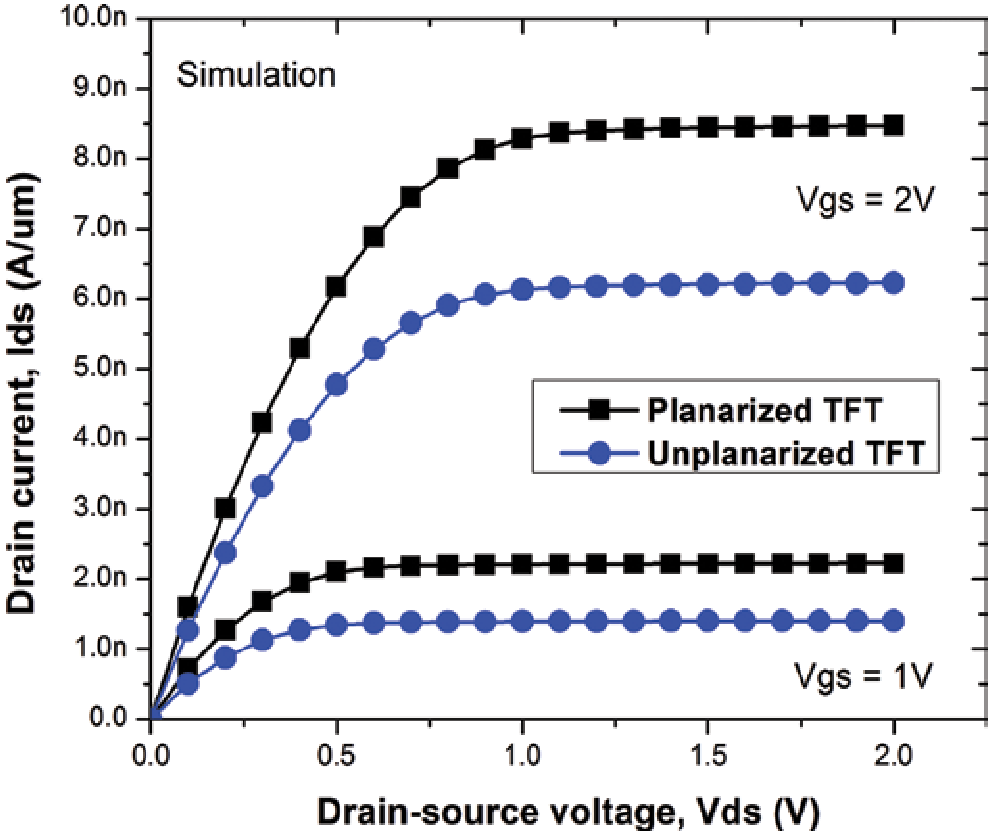

Figure 15. Simulated output characteristics of planarized and unplanarized TFTs.

4. Influence of metal-semiconductor interface on electrical stability of TFTs

Despite the high potential of TFTs to enable low-cost electronics, these devices have the disadvantage of threshold voltage shift after a prolonged application of gate bias stress. In a-Si TFTs, the threshold voltage shift mechanisms have been studied to estimate the long-term behaviour of TFT circuits. Because of the continuous growing application of novel material-based TFTs in electronics, an updated research for threshold voltage shift mechanisms is needed. The defect state creation in active layer and charge trapping in the gate dielectric is presumably the mechanisms responsible for the threshold voltage shift in TFTs. During the application of gate bias stress (or during normal operation), the charge trapping and defect state creation mechanisms occur simultaneously; therefore, the experimental results of threshold voltage shift do not provide any information about the quantitative effect of each of these mechanisms on the threshold voltage shift of the TFT. In addition, it has been proposed the relaxation of the threshold voltage after the annealing of the defect states in the active layer and the charge back tunnelling of trapped electrons inside the gate insulator [24–26]. However, the experimental published results for the relaxation of threshold voltage do not support the defect state annealing mechanism. While the estimations of charge trapping and de-trapping from gate insulator traps show a good agreement with the experimental threshold voltage relaxation. Therefore, from the threshold voltage shift mechanisms, charge trapping in the gate insulator is reversible [26–30].

On the other hand, the proposed mechanisms responsible for threshold voltage shift are directly related to the insulator-semiconductor interface. However, it has been also reported that quality of the metal-semiconductor interface strongly influences the kinetics of threshold voltage shift and relaxation of TFTs [31]. Based on the results reported for the charge trapping and defect state creation mechanisms of threshold voltage shift, a general conclusion cannot be drawn. The kinetics of the mechanisms strongly depends on the fabrication process of the TFTs. It is important to consider that deposition conditions of the active layer also affect the rate of the creation of the extra defect states in the active layer.

In this section, a comparison of the threshold voltage shift in TFTs with the same insulator-semiconductor interface but different metal-semiconductor interface is presented. The threshold voltage shift is calculated as a function of the stress time at gate bias stress of 20 V and $V_{ds} = 0$ V. These are the typical conditions for electrical stress in TFTs [32–36]. The complete fabrication procedure of the TFTs can be found elsewhere [14]. The gate insulator was deposited in two sets of devices using the same deposition conditions. After that the fabrication of the metal-semiconductor interface was different. In one set of devices, it was employed the over-etching and plasma processes described in Section 2.2. As passivation layer a silicon nitride film was used. On the other set of devices, the active layer and n+ contact region films were continuously deposited with no vacuum break in the chamber. As passivation layer a silicon oxide film was used. The schematic cross-section of the fabricated devices is shown in **Figure 16**.

Table 1 summarises the parameters extracted in both TFTs. Since both TFTs have identical insulator-semiconductor interface, the slight difference in values of subthreshold slope is

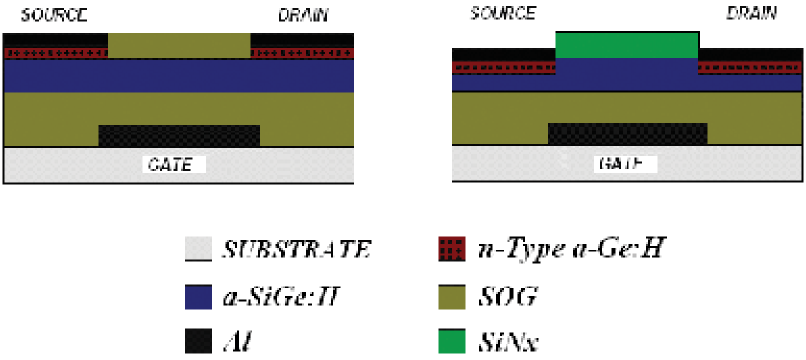

Figure 16. Schematic cross-section of the fabricated devices.

Parameter	TFT SiNx passivation (hydrogen plasma)	TFT SiO_2 passivation
SS	0.56 V/DEC	0.45 V/DEC
On/off-current ratio	10^6	$>10^5$
ΔV_T (6000 sec)	2.25 V	1.14 V
Field-effect mobility	0.85 cm^2/Vs	0.68 cm^2/Vs
Off-current	~0.3 pA	~0.95 pA

Table 1. Comparison of the parameters of the TFTs.

considered just statistical fluctuation. The values of off-current are of the same order of magnitude. The on/off-current ratio is very similar for both TFTs. However, an important difference in field-effect mobility is found. The mobility for TFTs using SiNx as a passivation layer (hydrogen plasma) was 0.85 cm^2/Vs, higher than the 0.68 cm^2/Vs for TFTs using SiO_2 passivation. This result is related to the metal-semiconductor interface, the higher value of mobility may indicate a lower contact resistance.

Figure 17 shows the threshold voltage shift ΔV_T as a function of the stress time. The figure shows a higher shift for TFTs using SiNx passivation. It is important to mention that the observed threshold voltage shift for both TFTs could not be recovered after a rest period of 48 hours and under the application of negative gate bias, suggesting that the shift is irreversible. Since the charge trapping in the gate insulator is reversible, therefore, under the applied gate bias conditions, the shift in the threshold voltage seems to be due to creation of defect states in the active layer.

The higher value of mobility results of a lower contact resistance, however, the higher instability of this TFT related to defect state creation suggests a dependency with the fabrication of the metal-semiconductor interface. Probably due to defects induced by the over-etching process. Also, the SiNx passivation layer may has influence on the electrical instability of the TFT. Further research is necessary to address these assumptions. Although both TFTs

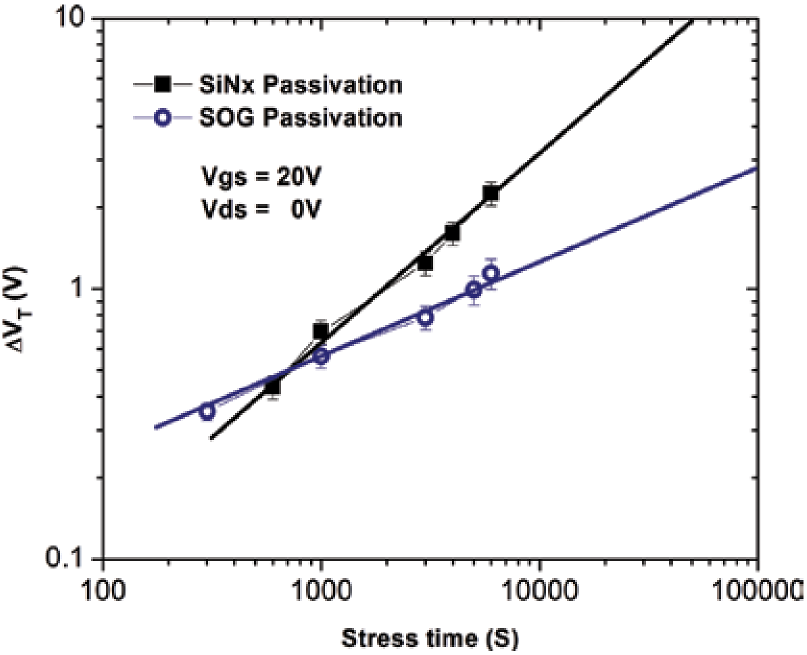

Figure 17. Threshold voltage shift ΔV_T as function of the stress time.

have the same insulator-semiconductor interface, the metal-semiconductor interface plays an important role in the electrical stability of these devices. The research of the kinetics of the mechanisms responsible for the instability on TFTs needs to be extensively explored for emergent TFT technologies.

5. Conclusions

In summary, some alternatives to improve the metal-semiconductor interface are analysed. An over-etching at the source/drain regions of the active layer can improve the TFT electrical performance, since this process gets close the n+ contact layer and the electron induced-channel. Moreover, the plasma-induced damage by the over-etching process is reduced after the application of a hydrogen plasma. On the other hand, the planarized TFTs exhibit better performance due mainly to the improved contact resistance. The simulations show an increase in the conduction band energy in the a-SiGe:H film at the metal-semiconductor interface. This increase acts as a barrier for the electrons, which results in an apparent increase of contact resistance. Finally, the influence of the metal-semiconductor interface in the electrical stability of TFTs is presented. Although the compared TFTs present the same insulator-semiconductor interface, the fabrication of the metal-semiconductor interface plays an important role in the electrical stability of these devices.

Acknowledgments

This work is partially supported by PRODEP-SEP, CONACyT-255062 and VIEP-BUAP-LULJ-EXC-2017.

Author details

Miguel Dominguez[1]*, Pedro Rosales[2], Alfonso Torres[2], Jose A. Luna-Lopez[1], Francisco Flores[1] and Mario Moreno[2]

*Address all correspondence to: madominguezj@gmail.com

1 Centro de Investigaciones en Dispositivos Semiconductores, Instituto de Ciencias, Benemérita Universidad Autónoma de Puebla (BUAP), Puebla, Mexico

2 Departamento de Electrónica, Instituto Nacional de Astrofísica, Óptica y Electrónica (INAOE), Puebla, Mexico

References

[1] Dominguez M, Pau J, Gómez M, Luna J, Rosales P. High mobility thin film transistors based on zinc nitride deposited at room temperature. Thin Solid Films. 2016;**619**:261-264

[2] Jeong J, Chung H, Mo Y, Kim H. Comprehensive study on the transport mechanism of amorphous indium-gallium-zinc oxide transistors. Journal of the Electrochemical Society. 2008;**155**:H873-H877

[3] Valletta A, Fortunato G, Mariucci L, Barquinha P, Martins R, Fortunato E. Contact effects in amorphous InGaZnO thin film transistors. Journal of Display Technology. 2014;**10**(11):956-961

[4] Dominguez M, Alcantara S, Soto S. Physically-based simulation of zinc oxide thin-film transistors: Contact resistance contribution on density of states. Solid-State Electronics. 2016;**120**:41-46

[5] Dominguez M, Flores F, Luna A, Martinez J, Luna-Lopez J, Alcantara S, Rosales P, Reyes C, Orduña A. Impact of active layer thickness in thin-film transistors based on zinc oxide by ultrasonic spray pyrolysis. Solid State Electronics. 2015;**109**:33–36

[6] Yabuta H, Sano M, Abe K, Aiba T, Den T, Kumomi H, Nomura K, Kamiya T, Hosono H. High-mobility thin-film transistor with amorphous In Ga Zn O 4 channel fabricated by room temperature rf-magnetron sputtering. Applied Physics Letters. 2006;**89**:112123

[7] Wang W, Li L, Lu C, Liu Y, Lv H, Xu G, Ji Z, Liu M. Analysis of the contact resistance in amorphous InGaZnO thin film transistors. Applied Physics Letters. 2015;**107**:063504

[8] Hur I, Bae H, Kim W, Kim J, Jeong H, Jo C, Jun S, Lee J, Kim Y, Kim D, Kim D. Characterization of intrinsic field-effect mobility in tfts by de-embedding the effect of parasitic source and drain resistances. IEEE Electron Device Letters. 2013;**34**(2):250-252

[9] Mativenga M, An S, Lee S, Um J, Geng D, Mruthyunjaya R, Heiler G, Tredwell T, Jang J. Intrinsic channel mobility of amorphous, In–Ga–Zn–O thin-film transistors by a gated four-probe method. IEEE Transactions on Electron Devices. 2014;**61**(6):2106-2112

[10] Jun S, Bae H, Kim H, Lee J, Choi S, Kim D, Kim D. Dual-sweep combinational transconductance technique for separate extraction of parasitic resistances in amorphous thin-film transistors. IEEE Electron Device Letters. 2015;**36**(2):144-146

[11] Dominguez M, Rosales P, Torres A, Flores F, Luna J, Alcantara S, Moreno M. Impact of planarized gate electrode in bottom-gate thin-film transistors. Rev. Mex. Fis. 2016; **62**:223–228

[12] Wu J, Lin H, Su B, Chen Y, Chu S, Liu S, Chang C, Wu C. Comparison of physical and electrical properties of GZO/ZnO buffer layer and GZO as source and drain electrodes of a-IGZO thin-film transistors. Journal of Alloys Compound. 2014;**592** :35-41

[13] Le Comber P, Spear W. Substitutional doping of amorphous silicon. Solid State Communications. 1975;**17**(9):1193-1196

[14] Dominguez M, Rosales P, Torres A, Flores F, Molina J, Moreno M, Luna J, Orduña A. Planarized ambipolar a-SiGe:H thin-film transistors: Influence of the sequence of fabrication process. Solid-State Electronics . 2014;**99** :45-50

[15] Dominguez M, Rosales P, Torres A. Performance improvement of low-temperature a-SiGe:H thin-film transistors. Solid State Electronics. 2012;**76**:44-47

[16] Kazmerski L. Polycrystalline and Amorphous Thin Films and Devices. 1st ed. Academic Press, New York; 1980

[17] Kanicki J, Martin S. Hydrogenated amorphous Silicon. In: Kagan C, Andry P, editors. Thin Film Transistors. 1st ed. Marcel Dekker Inc., New York; 2003

[18] Chen M, Chou J, Lee S. Planarization of amorphous silicon thin film transistors by liquid phase deposition of silicon dioxide. IEEE Transactions on Electronic Devices. 1995;**42**(11):1918-1923

[19] Cheon J, Bae J, Jang J. Inverted staggered poly-si thin-film transistor with planarized SOG gate insulator. IEEE Electron Device Letters. 2008;**29**(3):235-237

[20] Lan J, Kanicki J. Planarized copper gate hydrogenated amorphous-silicon thin-film transistors for AM-LCDs. IEEE Electron Device Letters. 1999;**20**(3):129-131

[21] Chen F, Lin Y, Chen T, Kung L. Efficient hole-injection in highly transparent organic thin-film transistors. Electrochemical and Solid-State Letters. 2007;**10**(6):H186-H188

[22] Bürgi L, Richards T, Friend R, Sirringhaus H. Close look at charge carrier injection in polymer field-effect transistors. Journal of Applied Physics. 2003;**94**(9):6129-6137

[23] Han D, Kang Y, Park J, Jeon H, Park J. Influence of molybdenum source/drain electrode contact resistance in amorphous zinc–tin-oxide (a-ZTO) thin film transistors. Materials Research Bulletin. 2014;**58**:174-177

[24] Jackson W. Role of band-tail carriers in metastable defect formation and annealing in hydrogenated amorphous silicon. Physical Review B. 1990;**41**:1059

[25] Libsch F, Kanicki J. Bias-stress-induced stretched-exponential time dependence of charge injection and trapping in amorphous thin-film transistors. Applied Physics Letters. 1993;**62**:1286

[26] Powell M, Berkel C, French I, Nicholls D. Bias dependence of instability mechanisms in amorphous silicon thin-film transistors. Applied Physics Letters 1987;**51**:1242-1244

[27] Subramaniam A, Cantley K, Stiegler H, Chapman R, Vogel E. Submicron ambipolar nanocrystalline silicon thin-film transistors and inverters. IEEE Transactions on Electronic Devices. 2012;**59**:359-366

[28] Yang Z, Yang J, Meng T, Qu M, Zhang Q. Influence of channel layer thickness on the stability of amorphous indium zinc oxide thin film transistors. Materials Letters 2016; **166**:46-50

[29] Cross R, De Souza M. Investigating the stability of zinc oxide thin film transistors. Applied Physics Letters. 2006;**89**:263513

[30] John F, Conley J. Instabilities in amorphous oxide semiconductor thin-film transistors. IEEE Transactions on Device Materials Reliability. 2010;**10**:460-474

[31] Akhavan A. Threshold Voltage Instability and Relaxation in Hydrogenated Amorphous Silicon Thin Film Transistors [thesis]. Canada: University of Waterloo; 2005.

[32] Wahl R, Wang F, Chung H, Kunnen G, Yip S, Lee E, Pun E, Raupp G, Allee, D. Stability and low-frequency noise in InAs NW parallel-array thin-film transistors. IEEE Electron Device Letters. 2013;**34**:765-767

[33] Jeon J, Kim J, Ryu M. Instability of an amorphous indium gallium zinc oxide TFT under bias and light illumination. Journal of the Korean Physical Society. 2011;**58**:158-162

[34] Jeong Y, Bae C, Kim D, Song K, Woo K, Shin H, Cao G, Moon J. Bias-stress stable solution-processed oxide thin film transistors. ACS Applied Materials And Interfaces. 2010;**2**:611-615

[35] Jeng J. Improvement of transistor characteristics and stability for solution processed ultra-thin high-valence niobium doped zinc-tin oxide thin film transistors. Journal of Alloys and Compounds. 2016;**676**:86-90

[36] Xu H, Xu M, Chen Z, Li M, Zou J, Tao H, Wang L, Peng J. Improvement of mobility and stability in oxide thin-film transistors using triple-stacked structure. IEEE Electron Device Letters. 2016;**37**:57-59

Section 4

Organic Field-Effect Transistors

Chapter 7

Organic Field-Effect Transistor: Device Physics, Materials, and Process

Jingjing Chang, Zhenhua Lin, Chunfu Zhang and
Yue Hao

Additional information is available at the end of the chapter

http://dx.doi.org/10.5772/intechopen.68215

Abstract

Organic field-effect transistors have received much attention in the area of low cost, large area, flexible, and printable electronic devices. Lots of efforts have been devoted to achieve comparable device performance with high charge carrier mobility and good air stability. Meanwhile, in order to reduce the fabrication costs, simple fabrication conditions such as the printing techniques have been frequently used. Apart from device optimization, developing novel organic semiconductor materials and using thin-film alignment techniques are other ways to achieve high-performance devices and functional device applications. It is expected that by combining proper organic semiconductor materials and appropriate fabrication techniques, high-performance devices for various applications could be obtained. In this chapter, the organic field-effect transistor in terms of device physics, organic materials, device process, and various thin-film alignment techniques will be discussed.

Keywords: organic field-effect transistors, device physics, organic semiconductor materials, device process, thin-film alignment

1. Introduction

Organic field-effect transistors (OFETs) have received much attention for plastic electronics due to their good solution processability, low temperature deposition, low cost, and compatibility with large-area printing technology. Although the conventional amorphous silicon-based semiconductors have achieved much progress with charge carrier mobility around 1.0 cm^2 V^{-1} s^{-1}, the thin-film deposition of conventional semiconductor usually needs high temperature process and dustless conditions which significantly increase the fabricating cost. Most importantly, the silicon-based materials are rare to be processed on flexible substrates due to their poor stretching characteristics. Nevertheless, compared to the conventional silicon-based semiconductors, the organic-based semiconductors exhibit low cost, good processibility and can be fabricated on

INTECH
open science | open minds

© 2017 The Author(s). Licensee InTech. This chapter is distributed under the terms of the Creative Commons Attribution License (http://creativecommons.org/licenses/by/3.0), which permits unrestricted use, distribution, and reproduction in any medium, provided the original work is properly cited.

flexible substrates. Hence, using organic semiconducting materials has become an important topic in the development of low-cost, large area, flexible, and lightweight devices.

Organic-based semiconductors have various applications as key components of numerous electronic and optoelectronic devices, including field-effect transistors (FETs), photovoltaics (PVs), and light-emitting diodes (LED). Especially for the field-effect transistor, a lot of efforts have been done to develop new organic materials to improve device performance with high charge carrier mobility and good air stability. Anyhow, OFETs have been considered as a key component of organic integrated circuits for application in flexible smart cards, low-cost radio frequency identification (RFID) tags, sensor devices, organic active matrix displays, and so on [1–6]. However, it is still far from satisfactory for practical applications. The focus of recent attention has been devoted to improving device performance and stability, reducing the fabrication cost, exploring new applications, and developing simple fabrication techniques. Overcoming these challenges relies on the novel organic semiconductor development and device optimization.

In this chapter, organic field-effect transistors will be discussed from three aspects: the device physics, device materials, and device processing. The first section will talk about the charge transport and related mechanisms in organic semiconductor materials and the techniques used to characterize the charge carrier mobility, such as time of flight, field-effect transistor, and space-charge limited current (SCLC) technique. In the second section, we discuss the organic field-effect transistor from basic principle, device structure, and the main parameters, such as charge carrier mobility, current on/off ratio, threshold voltage, subthreshold voltage, and the corresponding influence factors in the OFET. The third section will talk about the organic materials selection, including mostly used aromatic p-type semiconductors and n-type semiconductors. The forth section will discuss the fabrication techniques in the organic field-effect transistors, including vapor deposition, solution deposition, and some thin-film alignment methods.

2. Device physics

2.1. Charge transport and related mechanisms

The study of electron and hole transport in organic materials has a long history which dates back to 60 years ago. Many groups have done their efforts on this topic. In the mid-1970s, Scher group laid the theoretical description of hopping transport in disordered materials by using the continuous-time random walk model [7]. Until today, the exact nature of charge transport in organic semiconductors is still open to debate. However, a general idea can be obtained using the disordered semiconductors and highly ordered organic single crystals as the standards. In organic semiconductors, the charge carrier transport mechanism depends on the degree of order and falls between the band and hopping transport which are the two extreme transport cases. Typically, band transport could be observed in highly purified molecular crystals at low temperatures. However, the bandwidth in organic semiconductors is smaller than that in inorganic semiconductors (typically a few kT at room temperature only) due to the weak electronic delocalization [8]. Hence, the mobility value in molecular single crystals at room temperature reaches only in the range from 1 to 10 $\mathrm{cm}^2\ \mathrm{V}^{-1}\ \mathrm{s}^{-1}$. In the other extreme case of an amorphous organic solid, hopping transport prevails, which leads to much lower mobility values (at best around $10^{-3}\ \mathrm{cm}^2\ \mathrm{V}^{-1}\ \mathrm{s}^{-1}$).

When localization occurs in conjugated organic materials, the polarons resulting from the conjugated chain deformation under the charge action could be formed (or the charge is self-trapped by the deformation) [9]. This mechanism of self-trapping is often described through the creation of localized states in the gap between the valence and the conduction bands.

To better understand the charge transport in organic materials, a one-dimensional, one-electron model, the small polaron model, has been developed by Holstein [9]. In this model, the electron-electron interactions are assumed to be neglected, and the lattice energy, electron dispersion energy, and the polaron banding energy are the three terms which constitute the total energy of the system [9].

The charge carrier mobility is temperature and field dependence. For temperature-dependent mobility, when the mobility is extrapolated at the zero-field limit, the Monte Carlo (MC) fitting results lead to the following expression:

$$\mu(T) = \mu_0 \exp\left[-\left(\frac{T_0}{T}\right)^2\right] \tag{1}$$

where μ_0 is the mobility at room temperature and T_0 is the room temperature. Since the temperature helps in overcoming the barriers introduced by the energetic disorder in the system, the temperature talked about here only depends on the amplitude of the diagonal disorder width. This expression deviates from an Arrhenius-like law, and this expression generally fits the experimental data well, as a result of the limited range of temperatures available.

The impact of an external electric field is to lower the energy barrier for the electron conduction band transport since part of this energy could be provided by the driving force of the electric field. In the presence of energetic disorder only, the Monte Carlo results generally yield a Poole-Frenkel behavior when electric fields are larger than 10^4–10^5 V/cm:

$$\mu(E) = \mu_0 \exp(\beta\sqrt{E}) \tag{2}$$

where μ_0 is the low field mobility, β is Poole-Frenkel coefficient, and E is the applied electric field [10]. The field dependence becomes more pronounced as the extent of energetic disorder grows. The increase in electric field amplitude is also accompanied by an increased diffusion constant.

2.2. Characterization of charge carrier mobility

Charge carrier mobility can be determined by various techniques [11, 12]. The mobility measured by the methods with the measurement over macroscopic scales (~1 mm) is often dependent on the material order and purity. Instead, when the mobility measurement is over microscopic scales, the measurement result is less dependent on these characteristics. In this section, the basic principle of most used mobility measurement techniques, time-of-flight (TOF), field-effect transistor (FET), and space-charge limited current (SCLC) will be briefly described.

2.2.1. *Time-of-flight (TOF)*

For the TOF measurement, a few micron thick organic active layer is sandwiched between two metal electrodes (**Figure 1**). As shown in **Figure 1**, first, the material is irradiated to generate charges by a laser pulse near one electrode. Then, the photo-generated holes or electrons migrate across the material toward another electrode depending on the polarity of the applied bias and the corresponding electric field (in the 10^4–10^6 V/cm range). After that, the current at that electrode is recorded as a function of time. Finally, for ordered materials, a sharp signal will be obtained, while for disordered systems, a broadening of the signal will occur because of the distribution of transient times across the material. The hole or electron mobility is estimated via the following equation:

$$\mu = \frac{v}{F} = \frac{d}{Ft} = \frac{d^2}{Vt} \tag{3}$$

where d is the distance between the electrodes, F is the electric field, t is the averaged transient time, and V is the applied voltage. TOF measurements clearly show the impact of structural defects present in the material on charge carrier mobility. Charge carrier mobilities in organic materials were first measured with the TOF technique by Kepler [13] and Leblanc [14].

2.2.2. *Field-effect transistor (FET) configuration*

The electrical characteristics measured in a field-effect transistor (FET) configuration could also be used to extract the charge carrier mobilities (**Figure 2**). As previously Horowitz talked about [15], the derived current-voltage expressions for inorganic-based transistors in both

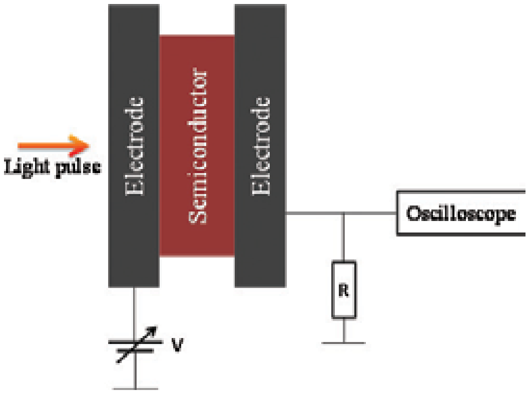

Figure 1. The setup of the TOF technique.

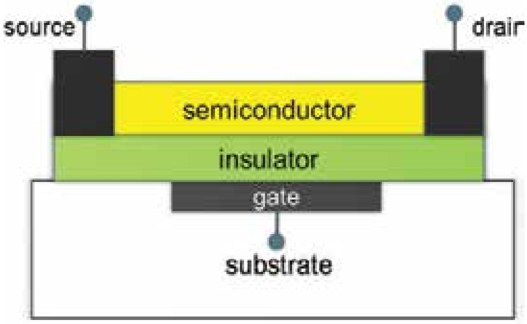

Figure 2. The structure of thin-film transistor.

linear and saturated regimes are also applicable to organic field-effect transistors (OFETs). These expressions in the linear regime are:

$$I_{DS} = \frac{W}{L} C_i \mu (V_G - V_T) V_D, V_D < V_G - V_T, \tag{4}$$

and in the saturated regime:

$$I_{DS} = \frac{W}{2L} C_i \mu (V_G - V_T)^2, V_D > V_G - V_T. \tag{5}$$

Here, I_{DS} and V_{DS} are the current and voltage bias between source and drain, respectively, V_G denotes the gate voltage, V_T is the threshold voltage, C_i is the capacitance of the gate dielectric, and W and L stand for the width and length of the conducting channel, respectively. In FETs, the charges migrate at the interface between the organic semiconductor and the dielectric within a few nanometer-wide channel [16, 17]. There are several factors that affect the charge transport, such as structural defects at the interface within the organic layer, the dielectric surface morphology and polarity, and the traps existing at the interface (that depends on the chemical structure of the gate dielectric surface). Contact resistances at the source and drain metal/organic interfaces also play significantly important roles, and when the channel length decreases and the transistor operates at low fields, it becomes more important. Anyhow, its effect can be accounted for via four-probe measurements [18].

The charge carrier mobilities extracted from the FET current-voltage curves in the saturated regime are generally higher than those in the linear regime due to different electric-field distributions. The mobility was found to be gate-voltage dependent [19], and it is often related to the presence of traps which is usually caused by structural defects and/or impurities and/or charge carrier density (which is modulated by V_G) [20].

The dielectric constant of the gate insulator is another important parameter. For instance, measurements on rubrene single crystals [21] and polytriarylamine chains [22] show that the charge carrier mobility decreases with the increased dielectric constant because of polarization effects across the interface. At the dielectric surface, the polarization induced by the charge carriers within the conducting channel of organic semiconductors couples to the carrier motion, which can be cast in the form of a Frolich polaron [23, 24].

2.2.3. Space-charge limited current (SCLC)

The mobilities can also be extracted from the electrical characteristics measured in a diode configuration with an organic layer sandwiched between two metal electrodes (**Figure 3**). In this case, we are assuming that carrier transport is bulk limited instead of contact limited. The electrode is chosen in such a way that at low voltage, only electrons or holes are injected. In the absence of traps and at low electric fields, the behavior of the current density J quadratically scaling with applied bias V is a space-charge limited current (SCLC) characteristic, and it corresponds to the current obtained when the number of injected charges reaches a maximum because their electrostatic potential prevents the injection of additional charges [25]. In this case, the charge density is maximum approaching the injecting electrode instead of uniform across the material [26]. In this regime, when diffusion contributions are neglected, we can describe J-V characteristics as:

$$J = \frac{9}{8}\varepsilon_0\varepsilon_r\mu\frac{V^2}{d^3} \tag{6}$$

where ε_r is the dielectric constant of the active layer and d denotes the device thickness. (Note that at high electric fields, it has to consider a field-dependence of the mobility.) With the presence of traps, the J-V curves become more complex. First, a linear regime with injection-limited transport is exhibited in the J-V curves. Then, a sudden increase occurs in the intermediate range of applied biases. Finally, the V^2 dependence of the trap-free SCLC regime is reached. The extent of the intermediate region is governed by the spatial and energetic distribution of trap states, which is generally modeled by a Gaussian [27] or exponential distribution [28].

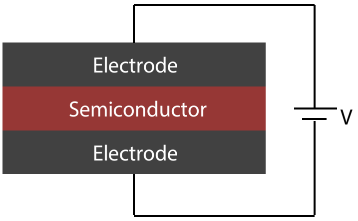

Figure 3. The structure of a SCLC-based device.

3. Organic field-effect transistors

3.1. Basic principles of field-effect transistors

In 1962, Weimer first introduced the concept of the thin-film transistor (TFT) [29]. This structure is well adapted to low conductivity materials and is currently used in amorphous silicon transistors. As shown in **Figure 2**, ohmic contacts are formed directly between the source and drain electrodes with conducting channel. Compared with the metal-insulation-semiconductor field-effect transistor (MISFET) structure, there are two crucial differences in the TFT structure. First, the depletion region to isolate the device from the substrate is absent. Second, instead of the inversion regime, the TFT operates in the accumulation regime although it is an insulated gate device. As a result, it should be especially careful when transferring the drain current equations from the MISFET to the TFT. In fact, the absence of a depletion region leads to a simplification of the equation as the following [30]:

$$I_d = \frac{W}{L} C_i \mu \left(V_G - V_T - \frac{V_D}{2} \right) V_D \tag{7}$$

Here, the threshold voltage is the gate voltage, and the channel conductance (at low drain voltages) is equal to that of the whole semiconducting layer.

3.2. Important parameters in OFET

3.2.1. Mobility

The FET *J*-*V* characteristics in different operating regimes can be analytically expressed by the gradual channel approximation assumption which means that the electric field parallel to the current flow generated by the drain voltage is much smaller compared with the field perpendicular to the current flow created by the gate voltage [30, 31].

In the linear regime, the drain current is directly proportional to V_G, and the field-effect mobility in the linear regime (μ_{lin}) can be extracted from the gradient of I_D versus V_G at constant V_D.

$$I_D = \frac{W}{L} C_i \mu \left(V_G - V_T - \frac{V_D}{2} \right) V_D, V_D < V_G - V_T \tag{8}$$

In the saturation regime, the channel is pinched off when $V_D = V_G - V_T$. The current cannot increase anymore and saturates. The square root of the saturation current is directly proportional to the gate voltage.

$$I_{Dsat} = \frac{W}{2L} C_i \mu (V_G - V_T)^2, V_D > V_G - V_T \tag{9}$$

$$\sqrt{I_{Dsat}} = \sqrt{\frac{W}{2L} C_i \mu} (V_G - V_T) \tag{10}$$

Eq. (10) predicts that plotting the square root of the saturation current against gate voltage would result in a straight line. The mobility is obtained from the slope of the line, while the threshold voltage corresponds to the extrapolation of the line at zero current. However, in the saturation regime, the density of charge varies largely along the conducting channel, from a maximum near the source electrode to practically zero at the drain electrode. Hence, the mobility in organic semiconductors largely depends on various parameters, including the density of charge carriers. Meanwhile, in the saturation regime, the mobility is not constant along the channel and the extracted value only represents a mean value. Therefore, it is often more rational to extract the mobility in the linear regime, in which the density of charge is more uniform. This is usually done through the transconductance g_m, which follows from the first derivative of Eq. (3) with respect to the gate voltage [30].

$$g_m = \frac{\partial I_D}{\partial V_G} = \frac{W}{L} C_i \mu V_D \tag{11}$$

This equation assumes that the mobility is gate voltage independent. However, the mobility is actually gate voltage dependent. In this case, an extra term $\partial\mu/\partial V_G$ should be involved in Eq. (5), so that this method is only applicable when the mobility varies slowly with the gate voltage [30]. Moreover, this method is very sensitive to the charge injection limitation and retrieval at source and drain electrodes.

3.2.2. *Current on/off ratio*

The current on/off ratio is another important FET parameter that can be extracted from the transfer characteristics. It is the ratio of the drain current in the on-state (at a particular gate voltage) and the drain current in the off-state (I_{on}/I_{off}). For best performing behavior of the transistor, this value should be as large as possible. When neglected the contact resistance effects at the source-drain electrodes, the on-current mainly depends on the mobility of the semiconductor and the capacitance of the gate dielectric. The off-current is mainly determined by gate leakage current. It can be increased for unpatterned gate electrodes and semiconductor layers due to the conduction pathways at the substrate interface and the bulk conductivity of the semiconductor. Moreover, the unintentional doping could also increase the off-current [31].

3.2.3. *Threshold voltage*

Threshold voltage originates from several effects and strongly depends on the organic semiconductor and dielectric used. Generally speaking, the threshold voltage could be caused by interface states, charge traps, built-in dipoles, impurities, and so on [31, 32]. And it can be reduced by increasing the gate capacitance, which induces more charges at lower applied voltages. In many cases, the threshold voltage is not always constant for a given device. The V_{th} tends to increase when organic transistors are operated under an extended time scale. This is called bias stress behavior, and it has a significant effect on the applicability of organic transistors in electric circuits and real applications. And thus is presently under intense investigation [33, 34]. A current hysteresis could be caused by the shift of the threshold voltage on the time scale of current-voltage measurements. Large stable threshold shifts, for example, induced by polarization of a ferroelectric gate dielectric, can be used in organic memory devices.

4. Organic semiconductor materials

The mobilities of organic semiconductors have achieved significant progress in OFETs from the initially reported 10^{-5} cm^2 V^{-1} s^{-1} for polythiophene in 1986 [35] to 10 cm^2 V^{-1} s^{-1} for present diketopyrrolopyrrole (DPP)-based polymers [36]. The high mobility of organic semiconductors over conventional amorphous silicon indicates large potential application of organic electronic devices. The remarkable progress of organic semiconductors provides a road for organic electronic industry. Generally, for high-performance organic semiconductors, some critical factors, such as molecular structure, molecular packing, electronic structure, energy alignment, and purity, play important roles. Among them, tuning the molecular packing is especially important for high-performance semiconductors since the charge carrier transport is along the molecular π orbitals. Hence, the overlap degree of neighboring molecular orbitals significantly determines the charge carrier mobility. Molecular packing with strong intermolecular interactions is favorable for efficient charge transport and high field-effect mobility. The electronic structure and energy levels are crucial for the materials and device stability. In order to obtain the high-performance and stable organic semiconductors, structural modification with electron donors and acceptors are necessary. Except the above talked aspects, the film morphologies such as grain boundaries also could affect the charge carrier transport. The grain boundaries and disordered domains could hamper the efficient intermolecular charge hopping between them. Hence, increasing the crystal grain size and film uniformity could efficiently improve the charge transport and mobility. In this section, we introduce some feature compounds with mobility of/over amorphous silicon and/or with high stability.

4.1. P-type semiconductors

In the last two decades, p-type semiconductor materials have achieved much progress because of their simple design and synthetic approach. P-type organic semiconductors mainly contain acene, heteroacene, thiophenes, as well as their correlated oligomers and polymers, and two-dimensional (2D) disk-like molecules. Several comprehensive reviews have given detailed information about these compounds [32, 36]. Among them, the polycyclic aromatic hydrocarbons are most representative of the class of compounds due to their unique features. Some representative p-type semiconductors are shown in **Chart 1**.

Pentacene (**1**), as the benchmark of organic semiconductors, was first reported in 1970s, but the numerous OFET applications were only conducted recently [37, 38]. With strong intermolecular interactions and herringbone packing motif, pentacene exhibits efficient charge transport. Hence, polycrystalline thin film of pentacene (**1**) and tetracene (**2**) showed surprisingly high mobility approaching 0.1 cm^2 V^{-1} s^{-1} [37] and 3.0 cm^2 V^{-1} s^{-1} [39], respectively. The substituted tetracene derivative rubrene (**3**) showed the highest charge carriers mobility with 20 cm^2 V^{-1} s^{-1} for single crystal device in the FET configuration [40]. This implies that the conjugated acene is a good building block for the p-type semiconductors. Later on, phthalocyanines (**4**) and more core-extended hexa-*peri*-benzocoronenes (HBC) (**5**) containing two-dimensional (2D) aromatic core were reported and showed typically discotic columnar liquid crystalline phases. As a result, the HBC showed enhanced mobility along the column due to the solid-state organization. Moreover, HBC-based OFETs by zone casting method exhibited a high mobility up to 0.01 cm^2 V^{-1} s^{-1} [41]. The chemistry based on acene has paved the way for designing efficient p-type semiconducting materials.

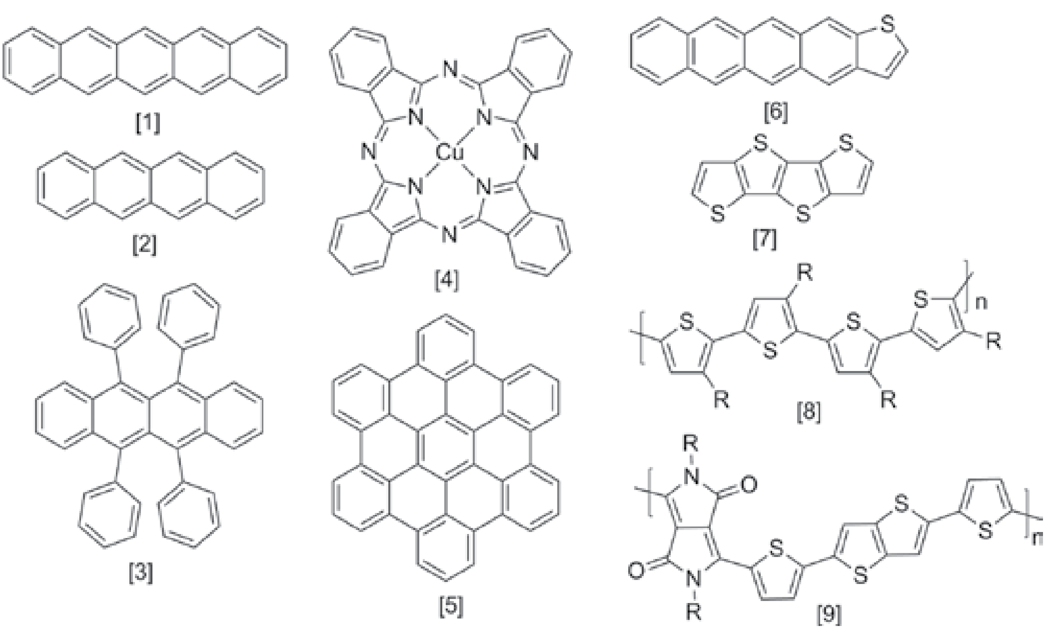

Chart 1. Chemical structures of some p-type semiconducting materials.

The sulfur containing heteroacenes and their derivatives constitute another large group of p-type aromatic hydrocarbons, as shown in **Chart 1**. The thienoacenes and their derivatives were also synthesized and investigated as semiconductors for p-type materials. The asymmetric oligoacene, such as the tetraceno-thiophene (**6**), was also synthesized and showed similar mobility (0.3 $cm^2 V^{-1} s^{-1}$) compared to their centrosymmetric counterparts processed in the same conditions [42]. The tetrathienoacene (**7**) with aryl groups had a higher mobility up to 0.14 $cm^2 V^{-1} s^{-1}$ by vapor deposition [43]. The sulfur-sulfur interaction in the packing motif was believed to enhance the charge carrier transport. The introduction of sulfur and other heteroatoms induced different energy alignments and crystal packing, which promotes the development of p-type materials.

Among the p-type polymers, poly(3-hexylthiophene) (P3HT) (**8**) has been studied extensively and showed high mobility due to its good crystalline properties and well-ordered lamella structure which facilitates the efficient charge transport [44]. And it has been widely used as electron donor in organic solar cells. DPP-based polymers, such as PDDPT-TT (**9**), have been shown as high-performance semiconductor materials with hole mobility over 10 $cm^2 V^{-1} s^{-1}$. Moreover, the device exhibited excellent shelf life and operating stabilities under ambient conditions. Finally, exceptionally high-gain inverters and functional ring oscillator devices on flexible substrates have been demonstrated [45, 46].

4.2. N-type semiconductors

Although the p-type semiconductor materials have achieved much progress, the development of n-type organic semiconductors still lags behind that of p-type organic semiconductors due to low device performance, ambient instability, and complex synthesis. Owing to their important roles in organic electronics, such as p-n junctions, bipolar transistors, and complementary circuits, it is desirable to develop stable n-type semiconductor materials with high charge carrier mobility for organic field-effect transistors.

To date, n-type organic semiconductors with high mobility are relatively rare and significantly lagging behind p-type semiconductors, and most of the n-type materials are still air unstable in ambient conditions due to its high lowest unoccupied molecular orbital (LUMO) energy level. De Leeuw et al. reasoned that the air unstable problem is due to redox reaction with oxygen and water [47]. Based on this result, we can calculate the LUMO energy level and it should be lower than -3.97 eV in order to be stable toward water and oxygen. N-type organic semiconductors mainly contain halogen or cyano-substituted n-type semiconductors that could be converted from p-type materials, perylene derivatives, naphthalene derivatives, fullerene-based materials, and so on (**Chart 2**).

The important n-type semiconductor material perfluoropentacene (**11**) was first reported by Sakamoto et al. [48]. This molecule adopted similar crystal packing to pentacene, and transistors fabricated from vacuum-deposited films showed a high mobility up to 0.11 $cm^2\ V^{-1}\ s^{-1}$ and an on/off ratio of 10^5. It was thought that attaching fluorine atoms could lower the LUMO energy level of this compound. However, the LUMO energy level is not low enough to make the OFET device stable in the ambient condition. Similarly, the 2,5,8,11,14,17-hexafluoro-hexa-*peri*-hexabenzocoronene was synthesized by Kikuzawa et al. from hexakis(4-fluorophenyl)-benzene [49]. This fluorinated compound was also suitable for the fabrication of n-channel transistors due to the decreased LUMO energy level, showing a mobility of 1.6×10^{-2} $cm^2\ V^{-1}$ s^{-1} and an on/off ratio of 10^4. Based on these results, they showed that the halogen substitution is a proper way to obtain n-type semiconductors.

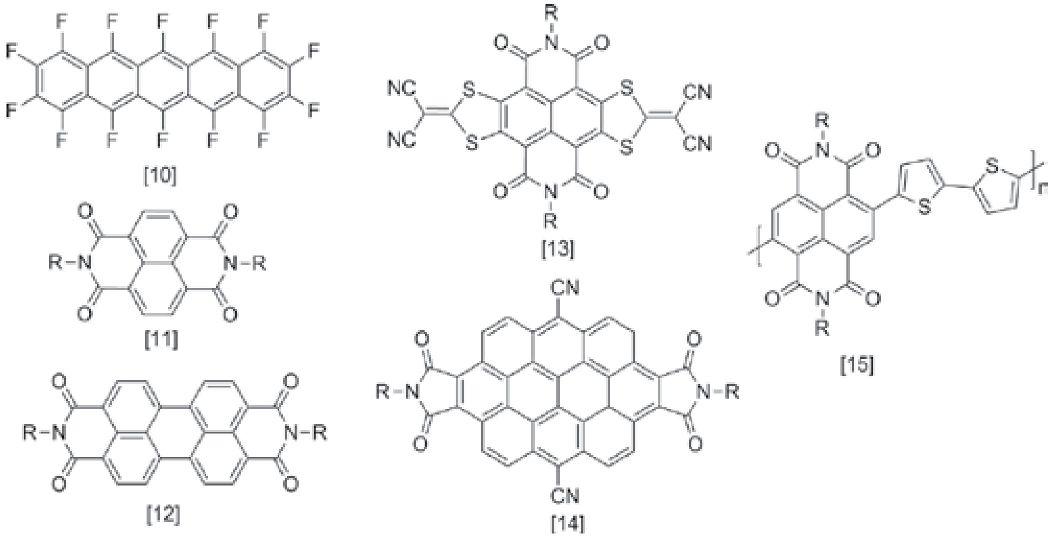

Chart 2. Chemical structures of some n-type semiconducting materials.

Naphthalene diimide (**12**) and perylene diimide (**13**) derivatives are two of the most studied n-type materials used in OFETs. Simple naphthalene and perylene diimides can be prepared from bisanhydrides and primary amines. Generally, the aromatic diimide in transistors shows an n-type character due to imide functionalization. Then, cyano or halogen was introduced to improve the air stability. Naphthalene diimide substituted with electron-withdrawing CN groups at the core position was reported by Jones et al. [50]. This molecule showed a mobility as high as 0.11 $cm^2\ V^{-1}\ s^{-1}$ as well as good ambient stability compared to unsubstituted compound. Cyano-substituted perylene diimide was also reported by the same group [51]. The good air stability was also observed, which indicates that cyano substituent is another efficient way to lower the LUMO energy level and achieve stable n-type materials. Later on, the core-expand NDI bearing two 2-(1,3-dithiol-2-ylidene)malonitrile moieties at the core (**14**) needs to be mentioned due to its good solution processability and good air stability [52].

Based on these results, it could be concluded that there is an efficient way to achieve stable n-type materials by combining imide functionalization and cyano or halogen substitutions. Electron-deficient aromatic diimides, such as ovalene diimide (ODI-CN), have attracted increasing attention as promising n-type semiconductors for OFETs (**15**) [53]. The materials of this class showed not only highly planar conjugated backbone but also easily tunable electronic properties through core and imide-nitrogen substituents with electron withdrawing groups and alkyl chains, respectively.

Similar to organic small molecules, the high-performance n-type polymers reported so far are much scarcer than that of p-type polymers. However, in order to achieve complementary circuits and plastic electronics, developing high-performance polymeric semiconductor with good air stability is essential. According to the previous works, the most promising results for n-type polymers is naphthalene-based polymer (P(NDI2OD-T2)), which exhibited an unprecedented high performance, with a mobility of >0.1 $cm^2\ V^{-1}\ s^{-1}$ (up to 0.85 $cm^2\ V^{-1}\ s^{-1}$) and on/off ratio of 10^6 and excellent air stability in ambient conditions. Furthermore, the semiconductors could be processed by gravure, flexographic, and inkjet printing technique, and achieve all-printed polymeric complementary inverters (with gain 25–65) [54].

5. Fabrication techniques

The deposition of semiconductors is the determining step of the OFET fabrication. And it will decide the performance of the devices significantly. Here, we will introduce some important techniques commonly used in the OFET fabrication.

5.1. Vacuum evaporation

This technique allows for deposition and purification of small molecule organic semiconductors. The process is performed in an ultrahigh vacuum environment. The organic semiconductor material is placed in a metal boat and heated by Joule effects or electron gun, and the substrate is placed above the boat to allow growth and formation of the organic materials. In principle, high molecular weight organic semiconductors cannot be deposited by this way, because they are too heavy to evaporate and tend to decompose at high temperatures. The main advantages of the vacuum evaporation are the facile control of the purity and thickness of the deposited film. Meanwhile, that highly ordered crystalline thin films can be realized by controlling the deposition rate and the temperature of the substrate. Its major deficiency is that it requires complicated instruments. This is different with the solution processing technique which is simple and low-cost.

5.2. Liquid deposition

Liquid deposition process is an important part of most OFET fabrication process, either to deposit the active layers or to manipulate layers deposited through other means. Many organic semiconductor materials have been engineered to be soluble or dispersible in solution, which gives a possibility toward the device fabrication. Many strategies have been applied to the deposition of organic semiconductors for utilization in OFETs. The common deposition methods include spin-coating, drop-casting, dip-coating, spray-coating, and roll-coating techniques (**Figure 4**) [55].

Printing comprises a family of techniques and can simultaneously deposit and pattern a target material. This technique mainly contains ejected drop printing, contact stamp printing, indirect and offset printing methods, and capillary stylus dispensing. The comparison of these techniques in terms of advantages and disadvantages has been reported by some comprehensive reviews [55, 56]. Among them, piezo inkjet printing has dominated OFET fabrication printing techniques due to its excellent compatibility and the availability of sophisticated print heads to the development community. In this technique, some parameters like ink viscosity, ink surface tension, and substrate surface energy are crucial for ejection and deposition of the droplets. It is necessary to control the droplet spreading and drying to avoid "coffee ring" effect and form

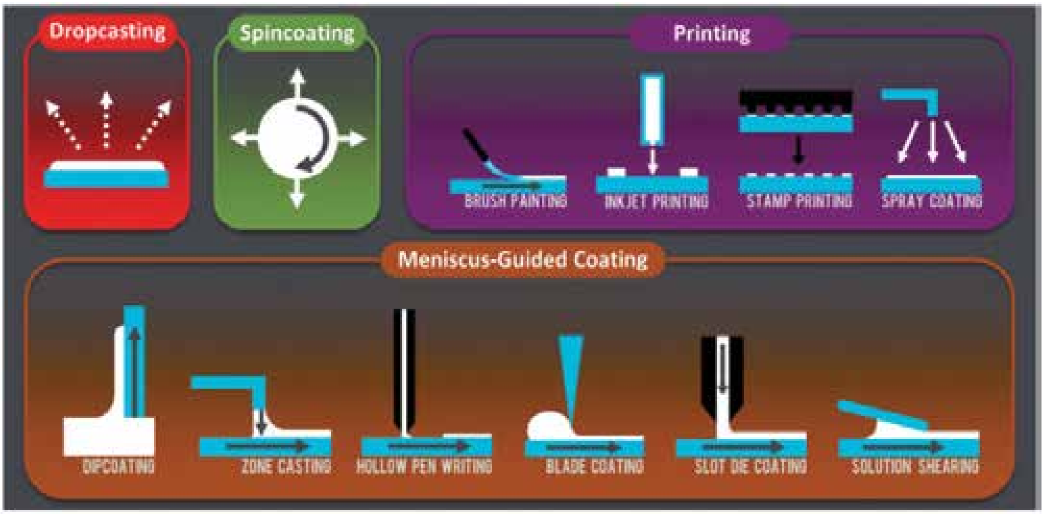

Figure 4. A schematic summary of the solution-based deposition techniques discussed. Reproduced with permission from Ref. [55]. Copyright 2014, The Royal Society of Chemistry.

precisely patterned arrays. Some method such as combining the antisolvent crystallization and inkjet printing has been used to produce highly crystalline organic semiconducting thin films. By this approach, thin-film transistors with average carrier mobilities as high as 16.4 $cm^2 V^{-1} s^{-1}$ have been achieved based on single crystalline thin films of 2,7-dioctyl[1]benzothieno[3, 2-b][1] benzothiophene (C8-BTBT) [57].

5.3. Thin-film alignment

Depositing of crystalline organic semiconductors with controlled in-plane orientation is one important issue for high-performance OFETs. It is generally accepted that charge transport in organic materials occurs via the hopping mechanism, which depends on the degree of orbital overlap between the molecules. Since charge carriers are preferentially transported along the π-π stacking direction in organic semiconductors, macroscopically aligned organic films have potentially higher mobilities and provide more unusual properties, such as optically and electrically anisotropic characteristics. Therefore, many deposition techniques have been investigated for patterning and alignment of organic semiconductors [56]. The techniques mainly contain (1) mechanical forces alignment, such as friction-transfer, nanoimprinting, and the Langmuir-Blodgett (LB) technique; (2) depositing the organic semiconductors directly on the alignment layers prepared by different methods, such as rubbing and photoirradiation; (3) growing the organic semiconductors on inorganic single crystals; (4) using magnetic or electric field-induced alignment; (5) using solution-processed technique to align organic semiconductors on isotropic substrates.

Among the solution processing techniques, the traditional techniques such as spin-coating and drop-casting cannot control the thin-film orientation. Therefore, some methods have been used to overcome this issue. For example, zone-casting offers a route to control the orientation of the deposited layers. In this process, a continuously supplied hot solution is deposited by means of a nozzle onto a moving, thermally controlled support. Under appropriate rates of solution supply and solvent evaporation, a stationary gradient of concentration is formed within the meniscus, which gives rise to directional crystallization [58]. Dip-coating is another technique to give a better thin-film alignment in solution-processed devices [59, 60]. This process can be controlled by the substrate lift rate, solvent evaporation, and capillary flow. Solvent choice is especially important because of its effect on the rate of solvent evaporation. The drying speed which influences the thin-film morphologies can be quantitatively controlled during the dip-coating process by adjusting the substrate lifting rate.

Solution-sheared deposition is a recently developed approach that can deposit highly crystalline and aligned thin films on isotropic substrates [61]. This method is related to doctor blading, which employs a blade to distribute a viscous solution over a substrate. A small volume of a diluted organic solution is sandwiched between two preheated silicon substrates, which move relatively to each other at a controlled speed. The top wafer acts as the shearing tool and is treated to be hydrophobic and the bottom wafer acts as the device substrate. The motion of the wafers exposes a liquid front that quickly evaporates to form a seeding film comprising multiple crystal grains. These crystals act as nucleation sites and allow the remaining molecules in solution to grow along the direction of the shearing direction (**Figure 5**) [61].

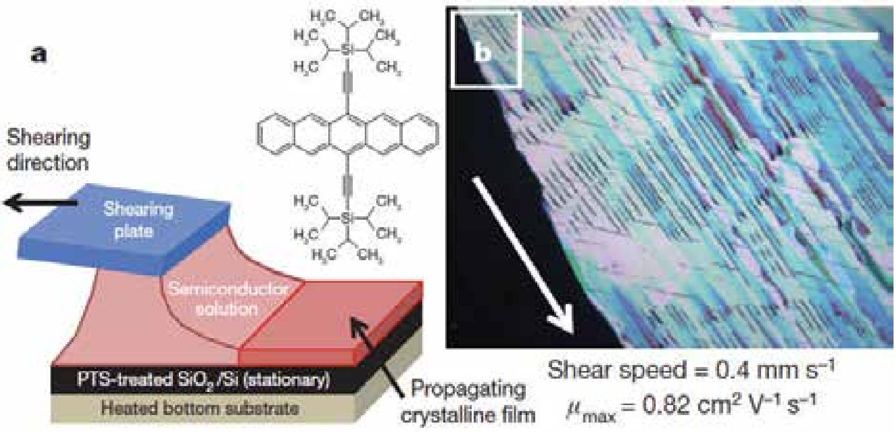

Figure 5. Schematic diagram of the solution-shearing method (a) and (b) cross-polarized optical microscope images of solution-sheared TIPS-pentacene thin films, formed with shearing speeds of 0.4 mm/s. Adapted with permission from Ref. [62]. Copyright 2011, Nature Publishing Group.

It has been reported that by using this method, metastable molecular packing motifs (or lattice-strained crystal structure) could be formed, which can alter the intermolecular π-π stacking distance and enhance the charge transport properties [62].

Slot-die coating is also a promising technique to control the thin-film alignment and self-assembly process for OFET applications. It has been proved to be a simplistic and manufacturable approach to fabricate large area high-performance field-effect transistors. This technique saves raw materials and controls film uniformity reliably, accurately, and reproducibly. The slot die coating is scalable to large areas and, therefore, applicable for the fabrication of large area low-cost electronics. We first applied this technique in the OFET fabrication [63]. **Figure 6** schematically illustrates this process. A temperature-controlled vacuum suction plate was used to fix and preheat the substrates to a certain temperature. A small volume of organic solution is deposited onto the modified substrate surface by a slot die with different coating gaps ranging

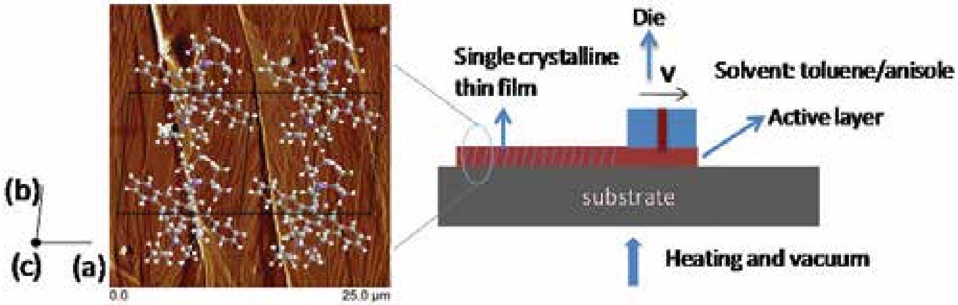

Figure 6. Schematic of slot-die coating and the AFM image of the film with molecular structure superimposed. (a), (b) and (c) indicate the crystal axises of the crystal structure. Adapted with permission [63]. *Copyright 2013, WILEY-VCH Verlag GmbH & Co. KGaA, Weinheim.*

from 15 to 90 μm. The depositing speed is controlled within the range of 0.1–19.9 mm/s. The pre-exposed seeding film can act as nucleation sites and allow the remaining molecules in the solution to grow along the coating direction [63].

6. Conclusions and future outlook

In general, impressive progress has been accomplished in the design, synthesis, and processing of organic semiconductors in the past few years. In the future, organic semiconductors will become more attractive due to comparable performance to traditional amorphous inorganic semiconductor materials, and their near-infinite tunability. Meanwhile, for large-scale fabrication of low-cost devices, solution-based film deposition processes at low temperatures with high charge carrier mobility are highly desirable.

Currently, more attention is focused on the solution-processable, air-stable high-performance organic n-type semiconductor; the relationship between the molecular structure of the organic semiconductor and device performance; and large area semiconductor thin-film alignment. Meanwhile, some important issues still need further investigation such as operational stability, low-cost and large area fabrication process, device integration, as well as functionalization in sensor fields. The study of the defect electronic structure of organic semiconductors will also be the important subject in the coming years.

In summary, although organic materials and devices still have some deficiencies, they can be improved and used in a wide range of low-cost functional devices to meet the needs of different markets, and they are sure to become a unique feature of our life in the future.

Author details

Jingjing Chang*, Zhenhua Lin, Chunfu Zhang and Yue Hao

*Address all correspondence to: jjingchang@xidian.edu.cn

State Key Discipline Laboratory of Wide Band Gap Semiconductor Technology, School of Microelectronics, Xidian University, Xi'an, China

References

[1] Crone B, Dodabalapur A, Lin Y, et al. Large-scale complementary integrated circuits based on organic transistors. Nature. 2000;**403**(6769):521–523. DOI: 10.1038/35000530

[2] Klauk H, Zschieschang U, Pflaum J, Halik M. Ultralow-power organic complementary circuits. Nature. 2007;**445**(7129):745–748. DOI: 10.1038/nature05533

[3] Gelinck GH, Huitema HEA, van Veenendaal E, et al. Flexible active-matrix displays and shift registers based on solution-processed organic transistors. Nature Materials. 2004;**3**(2):106–110. DOI: 10.1038/nmat1061

[4] Janata J, Josowicz M. Conducting polymers in electronic chemical sensors. Nature Materials. 2003;**2**(1):19–24. DOI: 10.1038/nmat768

[5] Roberts ME, Mannsfeld SCB, Queraltó N, et al. Water-stable organic transistors and their application in chemical and biological sensors. Proceedings of the National Academy of Sciences of the United States of America. 2008;**105**:12134–12139. DOI: 10.1073/pnas.0802105105

[6] Rogers JA, Bao Z, Baldwin K, et al. Paper-like electronic displays: Large-area rubber-stamped plastic sheets of electronics and microencapsulated electrophoretic inks. Proceedings of the National Academy of Sciences of the United States of America. 2001;**98**(9):4835–4840. DOI: 10.1073/pnas.091588098

[7] Scher H, Lax M. Stochastic transport in a disordered solid. I. Theory. Physical Review B. 1973;**7**(10):4491–4502. DOI: 10.1103/PhysRevB.7.4491

[8] Brütting W. Physics of Organic Semiconductors. 2006; WILEY-VCH Verlag GmbH & Co. KGaA, Weinheim ISBN 3-527-40550-X

[9] Holstein T. Studies of polaron motion: Part II. The "small" polaron. Annals of Physics-New York. 1959;**8**(3):343–389. DOI: 10.1016/0003-4916(59)90003-X

[10] Bassler H. Charge transport in disordered organic photoconductors a Monte Carlo simulation study. Physica Status Solidi (B). 1993;**175**(1):15–56. DOI: 10.1002/pssb.2221750102

[11] Horowitz G, Delannoy P. An analytical model for organic-based thin-film transistors. Journal of Applied Physics. 1991;**70**(1):469–475. DOI: 10.1063/1.350250

[12] Karl N. Charge carrier transport in organic semiconductors. Synthetic Metals. 133–134; 2003:649–657. DOI: 10.1016/S0379-6779(02)00398-3

[13] Kepler RG. Charge carrier production and mobility in anthracene crystals. Physical Review. 1960;**119**(4):1226–1229. DOI: 10.1103/PhysRev.119.1226

[14] LeBlanc OH. Hole and electron drift mobilities in anthracene. Journal of Chemical Physics. 1960;**33**(2):626. DOI: 10.1063/1.1731216

[15] Horowitz G. Organic field-effect transistors. Advanced Materials. 1998;**10**(5):365–377. DOI: 10.1002/1521-4095(199803)10

[16] Horowitz G. Organic thin film transistors: From theory to real devices. Journal of Materials Research. 2011;**19**(7):1946–1962. DOI: 10.1557/JMR.2004.0266

[17] Dodabalapur A, Torsi L, Katz HE. Organic transistors: Two-dimensional transport and improved electrical characteristics. Science. 1995;**268**(5208):270–271. DOI: 10.1126/science.268.5208.270

[18] Pesavento PV, Chesterfield RJ, Newman CR, Frisble CD. Gated four-probe measurements on pentacene thin-film transistors: Contact resistance as a function of gate voltage and temperature. Journal of Applied Physics. 2004;**96**(12):7312–7324. DOI: 10.1063/1.1806533

[19] Dimitrakopoulos CD, Shaw JM. Low-voltage organic transistors on plastic comprising high-dielectric constant gate insulators. Science. 1999;**283**(5403):822–824. DOI: 10.1126/science.283.5403.822

[20] Tanase C, Meijer EJ, Blom PWM, De Leeuw DM. Unification of the hole transport in polymeric field-effect transistors and light-emitting diodes. Physical Review Letters. 2003;**91**(21):216601. DOI: 10.1103/PhysRevLett.91.216601

[21] Stassen AF, De Boer RWI, Losad NN, Morpurgo AF. Influence of the gate dielectric on the mobility of rubrene single-crystal field-effect transistors. Applied Physics Letters. 2004;**85**(17):3899–3901. DOI: 10.1063/1.1812368

[22] Veres J, Ogier SD, Leeming SW, Cupertino DC, Khaffaf SM. Low-k insulators as the choice of dielectrics in organic field-effect transistors. Advanced Functional Materials. 2003;**13**(3):199–204. DOI: 10.1002/adfm.200390030

[23] Houili H, Picon JD, Zuppiroli L, Bussac MN. Polarization effects in the channel of an organic field-effect transistor. Journal of Applied Physics. 2006;**100**(2):023702. DOI: 10.1063/1.2214363

[24] Hulea IN, Fratini S, Xie H, et al. Tunable Fröhlich polarons in organic single-crystal transistors. Nature Materials. 2006;**5**(12):982–986. DOI: 10.1038/nmat1774

[25] Blom PWM, De Jong MJM, Vleggaar JJM. Electron and hole transport in poly(p-phenylene vinylene) devices. Applied Physics Letters. 1996;**68**(23):3308–3310. DOI: 10.1063/1.116583

[26] Fichou D. Handbook of Oligo- and Polythiophenes. Weinheim, New York: Wiley-VCH; 1999

[27] Bassler H. Charge transport in disordered organic photoconductors: A Monte Carlo simulation study. Physica Status Solidi. 1993;**175**(1):15–56. DOI: 10.1002/pssb.2221750102

[28] Horowitz G, Hajlaoui ME, Hajlaoui R. Temperature and gate voltage dependence of hole mobility in polycrystalline oligothiophene thin film transistors. Journal of Applied Physics. 2000;**87**(9):4456. DOI: 10.1063/1.373091

[29] Weimer PK. The TFT—A new thin-film transistor. Proceedings of the IRE. 1962;**50**:1462–1469. DOI: 10.1109/JRPROC.1962.288190

[30] Braga D, Horowitz G. High-performance organic field-effect transistors. Advanced Materials. 2009;**21**(14–15):1473–1486. DOI: 10.1002/adma.200802733

[31] Zaumseil J, Sirringhaus H. Electron and ambipolar transport in organic field-effect transistors. Chemical Reviews. 2007;**107**(4):1296–1323. DOI: 10.1021/cr0501543

[32] Veres J, Ogier S, Lloyd G, de Leeuw D. Gate insulators in organic field-effect transistors. Chemistry of Materials. 2004;**16**(23):4543–4555. DOI: 10.1021/cm049598q

[33] Salleo A, Street RA. Kinetics of bias stress and bipolaron formation in polythiophene. Physical Review B: Condensed Matter and Materials Physics. 2004;**70**(23):1–8. DOI: 10.1103/PhysRevB.70.235324

[34] Kagan CR, Afzali A, Graham TO. Operational and environmental stability of pentacene thin-film transistors. Applied Physics Letters. 2005;**86**(19):193505. DOI: 10.1063/1.1924890

[35] Tsumura A, Koezuka H, Ando T. Macromolecular electronic device: Field-effect transistor with a polythiophene thin film. Applied Physics Letters. 1986;**49**(18):1210–1212. DOI: 10.1063/1.97417

[36] Nielsen CB, Turbiez M, McCulloch I. Recent advances in the development of semiconducting DPP-containing polymers for transistor applications. Advanced Materials. 2013;**25**(13):1859–1880. DOI: 10.1002/adma.201201795

[37] Roberson LB, Kowalik J, Tolbert LM, et al. Pentacene disproportionation during sublimation for field-effect transistors. Journal of the American Chemical Society. 2005;**127**(9):3069–3075. DOI: 10.1021/ja044586r

[38] Watanabe M, Chang YJ, Liu SW, et al. The synthesis, crystal structure and charge-transport properties of hexacene. Nature Chemistry. 2012;**4**(7):574–578. DOI: 10.1038/nchem.1381

[39] Clemens W, Fix W, Ficker J, Knobloch A, Ullmann A. From polymer transistors toward printed electronics. Journal of Materials Research. 2004;**19**(7):1963–1973. DOI: 10.1557/JMR.2004.0263

[40] Podzorov V, Menard E, Borissov A, Kiryukhin V, Rogers JA, Gershenson ME. Intrinsic charge transport on the surface of organic semiconductors. Physical Review Letters. 2004;**93**(8):86602. DOI: 10.1103/PhysRevLett.93.086602

[41] Pisula W, Menon A, Stepputat M, et al. A zone-casting technique for device fabrication of field-effect transistors based on discotic hexa-perihexabenzocoronene. Advanced Materials. 2005;**17**(6):684–688. DOI: 10.1002/adma.200401171

[42] Tang ML, Okamoto T, Bao Z. High-performance organic semiconductors: Asymmetric linear acenes containing sulphur. Journal of the American Chemical Society. 2006;**128**(50):16002–16003. DOI: 10.1021/ja066824j

[43] Liu Y, Wang Y, Wu W, et al. Synthesis, characterization, and field-effect transistor performance of thieno[3, 2-b]thieno[2′,3′:4,5]thieno[2, 3-d]thiophene derivatives. Advanced Functional Materials. 2009;**19**(5):772–778. DOI: 10.1002/adfm.200800829

[44] Sirringhaus H, Brown PJ, Friend RH, Nielsen MM, Bechgaard K, Spiering AJH. Two-dimensional charge transport in self-organized, high-mobility conjugated polymers. Nature. 1999;**401**:685–688. DOI: 10.1038/44359

[45] Li J, Zhao Y, Tan HS, et al. A stable solution-processed polymer semiconductor with record high-mobility for printed transistors. Scientific Reports. 2012;**2**:754. DOI: 10.1038/srep00754

[46] Chang J, Lin Z, Li J, et al. Enhanced polymer thin-film transistor performance by carefully controlling the solution self-assembly and film alignment with slot die coating. Advanced Electronic Materials. 2015;**1**(7):1500036. DOI: 10.1002/aelm.201500036

[47] de Leeuw DM, Simenon MMJ, Brown AR, Einerhand REF. Stability of n-type doped conducting polymers and consequences for polymeric microelectronic devices. Synthetic Metals. 1997;**87**(1):53–59. DOI: 10.1016/S0379-6779(97)80097-5

[48] Sakamoto Y, Suzuki T, Kobayashi M, et al. Perfluoropentacene: High-performance p-n junctions and complementary circuits with pentacene. Journal of the American Chemical Society. 2004;**126**(26):8138–8140. DOI: 10.1021/ja0476258

[49] Kikuzawa Y, Mori T, Takeuchi H. Synthesis of 2,5,8,11,14,17-hexafluoro-hexa-peri-hexabenzocoronene for n-type organic field-effect transistors. Organic Letters. 2007;**9** (23):4817–4820. DOI: 10.1021/ol702158a

[50] Jones BA, Facchetti A, Marks TJ, Wasielewski MR. Cyanonaphthalene diimide semiconductors for air-stable, flexible, and optically transparent n-channel field-effect transistors. Chemistry of Materials. 2007;**19**(11):2703–2705. DOI: 10.1021/cm0704579

[51] Jones BA, Ahrens MJ, Yoon MH, Facchetti A, Marks TJ, Wasielewski MR. High-mobility air-stable n-type semiconductors with processing versatility: dicyanoperylene-3,4:9,10-bis (dicarboximides). Angewandte Chemie International Edition. 2004;**43**(46):6363–6366. DOI: 10.1002/anie.200461324

[52] Gao X, Di C, Hu Y, et al. Core-expanded naphthalene diimides fused with 2-(1,3-dithiol-2-ylidene)malonitrile groups for high-performance, ambient-stable, solution-processed n-channel organic thin film transistors. Journal of the American Chemical Society. 2010;**132** (11):3697–3699. DOI: 10.1021/ja910667y

[53] Li J, Chang JJ, Tan HS, et al. Disc-like 7, 14-dicyano-ovalene-3,4:10,11-bis(dicarboximide) as a solution-processible n-type semiconductor for air stable field-effect transistors. Chemical Science. 2012;**3**(3):846. DOI: 10.1039/c1sc00739d

[54] Yan H, Chen Z, Zheng Y, et al. A high-mobility electron-transporting polymer for printed transistors. Nature. 2009;**457**(7230):679–686. DOI: 10.1038/nature07727

[55] Diao Y, Shaw L, Bao Z, Mannsfeld SCB. Morphology control strategies for solution-processed organic semiconductor thin films. Energy and Environmental Science. 2014;**7** (7):2145. DOI: 10.1039/c4ee00688g

[56] Liu S, Wang WM, Briseno AL, Mannsfeld SCB, Bao Z. Controlled deposition of crystalline organic semiconductors for field-effect-transistor applications. Advanced Materials. 2009;**21**(12):1217–1232. DOI: 10.1002/adma.200802202

[57] Minemawari H, Yamada T, Matsui H, et al. Inkjet printing of single-crystal films. Nature. 2011;**475**(7356):364–367. DOI: 10.1038/nature10313

[58] Duffy CM, Andreasen JW, Breiby DW, et al. High-mobility aligned pentacene films grown by zone-casting. Chemistry of Materials. 2008;**20**(23):7252–7259. DOI: 10.1021/cm801689f

[59] Jang J, Nam S, Im K, et al. Highly crystalline soluble acene crystal arrays for organic transistors: Mechanism of crystal growth during dip-coating. Advanced Functional Materials. 2012;**22**(5):1005–1014. DOI: 10.1002/adfm.201102284

[60] Sele CW, Kjellander BKC, Niesen B, et al. Controlled deposition of highly ordered soluble acene thin films: Effect of morphology and crystal orientation on transistor performance. Advanced Materials. 2009;**21**(48):4926–4931. DOI: 10.1002/adma.200901548

[61] Becerril HA, Roberts ME, Liu Z, Locklin J, Bao Z. High-performance organic thin-film transistors through solution-sheared deposition of small-molecule organic semiconductors. Advanced Materials. 2008;**20**(13):2588–2594. DOI: 10.1002/adma.200703120

[62] Giri G, Verploegen E, Mannsfeld SCB, et al. Tuning charge transport in solution-sheared organic semiconductors using lattice strain. Nature. 2011;**480**(7378):504–508. DOI: 10.1038/nature10683

[63] Chang J, Chi C, Zhang J, Wu J. Controlled growth of large-area high-performance small-molecule organic single-crystalline transistors by slot-die coating using a mixed solvent system. Advanced Materials. 2013;**25**(44):6442–6447. DOI: 10.1002/adma.201301267

Section 5

Applications

Chapter 8

Field-Effect Transistors for Gas Sensing

Toshihiro Yoshizumi and Yuji Miyahara

Additional information is available at the end of the chapter

http://dx.doi.org/10.5772/intechopen.68481

Abstract

This chapter reviews gas-sensitive field-effect transistors (FETs) for gas sensing. Although various types of gas sensors have been reported, this review focuses on FET-based sensors such as catalytic-gate FETs, solid electrolyte-based FETs, suspended-gate FETs, and nanomaterial-based FETs. For recognition of analytes in the gas phase, the combination of cross-reactive gas sensor arrays with pattern recognition methods is promising. Cross-reactive sensor arrays consist of gas sensors that have broad and differential sensitivity. Signals from the cross-reactive sensor array are processed using pattern recognition methods. Reports of FET-based sensor arrays combined with pattern recognition methods are briefly reviewed.

Keywords: gas-sensitive field-effect transistor, gas sensor, cross-reactive sensor array, pattern recognition method

1. Introduction

The importance and demand for sensing gases, vapors, and volatile organic compounds (VOCs) have been increasing in fields such as diagnostics [1–4], environmental monitoring for industrial, agricultural, home safety, and so on [4, 5]. Various types of gas sensors and sensor arrays have been researched and developed [6–8], including field-effect transistor (FET)-based sensors. Following the report of pioneering work on catalytic-gate FETs, research on FET-based gas sensors has been extended to various types of gas-sensitive FETs. In this chapter, catalytic-gate FETs, suspended-gate FETs (SGFETs), and solid electrolyte-based FETs are introduced. Gas-sensitive FETs based on nanomaterials such as carbon nanotubes (CNTs), nanowires (NWs), graphene, and transition metal chalcogenides have also been investigated because the high surface-to-volume ratios of nanomaterials are attractive for improving sensor properties [5, 9]. These nanomaterial-based FETs are also reviewed.

INTECH
open science | open minds

© 2017 The Author(s). Licensee InTech. This chapter is distributed under the terms of the Creative Commons Attribution License (http://creativecommons.org/licenses/by/3.0), which permits unrestricted use, distribution, and reproduction in any medium, provided the original work is properly cited.

For recognition of gaseous and volatile analytes from sensing results, two main methods have been used [3]. The conventional recognition method uses selective sensors with specific receptors designed for selective interaction with target analytes [3, 6]. Another recognition method uses a combination of cross-reactive sensor arrays and pattern recognition methods [3, 6–8, 10]. These cross-reactive sensor arrays consist of gas sensors that are responsive to a broad range of analytes and have differential sensitivities. To date, various gas sensors have been applied in sensor arrays [6, 8], including gas-sensitive FETs. In this chapter, research on the combination of FET-based sensor arrays and pattern recognition methods is briefly reviewed.

2. Gas-sensitive FETs and field-effect devices combined with catalytic metal gates

Catalytic-gate FETs are one of types of gas-sensitive FETs. In 1975, Lundström et al. first reported a Pd-gate FET sensitive to hydrogen [11, 12]. Pioneering research on catalytic-gate FETs opened up the field of FET-based gas sensors and other gas-sensitive field-effect devices such as capacitor-based [13–17] and Schottky diode-based sensors [18, 19]. Catalytic-gate filed-effect devices feature a nanoscale layer of catalytic metals, such as palladium and platinum, as a gate electrode on insulating layers in a metal-insulator-semiconductor (MIS) structure [20]. **Figure 1** shows reported schematic illustrations of this structure and the threshold voltage shift of a Pd-gate FET that is sensitive to hydrogen [21]. In initial reports of catalytic-gate FETs, Pd as a catalytic-gate electrode was deposited onto the insulating layer of the MIS structure of the FET [11, 12, 21]. **Figure 2** shows changes observed in the threshold voltage [11] on hydrogen introduction to Pd-gate FETs. The gas-sensitive mechanisms of catalytic-gate FETs and catalytic-gate field-effect devices have been described in earlier reviews [20, 21].

Porous metal gates in catalytic-gate field-effect devices have allowed for important progress in NH_3 sensing [20, 22]. **Figure 3** shows reported TEM observations of 3- and 7-nm-thick Pt layers evaporated onto SiO_2. These thin Pt layers consist of discontinuous metals [22]. The choice of catalytic materials, the structure of the catalytic layer, and the operating temperature affect the sensitivity and selectivity of catalytic-gate field-effect devices [14, 15, 20]. Furthermore, the type of insulating materials used in the MIS structure also influences the responsive properties of gas-sensitive field-effect devices [16].

For operation at high temperatures, silicon carbide (SiC)-based FETs have been investigated. SiC is a wide-bandgap semiconductor, and can be used as a substrate for the MIS structure instead of the conventional Si substrate [17]. SiC can be used at high temperatures and harsh environments because of its chemical inertness [23–25]. SiC-based FETs have been applied to the sensing of CO [23], NH_3 [23, 24], NO_2 [24], and SO_2 [25]. As with conventional catalytic-gate FETs using an Si substrate, the catalytic-gate material used in SiC-based FETs influences the sensitivity and selectivity of the sensor [25].

Catalytic-gate devices consisting of high-electron mobility transistors (HEMTs) have also been studied for operation at high temperature. For example, GaN/AlGaN heterostructures that exhibit two-dimensional electron gas (2DEG) induced by spontaneous and piezoelectric polarization at the interface of the heterostructure have been applied to a catalytic-gate HEMT

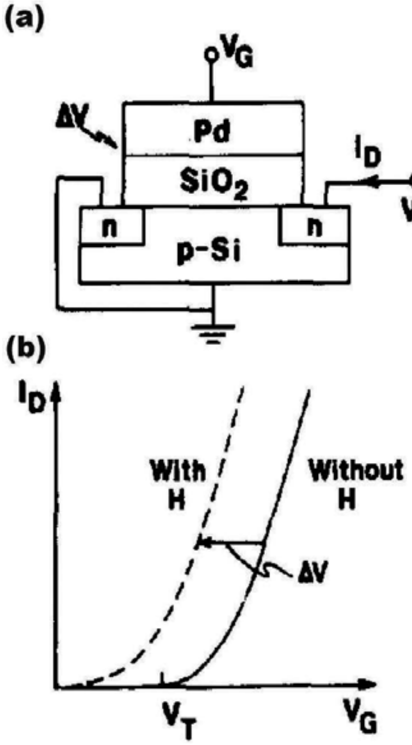

Figure 1. Schematic illustrations of the (a) structure and (b) threshold voltage shift of a Pd-gate FET sensitive to hydrogen. Reprinted with permission from Ref. [21]. Copyright 1993 Elsevier.

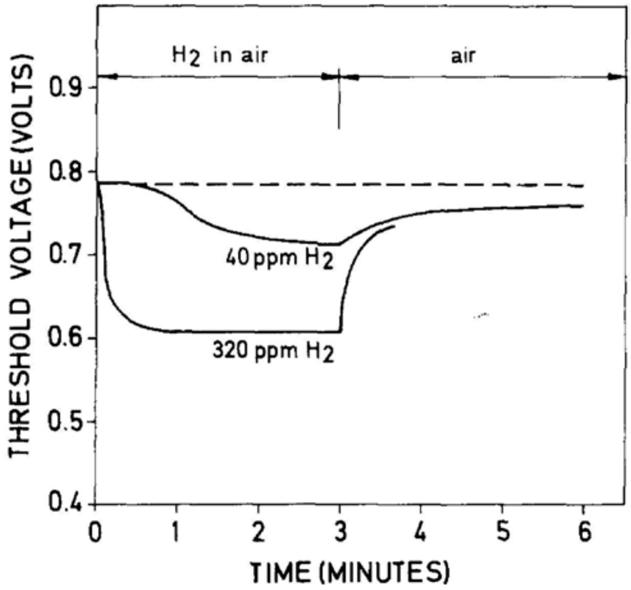

Figure 2. Changes in the threshold voltage toward H_2 at different concentrations at 150°C. Reprinted with permission from Ref. [11]. Copyright 1975 American Institute of Physics.

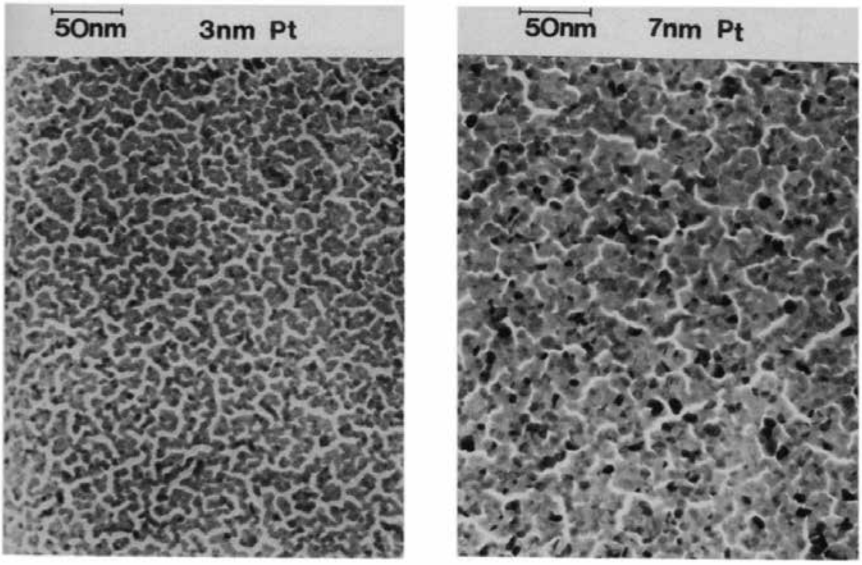

Figure 3. Transmission electron micrographs of 3- and 7-nm thick porous Pt metal layers on SiO_2. Reprinted with permission from Ref. [22]. Copyright 1987 Elsevier.

as a gas sensor [26]. In this report, the GaN/AlGaN-based HEMT combined with a Pt gate electrode was operated at about 400°C for sensing of H_2, CO, C_2H_2, and NO_2.

3. Solid electrolyte-based FETs

Solid electrolytes can also be applied to FET-based sensors. For example, an FET-based oxygen sensor using yttria-stabilized zirconia (YSZ) as a solid electrolyte (**Figure 4**) has been reported [27]. In this sensor, a YSZ film was formed on an insulating layer consisting of Si_3N_4 and SiO_2. Furthermore, a nanoscale layer of Pt was deposited on the YSZ film as a gate electrode. **Figure 5** shows responses of this sensor to oxygen and nitrogen (1 atm) [27]. At room temperature, a repeated stepwise response curve and a subsequent drift were observed. The response of the sensor showed a linear relationship against the partial pressure of oxygen in a logarithmic range between 0.01 and 1 atm. The sensitivity of the sensor to oxygen increased as the thickness of the Pt layer decreased.

To investigate the YSZ-based FET structure for use as an oxygen sensor, the crystalline structure and electrical properties were studied for a YSZ film deposited on a layer of Si_3N_4 by RF sputtering [28]. In the capacitance-voltage curve, hysteresis was observed, and was considered to be caused by the movement of oxygen ions and/or electrons in the YSZ film. This resulted in an unstable response at room temperature as mentioned above. Therefore, to increase the stability and quicken the response of the oxygen sensor at room temperature, the solid electrolyte-based FET would need to incorporate an electrolyte with a high diffusion coefficient for oxygen ions [28].

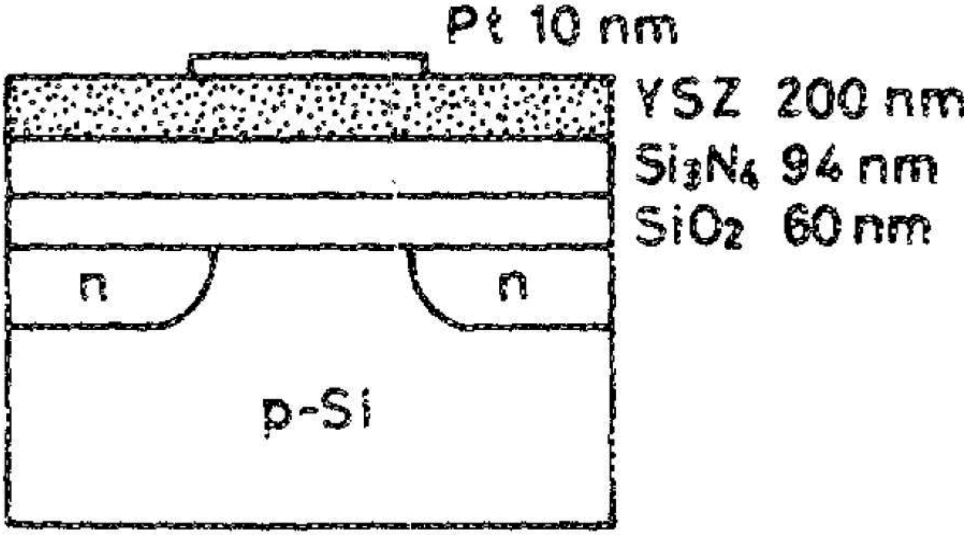

Figure 4. Schematic illustration of a YSZ-based FET. The YSZ-based FET is n-channel type and depletion-mode device. A nanoscale Pt layer is formed on a layer of YSZ. Reprinted with permission from Ref. [27]. Copyright 1988 American Institute of Physics.

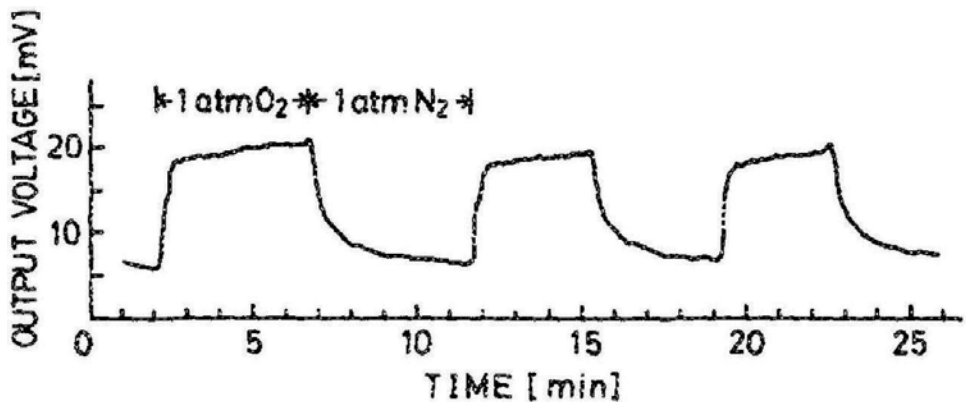

Figure 5. Responses at 20°C of a YSZ-based FET against O_2 and N_2. Reprinted with permission from Ref. [27]. Copyright 1988 American Institute of Physics.

4. Suspended-gate FETs

In 1983, Janata et al. reported an SGFET sensitive to dipolar molecules such as methanol and methylene chloride [29]. In the SGFET shown in **Figure 6**, fluid samples can penetrate into the gap between the insulating layer and the suspended metal mesh. Electrochemical surface modification using polypyrroles has been used to improve the selectivity of the SGFET [30]. This report described the preparation of SGFETs with differential selectivity by chemical modification with a polymer coating.

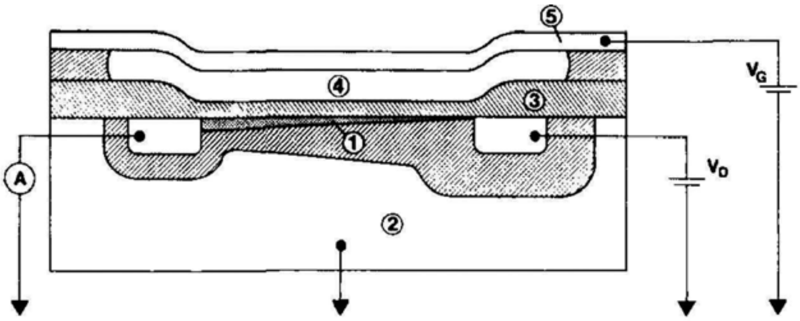

Figure 6. Schematic illustration of a suspended gate FET. Reprinted with permission from Ref. [29]. Copyright 1983 American Institute of Physics.

Improvement of fabrication processes is an important topic in SGFET research. Hybrid SGFETs prepared using an improved process and with diverse materials in the sensing layer have been reported [31]. In the fabrication process of hybrid SGFETs, the gate and body chip are prepared separately and then combined. This manufacturing technique has advantages over conventional methods because it allows for incorporation of a diverse range of sensitive materials in the structure. The flip-chip method has also been applied to the preparation of an SGFET for sensing ammonia [32]. In this report, a polyacrylic acid layer was formed on the gate structure by a spraying process.

The air gap in the gate structure of an SGFET causes undesirable effects on the sensing stability because of a lack of passivation, small W/L ratio, and a low gate capacity [33]. To overcome these drawbacks, research on SGFETs has been expanded to capacitively controlled FETs (CCFETs) [33] and floating-gate GasFETs (FGFETs) [34]. CCFETs contain an FET structure and a gas-sensitive capacitor with an air gap. FGFETs are a modification of CCFETs that use a floating gate for improved signal stability [34]. An FGFET with a hybrid-mounted gas-sensitive top electrode has been reported (**Figure 7a**) [34]. In this structure, the gas-sensitive capacitor and read-out transistor were integrated in one chip. **Figure 7b** shows the equivalent circuit diagram of the FGFET. The gate and the plate are electrically floating because they are isolated by the SiO_2 layer. This FGFET was used for sensing H_2 (500 ppm).

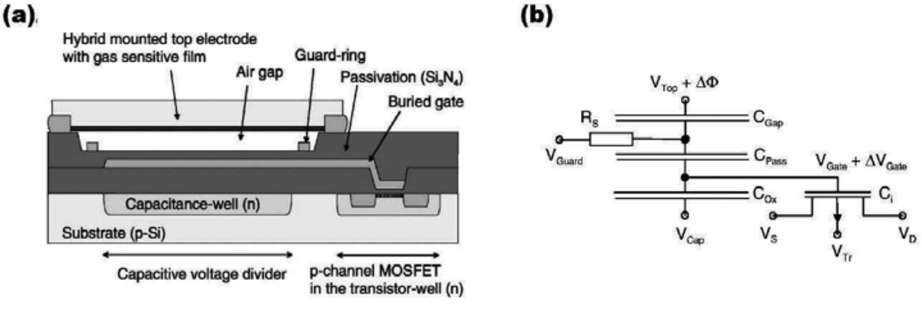

Figure 7. (a) Schematic illustration and (b) equivalent circuit diagram of a reported FGFET. Reprinted with permission from Ref. [34]. Copyright 2003 Elsevier.

Different FET-based sensors can be combined to extend the sensitivity range. For example, an SGFET responsive to high concentrations of H_2 and a catalytic-gate FET with good sensitivity for low concentrations of H_2 have been combined in one chip to increase the sensitivity range [35].

5. Nanomaterial-based FETs

FET-based gas sensors have been expanded to sensors containing nanomaterials. Nanomaterial-based FETs have large surface-to-volume ratios, which contribute to high sensitivity and fast response and recovery times [3]. Nanomaterials allow for high-packing densities because of their intrinsic small dimensions [5]. This section briefly reviews FET-based gas sensors using nanomaterials such as CNTs, NWs, graphene, and transition metal chalcogenides.

5.1. CNT-based FETs

The fabrication of CNT-based FETs was first reported in 1998 [36, 37]. A typical CNT-based FET consists of a CNT, source and drain electrodes, insulating layer, and a substrate as the back gate [38]. Both individual CNTs and random networks of CNTs can be used to prepare CNT-based FETs. Chemical-gating effects of an individual single-walled CNT-based FET caused by exposure to gaseous NH_3 or NO_2 were reported in 2000 [39]. To date, CNT-based FETs have been applied to sensing H_2 [40], CH_4 [40], CO [40], CO_2 [41], NO_2 [40], NH_3 [40], H_2S [40], alcohols [42], and breath samples [43].

To improve the sensitivity and selectivity of CNT-based FETs, they have been modified with nanoscale catalytic materials such as Pd [40, 44], Pt [40, 44], Rh [40], Au [40, 44], and Ag [44]. Furthermore, modifications with polymers [41], peptides [44], olfactory receptor proteins [45], and DNA [46, 47] have been reported.

5.2. NW-based FETs

5.2.1. Gas-sensitive FETs using Si NWs

As a gas-sensitive FET using one-dimensional nanomaterials, an application of an Si NW-based FET for sensing NH_3 was reported in 2006 [48]. After that, an FET-based sensor consisting of a highly ordered Si NW array on a bendable plastic substrate was prepared and applied to sensing NO_2 at parts per billion levels [49]. Furthermore, Si NW-based sensors have been applied to sensing H_2 [50].

Despite the potential of Si NW-based FETs for gas sensing, the sensitivity of bare Si NW-based FETs toward nonpolar volatile analytes is limited [51]. To overcome this, the native SiO_2 layer on the surface of the Si NWs has been chemically modified with silane monolayers [51]. Silane monolayer-modified Si NW-based FETs have been used for sensing nonpolar VOCs [51] and exhaled breath samples [52]. Modification with nanoparticles [50] has also been used to improve the responses of Si nanomaterial-based FETs to target analytes. In addition, an Si nanoribbon-based FET functionalized with an organic compound that is reactive toward nerve agents at sub-ppm levels has been reported [53].

5.2.2. Gas-sensitive FETs using metal oxide NWs or compound semiconductor NWs

Metal oxide NWs such as In_2O_3 [54, 55], SnO_2 [56–58], and α-Fe_2O_3 [59] have also been applied to FET-based gas sensors. For example, an In_2O_3 NW-based FET has been used for sensing NO_2 and NH_3 [54].

Surface modification of NWs with nanoparticles has been used to improve the sensitivity and selectivity of gas-sensitive metal oxide NW-based FETs. To date, Pd [56, 58], Pt [55], Ag [55], Au [55], ZnO [57], and NiO [57] nanoparticles have been used to improve the properties of metal oxide NW-based FETs for gas sensing. For example, Moskovis et al. reported modification of SnO_2 NW-based FETs with Pd nanoparticles, and the application of this device to sensing H_2 [58]. In this work, an unusual sensitivity to H_2 in the charge depletion region of the device was reported [58]. This device was used for sensing a H_2 concentration range from 10 to 2500 ppm [58].

Compound semiconductor NWs have also been applied in FET-based sensors [60, 61]. Gao and coworkers applied NWs of InAs, which is a III–V semiconductor, to fabrication of a gas-sensitive FET [60]. This FET-based sensor was responsive to several gases and alcoholic vapors [60].

5.3. 2D nanomaterial-based FETs

Because of their high surface-to-volume ratios in molecular-level interactions, two-dimensional nanomaterials are attractive for use in FET-based sensors [5, 62]. Applications of 2D nanomaterials such as graphene and transition metal chalcogenides to FET-type gas sensors have been studied.

Since the potential of graphene-based sensors for gas sensing was first reported [63], other studies have investigated gas sensing using graphene-based FETs [62, 64]. A reported graphene-based FET is shown in **Figure 8** [64]. **Figure 8a** shows an atomic force microscopy (AFM) image of the FET based on graphene. Schematic diagram of the back-gate-type FET is shown in **Figure 8b** [64]. In the structure, the FET consists of a graphene sample connected

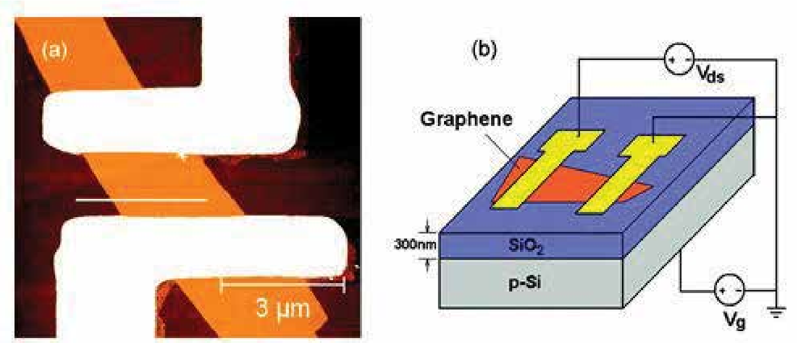

Figure 8. (a) AFM image and (b) schematic illustration of a graphene-based FET. Reprinted with permission from Ref. [64]. Copyright 2009 American Chemical Society.

with source and drain electrodes of Au/Cr, an SiO_2-insulating layer, and a p-Si substrate as the back gate. In this report, the sensor was used for sensing NH_3 vapors [64].

As 2D nanomaterials, the transition metal chalcogenides MoS_2 [65], $MoTe_2$ [66], and WS_2 [67] have also been applied in FET-based gas sensors. **Figure 9a** shows a schematic illustration of a back-gate FET based on MoS_2 [5]. **Figure 9b** shows an optical image of MoS_2-based FETs. In this FET, MoS_2 sheets were grown on an SiO_2/Si substrate, with Ti/Au as the source and drain electrodes. This sensor was responsive to 20 ppb NO_2 and 1 ppm NH_3 [5].

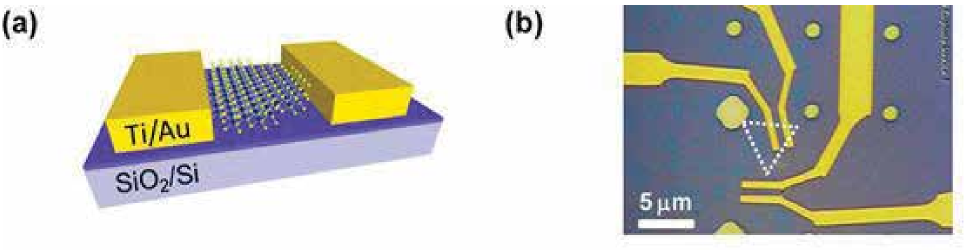

Figure 9. (a) Schematic illustration and (b) optical image of a back-gate MoS_2 nanowire-based FET. Reprinted with permission from Ref. [5]. Copyright 2014 American Chemical Society.

6. Combination of gas sensors and pattern recognition methods

According to an earlier review [6], receptors in mammalian olfactory systems do not show highly selective responses against specific analytes. Pattern recognition methods are thought to be a dominant mode used in processing signals from the broad responses of the mammalian olfactory system [6].

Cross-reactive chemical sensor arrays combined with pattern recognition methods to mimic mammalian olfactory systems have been studied as an alternative sensor system to traditional sensing devices that use a "lock-and-key" design [6]. In intelligent sensor arrays using pattern recognition methods, complex patterns generated by nonspecific cross-reactive sensors are analyzed for classification and identification of analytes [3, 6–8]. Cross-reactive sensor arrays are constructed using sensors that are responsive to a broad range of analytes and have differential sensitivity [3, 6]. Conventional semiconductor processes can be applied to miniaturize FET-based sensors for the fabrication of cross-reactive sensor arrays.

Before data analysis, complex signals obtained from sensor arrays can be preprocessed and normalized for the application of appropriate computational methods [7, 8, 10]. After preprocessing and feature extraction, the selected method is performed. Currently, there is no general rule for the selection of computational methods. Therefore, computational methods must be appropriately selected on the nature of the data and the particular situation [7].

Various types of gas sensor arrays have been used with pattern recognition methods [6–8], including FET-based gas sensor arrays. For example, Lundström et al. reported combination of catalytic-gate FET-based gas sensor arrays with pattern recognition methods [68, 69]. The signals from the FET-based sensor arrays were processed using conventional partial least-squares regression and an artificial neural network to predict the concentrations of individual gases [69]. Molecularly modified Si NW-based FET sensors have also been combined with an artificial neural network to recognize VOCs and estimate their concentrations [70].

7. Overview and outlook

For the introduction of gas-sensitive FETs, a broad overview of catalytic-gate FETs, solid electrolyte-based FETs, suspended-gate FETs, and nanomaterial-based FETs is given in this chapter. Arrays of these sensors can be combined with computational pattern recognition methods. As introduced, the combination of cross-reactive gas sensor arrays with pattern recognition methods is a promising method for the recognition of analytes in the gas phase. Cross-reactive sensor arrays should contain sensors that are responsive to a broad range of analytes and have differential sensitivity. Conventional semiconductor processes can be used for miniaturization of FET-based sensors. FET-based sensors may have advantages over other sensors used in device miniaturization of cross-reactive sensor arrays.

Acknowledgements

This work was supported by ImPACT Program of Council for Science, Technology and Innovation.

Author details

Toshihiro Yoshizumi* and Yuji Miyahara

*Address all correspondence to: yoshizumi.bsr@tmd.ac.jp

Institute of Biomaterials and Bioengineering, Tokyo Medical and Dental University, Tokyo, Japan

References

[1] Turner PFA, Magan N. Electronic noses and disease diagnostics. Nature Reviews. 2004;**2**: 161-166

[2] Konvalina G, Haick H. Sensors for breath testing: From nanomaterials to comprehensive disease detection. Accounts of Chemical Research. 2014;**47**:66-76

[3] Vishinkin R, Haick H. Nanoscale sensor technologies for disease detection via volatolomics. Small. 2015;**11**:6142-6164

[4] Potyralio AR. Multivariable sensors for ubiquitous monitoring of gases in the era of Internet of things and industrial Internet. Chemical Reviews. 2016;**116**:11877-11923

[5] Liu B, Chen L, Liu G, Abbas NA, Fathi M, Zhou C. High-performance chemical sensing using Schottky-contacted chemical vapor deposition grown monolayer MoS_2 transistors. ACS Nano. 2014;**8**:5304-5314

[6] Albert JK, Lewis SN, Schauer LC, Sotzing AG, Stitzel ES, Vaid PT, Walt RD. Cross-reactive chemical sensor arrays. Chemical Reviews. 2000;**100**:2595-2626

[7] Jurs CP, Bakken AG, McClelland EH. Computational methods for the analysis of chemical sensor array data from volatile analytes. Chemical Reviews. 2000;**100**:2649-2678

[8] Hierlemann A, Gutierrez-Osuna R. Higher-order chemical sensing. Chemical Reviews. 2008;**108**:563-613

[9] Chen X, Wong KYC, Yuan AC, Zhang G. Nanowire-based gas sensors. Sensors and Actuators B. 2013;**177**:178-195

[10] Göpel W. Chemical imaging: I. Concepts and visions for electronic and bioelectronic noses. Sensors and Actuators B. 1998;**52**:125-142

[11] Lundström I, Shivaraman S, Svensson C, Lundkvist L. A hydrogen-sensitive MOS field-effect transistor. Applied Physics Letters. 1975;**26**:55-57

[12] Lundström IK, Shivaraman SM, Svensson MC. A hydrogen-sensitive Pd-gate MOS transistor. Journal of Applied Physics. 1975;**46**:3876-3881

[13] Winquist F, Spetz A, Armgarth M, Nylander C, Lundström I. Modified palladium metal-oxide-semiconductor structures with increased ammonia gas sensitivity. Applied Physics Letters. 1983;**43**:839-841

[14] Lundström I, Spetz A, Winquist F, Ackelid U, Sundgren H. Catalytic metals and field-effect devices−a useful combination. Sensors and Actuators B. 1990;**1**:15-20

[15] Löfdahl M, Eriksson M, Johansson M, Lundström I. Difference in hydrogen sensitivity between Pt and Pd field-effect devices. Journal of Applied Physics. 2002;**91**:4275-4280

[16] Eriksson M, Salomonsson A, Lundström I, Briand D, Åbom EA. The influence of the insulator surface properties on the hydrogen response of field-effect gas sensors. Journal of Applied Physics. 2005;**98**:0349031-0349036

[17] Trinchi A, Kandasamy S, Wlodarski W. High temperature field effect hydrogen and hydrocarbon gas sensors based on SiC MOS devices. Sensors and Actuators B. 2008;**133**:705-716

[18] Steele CM, Maclver AB. Palladium/cadmium-sulfide Schottky diodes for hydrogen detection. Applied Physics Letters. 1976;**28**:687-688

[19] Ito K. Hydrogen-sensitive Schottky barrier diodes. Surface Science. 1979;**86**:345-352

[20] Lundström I, Sundgrean H, Winquist F, Eriksson M, Krantz-Rülcker C, Lloyd-Spetz A. Twenty-five years of field effect gas sensor research in Linköping. Sensors and Actuators B. 2007;121:247-262

[21] Lundstöm I, Svensson C, Spetz A, Sundgren H, Winquist F. From hydrogen sensors to olfactory images – twenty years with catalytic field-effect devices. Sensors and Actuators B. 1993;**13**:16-23

[22] Spetz A, Armgarth M, Lundström I. Optimization of ammonia-sensitive metal-oxide-semiconductor structures with platinum gates. Sensors and Actuators. 1987;**11**:349-365

[23] Andersson M, Pearce R, Spetz LA. New generation SiC based field effect transistor gas sensors. Sensors and Actuators B. 2013;**179**:95-106

[24] Bur C, Bastuck M, Spetz LA, Andersson M, Schütze A. Selectivity enhancement of SiC-FET gas sensors by combining temperature and gate bias cycled operation using multivariate statistics. Sensors and Actuators B. 2014;**193**:931-940

[25] Darmastuti Z, Bur C, Möller P, Rahlin R, Lindqvist N, Andersson M. SiC-FET based SO_2 sensor for power plant emission applications. Sensors and Actuators B. 2014;**194**:511-520

[26] Schalwig J, Müller G, Eickhoff M, Ambacher O, Stutzmann M. Gas sensitive GaN/AlGaN-heterostructures. Sensors and Actuators B. 2002;**87**:425-430

[27] Miyahara Y, Tsukada K, Miyagi H. Field-effect transistor using a solid electrolyte as a new oxygen sensor. Journal of Applied Physics. 1988;**63**:2431-2434

[28] Miyahara Y. Characterization of sputtered yttria-stabilized zirconia thin film and its application to a metal-insulator-semiconductor structure. Journal of Applied Physics. 1992;**71**:2309-2314

[29] Blackburn FG, Levy M, Janata J. Field-effect transistor sensitive to dipolar molecules. Applied Physics letters. 1983;**43**:700-701

[30] Josowicz M, Janata J. Suspended gate field effect transistor modified with polypyrrole as alcohol sensor. Analytical Chemistry. 1986;**58**:514-517

[31] Flietner B, Doll T, Lechner J, Leu M, Eisele I. Fabrication of a hybrid field-effect structure for gas detection with diverse sensitive materials. Sensors and Actuators B. 1994;**19**:632-636

[32] Oprea A, Simon E, Fleischer M, Frerichs PH, Wilbertz C, Lehmann M, Weimar U. Flip-chip suspended gate field effect transistors for ammonia detection. Sensors and Actuators B. 2005;**111-112**:582-586

[33] Gergintschew Z, Kornetzky P, Schipanski D. The capacitively controlled field effect transistor (CCFET) as a new low power gas sensor. Sensors and Actuators B. 1996;**36**:285-289

[34] Burgmair M, Frerichs PH, Zimmer M, Lehmann M, Eisele I. Field effect transducers for work function gas measurements: Device improvements and comparison of performance. Sensors and Actuators B. 2003;**95**:183-188

[35] Wilbertz C, Frerichs PH, Freund I, Lehmann M. Suspended-gate- and Lundstrom-FET integrated on a CMOS-chip. Sensors and Actuators A. 2005;**123-124**:2-6

[36] Tans JS, Verschueren RMA, Dekker C. Room-temperature transistor based on a single carbon nanotube. Nature. 1998;**393**:49-52

[37] Martel R, Schmidt T, Shea RH, Hertel T, Avouris P. Single- and multi-wall carbon nanotube field-effect transistors. Applied Physics Letters. 1998;**73**:2447-2449

[38] Wilbertz C, Frerichs PH, Freund I. Carbon nanotube gas and vapor sensors. Angewandte Chemie. 2008;**47**:6550-6570

[39] Kong J, Franklin RN, Zhou C, Chaplin GM, Peng S, Cho K, Dai H. Nanotube molecular wires as chemical sensors. Science. 2000;**287**:622-625

[40] Star A, Joshi V, Skarupo S, David T, Gabriel CPJ. Gas sensor array based on metal-decorated carbon nanotubes. The Journal of Physical Chemistry B. 2006;**110**:21014-21020

[41] Star A, Han RT, Joshi V, Gabriel CPJ, Grüner G. Nanoelectronic carbon dioxide sensors. Advanced Materials. 2004;**16**:2049-2052

[42] Someya T, Small J, Kim P, Nuckolls C, Yardley TJ. Alcohol vapor sensors based on single-walled carbon nanotube field effect transistors. Nano Letters. 2003;**3**:877-881

[43] Peng G, Tisch U, Haick H. Detection of nonpolar molecules by means of carrier scattering in random network of carbon nanotubes: Toward diagnosis of diseases via breath samples. Nano Letters. 2009;**3**:347-351

[44] Kuang Z, Kim NS, Crookes-Goodson JW, Farmer LB, Naik RR. Biomimetic chemosensor: Designing peptide recognition elements for surface functionalization of carbon nanotube field effect transistors. ACS Nano. 2010;**4**:452-458

[45] Goldsmith RB, Mitala JJ, Josue J, Castro A, Lerner BM, Bayburt HT, Khamis MS, Jones AR, Brand GJ, Sligar GS, Luetje WC, Gelperin A, Rhodes AP, Discher MB, Johnson CAT. Biomimetic chemical sensors using nanoelectronic readout of olfactory receptor proteins. ACS Nano. 2011;**5**:5408-5416

[46] Staii C, Johnson TA. DNA-decorated carbon nanotubes for chemical sensing. Nano Letters. 2005;**5**:1774-1778

[47] Kuang Z, Kim NS, Crookes-Goodson JW, Farmer LB. Naik RR. Differentiation of complex vapor mixtures using versatile DNA−carbon nanotube chemical sensor arrays. ACS Nano. 2013;**7**:2800-2807

[48] Talin AA, Hunter LL, Léonard F, Rokad B. Large area, dense silicon nanowire array chemical sensors. Applied Physics Letters. 2006;**89**:1531021-1531023

[49] Mcalpine CM, Ahmad H, Wang D, Heath RJ. Highly ordered nanowire arrays on plastic substrates for ultrasensitive flexible chemical sensors. Nature Materials. 2007;**6**:379-384

[50] Chen HZ, Jie SJ, Luo BL, Wang H, Lee SC, Lee TS. Applications of silicon nanowires functionalized with palladium nanoparticles in hydrogen sensors. Nanotechnology. 2007;**18**:345502

[51] Paska Y, Stelzner T, Christiansen S, Haick H. Enhanced sensing of nonpolar volatile organic compounds by silicon nanowire field effect transistors. ACS Nano. 2011;**5**: 5620-5626

[52] Shehada N, Brönstrup G, Funka K, Christiansen S, Leja M, Haick H. Ultrasensitive silicon nanowire for real-world gas sensing: Noninvasive diagnosis of cancer from breath volatolome. Nano Letters. 2015;**15**:1288-1295

[53] Clavaguera S, Carella A, Caillier L, Celle C, Pécaut J, Lenfant S, Vuillaume D, Simonato PJ. Sub-ppm detection of nerve agents using chemically functionalized silicon nanoribbon field-effect transistors. Angewandte Chemie. 2010;**49**:4063-4066

[54] Li C, Zhang D, Liu X, Han S, Tang T, Han J, Zhou C. In_2O_3 nanowires as chemical sensors. Applied Physics Letters. 2003;82:1613.

[55] Zou X, Wang J, Liu X, Wang C, Jiang Y, Wang Y, Xiao X, Ho CJ, Li J, Jiang C, Fang Y, Liu W, Liao L. Rational design of sub-parts per million specific gas sensors array based on metal nanoparticles decorated nanowire enhancement-mode transistors. Nano Letters. 2013;**13**:3287-3292

[56] Kolmakov A, Klenov OD, Stemmer S, Moskovits M. Enhanced gas sensing by individual SnO_2 nanowires and nanobelts functionalized with Pd catalyst particles. Nano Letters. 2005;**5**:667-673

[57] Kuang Q, Lao SC, Li Z, Liu ZY, Xie XZ, Zheng SL, Wang LZ. Enhancing the photon- and gas-sensing properties of a single SnO_2 nanowire based nanodevice by nanoparticle surface functionalization. The Journal of Physical Chemistry C. 2008;**112**:11539-11544

[58] Mubeen S, Moskovits M. Gate-tunable surface processes on a single-nanowire field-effect transistor. Advanced Materials. 2011;**23**:2306-2312

[59] Liao L, Zheng Z, Yan B, Zhang XJ, Gong H, Li CJ, Liu C, Shen XZ, Yu T. Morphology controllable synthesis of α-Fe_2O_3 1D nanostructures: Growth mechanism and nanodevice based on single nanowire. The Journal of Physical Chemistry C. 2008;**112**:10784-10788

[60] Du J, Liang D, Tang H, Gao PAX. InAs nanowire transistors as gas sensor and the response mechanism. Nano Letters. 2009;**9**:4348-4351

[61] Zhang X, Fu M, Li X, Shi T, Ning Z, Wang X, Yang T, Chen Q. Study on the response of InAs nanowire transistors to H_2O and NO_2. Sensors and Actuators B. 2015;**209**:456-461

[62] Kulkarni SG, Reddy K, Zhong Z, Fan X. Graphene nanoelectronic heterodyne sensor for rapid and sensitive vapour detection. Nature Communications. 2014;**5**:4376

[63] Schedin F, Geim KA, Morozov VS, Hill WE, Blake P, Katsnelson IM, Novoselov SK. Detection of individual gas molecules adsorbed on graphene. Nature Materials. 2007;**6**:652-655

[64] Dan Y, Lu Y, Kybert JN, Luo Z, Johnson TCA. Intrinsic response of graphene vapor sensors. Nano Letters. 2009;**9**:1472-1475

[65] Li H, Yin Z, He Q, Li H, Huang X, Lu G, Fam WHD, Tok LYA, Zhang Q, Zhang H. Fabrication of single- and multilayer MoS_2 film-based field-effect transistors for sensing NO at room temperature. Small. 2012;**8**:63-67

[66] Lin FY, Xu Y, Lin YC, Suen WY, Yamamoto M, Nakaharai S, Ueno K, Tsukagoshi K. Origin of noise in layered $MoTe_2$ transistors and its possible use for environmental sensors. Advanced Materials. 2015;**27**:6612-6619

[67] Huo N, Yang S, Wei Z, Li SS, Xia BJ, Li J. Photoresponsive and gas sensing field-effect transistors based on multilayer WS_2 nanoflakes. Scientific Reports. 2014;**4**:5209

[68] Sundgren H, Lundström I, Winquist F, Lukkari I, Carlsson R, Wold S. Evaluation of a multiple gas mixture with a simple MOSFET gas sensor array and pattern recognition. Sensors and Actuators B. 1990;**2**:115-123

[69] Sundgren H, Winquist F, Lukkar I, Lundström I. Artificial neural networks and gas sensor arrays: Quantification of individual components in a gas mixture. Measurement Science and Technology. 1991;**2**:464-469

[70] Wang B, Cancilla CJ, Torrecilla SC, Haick H. Artificial sensing intelligence with silicon nanowires for ultraselective detection in the gas phase. Nano Letters. 2014;**14**:933-938

Chapter 9

Transistors as an Emerging Platform for Portable Amplified Biodetection in Preventive Personalized Point-of-Care Testing

Zhihui Yi and Jonathan Sayago

Additional information is available at the end of the chapter

http://dx.doi.org/10.5772/67794

Abstract

The impressive improvement in biomolecular detection has gone from simple chemical methods to sophisticated high throughput laboratory machines capable of accurately measuring the complex biological components and interactions. In the following chapter, we focus our attention on transistor-based devices as an emerging platform for easy-to-use, portable amplified biodetection for preventive personalized medical applications and point-of-care testing. Electronic sensing devices comprise biosensors based on field-effect transistors (bio-FETs) and organic electrochemical transistors (OECTs). Transistor sensing devices can transduce electronic and ionic signals thereby creating an effective human-machine communication channel. In this chapter, we survey the progress done on the development of transistor innovative concepts to examine biological processes, i.e., biosensors integrated with textiles, flexible substrates, and biocompatible materials. Electrochemical and field-effect transistors can operate at low voltages possibly serving for highly sensitive, selective, and real-time sensing devices. The exploration of biosensors integrates different disciplines such as organic electronics, biology, electrochemistry, and materials science.

Keywords: bio-FETs, OECTs, transistor biosensors, electrolyte-gated transistors

1. Introduction

Biosensors are devices that incorporate biological sensing elements or bioreceptors to detect specific molecule/chemical analytes and produce a measurable signal (current, voltage, and

INTECH
open science | open minds

© 2017 The Author(s). Licensee InTech. This chapter is distributed under the terms of the Creative Commons Attribution License (http://creativecommons.org/licenses/by/3.0), which permits unrestricted use, distribution, and reproduction in any medium, provided the original work is properly cited.

color change). Enzymes are protein molecules that act as biological catalysts that bind/react highly specific to certain molecules therefore enzymes can be excellent bioreceptors. The transducer is the mechanism by which selective binding of analytes and bioreceptors is converted into a measurable signal. Common transducers are based on optical, electrochemical, and electronic signal modulations upon addition of the analyte.

Electronic devices based on polymer electrodes, organic thin-film transistors, and organic light-emitting diodes can be interfaced with biological moieties, i.e., cells, microorganisms, proteins, oligonucleotides, small molecules, for medical applications, and environmental and food quality control [1–7]. The scope of bioelectronics is shown in **Figure 1** [7]. Transistors, polymer electrodes, and organic light-emitting diodes can be coupled with recognition element bioreceptors, i.e., enzymes, nucleic acids (DNA), or antibodies to selectively detect an analyte, i.e., proteins, complementary DNA chains, viruses, nutrients, hormones, collected from blood, urine, or saliva [8, 9]. Transistor-based biosensors can be divided into field-effect transistor biosensors (bio-FETs), discussed in Section 2 and organic electrochemical transistors (OECTs), discussed in Section 3.

1.1. Background of biosensors and main transducer mechanisms

Since the introduction of insulin as a treatment for diabetes, monitoring glucose in blood became an important issue. Glucose sensors are nowadays by far the most successful commercial application of biosensors with more than 85% share of a multibillion dollar market in the USA [8, 10]. For this reason, glucose biosensors lead the path toward the development of new biosensing concepts.

The main transducer mechanisms involve optical, electrochemical, and electronic processes.

1.1.1. Optical transducers

The early glucose biosensors were based on colorimetry. Colorimetry is a technique in which the color of a solution is taken as an index of the composition of the solution. The color of the

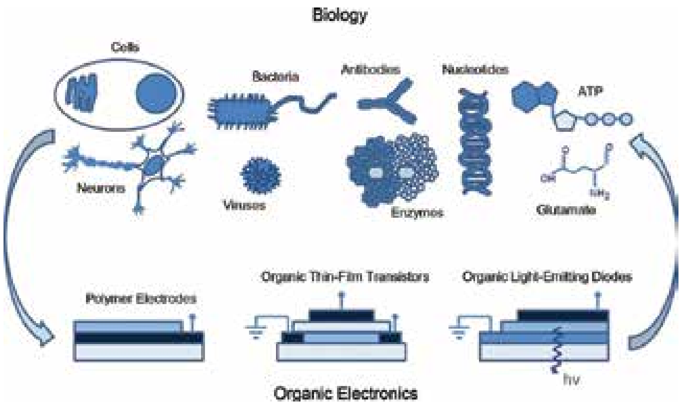

Figure 1. A cartoon showing the scope of organic bioelectronics [7]. Copyright © Materials Research Society 2010.

solution can be modified by a chemical reaction and the concentration of its constituents can be revealed by comparison with a suitably prepared set of color standards in a color comparator [11]. The color comparison of the solution with its standard can be made visually or with a colorimeter. Colorimeters are devices that measure light absorption or reflection in the visible spectrum.

Most of the colorimetric methods to measure glucose in blood produce a color change by the reduction of an aromatic organic compound. The introduction of Dextrostix (Ames Co.) in 1964 provided a simple tool to measure blood glucose. Dextrostix is a cellulose strip with reagents that vary in color and intensity as a function of the amount of glucose present in the blood [12]. The reagents in Dextrostix are glucose oxidase, peroxidase, and a chromogen (i.e., tetramethylbenzidine). Glucose in blood samples is first oxidized into gluconolactone and eventually into gluconic acid [13]. This oxidation reaction is assisted by the enzyme glucose oxidase (GOx) biological catalyst. Oxygen dissolved in blood is necessary to carry this oxidation process and the by-product is hydrogen peroxide (H_2O_2). Hydrogen peroxide then reacts with the chromogen system to result in a specific color pattern specific to the glucose concentration in blood.

To avoid the operator subjective comparison of the strips by visual inspection, the color change in Dextrostix strips can be evaluated with a simple reflectance meter or with more sophisticated spectrophotometers.

Despite the simplicity of optical transducers, its early development was hampered by the requirement of bulky and costly optical equipment or by the intrinsic inaccuracy of visual inspection [14].

One possible solution may be replacing costly reflectance meters or spectrophotometers with software algorithms to enable digital cameras in smartphones quantitative screening when fast diagnosis is needed. Common CMOS cameras found in smartphones have successfully monitored glucose, protein, and pH in artificial urine with interphone repeatability and minimal operator intervention [15].

Silicon optical photonic-crystal waveguide arrays capable of sensing up to 128 compounds within a few millimeters of space with excellent signal-to-noise ratio have been recently reported [16, 17]. The operating principle is similar to that in surface plasmon resonance sensors that measure the change in reflectivity of a thin gold metal film deposited on a glass prism upon addition of the analyte. Photonic-crystals are optical structures in which a periodic modulation of the refractive index exists for a given material. Depending on the exact periodic modulation, a given bandwidth of light cannot be transmitted through such material thus defining a photonic band gap. A given bandwidth of light can be confined in the waveguide. Since the band gap is very sensitive to the refractive index at the crystal surface, when in contact with aqueous medium, biomolecules adhere to the crystal surface and modify the refractive index resulting in a shift in the band gap. This property can be utilized for biosensing.

Surface functionalization with a binding bioreceptor of the photonic-crystal can be employed to improve analyte selectivity. While the requirement of additional optical and electronic components makes photonic-crystal biosensors relatively complex they can be made ultracompact in a single integrated chip embedded in an easy-to-use and portable device.

1.1.2. Electrochemical transducers

Electrochemical sensors originally called "enzyme electrodes"emerged as highly sensitive, easy-to-use, portable, and user-friendly sensing devices. Electrochemical biosensors are nowadays the most widespread transducers for glucose sensing [18].

Electrochemical sensors measure electrochemical processes occurring in an electrode functionalized with enzyme bioreceptors immersed in an electrolyte solution containing the analytes. Electrochemical processes include the measurement of tiny changes of voltage (potentiometry), current (amperometry), or resistance/conductance (conductometry) specific to the presence of an analyte. Electrochemical sensors usually involve two electrodes, the working electrode and the counter electrode under which a voltage is applied. A third reference electrode can be employed to set and monitor the potentials vs an absolute reference value.

In the absence of the reference electrode, it is somewhat difficult to measure a small current change in a reproducible way, thus the reproducibility of electrochemical sensors is generally less accurate than those employing optical transducers [19]. However, because electrochemical sensors can be miniaturized and manufactured inexpensively, they actually dominate the biosensor market [10, 19, 20].

Electrochemical glucose sensors alike their analogue glucose optical sensors employ glucose oxidase (GOx) enzyme to bind the glucose molecule and facilitate its oxidation process. Oxygen and GOx oxidize glucose into gluconic acid and generate hydrogen peroxide as by-product. During this process, GOx is reduced and can be regenerated (oxidized) by adding ferricyanide which in turn is reduced into ferrocyanide. A metal electrode can regenerate ferrocyanide (reduced form) into ferricyanide. The reduction-oxidation cycle of glucose generates electrons at the metal electrode and can induce a spontaneous electric current (with no voltage applied) proportional to the glucose concentration. To obtain a quick glucose measurement, a change in the electrical current is measured as a function of a voltage applied between the electrolyte and the metal electrode.

Another popular redox system to detect glucose is based on enzyme glucose dehydrogenase as catalyzer and nicotinamide adenine dinucleotide, replacing oxygen to oxidize glucose [21, 22].

1.1.3. Electronic transducers

After the discovery of the enzyme electrode, ion-sensitive field-effect transistors (ISFETs), **Figure 2** (right), in which the gate electrode in a conventional metal-organic field-effect transistor (MOSFET), **Figure 2** (left), is replaced by an aqueous solution and a reference electrode, emerged to measure ionic species in electrochemical and biological environments. Double layers formed at the oxide electrolyte interface result in a different conductive state at the transistor channel proportional to the electrolyte ion concentration [23]. The gate oxide can be sensitive to specific ions similar to a glass electrode [24] or can be modified with a selective membrane or molecular receptors to filter specific ions [25, 26]. ISFETs are not strictly biosensors because they do not employ a biomolecular receptor as an active component to sense ions but they laid the foundation toward field-effect transistor biosensors (bio-FETs).

Electronic transducers include the field-effect transistor and the organic electrochemical transistor, reviewed in greater detail in the following sections.

http://dx.doi.org/10.5772/67794

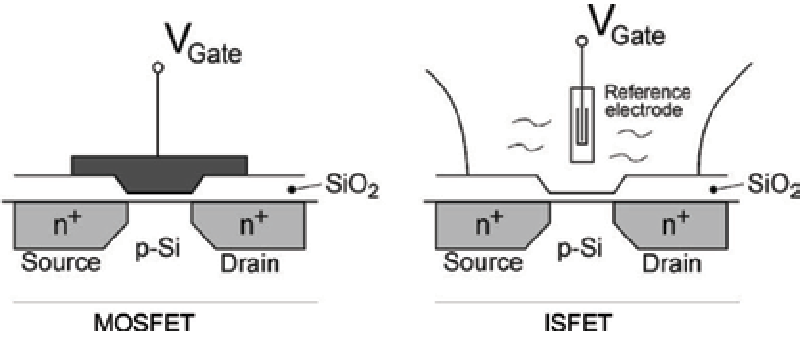

Figure 2. Schematic representation of MOSFET (left) and ISFET (right) typical structures [27]. Copyright © 2002 Elsevier Science B.V.

2. Field-effect transistor-based biosensors

ISFETs can be considered a close version of field-effect transistor-based biosensors (bio-FETs). Bio-FETs have the transistor semiconductor channel directly coupled with molecular bioreceptors sensitive to specific analyte molecules in the electrolyte without an insulating layer and can be directly gated through an electrolyte medium or through a back gate/gate-insulator as shown in **Figure 3**. The molecular bioreceptors act as a filter that allows only one type of analyte to selectively interact with the semiconductor channel. The analyte of interest can bind covalently to a specific molecular bioreceptor and change the semiconductor doping state. The conductive state of the functionalized semiconductor channel can be tracked by measuring the transistor drain-source current as a function of the electrolyte analyte concentration and the voltages applied.

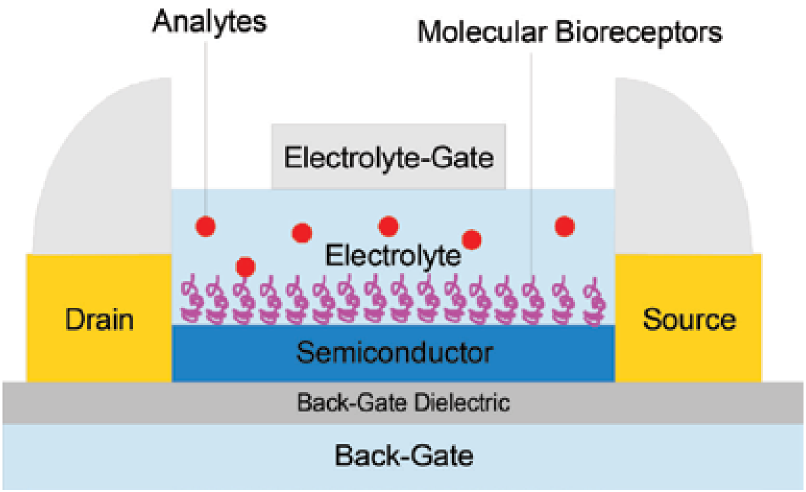

Figure 3. Schematic structure of field-effect transistor-based biosensors (bio-FETs).

Sensing mechanism may differ significantly when applied to different analyte molecules despite the common architectures among bio-FETs. As a thought experiment, a substance impermeable to ions that prevents the ionic doping of the semiconductor can be placed on top of the transistor channel. If the permeability of this substance changes following an interaction with a specific analyte allowing access of ions from the electrolyte into the semiconductor, the increased permeability of the barrier can be revealed by the modulation of the semiconductor conductive state as a function of a gate voltage [28]. Ions in proximity with the semiconductor can induce a doping/dedoping process by the field-effect or tune the effective energy barrier height required to inject charge carriers from the drain-source metal electrodes into the semiconductor. Because the chemical structure of the semiconductor remains unmodified, desorption of the analyte or ionic species from the semiconductor surface is possible for real-time reversible sensor detection.

Sensing DNA hybridization with FET devices is paving the way toward virus sensing and DNA disease prevention [29]. The working mechanism of DNA field-effect transistor sensors deserves attention. Carbon nanotube FETs typically operate as unconventional Schottky barrier transistors in which current modulation occurs primarily by tuning the contact resistance rather than the channel conductance [30].

Synthetic DNA hybridization consisting of random generated sequences and different oligo lengths (15 and 30 mer) was detected with bio-FETs made of gold drain-source electrodes functionalized with MercaptoHexanol and single-walled carbon nanotube channel material, **Figure 4** (left). Selective response to addition of complementary DNA was observed and almost no change occurred upon addition of phosphate-buffered saline (PBS) solution or mismatched DNA, **Figure 4** (right). MercaptoHexanol self-assembled monolayer provides a nice passivation on gold electrodes against nonspecific binding of mismatched DNA and provides ideal conditions for efficient hybridization with nearly 100% binding efficiency of analytes carrying complementary sequences. The formation of double stranded DNA on gold electrodes lowered the effective work function of gold facilitating charge carrier injection.

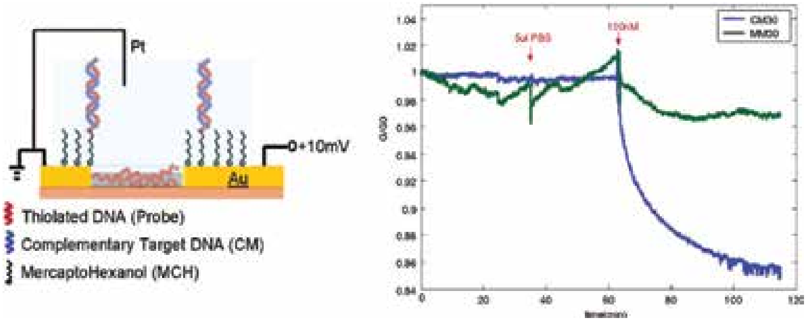

Figure 4. Schematic illustration of DNA FETs sensing device in operation (left) and real-time normalized conductance monitoring of 30 mer DNA hybridization in phosphate-buffered saline solution, pH 7.4. Two other devices were used to simultaneous test complementary (CM30) and mismatched (MM30) DNA buffer solutions. Selective response to addition of complementary DNA is observed and almost no change upon addition of phosphate-buffered saline solution or mismatched DNA [29]. Copyright © 2006 American Chemical Society.

Real-time DNA biosensors to detect cystic fibrosis genes have been demonstrated with sensitivities up to the femtomolar range [31]. These bio-FETs hinge on silicon nanowire (SiNWs) channels functionalized with peptide nucleic acid receptors that are complementary to the wild type of cystic fibrosis genes. Tailoring SiNWs is relatively easy due to the well-known modification of silicon oxide surfaces as opposed to graphene or carbon complex surfaces. Although a nonspecific interaction of negatively charged oligonucleotides with NW sensors was observed, specific detection was possible by analyzing the magnitude of the conductance change following introduction of wild vs mutant DNA sample solutions. After detection, the conductance was reversible to its original state upon addition of DNA-free solution.

Highly selective and sensitive real-time protein detection was reported with SiNW bio-FETs [25]. Nanotube/nanowire semiconductor channels offer higher surface area than planar devices and increase sensitivity to the point that single-molecule detection is possible. Sensing of calcium ions (Ca^{2+}) was possible by immobilizing calmodulin onto SiNW surfaces. A drop in conductance upon addition of 25 μM Ca^{2+} solution was observed with a subsequent recovery in conductance when the device was rinsed with a Ca^{2+} free solution, **Figure 5**. Control experiments with unmodified SiNWs did not show a change in conductance when Ca^{2+} ions were added.

SiNW arrays modified with antibodies for influenza A or adenovirus displayed selective conductance change corresponding to single-virus binding/unbinding of influenza A and paramyxovirus [32]. Many bio-FETs can be built in parallel for multiplexed biodetection.

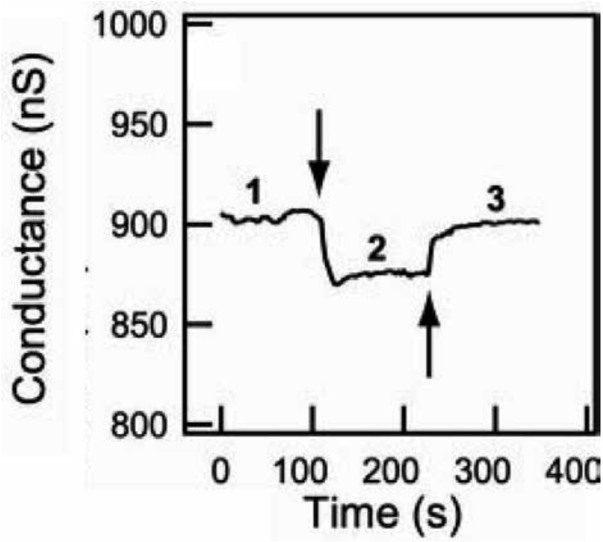

Figure 5. Real-time detection of calcium ions. Plot of conductance vs time of a bio-FET channel of calmodulin-terminated silicon nanowire where regions 1 and 3 correspond to the operation under pure buffer solution and region 2 corresponds the operation under 25 μM Ca^{2+} solution [25]. Copyright © 2001 by the American Association for the Advancement of Science.

No purification of virus samples was required in these measurements. **Figure 6** shows the conductance vs time recorded simultaneously for influenza A (nanowire 1) and adenovirus group III (nanowire 2) sensors set in proximity with a microfluidic system that allows the sequential flow of 1–4 adenovirus, influenza A, pure solution, and 1:1 mix solution of adenovirus and influenza A, respectively. Adenovirus is negatively charged in the solution resulting in a positive conductance change of nanowire 2 with an on-time duration of ca 16 s. Negative conductance change of similar duration was observed when influenza A was introduced and binded to nanowire 1. Bottom arrows in **Figure 6** indicate singularities in which the proximity of adenovirus in device 1 resulted in a short-lived positive change of conductance ca 0.4 s, and similarly, the proximity of influenza A resulted in a short-lived negative change of conductance in device 2. The excellent binding selectivity, single viral particle sensitivity and selective multiplexed detection enables rapid identification of viral samples as required for robust medical solutions, fundamental virology, and drug discovery.

Label-free amplified biodetection has been reported with floating-gate transistor architectures, **Figure 7** (left), in which the gate voltage is indirectly applied via a secondary electrolyte [33]. In such structures, the semiconductor does not need to be modified with selective bioreceptors and is not in direct contact with the analytes therefore the semiconductor can be selected on its electronic performance and doping mechanism (field-effect vs electrochemical) and not on the ease of its chemical modification or robustness in electrolytes, thereby reducing fabrication complexity. Bioreceptors are set on one part of the floating gate coupled with a secondary electrolyte compartment and entirely separated

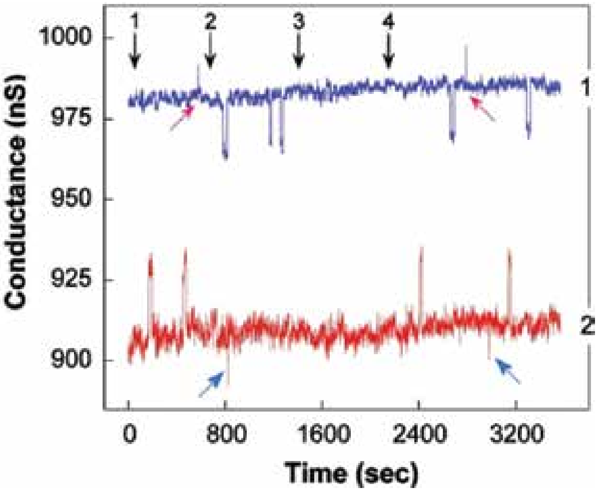

Figure 6. Conductance vs time recorded simultaneously from two silicon nanowire sensors, nanowire 1 was modified with influenza A antibody (top) and nanowire 2 was modified with adenovirus group III antibody (bottom). Arrows 1–4 correspond to the introduction of (1) adenovirus, (2) influenza A, (3) pure buffer, and (4) 1:1 mixture solution of adenovirus and influenza A. Bottom arrows highlight short-duration conductance changes corresponding to nonspecific diffusion of viral particles. Solutions made by 40 viral particles per μl in phosphate buffer 10 μM, pH 6.0 [32]. Copyright © 2014 National Academy of Sciences.

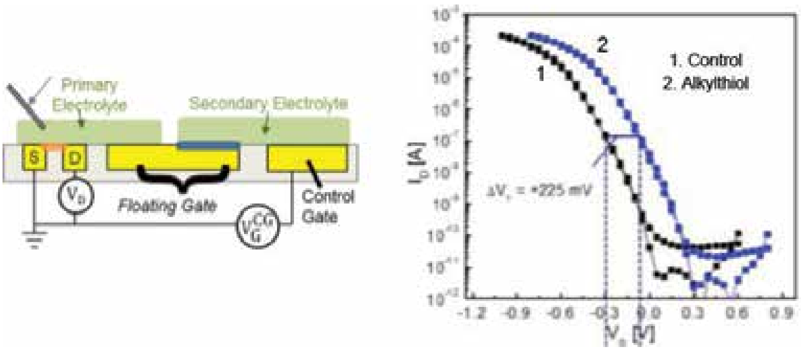

Figure 7. Device architecture of the floating-gate transistor structure (left) and transistor transfer characteristics (right), drain-source current (I_{ds}) vs gate voltage (V_{gs}), of control device, curve 1 and floating-gate functionalized with alkylthiol derivatives right-shifted 225 mV from the control device, curve 2 [33]. Copyright © 2015 American Chemical Society.

from the primary electrolyte [34–36]. The bioreceptor-free gate electrode is coupled with the primary electrolyte. Well established self-assembled monolayer chemistry on metal electrodes can be employed to tune the effective potential of the floating gate for bioelectric signal amplification [37]. Geometric considerations of the gate electrode play a crucial role in the device operation [38, 39]. Self-assembled monolayers of alkylthiol derivatives on the floating gate had a measurable voltage shift (ca. 200 mV) on the transistor electric characteristics, **Figure 7** (right).

Label-free DNA hybridization has been sensed by a floating-gate transistor based on poly(3-hexylthiophene) and an ion gel electrolytes [36]. The DNA is hybridized at the floating gate resulting in a shift in the threshold voltage of the transistor with a relative magnitude proportional to the DNA mismatch. The response of DNA with three mismatched base pairs was undistinguishable from a fully random DNA sequence.

3. Organic electrochemical transistor biosensors

Organic electrochemical transistors (OECTs) are emerging as a promising platform for amplified biodetection with enhanced sensitivity and low voltage (<1 V) operation [33, 40, 41]. OECTs typically consist of a polymer semiconductor included between source and drain electrodes and coupled with a gate electrode through an electrolyte. Polymer semiconductor materials are based on pi-conjugated carbon and hydrogen backbone structures that are relatively soft, flexible, and permeable to ionic species. Polymers can be soluble in organic solvents and be printed on flexible substrates. The gate electrode and the semiconductor channel can be approached as the electrodes of a conventional electrochemical sensor (two electrodes) assigning the transistor channel together with drain and source electrodes as the working electrode and the gate electrode as the counter electrode. By modifying the channel, electrolyte or gate electrode with biochemical receptors, chemical binding events can result in large changes in conductivity in the semiconducting channel. This effect can be the basis for bioelectric signal amplification [28, 34, 42, 43].

To mitigate the reproducibility and sensibility issues related with electrochemical biosensors, a simplified electrochemical transistor architecture can be employed in which the use of high surface area activated carbon electrodes results in sub-1 V operation and renders unnecessary presence of a reference electrode to control the applied potentials [38, 44].

Early OECTs consisted in Au microelectrodes drain-source and gate electrodes and polypyrrole channels in aqueous electrolyte media, i.e., CH_3CN/0.1 M [n-Bu_4N]ClO_4 displaying typical transistor p-type characteristics [45]. When the gate is held at negative voltages, polypyrrole is dedoped and the device is switched off. When the gate voltage is positive, polypyrrole is oxidized resulting in an increase in the channel current, the device is switched on.

Nowadays, polystyrenesulfonate-doped poly(3,4-ethylenedioxythiophene) (PEDOT:PSS) is the most commonly employed channel material in OECTs. PEDOT:PSS is intrinsically a p-type conducting polymer, stable in water, and nontoxic.

Enzymatic glucose OECT biosensors have been reported [46–48]. Hydrophilic ionic liquids like triisobutyl-(methyl)-phosphonium tosylate ([$P_{1,4,4,4}$][Tos]) are particularly interesting as effective enzyme immobilization medium in biological environments [49]. Sensing experiments were carried out by placing enzyme-glucose oxidase (GOx, 500 units per mL) and ferrocene mediator [bis(η-5-cyclopentadienyl)iron] (Fc, 10 mM) in 1.43 mL of [$P_{1,4,4,4}$][Tos] and 50 mL glucose-PBS solution.

Glucose is oxidized by the application of a gate voltage while the enzyme (GOx) is reduced. In the back cycle, oxidation of GOx is coupled with the conversion of Fc to ferricenium ion (Fc^+) which shuttles electrons to the gate electrode (**Figure 8a**) and cations into PEDOT:PSS. PEDOT:PSS is dedoped by metal cations (M^+) (**Figure 8b**) decreasing the drain-source current as a function of glucose concentration. The measured sensitivity of such devices is in the range of 10^{-7}–10^{-2} M [49].

OECTs hormone biosensors have been reported by incorporating Nafion, a material that has high specific affinity for epinephrine hormone molecules, on top of the gate electrode [50]. The sensitivity was improved by introducing gate electrodes modified with SWNTs and graphene flakes which enhanced electrocatalytic activity of the gate electrode compared to that with platinum gates thus improving the detection limit of the device. Sensitivities up to 0.1 nM were obtained.

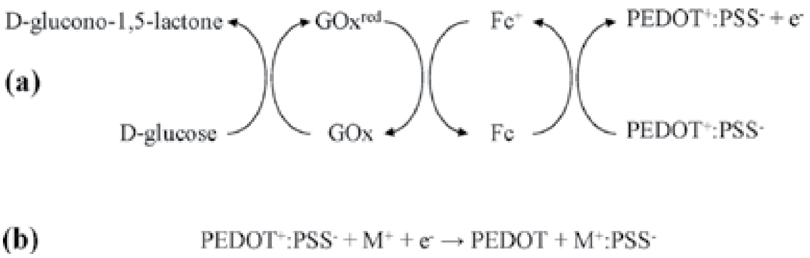

Figure 8. Reactions at (a) the gate electrode and (b) the channel of the OECT [49]. Copyright © 2010, Royal Society of Chemistry.

Label-free, flexible DNA OECT sensors have been demonstrated in flexible microfluidic systems [51]. Single-stranded DNA (ssDNA) probes were immobilized on gold gate electrodes and poly(dimethylsiloxane) (PDMS) microfluidic channels were fixed on top of prepatterned PEDOT:PSS channels (**Figure 9a**) set in contact with gold drain and source electrodes. The device was able to bend on both sides (**Figure 9b**) and its electric characteristics remained consistent before and after bending (**Figure 9c**). Transient curves indicate that the drain-source current reaches a stable plateau value after several seconds of applied gate voltages (**Figure 9d**) revealing ion permeation into the transistor channel [52]. Further investigations revealed that the maximum bending strain was about 5% with negligible effect on the PEDOT:PSS film conductance.

Biocompatible materials have been investigated due to the rapid development of OECTs and their potential use in biological applications. Skin itself can be utilized as a nonconventional gate electrode to sense heart beatings, **Figure 10a**. Campana et al. demonstrated transparent transistors fabricated on biodegradable poly(lactic-co-glycolic acid) substrates to sense heart beatings [53]. Traditional electrocardiograms utilize Ag/AgCl to establish a Faradaic contact between the skin and the electrodes and to sense small voltage

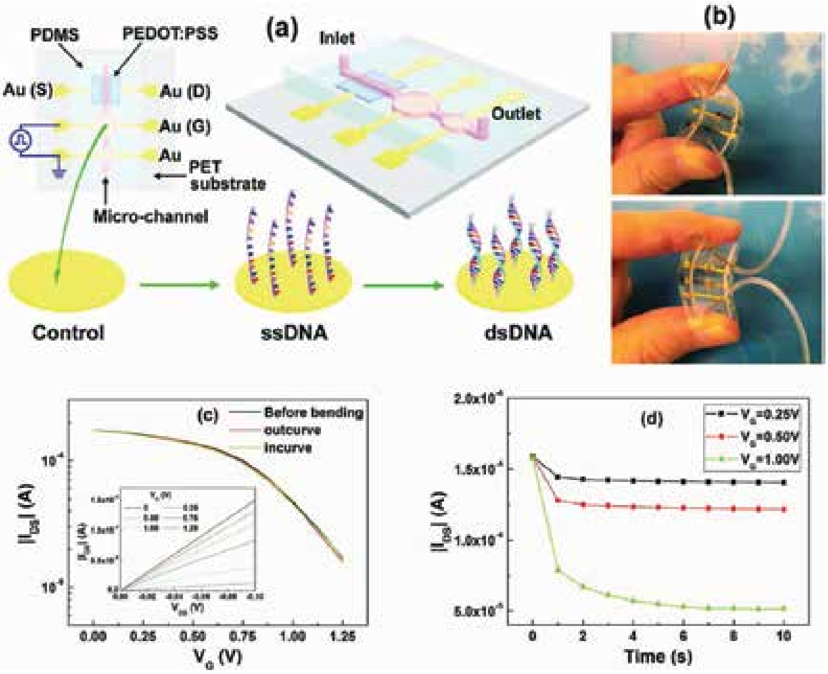

Figure 9. (a) Schematic diagram of the OECT integrated with a flexible microfluidic system and gate gold electrodes before (control) and after DNA modification and DNA hybridization. (b) Photographs of a device bent on both sides. (c) Transfer characteristics (I_{ds} vs V_{gs}) of the OECT measured before and after bending it on both sides, inset shows the output characteristics (I_{ds} vs V_{gs}). (d) Time-dependent channel current of the OECT measured after applying different gate voltages. The drain-source voltage (V_{ds}) in the transfer and time-dependent characteristics was −0.1 V [51]. Copyright © 2011 WILEY-VCH Verlag GmbH & Co. KGaA, Weinheim.

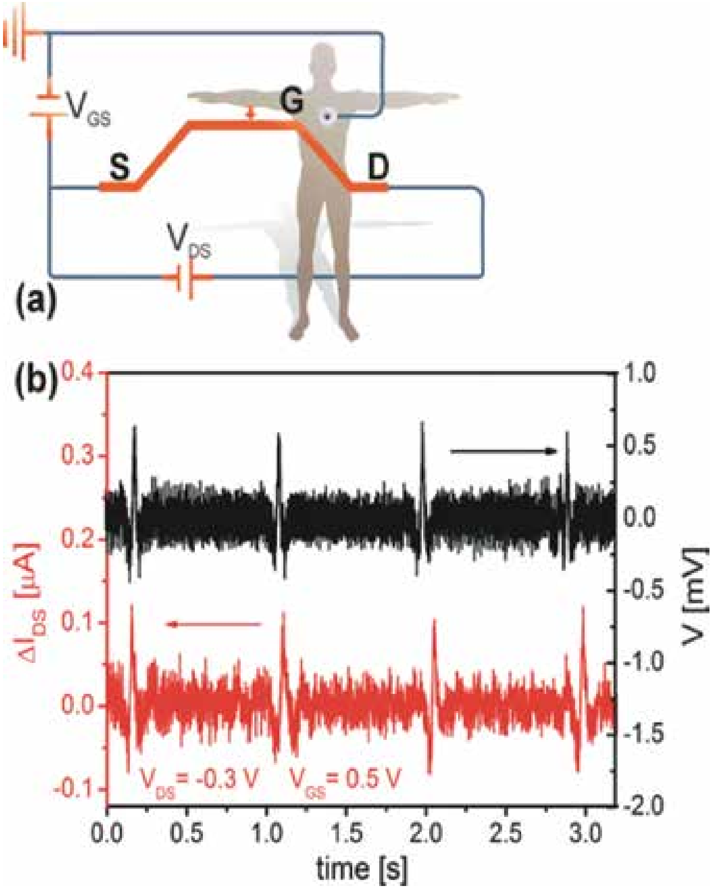

Figure 10. ECG recording with a bioresorbable OECT operated in direct contact with the skin. (a) Wiring diagram of the experiment. (b) Measured drain-source current (bottom, left axis) as obtained during transistor recording (V_{gs} = 0.5 V, V_{ds} = −0.3 V) and comparison with a normal electrocardiogram potentiometric recording with standard disposable leads (top, right axis) [53]. Copyright © 2014 WILEY VCH Verlag GmbH & Co. KGaA, Weinheim.

perturbations that exist on the skin per heart beatings [54]. To reduce the skin's impedance, an electroconductive gel was employed between the skin and PEDOT:PSS channels. The OECTs recorded heartbeats with I_{ds} amplitude of ca 0.1 μA equivalent to measuring signals at the gate with amplitudes of ca 50 μV whereas traditional electrocardiograms monitor spikes at ca 500 μV, **Figure 10b**.

Wearable electrochemical transistors as a platform for real-time detection of biomarkers in external biological fluids was demonstrated with a simple device structure [55]. Drain, source, and gate PEDOT:PSS electrodes were screen printed on textile fabrics. Adrenaline, dopamine, and ascorbic acid in artificial sweet were sensed in the order of tenths of μM concentrations. The device operation was stable despite several hand-washing cycles and deformations.

Flexible lactate sensors with ionogel solid-state electrolytes have been developed [56]. The concentration of lactate in blood can indicate circulatory effectiveness of anaerobic metabolism. The ionogel was prepared by dissolving ferrocene mediator (Fc) in hydrophilic ionic liquid 1-ethyl-3-methylimidazolium ethylsulfate $[C_2mIm][EtSO_4]$ followed by mixing it with monomer N-isopropylacrylamide (NIPAAm) cross-linker N,N′-methylenebis(acrylamide) (MBAAm) and photoinitiator (dimethoxyphenyl)acetophenone DMPA. Under application of a gate voltage, lactic acid was oxidized to pyruvate and Fc was converted to ferricenium ion (Fc^+). Fc^+ transduce electrons to the gate electrode and the PEDOT:PSS channel is dedoped with cations from the solution which leads to a decrease in the drain-source current.

A disposable alcohol breath sensor, to estimate the content of alcohol in the blood, was demonstrated using organic electrochemical transistors [57]. Alcohol dehydrogenase and nicotinamide adenine dinucleotide (NAD^+) enzymes were immobilized on a collagen-based gel. PEDOT:PSS was employed as drain, source, and gate electrodes. When NAD^+ is in contact with ethanol and alcohol dehydrogenase, it can get reduced to NADH and oxidized back to NAD^+, freeing two electrodes that can change the conductivity state of PEDOT:PSS.

4. Conclusion

In this chapter, we reviewed emerging concepts of biosensors based on transistor structures with relevance in the field of easy-to-use, portable, and user-friendly devices for preventive personalized medical applications and point-of-care testing. Soaring healthcare costs, trips to the hospital and the stress and pain related to draw blood for testing represent major inconveniences in patients that require being examined regularly, i.e., insulin-dependent. We believe that the staggering progress done in biosensors based on field-effect transistors and organic electrochemical transistors represents a major opportunity to empower people globally with medical information in a timely and cost-effective way.

Author details

Zhihui Yi[1,2] and Jonathan Sayago[3]*

* Address all correspondence to: jjsayago@ier.unam.mx

1 Department of Materials Science and Engineering, University of Toronto, Toronto, Ontario, Canada

2 Center for Biocomposites and Biomaterials Processing, Faculty of Foresty, University of Toronto, Toronto, Ontario, Canada

3 Instituto de Energías Renovables, Universidad Nacional Autónoma de México, Temixco, Morelos, Mexico

References

[1] Rivnay, J., Owens, R.M., and Malliaras, G.G. (2014) The rise of organic bioelectronics. *Chem. Mater.*, **26** (1), 679–685.

[2] Smela, E. (2003) Conjugated polymer actuators for biomedical applications. *Adv. Mater.*, **15** (6), 481–494.

[3] Yang, W., Thordarson, P., Gooding, J.J., et al. (2007) Carbon nanotubes for biological and biomedical applications. *Nanotechnology*, **18** (41), 412001.

[4] Martin, D.C. (2007) Organic electronics: polymers manipulate cells. *Nat. Mater.*, **6** (9), 626–627.

[5] Berggren, M., and Richter-Dahlfors, A. (2007) Organic bioelectronics. *Adv. Mater.*, **19** (20), 3201–3213.

[6] Svennersten, K., Larsson, K.C., Berggren, M., and Richter-Dahlfors, A. (2011) Organic bioelectronics in nanomedicine. *Biochim. Biophys. Acta BBA – Gen. Subj.*, **1810** (3), 276–285.

[7] Owens, R.M., and Malliaras, G.G. (2010) Organic electronics at the interface with biology. *MRS Bull.*, **35** (06), 449–456.

[8] Yoon, J.-Y. (2013) Introduction, in *Introduction to Biosensors*, Springer New York, New York, NY, pp. 1–14.

[9] Turner, A.P.F., and Karube, I. (eds.) (1989) *Biosensors: Fundamentals and Applications*, Oxford Univ. Press, Oxford.

[10] Turner, A.P.F. (2013) Biosensors: sense and sensibility. *Chem. Soc. Rev.*, **42** (8), 3184–3196.

[11] Standards, U.S.N.B. of (1973) *Publications of the National Bureau of Standards. Catalog*, U.S. Department of Commerce, National Bureau of Standards.

[12] Krynski, I.A., and Logan, J.E. (1967) Dextrostix as a quantitative test for glucose in whole blood. *Can. Med. Assoc. J.*, **97** (17), 1006–1011.

[13] Yoon, J.-Y. (2013) Spectrophotometry and optical biosensor, in *Introduction to Biosensors*, Springer, New York, NY, pp. 121–139.

[14] Danielsson, B. (1990) Calorimetric biosensors. *J. Biotechnol.*, **15** (3), 187–200.

[15] Yetisen, A.K., Martinez-Hurtado, J.L., Garcia-Melendrez, A., et al. (2014) A smartphone algorithm with inter-phone repeatability for the analysis of colorimetric tests. *Sens. Actuators B Chem.*, **196**, 156–160.

[16] Skivesen, N., Têtu, A., Kristensen, M., et al. (2007) Photonic-crystal waveguide biosensor. *Opt. Express*, **15** (6), 3169–3176.

[17] Janz, S., Xu, D.-X., Vachon, M., et al. (2013) Photonic wire biosensor microarray chip and instrumentation with application to serotyping of *Escherichia coli* isolates. *Opt. Express*, **21** (4), 4623–4637.

[18] Updike, S.J., and Hicks, G.P. (1967) The enzyme electrode. *Nature*, **214** (5092), 986–988.

[19] Wang, J. (2008) Electrochemical glucose biosensors. *Chem. Rev.*, **108** (2), 814–825.

[20] Newman, J.D., and Turner, A.P.F. (2005) Home blood glucose biosensors: a commercial perspective. *Biosens. Bioelectron.*, **20** (12), 2435–2453.

[21] Kotzian, P., Janku, T., Kalcher, K., and Vytřas, K. (2007) Catalytic activity of iron hexacyanoosmate(II) towards hydrogen peroxide and nicotinamide adenine dinucleotide and its use in amperometric biosensors. *Anal. Chim. Acta*, **599** (2), 287–293.

[22] Zafar, M.N., Beden, N., Leech, D., et al. (2012) Characterization of different FAD-dependent glucose dehydrogenases for possible use in glucose-based biosensors and biofuel cells. *Anal. Bioanal. Chem.*, **402** (6), 2069–2077.

[23] Bergveld, P. (1972) Development, operation, and application of the ion-sensitive field-effect transistor as a tool for electrophysiology. *IEEE Trans. Biomed. Eng.*, **BME-19** (5), 342–351.

[24] Scholz, F. (2009) From the Leiden jar to the discovery of the glass electrode by Max Cremer. *J. Solid State Electrochem.*, **15** (1), 5–14.

[25] Cui, Y. (2001) Nanowire nanosensors for highly sensitive and selective detection of biological and chemical species. *Science*, **293** (5533), 1289–1292.

[26] Gao, N., Gao, T., Yang, X., et al. (2016) Specific detection of biomolecules in physiological solutions using graphene transistor biosensors. *PNAS*, **113** (51), 14633–14638.

[27] Bergveld, P. (2003) Thirty years of ISFETOLOGY: What happened in the past 30 years and what may happen in the next 30 years. *Sens. Actuators B Chem.*, **88** (1), 1–20.

[28] Yaghmazadeh, O., Cicoira, F., Bernards, D.A., et al. (2011) Optimization of organic electrochemical transistors for sensor applications. *J. Polym. Sci. Part B Polym. Phys.*, **49** (1), 34–39.

[29] Tang, X., Bansaruntip, S., Nakayama, N., et al. (2006) Carbon nanotube DNA sensor and sensing mechanism. *Nano Lett.*, **6** (8), 1632–1636.

[30] Heinze, S., Tersoff, J., Martel, R., et al. (2002) Carbon nanotubes as Schottky barrier transistors. *Phys. Rev. Lett.*, **89** (10), 106801.

[31] Hahm, J., and Lieber, C.M. (2004) Direct ultrasensitive electrical detection of DNA and DNA sequence variations using nanowire nanosensors. *Nano Lett.*, **4** (1), 51–54.

[32] Patolsky, F., Zheng, G., Hayden, O., et al. (2004) Electrical detection of single viruses. *Proc. Natl. Acad. Sci. U. S. A.*, **101** (39), 14017–14022.

[33] White, S.P., Dorfman, K.D., and Frisbie, C.D. (2016) Operating and sensing mechanism of electrolyte-gated transistors with floating gates: building a platform for amplified biodetection. *J. Phys. Chem. C*, **120** (1), 108–117.

[34] Demelas, M., Lai, S., Spanu, A., et al. (2013) Charge sensing by organic charge-modulated field effect transistors: application to the detection of bio-related effects. *J. Mater. Chem. B*, **1** (31), 3811–3819.

[35] Spanu, A., Lai, S., Cosseddu, P., et al. (2015) An organic transistor-based system for reference-less electrophysiological monitoring of excitable cells. *Sci. Rep.*, **5**, 8807.

[36] White, S.P., Dorfman, K.D., and Frisbie, C.D. (2015) Label-free DNA sensing platform with low-voltage electrolyte-gated transistors. *Anal. Chem.*, **87** (3), 1861–1866.

[37] Chaki, N.K., and Vijayamohanan, K. (2002) Self-assembled monolayers as a tunable platform for biosensor applications. *Biosens. Bioelectron.*, **17** (1–2), 1–12.

[38] J. Sayago, F. Soavi, Y. Sivalingam, et al. (2014) Low voltage electrolyte-gated organic transistors making use of high surface area activated carbon gate electrodes. *J. Mater. Chem. C*, **2** (28), 5690–5694.

[39] Kergoat, L., Herlogsson, L., Piro, B., et al. (2012) Tuning the threshold voltage in electrolyte-gated organic field-effect transistors. *Proc. Natl. Acad. Sci.*, **109** (22), 8394–8399.

[40] Kim, S.H., Hong, K., Xie, W., et al. (2013) Electrolyte-Gated Transistors for Organic and Printed Electronics. *Adv. Mater.*, **25** (13), 1822–1846.

[41] Strakosas, X., Bongo, M., and Owens, R.M. (2015) The organic electrochemical transistor for biological applications. *J. Appl. Polym. Sci.*, **132** (15), 41735.

[42] Bartic, C., and Borghs, G. (2005) Organic thin-film transistors as transducers for (bio) analytical applications. *Anal. Bioanal. Chem.*, **384** (2), 354–365.

[43] Tarabella, G., Santato, C., Yang, S.Y., et al. (2010) Effect of the gate electrode on the response of organic electrochemical transistors. *Appl. Phys. Lett.*, **97** (12), 123304.

[44] Tang, H., Kumar, P., Zhang, S., et al. (2015) Conducting polymer transistors making use of activated carbon gate electrodes. *ACS Appl. Mater. Interfaces*, **7** (1), 969–973.

[45] White, H.S., Kittlesen, G.P., and Wrighton, M.S. (1984) Chemical derivatization of an array of three gold microelectrodes with polypyrrole: fabrication of a molecule-based transistor. *J. Am. Chem. Soc.*, **106** (18), 5375–5377.

[46] Zhu, Z.-T., Mabeck, J.T., Zhu, C., et al. (2004) A simple poly(3,4-ethylene dioxythiophene)/poly(styrene sulfonic acid) transistor for glucose sensing at neutral pH. *Chem. Commun.*, **13**, 1556–1557.

[47] Lin, P., Yan, F., Yu, J., et al. (2010) The application of organic electrochemical transistors in cell-based biosensors. *Adv. Mater.*, **22** (33), 3655–3660.

[48] Liao, C., Zhang, M., Niu, L., et al. (2013) Highly selective and sensitive glucose sensors based on organic electrochemical transistors with graphene-modified gate electrodes. *J. Mater. Chem. B*, **1** (31), 3820–3829.

[49] Yang, S.Y., Cicoira, F., Byrne, R., et al. (2010) Electrochemical transistors with ionic liquids for enzymatic sensing. *Chem. Commun.*, **46** (42), 7972–7974.

[50] Mak, C.H., Liao, C., Fu, Y., et al. (2015) Highly-sensitive epinephrine sensors based on organic electrochemical transistors with carbon nanomaterial modified gate electrodes. *J. Mater. Chem. C*, **3** (25), 6532–6538.

[51] Lin, P., Luo, X., Hsing, I.-M., and Yan, F. (2011) Organic electrochemical transistors integrated in flexible microfluidic systems and used for label-free DNA sensing. *Adv. Mater.*, **23** (35), 4035–4040.

[52] Jonathan Sayago, Xiang Meng, Francis Quenneville, et al. (2015) Electrolyte-gated polymer thin film transistors making use of ionic liquids and ionic liquid-solvent mixtures. *J. Appl. Phys.*, **117** (11), 112809.

[53] Campana, A., Cramer, T., Simon, D.T., et al. (2014) Electrocardiographic recording with conformable organic electrochemical transistor fabricated on resorbable bioscaffold. *Adv. Mater.*, **26** (23), 3874–3878.

[54] Searle, A., and Kirkup, L. (2000) A direct comparison of wet, dry and insulating bioelectric recording electrodes. *Physiol. Meas.*, **21** (2), 271.

[55] Gualandi, I., Marzocchi, M., Achilli, A., et al. (2016) Textile organic electrochemical transistors as a platform for wearable biosensors. *Sci. Rep.*, **6**, 33637.

[56] Khodagholy, D., Curto, V.F., Fraser, K.J., et al. (2012) Organic electrochemical transistor incorporating an ionogel as a solid state electrolyte for lactate sensing. *J. Mater. Chem.*, **22** (10), 4440–4443.

[57] Bihar, E., Deng, Y., Miyake, T., et al. (2016) A Disposable paper breathalyzer with an alcohol sensing organic electrochemical transistor. *Scientific Reports*, **6**, 27582.

Edited by Momcilo M. Pejovic and Milic M. Pejovic

In 1959, Atalla and Kahng at Bell Labs produced the first successful field-effect transistor (FET), which had been long anticipated by other researchers by overcoming the “surface states” that blocked electric fields from penetrating into the semiconductor material. Very quickly, they became the fundamental basis of digital electronic circuits. Up to this point, there are more than 20 different types of field-effect transistors that are incorporated in various applications found in everyday’s life. Based on this fact, this book was designed to overview some of the concepts regarding FETs that are currently used as well as some concepts that are still being developed.

Photo by Dmitri Popov / iStock

IntechOpen

ISBN 978-953-51-4804-3